UNIVERSITY OF CALIFORNIA SAN DIEGO

Mechanochemical modeling of structural plasticity in synapses

A dissertation submitted in partial satisfaction of the
requirements for the degree
Doctor of Philosophy

in

Engineering Sciences with a Specialization in Multiscale Biology

by

Miriam Bell

Committee in charge:

Professor Padmini Rangamani, Chair
Professor James Friend
Professor Andrew McCulloch
Professor David Saintillan
Professor Jin Zhang

2022

The dissertation of Miriam Bell is approved, and it is acceptable in quality and form for publication on microfilm and electronically.

University of California San Diego

2022

DEDICATION

To anyone who doesn't think they can do it.

And to my late yellow lab Ranger. Such a good-natured and determined character is rare to find in any species.

EPIGRAPH

Real stupidity beats artificial intelligence every time.

—Terry Pratchett (Hogfather)

It's still magic even if you know how it's done

—Terry Pratchett (A Hat Full of Sky)

TABLE OF CONTENTS

LIST OF FIGURES

LIST OF TABLES

ACKNOWLEDGEMENTS

First, I would like to thank my advisor, Professor Padmini Rangamani, without whom this journey would not have taken place. She has taught me so much more than how to be a scientist. She took a chance on a physicist with no computational background, and supported me through the ups and downs of a PhD journey with a global pandemic thrown in for good measures. She is the best advisor I could have asked for, and I hope to someday achieve a fraction of the poise that she displays in both research and life.

I would like to thank my PhD committee members including Professor James Friend, Professor Andrew McCulloch, Professor David Saintillan, Professor Jin Zhang, and the late Professor Juan Lasheras. They have always been supportive of my ideas and my scientific journey. I would also like to specifically thank Professor Andrew McCulloch for his support of me through the Interfaces Graduate Training Program at UCSD, and Professor Jin Zhang for acting as my co-mentor for that program.

Thanks to everyone who helped me along this adventure in little ways and big ways. I would like to thank my previous professors and research advisors from Harvey Mudd College, Penn State University, and UC Davis. In particular I would like to thank Professors Sharon Gerbode and Elizabeth Orwin who welcomed me into their labs at Mudd and let me explore hands on science. Thank you as well to Professor Lori Bassman who taught my first ever mechanical engineering course which was a big factor in my decision to pursue a PhD in that field.

Looking a bit further back, I would like to thank my high school teachers, in particular my AP physics teacher Mr. Richardson and my AP biology teacher Mr. Peevyhouse, for solidifying my interest in those fields and highlighting that science and the process of learning can be both funny and fun.

Thanks to my lab mates who believed in me and kept me company, current and

former, including Haleh, Ritvik, Chris, Arijit, Allen, Justin, Maven, Cuncheng, Jennifer, Kiersten, Donya, Morgan, Mrunal, Mayte, María, Nate, and many more (wow, the lab has grown!)! Thank you to Allen, Mayte, and María for proofreading this thesis! Thanks to my friends for support and humor including Sam, Jonathan, Jessica, Amy, Caleb, Philip, Travis, Jessie, and many more. An anti-thanks to my orange tabby cat, Rex, who singlehandedly tried to derail my whole education.

Thanks to the UCSD women's club soccer team and UCSD triathlon club team for much needed distractions and exercise.

Thanks to Tapioca Express and chocolate for fueling me. Thanks to ODESZA for awesome music, in particular their A Moment Apart album that got me through both my Department Qualifying Exam and writing this thesis.

Thanks to my pets – Rex, Ranger, Sunny, Ella, and all the hens (except Johnny) – for companionship and their reminders that we are the same. A special thanks to my childhood dog Ranger, who taught me to never give up and to approach every situation with a happy heart.

Thanks to my family – Mark, Renée, Martin, Leila, and Lisa – for instilling in me a love of nature and interest in science, and for their support and love.

Finally, thanks to my partner, Ramy, for too many things to list here, so in summary, for everything.

I would like to thank the many collaborators who have contributed to my thesis. I list each of these contributions below.

Chapter 2, in full, is a reprint of the material as it appears in Design decisions for incorporating spatial and mechanical aspects in models of signaling networks in Current Opinion in Systems Biology, 2021. Bell, Miriam; Rangamani, Padmini, COISB, 2021 [1]. The dissertation author was the primary investigator and author of this material. For

Chapter 2, I would like to acknowledge my coauthor Professor Padmini Rangamani. We thank our various collaborators for discussions on elephants and spherical cows over the years. We also thank Dr. Sage Malingen and Dr. Christopher T. Lee for their comments. I would like to acknowledge my funding from a National Defense Science and Engineering Graduate (NDSEG) Fellowship and Air Force Office of Scientific Research FA9550-18-1-0051 to P.R.

Chapter 3, in full, is a reprint of the material as it appears in Gαq-mediated calcium dynamics and membrane tension modulate neurite plasticity in Molecular Biology of the Cell, 2020. Pearce, Katherine; Bell, Miriam; Linthicum, Will H.; Wen, Qi; Srinivasan, Jagan; Rangamani, Padmini; Scarlata, Suzanne, MBoC, 2020 [2]. The dissertation author was the co-primary investigator and co-author of this paper. For Chapter 3, I would like to acknowledge my coauthors Katherine Pearce, Will H. Linthicum, Professor Qi Wen, Professor Jagan Srinivasan, Professor Padmini Rangamani, and Professor Suzanne Scarlata. We thank various members of the Rangamani and Scarlata labs for valuable discussion and manuscript review. We thank Sayed Iman Mousavi (Yale University) and Erkan Tuzel (Temple University) for writing the Re-Track program. I would like to acknowledge my funding from the UCSD Interfaces Graduate Training Program and the San Diego Fellowship, from a National Defense Science and Engineering Graduate (NDSEG) Fellowship, AFOSR Multidisciplinary Research Program of the University Research Initiative (MURI) grant FA9550-18-1-0051 to P.R., and the National Institutes of Health (Grant T32EB009380).

For Chapter 4, I wish to acknowledge Professor Brenda Bloodgood, Professor Padmini Rangamani, Evan Campbell, Jacqueline Griswold, Cuncheng Zhu, and Christopher Lee for valuable discussion.

Chapter 5, in full, is a reprint of the material as it appears in Dendritic spine

geometry and spine apparatus organization govern the spatiotemporal dynamics of calcium in Journal of General Physiology, 2019. Bell, Miriam; Bartol, Tom; Sejnowski, Terrence; Rangamani, Padmini, JGP, 2019 [3]. The dissertation author was the primary investigator and author of this material. For Chapter 5, I would like to acknowledge my coauthors Dr. Tom Bartol, Professor Terrence Sejnowski, and Professor Padmini Rangamani. I would like to thank various members of the Rangamani Lab for valuable discussion, Mariam Ordyan for manuscript review, and Professor Brenda Bloodgood and Evan Campbell for their expertise. We thank Professor Pietro De Camilli and his laboratory for supplying images used to construct the mesh seen in Fig. 5.5d. I would like to acknowledge my funding from the UCSD Interfaces Graduate Training Program and the San Diego Fellowship, AFOSR Multidisciplinary Research Program of the University Research Initiative (MURI) grant FA9550-18-1-0051 to P.R., and the National Institutes of Health (Grant T32EB009380).

Chapter 6, in full, is a reprint of the submitted material Stochastic simulations reveal that dendritic spine morphology regulates synaptic plasticity in a deterministic manner, 2021. Holst, Maven; Bell, Miriam; Lee, Christopher T.; Rangamani, Padmini, 2021 [4]. The dissertation author was the co-primary investigator and co-author of this material. For Chapter 6, I would like to acknowledge my coauthors Maven Holst, Dr. Christopher T. Lee, and Professor Padmini Rangamani. I would like to acknowledge my funding from a National Defense Science and Engineering Graduate (NDSEG) Fellowship.

Chapter 7, in full, is a reprint of the submitted material Crosstalk between biochemical signaling & trafficking governs AMPAR dynamics in synaptic plasticity, 2022. Bell, Miriam; Rangamani, Padmini, 2022 [5]. The dissertation author was the primary investigator and author of this material. For Chapter 7, I would like to acknowledge my coauthor Professor Padmini Rangamani, and my funding from a National Defense Science and Engineering Graduate (NDSEG) Fellowship. We thank members of the Rangamani

Lab for their comments and support.

Chapter 8 contains material from Mechanochemical modeling of AMPAR trafficking by Miriam Bell, Christopher T. Lee, and Padmini Rangamani, which is being prepared for submission. This dissertation author was the primary investigator and author of this paper. For Chapter 8, I would like to acknowledge my coauthors Dr. Christopher T. Lee, and Professor Padmini Rangamani. We thank Dr. Mayte Bonilla Quintana and Dr. Sage Malingen for manuscript feedback. This work was supported by a National Defense Science and Engineering Graduate (NDSEG) Fellowship to M.K.B., a Hartwell Foundation Postdoctoral Fellowship to C.T.L., and Air Force Office of Scientific Research FA9550-18-1-0051 to P.R..

VITA

2016	B. S. in Physics, Harvey Mudd College, Claremont, California
2019-2022	NDSEG Fellow
2022	Ph. D. in Engineering Sciences with a Specialization in Multiscale Biology, University of California San Diego, La Jolla, California

PUBLICATIONS

Miriam Bell, Tom Bartol, Terrence Sejnowski, and Padmini Rangamani: Dendritic spine geometry and spine apparatus organization govern the spatiotemporal dynamics of calcium. The Journal of General Physiology. Aug 2019, 151 (8) 1017-1034; DOI: 10.1085/jgp.201812261

Katherine Pearce*, Miriam Bell*, Will H. Linthicum, Qi Wen, Japan Srinivasan, Padmini Rangamani, and Suzanne Scarlata. Gq-mediated calcium dynamics and membrane tension modulate neurite plasticity. Molecular Biology of the Cell. 31.7 (2020): 683-694. DOI: 10.1091/mbc.E19-09-0536

Rhodora Calizo*, Miriam Bell*, Amit Ron, Mufeng Hu, Smiti Bhattacharya, Nicholas Wong, William Janssen, Geoffrey Perumal, Pal Pederson, Suzanne Scarlata, James Hone, Evren Azeloglu, Padmini Rangamani, and Ravi Iyengar. Cell shape regulates subcellular organelle location to control early Ca2+ signal dynamics in vascular smooth muscle cells. Scientific Reports 10.1 (2020): 1-17. DOI: 10.1038/s41598-020-74700-x

Miriam Bell, Padmini Rangamani. Design decisions for incorporating spatial and mechanical aspects in models of signaling networks. Current Opinion in Systems Biology (2021). DOI: 10.1016/j.coisb.2021.03.004

Haleh Alimohamadi, Miriam Bell, Shelley Halpain, and Padmini Rangamani: Mechanical principles governing dendritic spine shapes. Frontiers in Physiology, 12 (2021).

Maven Holst*, Miriam Bell*, Christopher Lee, and Padmini Rangamani. Stochastic simulations reveal that dendritic spine morphology regulates synaptic plasticity in a deterministic manner. (in revision)

Evan P. Campbell, Ahmed A. Abushawish, Miriam K. Bell, Melita Haryono, Padmini Rangamani, and Brenda L. Bloodgood. Electrical signals in neuronal ER: large, linear, and spatially restricted. (in revision)

Miriam Bell and Padmini Rangamani: Crosstalk between biochemical signaling & trafficking governs AMPAR dynamics in synaptic plasticity. (in revision)

Miriam Bell, Christopher Lee, and Padmini Rangamani: Mechanochemical modeling of AMPAR trafficking. (in preparation)

Miriam Bell*, Christopher Lee*, and Padmini Rangamani: Biophysics of membrane-protein interactions in dendritic spines. (in preparation)

ABSTRACT OF THE DISSERTATION

Mechanochemical modeling of structural plasticity in synapses

by

Miriam Bell

Doctor of Philosophy in Engineering Sciences with a Specialization in Multiscale Biology

University of California San Diego, 2022

Professor Padmini Rangamani, Chair

The ability to adapt is a hallmark of the brain. Unlike most cells in the body, most neurons are not replaced as one ages. Therefore, neurons are highly plastic, modifying themselves biochemically and structurally across multiple lengthscales in a process called synaptic plasticity. The backbone of these modifications lies in a neuron's ability to modulate the strength of its synapses, the connections between neurons. Most excitatory synapses are housed in small subcompartments, $\sim$ 0.1 femtoliter in volume, called dendritic spines. Dendritic spines have characteristic shapes and sizes that correlate to disease, learning, and aging. These spine shapes and sizes change during synaptic plasticity and more specifically structural plasticity. When a dendritic spine receives a signal, it triggers complex biochemical signaling networks that can modulate the synaptic strength

of the dendritic spine, or its synapse, by modulating the number of receptors on its membrane, amongst other modifications. Therefore, there is a coupling and feedback between the biochemical signaling underlying synaptic plasticity and the morphology of dendritic spines.

In this work, we utilize computational and mathematical models to investigate this structure-function relationship in dendritic spines, as well as in larger lengthscale components such as dendrites and neurons. We start with an example of extreme structural plasticity, where a biochemical signal can rupture connections between cells. We show that biochemical signaling can trigger mechanical forces to modulate cellular morphology and neural connections. Next, we investigate how neuronal morphology influences biochemical signaling more closely in the context of synaptic plasticity in dendritic spines. We consider different timescales of signaling starting with voltage propagation during spine activation, and calcium influx into dendritic spines of different morphologies. We find that spine morphology and ultrastructure can impact signaling dynamics even at these early timescales. Finally, we use both a compartmental model and a spatial model to consider the biochemistry underlying synaptic plasticity, and how signaling and receptor trafficking couple during synaptic plasticity. We find that model architecture filters the influence of upstream signaling on synaptic plasticity readouts and that spine morphology, in particular spine size, can act to regulate synaptic plasticity to prevent excessive receptor change. This work strives to emphasize the coupling between spine morphology and biochemical signaling networks that govern synaptic plasticity, creating a foundation for future work to investigate structural plasticity in more detail.

Chapter 1

Structural plasticity: A multi-scale problem

1.1 Introduction

This thesis is a series of investigations into synaptic plasticity, more specifically structural plasticity, organized by timescales and geometric complexity. Synaptic plasticity refers to a synapse's ability to modify its connection strength between its presynaptic and postsynaptic terminals. In this thesis, we focus on modifications to the postsynaptic terminal. The majority of excitatory synapses are housed in small protrusions along the dendrites of neurons called dendritic spines [6]. How dendritic spines modify is of great importance due to their key role in synaptic and neural function.

1.1.1 Synaptic plasticity as neural function

Information propagates through synaptic connections between neurons that compose neural circuits. Synapses must be able to modify their connections for proper neural

function. Neural communication is inherently a multiscale process in regards to length-scales and timescales. Connections occur at individual synapses; synaptic responses sum to create changes on the neuronal level; and neurons propagate the signal to their connections, with rewiring and connection strength changing for the whole circuit. A functional brain depends on each level in this process operating correctly; and the fundamental unit within this large neural process is the synapse. The ability to regulate synaptic strength is the basis of the whole neural network. Therefore, it is vital to understand the process of synaptic, and subsequently structural, plasticity. Within synaptic plasticity, the connection strength of a synapse is referred to as synaptic strength or synaptic weight [7]. In the following, we outline the main biochemical and structural components of structural plasticity and several open questions regarding their interplay.

1.1.2 Biochemical processes underlying synaptic plasticity

Synaptic, and specifically structural, plasticity involves a combination of electrical, biochemical, and mechanical responses. Synapses receive a biochemical signal from the presynaptic terminal, often in the form of a neurotransmitter such as glutamate, which triggers an electrical response in the postsynaptic spine. This electrical response is coupled to a biochemical signaling response that triggers cascades of signaling networks [8]. More specifically, receptors such as α-Amino-3-hydroxy-5-methyl-4-isoxazolepropionic acid receptors (AMPARs) bind glutamate and open, allowing ions to flow down their gradients and electrical potentials, depolarizing the membrane. This initial depolarization can trigger other receptors and channels, such as N-methyl-D-aspartate receptors (NMDARs) and voltage sensitive calcium channels (VSCCs) to open, further depolarizing the membrane. While many ions can flood into or out of the dendritic spine, Ca^{2+} is particularly important as a second messenger that triggers numerous signaling cascades [9].

A plenitude of biochemical signaling species are involved in this pathway, with complex feedback loops, interdependencies, and cascades. Ultimately, these pathways trigger changes to the number of AMPARs at the synapse [10]. This change in AMPAR number effectively modifies how sensitive the synapse is to glutamate release from the presynaptic terminal, adjusting synaptic strength. Therefore, synaptic plasticity is a complex feedback loop where a synapse modifies its connection strength based on its previous history of activation.

Calcium and subsequently CaMKII as key players in synaptic plasticity

There are many unknowns within this biochemical process; in particular, the dependency of AMPAR on various upstream signaling species remains unclear. It is known that calcium plays a key role as a second messenger to propagate spine activation to downstream signaling species [11]. Due to its importance as a signaling molecule in neurons, it has been proposed that Ca^{2+} levels can be correlated to synaptic weight. Several models and theories have been proposed to predict synaptic weight change based on Ca^{2+} dynamics at dendritic spines [12, 13].

A few steps downstream of Ca^{2+} is CaMKII which is one of the most abundant proteins in dendritic spines and is known to be associated with and required for synaptic plasticity [14, 15]. Historically, it was thought that CaMKII dynamics alone could determine synaptic plasticity. However, if CaMKII activity directly determines AMPAR dynamics remains an open question.

AMPAR as a readout for synaptic plasticity

AMPAR density at the synapse is a vital factor that governs synaptic weight and sensitivity to presynaptic input. Therefore, it is a key factor that regulates synaptic strength [16]. However, what is less clear is what factors influence AMPAR dynamics.

CaMKII is known to be biochemically upstream of AMPAR, but additional biophysical factors are proposed to influence AMPAR dynamics. In particular, AMPAR exists in several locations in dendritic spines - on endosomes in the cytoplasm where they can undergo endocytosis and exocytosis, on the spine membrane diffusing laterally, in extrasynaptic pools on dendrites, and bound to scaffolding molecules at the postsynaptic density [17]. How these various pools of AMPAR interact and what governs their exchange and dynamics are not well understood.

1.1.3 Structural processes during structural plasticity

As mentioned above, complex signaling cascades trigger changes to the number of AMPAR at the membrane, modifying the biochemical profile of the synapse. However, these signaling cascades also lead to structural changes in the shape and size of the synapse. During synaptic plasticity, the morphology of the dendritic spine can change as biochemical signaling triggers changes in the actin cytoskeleton [18]. Structural plasticity specifically refers to a neuron's ability to regulate its morphology. An increase in spine volume typically accompanies an increase in AMPAR, while a decrease in spine volume accompanies a decrease in AMPAR. The exact consequences of these increases and decreases in volume are not fully understood.

Additionally, dendritic spines are spatial subcompartments with distinct morphologies [19, 20]. They come in characteristic shapes – filopodial, stubby, thin, and mushroom. These various morphologies have been shown to correspond to distinct developmental stages of the brain and to various disease states [21–23]. Different spine sub-types have been observed to display different structural dynamics; in particular larger mushroom spines are quite stable compared to smaller thin spines which are more dynamic in their structural changes [18]. Therefore, dendritic spines show structure-function relationships,

although those relationships are not fully understood.

Consequences of neuronal morphology on signaling

What remains to be fully understood are the consequences of spine morphology on neuronal events across different lengthscales and timescales. Dendritic spines propagate signals electrically through ion movement and flux across the plasma membrane. What impact does morphology have on fast ion movement and diffusion in dendritic spines and dendrites? Ca^{2+} is one of the ions involved in membrane depolarization in spines and has significant downstream signaling consequences. It is vital to consider how dendritic spine morphology could alter this first step in signal propagation. Furthermore, further downstream AMPAR dynamics could depend on inherently spatial trafficking mechanisms such as membrane diffusion and endocytosis/exocytosis, which are known to have morphological dependencies [24–26].

Spine morphology serves a purpose within synaptic plasticity. While not fully understood, there is a signaling-morphology feedback loop, where biochemical signaling can modify spine morphologies, which in turn affect their signaling dynamics and ultimately their function, see Figure 1.1. Both arrows within this feedback loop need to be considered and depend on a complex interplay between biochemistry and mechanics. More specifically, spine morphology would depend on a combination of actin mechanics and membrane tension [27], which both depend on a combination of biochemical and biophysical factors such as membrane composition, protein-membrane interactions, and osmolarity [28].

1.1.4 Mechanochemical modeling of structural plasticity

Thus, there are many open questions regarding structural plasticity and we can utilize computational tools to start to address them. As experimental tools such as biosensors

and electron microscopy have improved [29], we have observed dendritic spines and synaptic plasticity at finer resolutions and have found increasing complexity. The basis of neural functionality lies in a synapse regulated by a complex interplay between biochemistry and biophysics. In this thesis, we focus on how mathematical and computational models can provide insights into and predictions of the process of structural plasticity, and its coupling between signaling and morphology. Chapter 2 is focused on summarizing the biochemical and biophysical considerations to modeling. This provides a methods background to how we can think about using models to shed light on biological processes. Chapter 3 focuses on an example of extreme structural plasticity where a biochemical signaling network can trigger the destruction of synapses. Chapter 4 delves into how spine morphology could influence membrane voltage propagation at fast timescales. Chapters 5 and 6 consider how dendritic spine morphology could influence fast Ca^{2+} dynamics in both deterministic and stochastic systems and how those Ca^{2+} dynamics could translate to synaptic weight updates. Chapters 7 and 8 focus on the translation of CaMKII dynamics to AMPAR dynamics, the impact of AMPAR trafficking, and how spine morphology influences those biochemical and trafficking effects. We finish with concluding remarks and possible future directions in Chapter 9, with emphasis on coupling between biochemical signaling and structural complexities across multiple lengthscales in neurons.

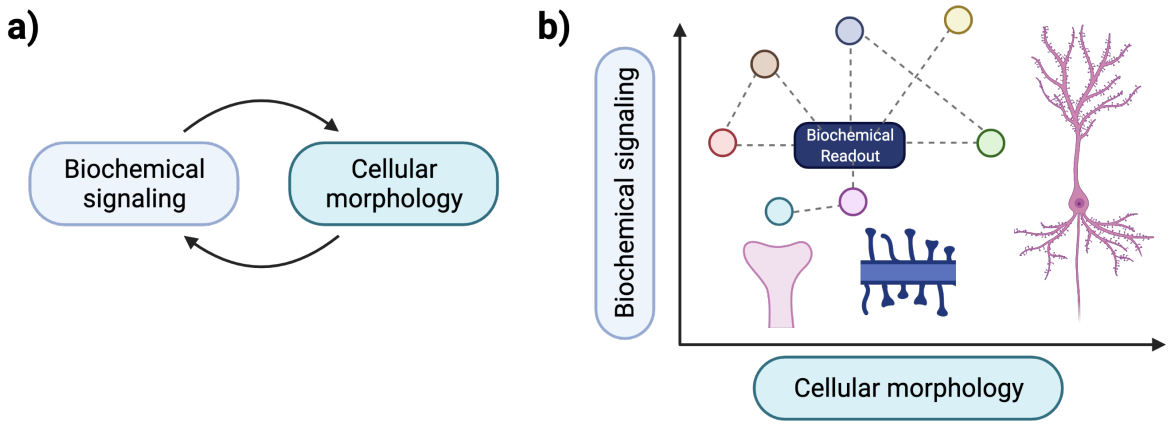

Figure 1.1: Structural plasticity is a feedback loop between biochemical signaling and cellular morphology (a), and involves various length and timescales (b). Created with BioRender.com.

Chapter 2

Design decisions for incorporating spatial and mechanical aspects in models of signaling networks

Available online at www.sciencedirect.com

ScienceDirect

Current Opinion in Systems Biology

Design decisions for incorporating spatial and mechanical aspects in models of signaling networks

Miriam K. Bell and Padmini Rangamani

Abstract

Systems biology is a powerful approach to study complex and expansive biological systems and functions. Recently, advances in experimental imaging, experimental techniques, and model frameworks have emphasized the role of cellular geometry and mechanical forces on signaling dynamics. The complexity of biochemical and biophysical features in cells makes disentangling individual contributions challenging. With nuanced biological details and often subtle differences triggering significant downstream events, decoding signaling dynamics in cells benefits from a multipronged and multidisciplinary approach. Here we discuss the role of cell geometry and mechanics on cellular signaling and discuss exciting advances for integrating geometric information and mechanochemical feedback loops to investigate cellular function and signaling dynamics.

Addresses

Department of Mechanical and Aerospace Engineering, University of California San Diego, Jacobs School of Engineering, 9500 Gilman Drive #0411, La Jolla, CA, 92093, USA

Corresponding author: Rangamani, Padmini (prangamani@ucsd.edu)

Current Opinion in Systems Biology 2021, **25**:70–77

This review comes from a themed issue on **Mathematical Modelling**

Edited by **Stacey D. Finley** and **Vassily Hatzimanikatis**

For a complete overview see the Issue and the Editorial

Available online 25 March 2021

https://doi.org/10.1016/j.coisb.2021.03.004

Keywords

Computational model, Cellular morphology, Ultrastructure, Signaling networks, Mechanics, Feedback loops, Multiscale modeling.

Introduction

The use of mathematical and computational modeling in deciphering signal transduction mechanisms and identifying emergent properties is now fairly commonplace [1]. Owing to the intricate and expansive nature of biological systems, systems biology takes a multidisciplinary approach using theoretical, analytical, and computational models to parse out underlying design principles and emergent properties that aid in cellular function and decision-making. Such models have provided insight into fundamental principles of temporal signaling network dynamics, identification of network motifs, and perhaps most importantly, insights into physiological and diseased states [2,3]. Advances in imaging and fluorescent sensor technologies have revealed that spatiotemporal aspects of signaling are important in identifying the design principles that systems biology models seek [4]. Therefore, mathematical models need to consider the different factors that can give rise to spatial heterogeneity of signaling molecules in cells. For example, increasing evidence points to the role of geometric features of a cell — cell shape, local curvature, spatial localization of signaling molecules, and organelle ultrastructure and location — as important determinants of the dynamics of signaling molecules [5•,6••,7]. Another important emerging area in systems biology is the role of mechanochemical coupling — signaling that is induced due to mechanical forces and the feedback between signaling and cell mechanics [8]. Given that mechanics alters the geometric features listed above, due to alterations of the cytoskeleton at longer timescales, there is tight mechanochemical feedback between signaling, mechanics, and cell shape. Here, we survey recent efforts to capture this feedback in modeling and experiments using the dynamics of calcium and cyclic adenosine monophosphate (cAMP) as model read-outs in different cases. In addition to discussing the insights gained from these models, we also highlight the costs and benefits of building models of increasing spatiotemporal and mechanochemical complexity. Such analyses are important in making design decisions during the model building process as shown in Figure 1.

Considerations of cellular geometry

The continuous improvement of tools such as FRET biosensors and their accompanying analysis techniques provide more detailed insights into cellular spatiotemporal signaling dynamics *in vivo* [9–11]. For instance, recent use of FRET biosensors in β cells has identified the cAMP spatial compartmentalization driven by liquid–liquid phase separation of protein kinase-A (PKA) [12]. Coupled to these imaging advances are new analysis techniques to interpret data. For example, power spectrum analysis and spatiotemporal correlation were used to identify calcium puff events obscured by global calcium elevations due to IP_3 activity [13]. This

Figure 1

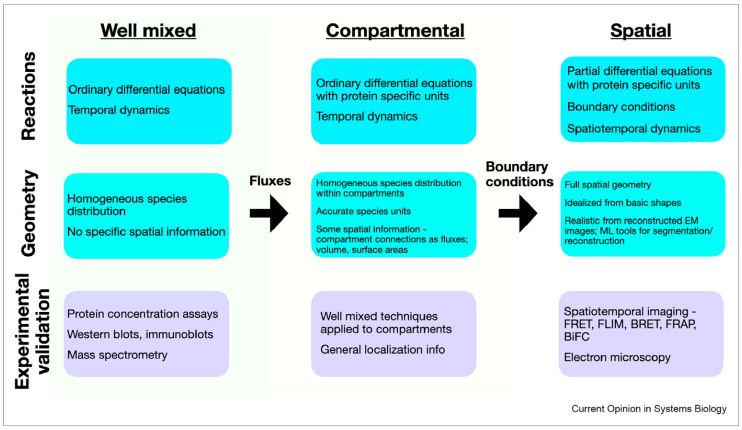

Many options exist for computational modeling of protein signaling dynamics. When constructing a model, one must consider the complexity of reaction and spatial geometry, along with available experimental data for both comparison and validation.

approach, along with TIRF and LLS microscopy, was used to further show that there are two modes of IP_3-mediated calcium release that respond to different calcium dynamics — transient, localized calcium increases versus sustained, global calcium increases [14].

If we consider the above spatially resolved dynamics of calcium and cAMP, what are the modeling aspects that we would need to take into account? To construct a spatial model of a signaling pathway, we first note that a compartmental or well-mixed model can be extremely valuable in setting the nominal timescale for the model response [15,16]. Recent computational models have highlighted the molecular complexity of calcium and cAMP temporal dynamics, identifying signaling frequency filters and linking their dynamics in dendritic spines to synaptic plasticity [17,18••]. These temporal models conduct sensitivity analyses and also help identify the range of kinetic parameters by comparison against experiment [19]. The translation of a well-mixed system, often represented by a system of ordinary differential equations to a spatial system, often represented by partial differential equations (PDEs) capturing reaction–diffusion dynamics, requires not just the specification of initial distributions but also boundary conditions for various compartments, refer Figure 1. Recently, we and others have shown that when membrane bound reactions are written as boundary conditions, they can affect the timescale of localized and global calcium and cAMP dynamics [5•,20,21,22,23,24]. In particular, the relative sizes of different geometric features, such as the volume of the cytoplasm, surface area of the membrane, and distance to internal organelles, can accentuate the consequences of these boundary conditions, skewing spatiotemporal signaling dynamics from well mixed predictions. These boundary conditions are also a powerful way of representing membrane localization of certain protein complexes as we will discuss later in Section "The role of the membrane: more than just a boundary". Next, we need to consider the geometry in which to simulate these PDEs. Idealized geometries such as spheres and ellipsoids are often used as starting places for such models to identify the effect of cell size and shape because they capture the spatial aspects but do away with the internal complexity of a cell [25,20]. Recently, idealized geometry models have been able to provide great insight into the link between cell signaling and shape such as how the height of filopodia in fibroblasts can enhance PKC activation of MARCKs and thus subsequent signaling feedback [26]. An added advantage of idealized models is that the ability to finely tune the geometries of interest allows for specific spatial factors such as plasma membrane to sacroplasmic reticulum (PM-SR)/plasma membrane to endoplasmic reticulum distance (PM-ER) and cellular curvature to be investigated [5•, 20, 22], further discussed in Section "Organelle location and ultrastructure add layers of complexity to spatiotemporal dynamics of signaling molecules". Although many of these manipulations cannot yet be conducted experimentally, computational models allow us to identify if such features are important and what role they may play in tuning the spatiotemporal dynamics of the species of interest.

Although idealized geometries provide insight into the role of certain geometric features and possible design principles, they do not completely capture the complexity of the plasma membrane topology or cellular organization. Indeed, advances in imaging technologies and reconstruction methods have shed light on the surface topology of the plasma membrane and it is far from smooth or flat [27–29]. Do such topological changes matter for signaling dynamics? Studies from mechanics of membrane–protein interactions suggest that local curvature can act as a diffusion barrier for membrane proteins and amplify local concentrations creating a positive feedback between a microdomain and signaling molecules [30–33]. Recent studies using realistic geometries have revealed the estimated calcium dynamics in the absence of fluorescent probes and fate maps of calcium in dendritic spines [34] and showed how microdomain spread of calcium and CaMKII differ along dendrites, depending on coupling between biophysical and biochemical factors [35]. A study of both idealized and realistic cardiac myocyte geometries have emphasized how realistic flux distribution and dyad placement emphasizes spatial heterogeneity and realistic geometries showed different signaling waveforms compared with idealized [36].

Organelle location and ultrastructure add layers of complexity to spatiotemporal dynamics of signaling molecules

In addition to insights on the topology of the plasma membrane, the techniques described above have also opened windows into the locations, sizes, and shapes of organelles [37,27]. These features raise new questions about our understanding of the movement of molecules within the cell. Are these organelles purely diffusion [38•]? Are they active participants in organizing the spatiotemporal dynamics that we observe? Or both? Consider, for example, calcium dynamics in cells — they are regulated by channels on the plasma membrane, mitochondria, and the endoplasmic reticulum. It is well known that internal organelles can act as internal stores for signaling molecules; the endoplasmic reticulum and sarcoplasmic reticulum, for example, are known calcium stores, engaging in calcium buffering and dynamics modulation, but how the morphology or location of the ER or SR influences its buffering capacity or signaling dynamics remains an important consideration. Key examples of these cases are dendritic spines and cardiomyocytes, both of which will be discussed in the following context.

Although the ER exists throughout dendrites and neurons, some portion of dendritic spines have specialized ER structures called spine apparatus in their spine heads. Again, idealized geometries provide insight into how organelles can influence intracellular signaling dynamics. Through spatial modeling efforts that vary geometric factors in idealized spines and spine apparatus, we found that the size of the spine apparatus modulates the calcium dynamics in the spine [20]. Two similar idealized geometry studies demonstrated that the precise location of RyR-containing spine ER determines spine-to-dendrite calcium communication and fast calcium transients [39,40], whereas another found that calcium release from IP_3 receptors selectively mitigates runaway synaptic strengthening at spines with spine apparatus [25]. Other analyses of reconstructed real dendrites have emphasized how ER and other organelle structure and localization could be tied to synaptic function [6••,41]. Experiments suggest that localized signaling subcompartments play key roles in nuanced information transfer such as how ER selectively visits dendritic spines to potentially prevent runaway potentiation of individual synapses [42•,43]. Similarly, the ultrastructure of the ER can introduce additional complexity through complex membrane folding and network structure [20]. For example, in cardiomyocytes, it is well known that the structure of t-tubules and placement of SR is a vital factor for calcium induced calcium release (CICR) [44]. Additionally, the discovery of PM-ER, ER-mitochondria, and ER-membraneless organelle contact sites shows that complex signaling subcompartments exist within cells [45,46].

Just as cellular morphology has been found to influence cellular signaling dynamics, it is safe to assume that ultrastructure morphology will likewise modulate signaling dynamics and add additional control and nuance to cellular signaling capabilities. Therefore the same complexity decisions for cellular geometries also apply to ultrastructure geometries; based on the key questions at hand, trade-offs between biochemical and biophysical complexity versus traceable models and interpretable results must also be decided for ultrastructure models. The use of realistic geometries in modeling signaling is not without its challenges, which we will review in Section "Outlook and future directions".

The role of the membrane: more than just a boundary

Membranes are key components of cells and intracellular organelles, compartmentalizing and protecting cellular components. However, cellular membranes play a much more important role than just as passive boundaries. To communicate and navigate, cells must interact with their environment and therefore must process information through their cellular membrane. The composition of the membrane itself has significant consequences for membrane structure, signaling dynamics, and localization [47,48]. Membrane-protein interactions of membrane-bound, peripheral, and cytosolic proteins are all significant for signaling dynamics. From a spatial modeling perspective, bulk–surface

interactions are particularly interesting because they are implemented as boundary conditions and the dimensionality difference can lead to interesting signaling dynamics [49]. For instance, the interplay between bulk and surface interactions representing ligands and receptors drives protein aggregation and pattern formation [50], while functional protein switching between the membrane and cytoplasm also leads to pattern formation [51]. Furthermore, surfaces have limited diffusion options compared with volumes in 3D, which has implications on diffusion, crowding, and confinement [52•]. Feedback effects between proteins and the membrane can lead to both protein localization and membrane curvature [53].

Much of the cellular input comes through receptors, channels, and other species that interact with the extracellular or external environment, and thus act as the gatekeepers for signaling cascades. The localization of these various stimulus-sensing species can be influenced by membrane composition. For instance, lipid rafts have been found to influence receptor localization and vice versa for key immune receptors such as T cell and B cell receptors [54,55]. Lipid rafts are associated with the concept of liquid–liquid phase separation which is another important driver of signaling localization. As another example, phase separation is believed to drive the formation of synaptic clusters in the postsynaptic density of dendritic spines [56]. The consequential patterning of membrane associated proteins has downstream effects on signaling dynamics. This patterning was demonstrated in β cells where nanodomains of adenylyl cyclases (ACs) versus phosphodiesterases lead to different cAMP dynamics [57]. New experimental and computational methods continue to be developed to investigate the complexity of the cellular membrane [58]. The localization of signaling species to the membrane and the role of lipids themselves in regulating signaling are important factors that influence the spatiotemporal dynamics of signaling molecules.

The role of mechanics: how cells experience the world and push back

Cells exist in a 3D environment and depend on mechanical cues in addition to biochemical cues to investigate and navigate their environment [59]. Mechanics influences signaling but signaling also influences mechanics; this mechanochemical feedback loop gives cells their vital adaptability to their environments. The coupling between mechanical features of the pericellular environment [60] and cell signaling [61,62] leads to regulation of cell size and shape [63,64]. A specific example of this process is how cells sense substrate stiffness and convert that into chemical activity of downstream signaling molecules. Force transduction at the level of integrins, Src-kinases, and focal adhesion kinases are critical for reading the cellular environment [64,65]. Axonal growth cones must both interpret their mechanical environment as they search for postsynaptic targets and translate signals into intracellular movement; studies have showed important coupling between external and internal mechanical and biochemical cues during axonal growth [66,67]. The activation of G-proteins by shear stress is another example of external stimuli triggering biochemical responses [68]. Converting these molecular details to a continuum description is often done by assuming a function that is reminiscent of Michaelis–Menten kinetics [69–71]. While this type of modeling provides an elegant way to capture the mechanical and chemical interplay for signaling, finding data to validate the model parameters can be challenging since this requires the mapping of activity of many molecules in the pathway of interest as a function of substrate stiffness. To our knowledge, such data are limited or scattered across multiple systems, leaving gaps in model validation.

There are a few other major considerations in this mechanochemical coupling. Changes to the ECM environment naturally change cell shape and ultrastructure and cells respond by reorganizing their cytoskeleton. A model of cell–substrate interactions during cell crawling demonstrates how mechanical feedback loops lead to stick-slip dynamics and cellular protrusions [72]. Similarly, a combined modeling and experimental work on actin polymerization found that actin-membrane link depletion is necessary for membrane protrusion initiation [73]. Cell–cell interactions include mechanical interplay between cells that can regulate intracellular components; for example, intercellular forces can determine intracellular pressure and impact individual cell membrane tension [74] and affect cellular responses through biochemical signaling [75]. Because of the biochemical complexity underlying many intracellular load-bearing structures such as actin and myosin dynamics, it is often useful to use phenomenological or simplified coupling dynamics to link biochemical signaling and mechanics. This approach has been used to link GTPase activity to cellular contraction and relaxation waves [76] and GPCR activation and ER calcium release to neurite retraction [77]. Recently, we developed a model that used a modular approach to investigate how cellular morphology coupled with mechanical forces due to substrate stiffness and cytoskeletal stiffness alters the nuclear translocation of YAP/TAZ, an important transcription factor [70••]. Another approach to modeling cellular mechanics is to simplify the biochemical molecular machinery underlying the mechanical force generation by abstracting out the details and using lumped parameters. This approach has been used to study actin dynamics within dendritic spines and found that spine shape fluctuations depend on the number of actin polymerization foci [78••].

Figure 2

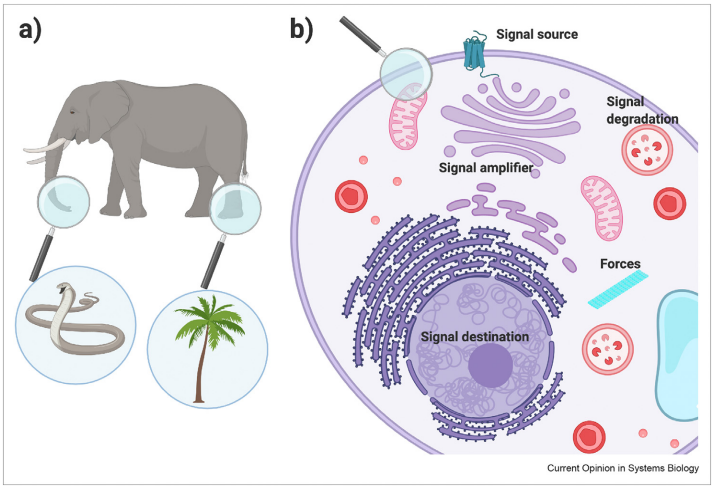

Just as a limited view of an elephant will lead to wildly varying conclusions on what an elephant is **(a)**, we are at risk of making similar mistakes in systems biology if we only consider singular isolated views of the cell **(b)**. Therefore, we must take a multidisciplinary and varied approach to studying cellular function and dynamics. Created with BioRender.com.

Outlook and future directions

As with all fields of modeling, systems biology continues to find the balance between simplification versus oversimplification and idealization versus complexity. In other words, how much detail can we leave out and still be able to identify meaningful underlying biological principles? Systems biology always requires some simplification of signaling networks due to the sheer number of proteins and chemical interactions in the cell; not every pathway can be considered in every system of interest. Similar considerations are needed for spatial and mechanical aspects of modeling. The goal is not to reconstruct the entire cell in a computer but to gain insights in health and disease.

As described above, the field has made significant advances in incorporating spatial and mechanical aspects that affect signaling in many clever ways. Future opportunities lie in our ability to use the large amount of volume EM coming online as realistic geometries in the simulation framework. There are numerous computational and technical challenges — most notably in segmentation, meshing, and the use of appropriate numerical solvers — that present themselves as opportunities for technical innovation. A bigger challenge lies in transforming the volume EM data into meshes that are compatible with finite element simulations. Currently, obtaining such meshes is an onerous, human labor intensive task. This is because segmentation and reconstruction requires multiple expertise in imaging, segmentation and cellular anatomy identification, meshing algorithms, and computational modeling skills [79••,80]. Although efforts are underway to use machine learning techniques for image segmentation and mesh curation [81,82], complications persist and these tasks are often performed manually or with substantial manual intervention. Continued efforts in automating these steps in the pipeline will greatly accelerate this process [83–85]. These are discussed in detail in a study by Vasan et al. [86].

Once realistic geometries are refined and can be used as geometries for spatial models, the complex geometries and non-linear signaling kinetics require the development of numerical solvers that are robust for large systems of coupled PDEs across multiple compartments. Working closely with computational scientists to ensure that the new robust solvers can be developed is important to ensure that simulations are producing reliable numerical results. Another complexity arises in the choice of kinetic parameters for the reactions being modeled. Development of deep learning methods for parameter estimation and uncertainty quantification of kinetic parameters are necessary to build confidence in models [87–90].

The messiness of biology is, in fact, the result of millions of years of evolution, and thus we must be careful to not

discount potential functions to that messiness. Every tim,e we make a simplification in systems biology we run the risk of losing sight of complex, non-obvious cellular functions, refer Figure 2. The future of modeling signaling networks in systems biology lies at the amalgamation of many different fields — machine learning, computational mathematics, computer vision and graphics, biophysics, cell and molecular biology, and bioinformatics. In isolation, each of these fields has made incredible progress in their own space but the modern challenges in systems biology require these fields to come together to build something bigger than the individual fields (the LIGO project in physics is an excellent recent example of this [91]). And when they do come together, the hope is that we can push the frontiers of knowledge and identify system biology's deep well-kept secrets.

Conflict of interest statement

Nothing declared.

Acknowledgements

The authors thank their various collaborators for discussions on elephants and spherical cows over the years. They also thank Dr. Sage Malingen and Dr. Christopher T. Lee for their comments. This work was supported by a National Defense Science and Engineering Graduate (NDSEG) Fellowship to M.K.B. and Air Force Office of Scientific Research FA9550-18-1-0051 to P.R.

References

Papers of particular interest, published within the period of review, have been highlighted as:

- • of special interest
- •• of outstanding interest

1. Brodland GW: **How computational models can help unlock biological systems**. In *Seminars in cell & developmental biology*, vol. 47. Elsevier; 2015:62–73.

2. Pyronneau A, He Q, Hwang JY, Porch M, Contractor A, Zukin RS: **Aberrant Rac1-cofilin signaling mediates defects in dendritic spines, synaptic function, and sensory perception in fragile X syndrome**. *Sci Signal* 2017, **10**.

3. Pchitskaya E, Popugaeva E, Bezprozvanny I: **Calcium signaling and molecular mechanisms underlying neurodegenerative diseases**. *Cell Calcium* 2018, **70**:87–94.

4. Levitt JA, Poland SP, Krstajic N, Pfisterer K, Erdogan A, Barber PR, Parsons M, Henderson RK, Ameer-Beg SM: **Qantitative real-time imaging of intracelluar FRET biosensor dynamics using rapid multi-beam confocal FLIM**. *Sci Rep* 2020, **10**:1–9.

5. • Calizo R, Bell M, Ron A, Hu M, Bhattacharya S, Wong N, Janssen W, Perumal G, Pederson P, Scarlata S, *et al.*: **Cell shape regulates subcellular organelle location to control early Ca 2+ signal dynamics in vascular smooth muscle cells**. *Sci Rep* 2020, **10**:1–17.
This combined experimental and computational study investigates how vascular smooth muscle cell shape and subsequent PM-SR distance in uences calcium and downstream signaling dynamics.

6. •• Chirillo MA, Waters MS, Lindsey LF, Bourne JN, Harris KM: **Local resources of polyribosomes and SER promote synapse enlargement and spine clustering after long-term potentiation in adult rat hippocampus**. *Sci Rep* 2019, **9**:1–14.
This study considers the downstream synaptic consequences of spine clusters. Their analysis highlights how spine cluster resource distribution appears to modulate long term potentiation within clusters and surrounding dendritic neighborhoods.

7. Omar MH, Scott JD: **AKAP signaling islands: venues for precision pharmacology**. *Trends Pharmacol Sci* 2020, **41**:933–946.

8. Frey F, Idema T: **More than just a barrier: using physical models to couple membrane shape to cell function**. *Soft Matter* 2021. -:-.

9. Mo GC, Posner C, Rodriguez EA, Sun T, Zhang J: **A rationally enhanced redfluorescent protein expands the utility of FRET biosensors**. *Nat Commun* 2020, **11**:1–9.

10. Linghu C, Johnson SL, Valdes PA, Shemesh OA, Park WM, Park D, Piatkevich KD, Wassie AT, Liu Y, An B, *et al.*: **Spatial multiplexing of fluorescent reporters for imaging signaling network dynamics**. *Cell* 2020, **183**:1682–1698.

11. Thomsen J, Sletfjerding MB, Jensen SB, Stella S, Paul B, Malle MG, Montoya G, Petersen TC, Hatzakis NS: **DeepFRET, a software for rapid and automated single-molecule FRET data classification using deep learning**. *Elife* 2020, **9**, e60404.

12. Zhang JZ, Lu TW, Stolerman LM, Tenner B, Yang JR, Zhang JF, Falcke M, Rangamani P, Taylor SS, Mehta S, *et al.*: **Phase separation of a PKA regulatory subunit controls cAMP compartmentation and oncogenic signaling**. *Cell* 2020, **182**:1531–1544.

13. Swaminathan D, Dickinson GD, Demuro A, Parker I: **Noise analysis of cytosolic calcium image data**. *Cell Calcium* 2020, **86**:102152.

14. Lock JT, Parker I: **IP3 mediated global Ca2+ signals arise through two temporally and spatially distinct modes of Ca2+ release**. *Elife* 2020, **9**, e55008.

15. Han JM, Tanimura A, Kirk V, Sneyd J: **A mathematical model of calcium dynamics in HSY cells**. *PLoS Comput Biol* 2017, **13**, e1005275.

16. Han JM, Periwal V: **A mathematical model of calcium dynamics: obesity and mitochondria-associated ER membranes**. *PLoS Comput Biol* 2019, **15**, e1006661.

17. Ohadi D, Schmitt DL, Calabrese B, Halpain S, Zhang J, Rangamani P: **Computational modeling reveals frequency modulation of calcium-cAMP/PKA pathway in dendritic spines**. *Biophysical Journal* 2019, **117**:1963–1980.

18. •• Mäki-Marttunen T, Iannella N, Edwards AG, Einevoll GT, Blackwell KT: **A unified computational model for cortical post-synaptic plasticity**. *Elife* 2020, **9**, e55714.
This work is a true tour de force of systems biology and takes a very thorough examination of the signaling network linking dendritic spine activation and synaptic plasticity through AMPAR changes.

19. Qian G, Mahdi A: **Sensitivity analysis methods in the biomedical sciences**. *Math Biosci* 2020, **323**:108306.

20. Bell M, Bartol T, Sejnowski T, Rangamani P: **Dendritic spine geometry and spine apparatus organization govern the spatiotemporal dynamics of calcium**. *J Gen Physiol* 2019, **151**:1017–1034.

21. Ohadi D, Rangamani P: **Geometric control of frequency modulation of cAMP oscillations due to calcium in dendritic spines**. *Biophys J* 2019, **117**:1981–1994.

22. Cugno A, Bartol TM, Sejnowski TJ, Iyengar R, Rangamani P: **Geometric principles of second messenger dynamics in dendritic spines**. *Sci Rep* 2019, **9**:1–18.

23. Lindberg KR, Dougherty: **ET: location specificity of transcranial electrical stimulation on neuronal electrodynamics: a mathematical model of ion channel gating dynamics and ionic flux due to neurostimulation**. *Front Comput Neurosci* 2019, **13**:17.

24. Chamakuri N, Neubert W, Gilbert S, Vierheller J, Warnecke G, Falcke M: **Multiscale modeling and numerical simulation of calcium cycling in cardiac myocytes**. *Multiscale Model Simul* 2018, **16**:1115–1145.

25. Mahajan G, Nadkarni S: **Intracellular calcium stores mediate metaplasticity at hippocampal dendritic spines**. *J Physiol* 2019, **597**:3473–3502.

26. Mohan K, Nosbisch JL, Elston TC, Bear JE, Haugh JM: **A reaction-diffusion model explains amplification of the PLC/PKC pathway in fibroblast chemotaxis**. *Biophys J* 2017, **113**: 185–194.

27. Wu Y, Whiteus C, Xu CS, Hayworth KJ, Weinberg RJ, Hess HF, De Camilli P: **Contacts between the endoplasmic reticulum and other membranes in neurons**. *Proc Natl Acad Sci Unit States Am* 2017, **114**:E4859–E4867.

28. Schöneberg J, Dambournet D, Liu TL, Forster R, Hockemeyer D, Betzig E, Drubin DG: **4D cell biology: big data image analytics and lattice light-sheet imaging reveal dynamics of clathrin-mediated endocytosis in stem cell–derived intestinal organoids**. *Mol Biol Cell* 2018, **29**:2959–2968.

29. Hoffman DP, Shtengel G, Xu CS, Campbell KR, Freeman M, Wang L, Milkie DE, Pasolli HA, Iyer N, Bogovic JA, *et al.*: **Correlative three-dimensional super-resolution and block-face electron microscopy of whole vitreously frozen cells**. *Science* 2020, **367**, eaaz5357.

30. Rojas Molina R, Liese S, Carlson A: **Diffusion on membrane domes, tubes, and pearling structures**. *Biophys J* 2021, **120**: 424–431.

31. Rosholm KR, Leijnse N, Mantsiou A, Tkach V, Pedersen SL, Wirth VF, Oddershede LB, Jensen KJ, Martinez KL, Hatzakis NS, *et al.*: **Membrane curvature regulates ligand-specific membrane sorting of GPCRs in living cells**. *Nat Chem Biol* 2017, **13**: 724.

32. Löwe M, Kalacheva M, Boersma AJ, Kedrov A: **The more the merrier: effects of macromolecular crowding on the structure and dynamics of biological membranes**. *FEBS J* 2020, **287**: 5039–5067.

33. Adrian M, Kusters R, Storm C, Hoogenraad CC, Kapitein LC: **Probing the interplay between dendritic spine morphology and membrane-bound diffusion**. *Biophys J* 2017, **113**: 2261–2270.

34. Bartol TM, Keller DX, Kinney JP, Bajaj CL, Harris KM, Sejnowski TJ, Kennedy MB: **Computational reconstitution of spine calcium transients from individual proteins**. *Front Synaptic Neurosci* 2015, **7**:17.

35. Basak R, Narayanan R: **Active dendrites regulate the spatio-temporal spread of signaling microdomains**. *PLoS Comput Biol* 2018, **14**, e1006485.

36. Colman MA, Pinali C, Trafford AW, Zhang H, Kitmitto A: **A computational model of spatio-temporal cardiac intracellular calcium handling with realistic structure and spatial ux distribution from sarcoplasmic reticulum and t-tubule reconstructions**. *PLoS Comput Biol* 2017, **13**, e1005714.

37. King C, Sengupta P, Seo AY, Lippincott-Schwartz J: **ER membranes exhibit phase behavior at sites of organelle contact**. *Proc Natl Acad Sci Unit States Am* 2020, **117**:7225–7235.

38. • Ma J, Do M, Le Gros MA, Peskin CS, Larabell CA, Mori Y, Isaacson SA: **Strong intracellular signal inactivation produces sharper and more robust signaling from cell membrane to nucleus**. *PLoS Comput Biol* 2020, **16**, e1008356.

This work highlights the effects of internal organelles as diffusion barriers and how signal inactivation can provide robustness to these barriers.

39. Breit M, Kessler M, Stepniewski M, Vlachos A, Queisser G: **Spine-to-dendrite calcium modeling discloses relevance for precise positioning of ryanodine receptor- containing spine endoplasmic reticulum**. *Sci Rep* 2018, **8**:1–17.

40. Basnayake K, Mazaud D, Bemelmans A, Rouach N, Korkotian E, Holcman D: **Fast calcium transients in dendritic spines driven by extreme statistics**. *PLoS Biol* 2019, **17**, e2006202.

41. Kulik YD, Watson DJ, Cao G, Kuwajima M, Harris KM: **Structural plasticity of dendritic secretory compartments during LTP-induced synaptogenesis**. *Elife* 2019, **8**, e46356.

42. • Perez-Alvarez A, Yin S, Schulze C, Hammer JA, Wagner W, Oertner TG: **Endo- plasmic reticulum visits highly active spines and prevents runaway potentiation of synapses**. *Nat Commun* 2020, **11**:1–10.

This experimental work examined ER dynamics during synaptic activity to find selective ER activity in individual dendritic spines to prevent excessive potentiation.

43. Terenzio M, Schiavo G, Fainzilber M: **Compartmentalized signaling in neurons: from cell biology to neuroscience**. *Neuron* 2017, **96**:667–679.

44. Kolstad TR, van den Brink J, MacQuaide N, Lunde PK, Frisk M, Aronsen JM, Norden ES, Cataliotti A, Sjaastad I, Sejersted OM, *et al.*: **Ryanodine receptor dispersion disrupts Ca2+ release in failing cardiac myocytes**. *Elife* 2018, **7**, e39427.

45. Lee JE, Cathey PI, Wu H, Parker R, Voeltz GK: **Endoplasmic reticulum contact sites regulate the dynamics of membraneless organelles**. *Science* 2020, **367**, eaay7108.

46. Chu Q, Martinez TF, Novak SW, Donaldson CJ, Tan D, Vaughan JM, Chang T, Diedrich JK, Andrade L, Kim A, *et al.*: **Regulation of the ER stress response by a mitochondrial microprotein**. *Nat Commun* 2019, **10**:1–13.

47. Sunshine H, Iruela-Arispe ML: **Membrane lipids and cell signaling**. *Curr Opin Lipidol* 2017, **28**:408.

48. Johannes L, Pezeshkian W, Ipsen JH, Shillcock JC: **Clustering on membranes: fluctuations and more**. *Trends Cell Biol* 2018, **28**:405–415.

49. Cusseddu D, Edelstein-Keshet L, Mackenzie JA, Portet S, Madzvamuse A: **A coupled bulk-surface model for cell polarisation**. *J Theor Biol* 2019, **481**:119–135.

50. Stolerman LM, Getz M, Smith SGL, Holst M, Rangamani P: **Stability analysis of a bulk–surface reaction model for membrane protein clustering**. *Bull Math Biol* 2020, **82**: 1–34.

51. Denk J, Kretschmer S, Halatek J, Hartl C, Schwille P, Frey E: **MinE conformational switching confers robustness on self-organized Min protein patterns**. *Proc Natl Acad Sci Unit States Am* 2018, **115**:4553–4558.

52. • Nawrocki G, Im W, Sugita Y, Feig M: **Clustering and dynamics of crowded proteins near membranes and their in uence on membrane bending**. *Proc Natl Acad Sci Unit States Am* 2019, **116**:24562–24567.

This study uses all-atom simulations to investigate nonspecific protein membrane interactions that leads to protein aggregation and depletion, along with membrane curvature.

53. Mahapatra A, Saintillan D, Rangamani P: **Transport phenomena in uid films with curvature elasticity**. *J Fluid Mech* 2020, **905**: A8.

54. Levental I: **Lipid rafts come of age**. *Nat Rev Mol Cell Biol* 2020:1. 1.

55. Sezgin E, Levental I, Mayor S, Eggeling C: **The mystery of membrane organization: composition, regulation and roles of lipid rafts**. *Nat Rev Mol Cell Biol* 2017, **18**:361.

56. Chen X, Wu X, Wu H, Zhang M: **Phase separation at the synapse**. *Nat Neurosci* 2020, **23**:301–310.

57. Tenner B, Getz M, Ross B, Ohadi D, Bohrer CH, Greenwald E, Mehta S, Xiao J, Rangamani P, Zhang J: **Spatially compartmentalized phase regulation of a Ca2+-cAMP-PKA oscillatory circuit**. *Elife* 2020, **9**, e55013.

58. Sankaran J, Wohland T: **Fluorescence strategies for mapping cell membrane dynamics and structures**. *APL Bioengineering* 2020, **4**, 020901.

59. Bajpai A, Tong J, Qian W, Peng Y, Chen W: **The interplay between cell-cell and cell-matrix forces regulates cell migration dynamics**. *Biophys J* 2019, **117**:1795–1804.

60. Scott KE, Rychel K, Ranamukhaarachchi S, Rangamani P, Fraley SI: **Emerging themes and unifying concepts underlying cell behavior regulation by the pericellular space**. *Acta Biomater* 2019, **96**:81–98.

61. Kluger C, Braun L, Sedlak SM, Pippig DA, Bauer MS, Miller K, Milles LF, Gaub HE, Vogel V: **Different vinculin binding sites use the same mechanism to regulate directional force transduction**. *Biophys J* 2020, **118**:1344–1356.

62. Wolfenson H, Yang B, Sheetz MP: **Steps in mechano-transduction pathways that control cell morphology**. *Annu Rev Physiol* 2019, **81**:585–605.

63. Perez Gonzalez N, Tao J, Rochman ND, Vig D, Chiu E, Wirtz D, Sun SX: **Cell tension and mechanical regulation of cell volume**. *Mol Biol Cell* 2018, **29**.

64. Perez-Gonzalez NA, Rochman ND, Yao K, Tao J, Le MTT, Flanary S, Sablich L, Toler B, Crentsil E, Takaesu F, *et al.*: **YAP and TAZ regulate cell volume**. *JCB (J Cell Biol)* 2019, **218**: 3472–3488.

65. Bradbury PM, Turner K, Mitchell C, Griffin KR, Middlemiss S, Lau L, Dagg R, Taran E, Cooper-White J, Fabry B, *et al.*: **The focal adhesion targeting domain of p130Cas confers a mechanosensing function**. *J Cell Sci* 2017, **130**: 1263–1273.

66. Franze K: **Integrating chemistry and mechanics: the forces driving axon growth**. *Annu Rev Cell Dev Biol* 2020, **36**: 61–83.

67. De Vincentiis S, Falconieri A, Mainardi M, Cappello V, Scribano V, Bizzarri R, Storti B, Dente L, Costa M, Raffa V: **Extremely low forces induce extreme axon growth**. *J Neurosci* 2020, **40**: 4997–5007.

68. Sriram K, Laughlin JG, Rangamani P, Tartakovsky DM: **Shear-induced nitric oxide production by endothelial cells**. *Biophys J* 2016, **111**:208–221.

69. Sun M, Spill F, Zaman MH: **A computational model of YAP/TAZ mechanosensing**. *Biophys J* 2016, **110**:2540–2550.

70. Scott KE, Fraley SI, Rangamani P: **A spatial model of YAP/TAZ signaling reveals how stiffness, dimensionality, and shape contribute to emergent outcomes**. *bioRxiv* 2020:2020. https://doi.org/10.1101/2020.10.14.340349, Accepted, 2021, Proc. Natl. Acad. Sci.
This work couples substrate stiffness sensing and signaling to predict how cell shape and substrate dimensionality can regulate YAP/TAZ nuclear translocation using a spatial model.

71. Cheng B, Lin M, Huang G, Li Y, Ji B, Genin GM, Deshpande VS, Lu TJ, Xu F: **Cellular mechanosensing of the biophysical microenvironment: a review of mathematical models of biophysical regulation of cell responses**. *Phys Life Rev* 2017, **22**: 88–119.

72. Sens P: **Stick–slip model for actin-driven cell protrusions, cell polarization, and crawling**. *Proc Natl Acad Sci Unit States Am* 2020, **117**:24670–24678.

73. Welf ES, Miles CE, Huh J, Sapoznik E, Chi J, Driscoll MK, Isogai T, Noh J, Weems AD, Pohlkamp T, *et al.*: **Actin-membrane release initiates cell protrusions**. *Dev Cell* 2020, **55**: 723–736.

74. Vasan R, Maleckar MM, Williams CD, Rangamani P: **DLITE uses cell-cell interface movement to better infer cell-cell tensions**. *Biophys J* 2019, **117**:1714–1727.

75. Isogai T, Park JS, Danuser G: **Cell forces meet cell metabolism**. *Nat Cell Biol* 2017, **19**:591–593.

76. Zmurchok C, Bhaskar D, Edelstein-Keshet L: **Coupling mechanical tension and GTPase signaling to generate cell and tissue dynamics**. *Phys Biol* 2018, **15**, 046004.

77. Pearce KM, Bell M, Linthicum WH, Wen Q, Srinivasan J, Rangamani P, Scarlata S: **Gαq-mediated calcium dynamics and membrane tension modulate neurite plasticity**. *Mol Biol Cell* 2020, **31**:683–694.

78. •• Bonilla-Quintana M, Wörgötter F, Tetzlaff C, Fauth M: **Modeling the shape of synaptic spines by their actin dynamics**. *Front Synaptic Neurosci* 2020, **12**:9.
This computational work addresses the mechanical forces on the membrane of dendritic spines due to actin during spontaneous shape uctuations. Through this model, they can predict the temporal shape dynamics of the dendritic spine dependent on different actin dynamics.

79. •• Lee CT, Laughlin JG, de La Beaumelle NA, Amaro RE, McCammon JA, Ramamoorthi R, Holst M, Rangamani P: **3D mesh processing using GAMer 2 to enable reaction-diffusion simulations in realistic cellular geometries**. *PLoS Comput Biol* 2020, **16**, e1007756.
This computational and mathematical work greatly improves realistic modeling approaches by presenting mesh curation software. This pipeline enables the use of real EM image stacks for mesh geometries in reaction diffusion models.

80. Antunes G, de Souza FMS: **3D modeling of dendritic spines with synaptic plasticity**. *JoVE* 2020, e60896.

81. Zeng T, Wu B, Ji S: **DeepEM3D: approaching human-level performance on 3D anisotropic EM image segmentation**. *Bioinformatics* 2017, **33**:2555–2562.

82. Xiao C, Liu J, Chen X, Han H, Shu C, Xie Q: **Deep contextual residual network for electron microscopy image segmentation in connectomics**. In *2018 IEEE 15th international symposium on biomedical imaging (ISBI 2018). IEEE*; 2018:378–381.

83. Li PH, Lindsey LF, Januszewski M, Tyka M, Maitin-Shepard J, Blakely T, Jain V: **Automated reconstruction of a serial-section EM Drosophila brain with ood filling networks and local realignment**. *Microsc Microanal* 2019, **25**:1364–1365.

84. Berg S, Kutra D, Kroeger T, Straehle CN, Kausler BX, Haubold C, Schiegg M, Ales J, Beier T, Rudy M, *et al.*: **Ilastik: interactive machine learning for (bio) image analysis**. *Nat Methods* 2019, **16**:1226–1232.

85. Haberl MG, Churas C, Tindall L, Boassa D, Phan S, Bushong EA, Madany M, Akay R, Deerinck TJ, Peltier ST, *et al.*: **CDeep3M–Plug-and-Play cloud-based deep learning for image segmentation**. *Nat Methods* 2018, **15**:677–680.

86. Vasan R, Rowan MP, Lee CT, Johnson GR, Rangamani P, Holst M: **Applications and challenges of machine learning to enable realistic cellular simulations**. *Frontiers in Physics* 2020, **7**:247.

87. Henriques D, Villaverde AF, Rocha M, Saez-Rodriguez J, Banga JR: **Data-driven reverse engineering of signaling pathways using ensembles of dynamic models**. *PLoS Comput Biol* 2017, **13**, e1005379.

88. Wang A, Cao S, Aboelkassem Y, Valdez-Jasso D: **Quantification of uncertainty in a new network model of pulmonary arterial adventitial fibroblast pro-fibrotic signalling**. *Philosophical Transactions Royal Society A* 2020, **378**:20190338.

89. Tennøe S, Halnes G, Einevoll GT: **Uncertainpy: a python toolbox for uncertainty quantification and sensitivity analysis in computational neuroscience**. *Front Neuroinf* 2018, **12**:49.

90. Yazdani A, Lu L, Raissi M, Karniadakis GE: **Systems biology informed deep learning for inferring parameters and hidden dynamics**. *PLoS Comput Biol* 2020, **16**, e1007575.

91. Abbott BP, Abbott R, Abbott T, Abernathy M, Acernese F, Ackley K, Adams C, Adams T, Addesso P, Adhikari R, *et al.*: **Observation of gravitational waves from a binary black hole merger**. *Phys Rev Lett* 2016, **116**, 061102.

Acknowledgements

Chapter 2, in full, is a reprint of the material as it appears in Design decisions for incorporating spatial and mechanical aspects in models of signaling networks in Current Opinion in Systems Biology, 2021. Bell, Miriam; Rangamani, Padmini, COISB, 2021 [1]. The dissertation author was the primary investigator and author of this material. For Chapter 2, I would like to acknowledge my coauthor Professor Padmini Rangamani. We thank our various collaborators for discussions on elephants and spherical cows over the years. We also thank Dr. Sage Malingen and Dr. Christopher T. Lee for their comments. I would like to acknowledge my funding from a National Defense Science and Engineering Graduate (NDSEG) Fellowship and Air Force Office of Scientific Research FA9550-18-1-0051 to P.R.

Chapter 3

Gαq-mediated calcium dynamics and membrane tension modulate neurite plasticity

MBoC | ARTICLE

Gαq-mediated calcium dynamics and membrane tension modulate neurite plasticity

Katherine M. Pearce[a,†], Miriam Bell[b,†], Will H. Linthicum[c], Qi Wen[c], Jagan Srinivasan[d], Padmini Rangamani[b,*], and Suzanne Scarlata[a,*]

[a]Department of Chemistry and Biochemistry, [c]Department of Biomedical Engineering, and [d]Department of Biology and Biotechnology, Worcester Polytechnic Institute, Worcester, MA 01609; [b]Mechanical and Aerospace Engineering Department, University of California, San Diego, La Jolla, CA 92093

ABSTRACT **The formation and disruption of synaptic connections during development are a fundamental step in neural circuit formation. Subneuronal structures such as neurites are known to be sensitive to the level of spontaneous neuronal activity, but the specifics of how neurotransmitter-induced calcium activity regulates neurite homeostasis are not yet fully understood. In response to stimulation by neurotransmitters such as acetylcholine, calcium responses in cells are mediated by the Gαq/phospholipase Cβ (PLCβ)/phosphatidylinositol 4,5-bisphosphate ($PI(4,5)P_2$) signaling pathway. Here, we show that prolonged Gαq stimulation results in the retraction of neurites in PC12 cells and the rupture of neuronal synapses by modulating membrane tension. To understand the underlying cause, we dissected the behavior of individual components of the Gαq/PLCβ/$PI(4,5)P_2$ pathway during retraction and correlated these with the retraction of the membrane and cytoskeletal elements impacted by calcium signaling. We developed a mathematical model that combines biochemical signaling with membrane tension and cytoskeletal mechanics to show how signaling events are coupled to retraction velocity, membrane tension, and actin dynamics. The coupling between calcium and neurite retraction is shown to be operative in the *Caenorhabditis elegans* nervous system. This study uncovers a novel mechanochemical connection between Gαq/PLCβ /$PI(4,5)P_2$ that couples calcium responses with neural plasticity.**

Monitoring Editor
John York
Vanderbilt University

Received: Sep 18, 2019
Revised: Dec 2, 2019
Accepted: Dec 5, 2019

INTRODUCTION

Throughout the course of an organism's life, different neuronal connections break and reform to generate new electrical patterns that allow optimal function during development and through adulthood. This plasticity of neuronal connections allows the rewiring of circuitry necessary for memory and learning (e.g., Licht *et al.*, 2011; Stuchlik, 2014; Takeuchi et al. 2014). Understanding the factors that permit appropriate and efficient rewiring is essential for understanding both developmental and neurodegenerative diseases.

Calcium is a key mediator of neuronal functions such as axonal growth, neurite protrusion, and spinogenesis (Clapham, 2007; Brini *et al.*, 2014). Previous studies have shown that spontaneous activity in neurons can result in a frequency-dependent rate of axon elongation that is inversely proportional to the frequency of calcium transients (Goldberg and Grabham, 1999; Gomez and Spitzer, 1999). The role of calcium in neurite growth and protrusions associated with development has been studied in different contexts (e.g., Mattson, 2007). This outgrowth process is stimulated by neurotrophic factors that carefully regulate the spatiotemporal aspects of intracellular calcium. Neurite growth can also be triggered by stress, pharmacological agents, or starvation (McKay *et al.*, 1999; Gilbert and Man, 2017). These factors may occur during disease states and contribute to inappropriate neurite growth, which can result in an

This article was published online ahead of print in MBoC in Press (http://www.molbiolcell.org/cgi/doi/10.1091/mbc.E19-09-0536) on December 11, 2019.

†These authors contributed equally to this work.

*Address correspondence to: Suzanne Scarlata (sfscarlata@wpi.edu); Padmini Rangamani (prangamani@ucsd.edu).

Abbreviations used: $PI(4,5)P_2$, phosphoinositol 4,5 bisphosphate; PLCβ, phospholipase Cβ.

increased number of smaller and nonproductive neurites, as seen in autism (Gilbert and Man, 2017).

Neurodegenerative diseases are associated with the disruption of normal calcium signaling. Specifically, diseases such as autism and amyotrophic lateral sclerosis (ALS) have been linked to overexcitation of neurons or excitotoxicity caused by abnormal calcium homeostasis (King *et al.*, 2016). However, the link between calcium homeostasis and the mechanical processes underlying neurite retraction remain poorly understood. Understanding the link between dysfunction of cellular calcium, especially prolonged signaling, and neuronal function is critical to understanding the mechanisms that underlie diseases typified by inappropriate neuronal excitation. While previous research has focused on the short-term effects of elevated cellular calcium after stimulation and its effects on neurite growth or on spontaneous spiking activity (Goldberg and Grabham, 1999; Gomez and Spitzer, 1999; Rosenberg and Spitzer, 2011), little is known about the effect of extended elevated calcium on these same neurites over time, that is, cases that mimic an extended overstimulated state. In this study, we investigate the effects of prolonged stimulation of the Gαq/PLCβ/PIP_2 /calcium signaling pathway by the neurotransmitter acetylcholine in a model neuronal cell line, PC12, and in the neuronal network in a small organism, *Caenorhabditis elegans*.

Calcium signals in neurites can be generated by several mechanisms. In synapses, postsynaptic cells receive an influx of calcium directly through the openings of transmembrane channels in response to neurotransmitter release (Voglis and Tavernarakis, 2006). Neurotransmitters, such as acetylcholine, activate G protein–coupled receptors (GPCRs) on the plasma membrane to cause the release of calcium from intracellular stores (McKay *et al.*, 1999). Furthermore, neurotropic factors activate receptor tyrosine kinases to increase intracellular calcium through another phospholipase C family, PLCγ. Downstream from these events is the opening of calcium-activated calcium channels on the endoplasmic reticulum (ER) membrane. Many of these channels are thought to respond to the increase in cytosolic calcium and to changes in the physical properties of the plasma membrane. These increases in cellular calcium regulate specific transcription factors and posttranscriptional processes that lead to appropriate downstream responses (West *et al.*, 2001).

In this study, we show that neurites will retract completely to the soma following extended stimulation of the GPCR/Gαq/PLCβ pathway. This pathway mediates signals from many hormones and neurotransmitters such as acetylcholine, dopamine, histamine, and melatonin (Kadamur and Ross, 2013). Signaling begins with ligand binding to its specific G protein–coupled receptor to activate the Gαq family of G proteins by exchange of GTP for GDP. The GTP-bound Gαq subunits then activate phospholipase Cβ (PLCβ). PLCβ catalyzes the hydrolysis of phosphatidylinositol 4,5-biphosphate (PIP_2) to inositol 1,4,5-triphosphate (IP_3) and diacylglycerol (DAG). IP_3 binds to receptors on the endoplasmic reticulum, allowing the release of calcium from intracellular stores into the cytoplasm. The elevated calcium can then change the activity of a variety of intracellular proteins to generate a specific cell response.

Incorporated into this pathway are a number of positive and negative feedback loops. The initial calcium release generated by PLCβ in turn stimulates the highly active PLCδ that synergizes the calcium response (Guo *et al.*, 2005). Increased calcium also opens calcium-induced calcium channels, further strengthening calcium responses (Lohmann and Wong, 2005). Negative feedback comes from the internalization of ligand-bound receptors into endosomes over a few minutes, which typically return unbound receptors to the plasma membrane over a period of 20–30 min (Freedman and Lefkowitz, 1996). Additionally, Gαq has GTPase activity that returns it to the basal state, and this activity is stimulated by the GTPase activating (GAP) activity of PLCβ (Berstein *et al.*, 1992), along with RGS proteins that quickly turn off the signal (Dohlman and Thorner, 1997). It is notable that these feedback loops are highly sensitive to the concentration of the pathway components and the concentrations of competing species, as well as the physical state of the plasma membrane, which drives aggregation of the ligand-bound receptor and internalization, the accessibility of $PI(4,5)P_2$ substrates to PLCβ and PLCδ, and the opening of calcium channels.

Components of the Gαq/PLCβ/$PI(4,5)P_2$ pathway are also involved in the regulation of membrane tension and cytoskeletal remodeling. The coupling between membrane tension and cytoskeletal adhesion through $PI(4,5)P_2$ was established nearly two decades ago by Sheetz and coworkers (Raucher *et al.*, 2000; Sheetz, 2001). In a series of elegant experiments, they showed that PIP_2 regulates cytoskeleton–plasma membrane adhesion (Raucher *et al.*, 2000) and that membrane tension plays a critical role in actin remodeling, membrane trafficking, and cell motility (van Rheenen and Jalink, 2002; Bittner and Holz, 2005; Diz-Munoz *et al.*, 2013). Subsequently, researchers continued to establish and identify increasing roles played by the plasma membrane tension and cortical tension in different cellular reorganization processes (Logan and Mandato, 2006; Rangamani *et al.*, 2011; Datar *et al.*, 2019). Specifically, in neurons, dynamics of growth cone formation, neurite protrusion, and axonal contractility have been shown to be mechanochemically coupled processes (Franze *et al.*, 2009; Kerstein *et al.*, 2015).

Despite these advances in neuronal biophysics, our understanding of synaptic rupture and neurite retraction remains incomplete, especially in terms of the mechanisms that underlie overexcitatory responses. In this study, we set out to investigate the effects of prolonged (i.e., several minutes) agonist stimulation of the Gαq signaling pathway in a model neuronal cell line (PC12). We find that prolonged stimulation results in tension-driven neurite retraction, unlike the behavior seen in shorter exposures to neurotransmitters. To understand the factors that underlie the observed neurite retraction, we followed the individual components during the process and developed a mathematical model to predict the effects of calcium stimulation by acetylcholine (ACh) and its extended response on retraction through mobilization of the pathways that impact neurite retraction.

Our predictive models showing that membrane tension and actin reorganization are coupled to calcium dynamics through Gαq/PLCβ/$PI(4,5)P_2$ were verified in cultured PC12 cells as well as in the neuronal network of the nematode *C. elegans*. The 302 neurons that comprise the nervous system of *C. elegans* (Sengupta and Samuel, 2009) have been well characterized, and these organisms have been used as models to understand neurite formation and retraction (Sengupta and Samuel, 2009). Because of its optical clarity, *C. elegans* allows us to monitor the effects of acetylcholine stimulation on synapses in real time by microscopy. We find that the *C. elegans* neural architecture exhibits the same retraction behavior when exposed to Gαq agonists showing rupture along the spine in the nerve ring, suggesting that the coupling between membrane tension and calcium dynamics occur on the organismal level. Taken together, our studies connect signaling processes with mechanical effects that allow us to predict the signaling conditions that shift from outgrowth and maintenance to retraction.

RESULTS

Prolonged exposure to carbachol causes neurite retraction

Cultured PC12 cells differentiate to a neuronal phenotype upon treatment with nerve growth factor (NGF), which initiates activation

through TrkA receptors (Greene and Tischler, 1976). This treatment results in growth of neurites from the cell body that extend to roughly three times the length of the body over a 36-h period. These neurites can then connect with neurites from other cells, resulting in long tubular structures (Drubin *et al.*, 1985).

Addition of a Gαq agonist to the cells activates PLCβ to catalyze the hydrolysis of $PI(4,5)P_2$. This hydrolysis releases $Ins(1,4,5)P_3$ into the cytosol, which then binds to $Ins(1,4,5)P_3$ receptors on the ER to release calcium from intracellular stores. In addition to eliciting calcium signals, $PI(4,5)P_2$ hydrolysis can exert mechanical effects on cells by altering membrane tension and actin–membrane adhesion (Raucher *et al.*, 2000; Sheetz, 2001; Logan and Mandato, 2006). We sought to understand the interactions between the Gαq/PLCβ pathway and mechanical features of membrane–actin interaction (Figure 1, A and B).

We found that when we added a Gαq agonist, such as carbachol or bradykinin, to PC12 cells, the well-formed neurites became thinner, their connections ruptured (compare Figure 1C with Figure 1E and Supplemental Figure S1), and they retract toward the soma after a period of 5–10 min (Figure 1, E and F). After retraction, the excess membrane appears as blebs around the sides of the cell (Figure 1G). This behavior was seen in every cell viewed in more than 100 experiments, but was not seen when a PLCβ inhibitor was added, or a Gαi agonist such as isoproterenol was used. The initiation and rate of retraction depended on the particular treatment and condition of the experiment, as described below. The extent of retraction in a specific time period was robust to the length and thickness of the neurite.

Neurite retraction is coupled with the Gαq/PLCβ/calcium pathway

We followed the activation of the Gαq/PLCβ/calcium signaling pathway upon stimulation in single PC12 cells using the fluorescent calcium indicator Calcium Green, to determine whether neurite retraction is concurrent with activation. Our approach was to follow some of the molecular constituents of the Gαq pathway and determine the temporal correlation between activation of the individual signal components and neurite retraction. The retraction velocities of a generic Gαq-coupled receptor (i.e., the bradykinin receptor type 2 or B2R) were measured by transfecting cells with a fluorescence-tagged construct and stimulating the cells with an agonist (i.e., bradykinin). We note that B2R is not endogenous to PC12 cells, thus allowing us to compare Gαq-associated retraction with that which results from stimulation of endogenous muscarinic receptors. We find retraction behavior for neurite retraction after stimulating the B2R transfected cells with bradykinin identical to that which results from carbachol stimulation (Figure 2). These results support a connection between neurite retraction and Gαq/PLCβ activation.

We calculated the velocity of neurite retraction by analyzing the decrease in length of each neurite at each time point during the experiment (see *Materials and Methods*). These velocities were analyzed for PC12 cells transfected with eCFP-B2R *(blue)* and for the plasma membrane *(orange)* as monitored by phase contrast imaging (Figure 2A). We find that the retraction of the plasma membrane is more gradual than that of the receptor, suggesting that movement of the receptor toward the soma precedes the membrane.

Activation of the PLCβ pathway through Gαq-GPCRs results in hydrolysis of the signaling lipid $PI(4,5)P_2$. We followed the change in the level and distribution of $PI(4,5)P_2$ of the plasma membrane surrounding the soma and neurite during retraction using a fluorescent $PI(4,5)P_2$ sensor (i.e., eGFP-PH-PLCδ1). Our data show that $PI(4,5)P_2$ moves from the neurite into the soma with a retraction velocity

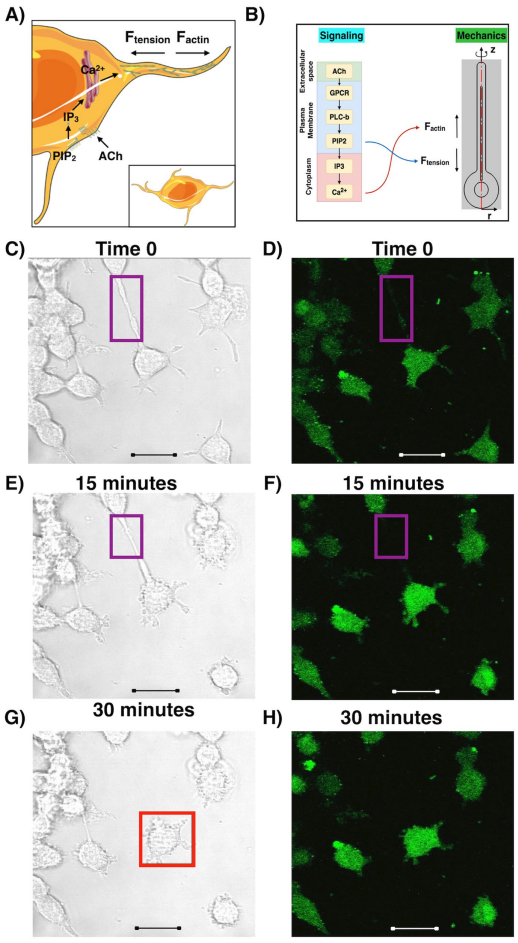

FIGURE 1: Neurite retraction in PC12 cells is induced by calcium stimulation. (A) Cartoon of the mechanochemical events underlying neurite retraction in a PC12 cell. The figure depicts the interconnection between calcium signaling and force regulation due to membrane cortical tension and actin remodeling. (B) Schematic showing the coupling between signaling and mechanical changes within the PC12 cell. We identify membrane cortical tension and actin dynamics as key players controlling neurite retraction rates and link calcium dynamics to actin reorganization and force generation, and $PI(4,5)P_2$ hydrolysis to membrane tension change and tension force generation. Using this coupled model, we are able to reproduce the neurite retraction behavior observed experimentally. (C, D) Sample images of differentiated PC12 cells before stimulation. Confocal phase contrast (C) and fluorescence images of cells loaded with a fluorescent calcium sensor, Calcium Green (D) are shown. (E–H) Stimulation of cells with carbachol results in neurite thinning, retraction, and synaptic rupture. At 15 min after the addition of carbachol, we observe membrane retraction (e.g., purple box) and thinning of the neurite (E, F). At 30 min after carbachol addition, we see a complete retraction of the neurites into the soma and membrane blebbing at the retraction sties (e.g., red box) (G, H). In all images, the scale bar is 20 μm. Identical behavior was seen in 20 cells.

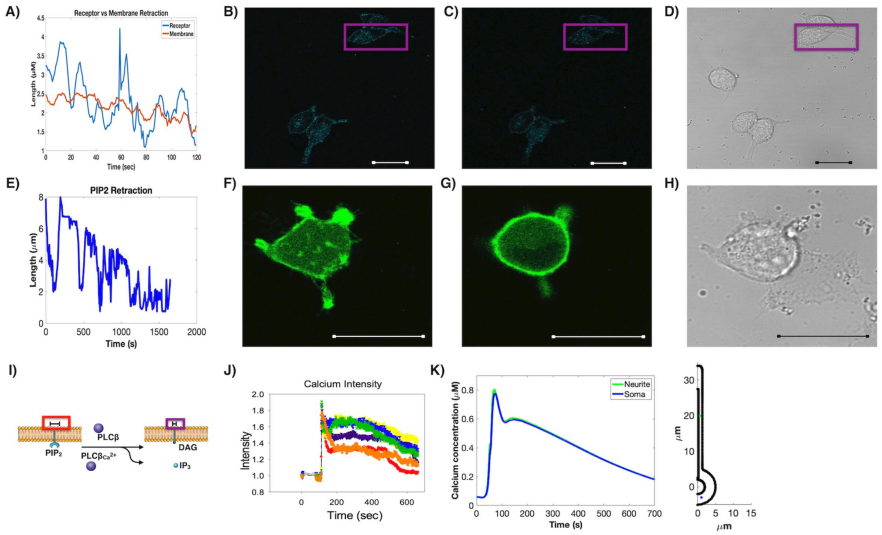

FIGURE 2: Neurite retraction of PC12 cells upon Gαq stimulation. (A) Decrease in neurite length of the B2R receptor in PC12 cells (blue) as compared with slow reduction in length of the membrane as followed by phase contrast (orange). (B) Images of differentiated PC12 cells expressing eCFP-B2R before stimulation with bradykinin and (C) 30 min after stimulation, where purple box shows the retraction data of A, and the corresponding phase contrast image is shown in D. (E) Decrease in neurite length as followed using a fluorescent PI(4,5)P_2 sensor, PH-PLCδ1 (Garcia et al., 1995), where distinct oscillations are seen. (F–H) Images of a differentiated PC12 cell expressing PH-PLCδ1 (F) before stimulation and (G) 30 min after stimulation with carbachol and (H) the corresponding phase contrast image. (I) Cartoon showing the hydrolysis of PI(4,5)P_2 to Ins(1,4,5)P_3 and DAG, depicting the larger head group of PIP_2, denoted by the scale bar (red box), as compared with the smaller DAG that remains in the membrane after hydrolysis (purple box). This decrease in the size of the membrane-bound molecule (PI(4,5)P_2 to DAG) leads to a local change in tension (denoted by the scale bars). IP_3 moves into the cytosol and the ER, causing a release of calcium. (J) Graph of calcium intensity in neurites of six different cells. This graph shows the lag time after the addition of carbachol, the initial spike in calcium, and the slow recovery. (K) Model replicating the intensity of calcium over time at two spatial locations (in the neurite and in the soma) after stimulation by carbachol. Inset: location of traces within the model geometry (in the neurite and in the soma). In all images, the scale bar is 20 μm, and $n > 15$ cells.

similar to that of the GPCR (Figure 2E). However, this movement is oscillatory, showing three precipitous drops and recoveries during the retraction event. These are three distinct movements of PI(4,5)P_2 during the observed retraction, which occur at similar times (–3, 10, and 15 min) for all cells tested and are interpreted as being due to PI(4,5)P_2 replenishment during the course of the retraction.

In general, Gαq activation produces an increase in calcium, typified by an initial spike in the first few minutes followed by a slow recovery. We followed the calcium behavior upon stimulation in single cells using Calcium Green (Figures 1, D, F, and H, and 2J). Correlating calcium responses with neurite retraction shows that retraction occurs even in this initial phase and continues through the duration of the recovery phase.

We constructed a spatial model of the Gαq/PLCβ/PI(4,5)P_2 signaling pathway using reaction–diffusion equations. The reactions, kinetic parameters, and diffusion constants are given in Tables S1–S4 in the Supplemental Material (SOM). The soma of the PC12 cell was modeled as a simplified geometry capturing the key features of these cells. Briefly, the soma was modeled as a sphere with a radius of 5 μm, and the neurite was modeled as a cylinder with a radius of 1.25 μm and a length of 30 μm. The endoplasmic reticulum was modeled as a cylinder with a radius of 0.25 μm and a length of 25 μm, and the nucleus as a sphere with a radius of 2 μm. Geometric details are given in Supplemental Table S5. The nucleus was treated as an excluded volume, while the ER was treated as a calcium source. Computational modeling of this pathway in a three-dimensional spatial model using finite elements captured the calcium transients with the same time scale as the experiments (compare Figure 2, J and K). This framework sets the stage for the mechanical coupling of calcium dynamics to neurite retraction.

Actin remodeling proteins affect the dynamics of neurite retraction

Actin filaments are the major cytoskeletal components of synapses and are the key modulators of neurite plasticity. An actin filament is a dynamic structure in which monomers disassemble from one end and reassemble on the other, a behavior known as molecular treadmilling. Retraction involves inward movement of the actin structure that defines the neurite shape, and so any model of retraction must incorporate actin disassembly. In neurites, actin filament remodeling is known to be associated with the drag forces related to protrusion (Datar *et al.*, 2019). Additionally, PI(4,5)P_2 hydrolysis is closely connected to membrane-actin adhesion and membrane tension regulation (Raucher *et al.*, 2000).

On the basis of our experimental observations (Figure 2), we coupled PI(4,5)P_2 hydrolysis and calcium release following carbachol

stimulation with a mechanical model that balances the forces due to actin depolymerization and membrane cortical tension change. Owing to the time-scale separation between the biochemical signaling dynamics and neurite retraction, we coupled the three-dimensional spatial model of the Gαq/PLCβ/calcium signaling pathway (Figure I, A and B) to an ordinary differential equation model of neurite mechanics, assuming uniform signaling dynamics at extended timescales (Section S1-2 in the SOM). Briefly, the mechanical model proposes a force balance acting on the tip of the neurite (Hassinger *et al.*, 2017). The force due to the actin cytoskeleton is acting outward, away from the soma, and the force exerted by the membrane cortical tension is acting toward the soma. In this case, we assume that the cortical tension is a function of the change in the area of the membrane. This change in membrane area can result from PI(4,5)P_2 hydrolysis (Sheetz and Dai, 1996; Raucher *et al.*, 2000), from endocytosis of GPCRs (Getz *et al.*, 2019), and from changes in tension (Simunovic *et al.*, 2017). The force exerted by the actin cytoskeleton is modeled phenomenologically as a function of calcium-mediated cofilin and retrograde flow (Bornschlogl *et al.*, 2013). Thus, the net force balance can be written as

$$\underbrace{-F_{\text{tension}}}_{\text{force due to cortical membrane tension}} + \underbrace{F_{\text{actin}}}_{\text{force due to actin dynamics}} = \underbrace{\frac{\eta}{k_L}\frac{dL}{dt}}_{\text{drag forces}} \quad (1)$$

where

$$\eta = \underbrace{\mu_e}_{\text{drag coefficient for external fluid}} + \underbrace{\frac{\mu_m}{\delta}}_{\text{drag coefficient for membrane}} \quad (2)$$

Modeling the neurite as a cylinder with a hemispherical end cap, we obtain the governing equation for the length of the neurite as

$$\underbrace{\frac{dL}{dt}}_{\text{rate of change of neurite length}} = \underbrace{\frac{k_L}{\eta}}_{\text{drag coefficients and length effects}} \underbrace{\left(-F_{\text{tension}} + F_{\text{actin}}\right)}_{\text{forces}} \quad (3)$$

This governing equation combines the force balance above with experimental observations that retraction velocity is proportional to neurite length. The force due to membrane cortical tension and actin dynamics depends on equations for τ and F_{actin}, respectively, given as

$$\frac{d\tau}{dt} = \underbrace{\frac{dArea}{dt}\left(f\left(PIP_2\right)\right)}_{\text{area change with PIP2 dependence}} \underbrace{F_{\text{perPIP}_2}}_{\text{tension change per PIP2}} \underbrace{\frac{k_{\text{tension}}}{A_0}}_{\text{unit correction}} \quad (4)$$

and

$$\frac{dF_{\text{actin}}}{dt} = \underbrace{\frac{F_{\text{per Actin}}k_{\text{actin}}}{L_0}}_{\text{force and length effects}} \underbrace{\left(k_{\text{const}} + k_{\text{cofilin}} + k_{\text{actin}} + k_{\text{drebrin}}\right)}_{\text{k contributions}} \frac{dL}{dt} \quad (5)$$

This is a phenomenological model with a combination of parameters from literature and constants fit to the experimental results (see SOM). In particular, Eqs. 4 and 5 depend on *f*(PIP2) and *g*(CofilinAct), which are sigmoidal functions that trigger in response to PI(4,5)P_2 and activated cofilin, respectively (Zmurchok *et al.*, 2018).

Using this model, we simulated calcium-mediated neurite retraction in control cells. We found that the model is able to capture the dynamics of neurite retraction events (Figure 3C). These models utilized experimental retraction data collected using differentiated PC12 cells transfected with small amounts of mCherry-actin to fit the phenomenological constants (Figure 3). Effectively, the model predicts that when the force exerted by actin is matched by the force due to tension, there is no change in the length of the neurite. Upon increase in PI(4,5)P_2 hydrolysis and calcium release into the cytosol, the forces due to membrane cortical tension increase, while the forces exerted by the actin decrease, and the neurite pulls back.

If this prediction is true, then we should be able to alter neurite retraction behavior by altering the expression of actin-related proteins or membrane tension separately. We next probed neurite retraction dynamics by varying the concentration of select

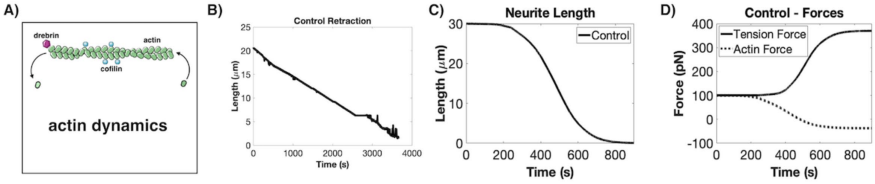

E)

Retraction Start Times of Control Cells	
Neurite 1	2.2 minutes
Neurite 2	2.4 minutes
Neurite 3	8.0 minutes
Neurite 4	7.8 minutes
Neurite 5	2.6 minutes
Neurite 6	4.0 minutes
Neurite 7	4.2 minutes
Neurite 8	2.5 minutes

FIGURE 3: Modeling of neurite retraction. (A) Simplified schematic of actin dynamics depicting assembly/disassembly as a combination of effects due to actin, cofilin, and drebrin concentration. (B) Example of retraction in response to carbachol stimulation of differentiated PC12 cells transfected with mCherry-actin. Identical behavior was seen over an average of eight neurites shown in E. (C) Computational results for neurite retraction determined from the described model. (D) Calculation of force plots due to increased tension in response to PI(4,5)P_2 hydrolysis, internalization of ligand-bound GPCRs, and tension effects. The force due to actin decreases and switches direction in response to actin breakdown and retrograde flow. (E) Table showing variation of retraction times under the same conditions.

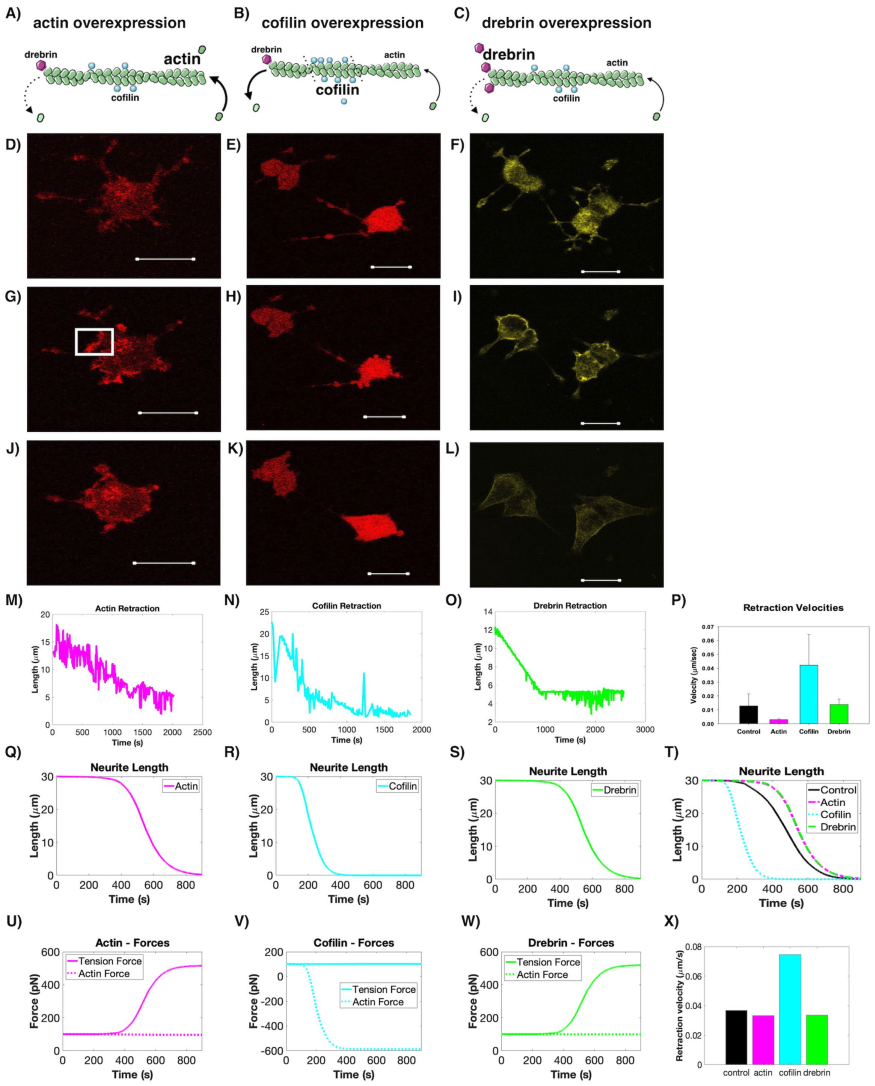

FIGURE 4: Experimental validation of model predictions. (A–C) Schematic of the experimental study to test the actin force model where mCherry-actin, mCherry-cofilin, or eYFP-Drebrin was expressed at varying levels in PC12 cells using increasing amounts of DNA in the transfections. The corresponding images are shown directly below. While cofilin activity is mediated by calcium, actin and drebrin dynamics depends on local concentrations. Column 1 (panels A, D, G, J, M, Q, U) is results from studies following mCherry-actin expressed in PC12 cells. The increase in actin, as estimated by Western blotting, reduces the change in the actin force. Panel D is an example image of cells before carbachol stimulation. G is 15 min poststimulation, showing the beginning stage of actin breakdown, indicated by the white box, and J is 30 min poststimulation. A representative retraction velocity curve is shown in M. Panels Q and U are the results of modeling the retraction velocity (Q) due to a tension force and an actin force (U). We note that the overexpression of actin leads to less of a decrease in actin force, since the increased actin concentration slows overall actin breakdown. Column 2 (panels B, E, H, K, N, R, V) shows how cofilin overexpression creates a large negative actin force to increase the rate of disassembly as shown in the schematic B. Panel E is an example image of cells expressing cofilin-RFP before carbachol stimulation, H is 7 min poststimulation, and K is 16 min poststimulation. A representative retraction velocity curve is shown in N. Panels R and V are the results of modeling the retraction velocity (R) due to the tension force and a larger negative actin force (V) since increased cofilin concentration increases actin breakdown. Column 3 (panels C, F, I, L, O, S, W) shows how drebrin overexpression slows the change in actin force as shown in

actin-related proteins such as cofilin, drebrin, and actin itself, both in experiments and in modeling.

Actin modulators regulate neurite retraction velocity

We followed actin disassembly in real time during carbachol-stimulated retraction using mCherry-actin in control cells and cells overexpressing cofilin or drebrin (Figure 4). Cofilin increases severing of actin filaments, increasing actin filament breakdown, while drebrin stabilizes actin filaments, inhibiting disassembly (McCullough *et al.*, 2008; Mikati *et al.*, 2013; Calabrese *et al.*, 2014; Grintsevich and Reisler, 2014). Figure 4, D–L, shows screen shots of the time lapse video made during retraction: Figure 4, D–F, shows representative cells before stimulation with carbachol, Figure 4, G–I, shows the same cells at the beginning of retraction, and Figure 4, J–L, shows the cells at longer times. Movies of retraction (SOM2) were analyzed to obtain the retraction velocities under the three different conditions (Figure 4, M–P). This quantification enables the comparison of the neurite retraction dynamics of actin in our controls versus actin when cofilin and drebrin are overexpressed. As expected, overexpression of cofilin enhances the rate of neurite retraction (Figure 4, M vs. N), and complete retraction results in cells with a trapezoidal morphology rather than the circular one typifying undifferentiated PC12 cells. This altered morphology likely stems from the smaller number of actin filaments throughout the cell due to cofilin overexpression (Pavlov *et al.*, 2007).

We expected that transfection of the cells with drebrin would strongly impede neurite retraction in the presence of carbachol, because drebrin is known to bind assembled actin filaments (F-actin) and stabilize them (Sharma *et al.*, 2011; Mikati *et al.*, 2013; Nair *et al.*, 2017). Small amounts of actin allowed a sustained linear decrease (Figure 4O) whose compiled average was within error of mCherry-actin alone (Figure 4P). These data support the idea that disruption of the intact actin network and its dynamic modeling when impeded by cofilin overexpression (increased severing) or by drebrin overexpression (inhibition of disassembly and remodeling) are key driving forces in governing retraction dynamics.

We modeled overexpression of cofilin, drebrin, and actin in the mechanical framework by altering the F_{actin} terms (Eq. 5) to represent the known effects of these proteins through the k contributions for each protein. We modeled actin force overall as a stress–strain relationship, where the k terms captured the contribution of each protein to overall actin force dynamics. For example, cofilin expression was incorporated into our constitutive equation as an increase in the total cofilin available for calcium activation, which therefore caused a faster decrease in F_{actin} by increasing the magnitude of the rate of change of F_{actin} through the $k_{cofilin}$ term. As a result, our model predicts that neurite retraction velocity is higher for cofilin overexpression than for controls (Figure 4, R and V). Similarly, we modeled drebrin overexpression by increasing drebrin concentration within the $k_{drebrin}$ term, consistent with experimental observations that a higher drebrin concentration slows actin depolymerization and thus slows the decrease in F_{actin} (Sharma *et al.*, 2011; Mikati *et al.*, 2013). Therefore, our model predicts that drebrin overexpression slows neurite retraction velocity relative to that in controls (Figure 4, S and W). Actin overexpression can be modeled in a similar manner to that of drebrin and is captured through the k_{actin} term. Thus, increasing actin concentration is essentially increasing the actin-to-cofilin ratio and therefore slowing the decrease in F_{actin}. Our model predicts that actin overexpression will slow neurite retraction velocities from those for controls (Figure 4, Q and U).

The results in Figure 4 show that by varying cofilin, drebrin, and actin concentrations, we predict different actin force dynamics that translate to different neurite retraction rates. Specifically, we predict that cofilin, actin, and drebrin overexpression leads to more rapid, slower, and slightly slower neurite retraction velocities than in controls, respectively. Our modeling results agree with experimental observations and suggest that actin disassembly and inhibition of reassembly are necessary for retraction. To support these studies, we quantified experiments that measured retraction of control cells and cells that overexpressed actin, cofilin, and drebrin. The experimental velocities of the retractions are plotted in Figure 4P and validate our model predictions in Figure 4X.

Neurite retraction can be driven by membrane tension.

Given that there are two contributions to the force acting on the neurite, one from actin and the other from membrane cortical tension, we next asked whether neurite retraction could be driven by changes to the membrane cortical tension alone. We directly tested this idea using hyperosmotic stress to increase membrane tension. Increasing the hyperosmotic stress from 300 to 600 mOsm on cultured PC12 cells resulted in the same retraction behavior and time scale as seen with carbachol stimulation (Figure 5A). To determine the change in membrane tension induced by this change in osmolarity, we measured tension by atomic force microscopy (AFM). This method allowed us to assess the stiffness of cells by measuring the amount of deflection experienced by a cantilever with a known spring constant as it indented the surface of the cell. For undifferentiated, differentiated, and retracted PC12 cells, AFM measurements were taken at the bases of the neurites or retracted neurites. The stiffness of each cell was determined by averaging the stiffness values at three separate locations on each cell in order to combat the inherent heterogeneity in cell structure while ensuring no localized damage from a previous measurement. Undifferentiated cells were the stiffest condition tested, followed by retracted and then differentiated (Figure 5B).

We also used AFM to determine the stiffness of cells subjected to hypoosmotic and hyperosmotic stress for undifferenced and differentiated PC12 cells. Hypoosmotic and hyperosmotic stress, which lead to cell swelling and cell dehydration, respectively, result in an increase and a decrease in cell stiffness, respectively (Figure 5B). Force curves that are representative of the average stiffness value for each condition show a smooth Hertz model relationship between indentation depth and applied force, as expected (Figure 5, C and D). Taken together, these studies show a direct correlation between cell stiffness and osmotic stress, which is also correlated with retraction.

schematic C. Panel F is an example image of cells expressing drebrin-eYFP before carbachol stimulation. I is 15 min poststimulation, and L is 30 min poststimulation. A representative retraction velocity curve is shown in O.
A representative retraction velocity curve is shown in O. Panels S and W are the results of modeling the retraction velocity (S) due to the tension force and the actin force (W). We note that increased drebrin concentration resists actin breakdown. Panels P, T, and X are compiled retraction velocities obtained experimentally (P) control ($n = 4$), actin ($n = 4$), cofilin ($n = 3$), and drebrin ($n = 4$) showing standard error, and computationally (T) and (X), showing the very close correlation between experimental and theoretical results. All scale bars = 20 μm.

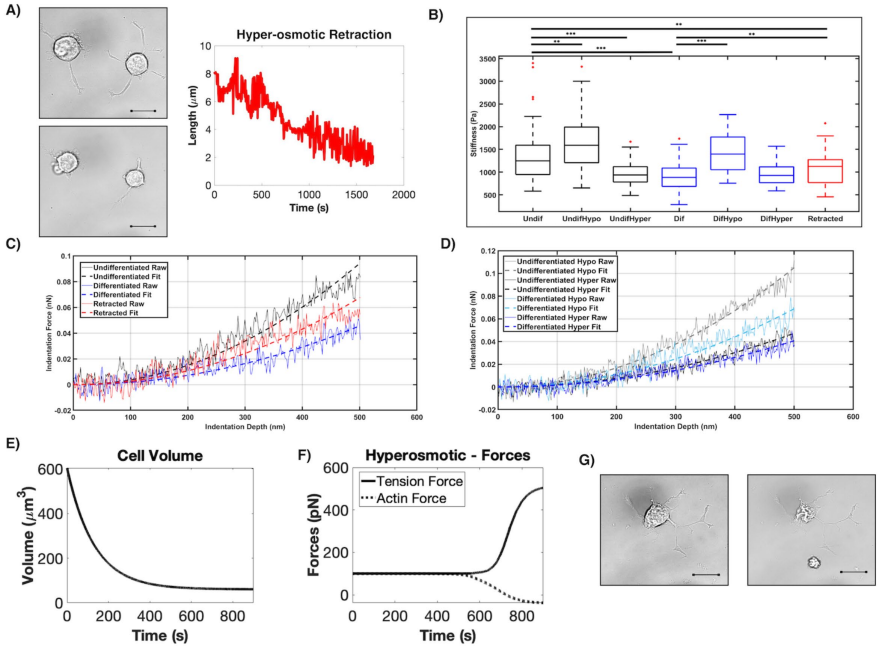

FIGURE 5: Neurite retraction can be induced by membrane tension in response to hyperosmotic stress. (A) Phase contrast images of PC12 cells under isotonic conditions (300 mOsm, top left) and hyperosmotic conditions (450 mOsm, bottom left) after 10 min. The corresponding neurite retraction curve for the cell on the left is shown to the right. (B) Cell stiffness as measured by atomic force microscopy of undifferentiated and differentiated PC12 cells under isotonic conditions and cells subjected to hypoosmotic (150 mOsm) or hyperosmotic (450 mOsm) stress, where the number of cells $n = 14–46$, and where $^{**}p < 0.01$, $^{***}p < 0.001$. (C, D) Force curves representative of the average stiffness values in B with automated Hertz model fitting (see methods) over 500 nm indentation for untreated cells (left) and hypoosmotic/hyperosmotic treated cells (right). (E, F) Hyperosmotic stress is modeled as an instantaneous increase in membrane tension due to the reduction in volume–to–surface area ratio, which causes a membrane tension increase and a smaller cytoskeletal force (E) and triggers neurite retraction through an increase in primary tension force (F), in the absence of ligand input. (G) Phase contrast images of differentiated PC12 cells before the application of osmotic stress (left) and after increasing the osmolarity from 300 to 600 mOsm in calcium-free medium. Note the loss in cell volume seen by membrane puckering but without retraction (right)

Within our model, we can also probe neurite retraction dynamics by varying the contribution of tension, the τ component of the mechanical model. Membrane cortical tension is altered under hyperosmotic conditions when water expulsion from the cell leads to a reduction in volume–to–surface area ratio. Therefore, to model hyperosmotic conditions instead of a carbachol stimulus, we predict that this volume–to–surface area ratio change causes an increase in membrane cortical tension. Therefore, we model a slightly elevated membrane cortical tension initial condition that triggers a related force (Figure 5E) and neurite retraction (Figure 5F). We also see a change in actin force, triggered by the coupling between actin and tension in the model, which is also predicted experimentally due to the necessary actin reorganization during retraction caused by hyperosmotic conditions. Therefore, our model predicts neurite retraction in the absence of a ligand stimulus with hyperosmotic conditions (Figure 5F), indicating that membrane cortical tension is a key component governing neurite retraction dynamics.

We tested whether the retraction that results from osmotic stress is convergent with the Gαq/PLCβ pathway. Keeping in mind that membrane compression regulates calcium flux to drive actin dynamics in model systems (Hartzell *et al.*, 2016; Nourse and Pathak, 2017; He *et al.*, 2018), we determined whether hyperosmotic stress would open calcium channels to allow divalent cation influx to relieve the osmotic stress. Using a fluorescent calcium indicator, we found that increasing the osmotic strength from 300 to 600 mOsm resulted in a small increase in intracellular calcium by ~10% of the increase seen for ACh stimulation. To verify that calcium is mediating retraction, we removed extracellular calcium from the media and found that even though increasing the osmotic strength through the addition of KCl caused membrane folds and puckering, consistent with a loss in cell volume, neurite length remained constant (Figure 5G). This result indicates that the two types of retraction pathways converge on calcium levels, those initiated by Gαq/PLCβ stimulation and those initiated by extracellular calcium influx by tension-sensitive calcium channels.

Prolonged exposure to Gαq agonists leads to nerve ring disruption in *Caenorhabditis elegans*

To determine whether we could disrupt neuronal connections and retract neurites in a neuronal network, we used the optically clear

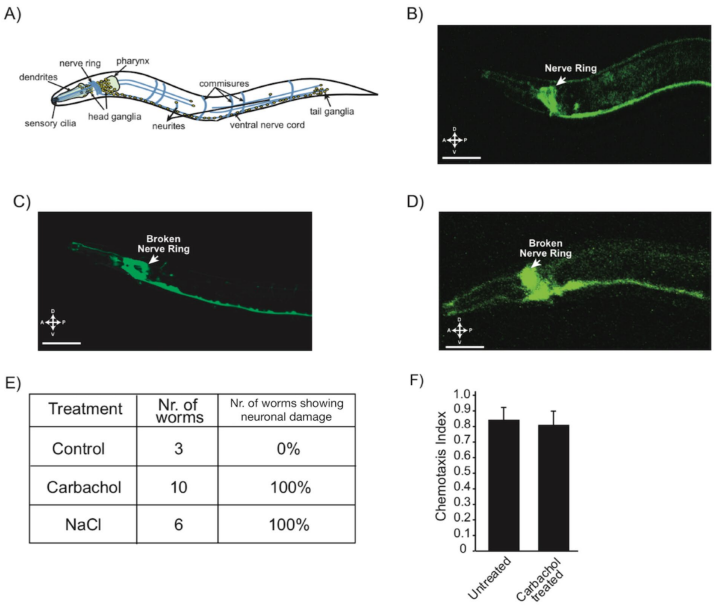

Treatment	Nr. of worms	Nr. of worms showing neuronal damage
Control	3	0%
Carbachol	10	100%
NaCl	6	100%

FIGURE 6: Neurite retraction induced by membrane tension is seen in the neural network of *C. elegans*. (A) General schematic of the nervous system of *C. elegans*. (B) Untreated *C. elegans* that expresses GFP G-CAMP through the nerve ring and ventral nerve. (C) A representative worm with 1 mM carbachol for 30 min showing a broken nerve ring and pilling ventral nerve. (D) A representative worm subjected to hyperosmotic stress showing a broken nerve ring. (E) Table showing the compiled results of each experimental condition and the number of resulting nerve rings that were broken. (F) Results of a chemotaxis assay testing movement of *C. elegans* with and without l mM carbachol treatment.

model system C. *elegans*. We first used a strain of *C. elegans* (QWl166) that expresses an integrated fluorescent calcium sensor G-CaMP throughout the nervous system. This system allows us to visualize by fluorescence the neurons that show increased calcium levels in response to acetylcholine stimulation. This specific strain has fluorescence in every neuron in the nerve ring, allowing us to look at the ring as a whole, as well as fluorescence in the entire ventral nerve of the worm, which extends the entire length of the worm. We focused on acetylcholine signals emanating from neurons within the nerve ring located in the head of the worm and along the ventral nerve cord (Figure 6A). Normal signal transmission can be seen in the images in Figure 6B. For these studies, we wished to determine only whether there is broad neuronal rupture and retraction within the nerve ring and along the ventral nerve, which would be indicated by the lack of fluorescence in the center in the ring and dark spots along the ventral nerve. In every worm tested ($n = 10$), we find neuronal rupture with acetylcholine stimulation that occurs in the nerve ring close to the organism's mouth (Figure 6C). Additionally, we see a distinct pilling of the ventral nerve, which displays thinning and clustering, and portions that are no longer fluorescent, indicating large-scale neuronal damage.

We confirmed the connection between neuronal network disruption produced by extended acetylcholine stimulation to membrane tension by subjecting the worms to hyperosmotic stress (increasing the salt solution concentration by 50%). After osmotic stress, these organisms showed a lack of fluorescence in the nerve ring, indicating rupture and retraction of neurons. Also, we see much larger segments of the ventral nerve that have been disrupted with less pilling than seen for acetylcholine stimulation (Figure 6D). The somewhat different morphological effects on the ventral nerve seen in osmotic stress are most likely due to the ability of the stress to be distributed uniformly along the length of the organism, as opposed to carbachol, whose receptors are concentrated mostly in the mouth.

To support neuronal disruption of the worms by acetylcholine, we followed changes in movement of the whole organisms, using a chemotaxis assay with and without acetylcholine stimulation. These studies were also done using the *C. elegans* QWl166 strain. We see that after treatment with acetylcholine, 83% of the worms moved toward the attractant, while the remaining 17% did not move at all (Figure 6F).

DISCUSSION

For an organism to learn, neurons must break and reform connections with neighboring neurons, and disruptions in these processes underlie learning-based neurological diseases and neurodegeneration. Despite the importance of synapse severing and formation, the mechanisms that underlie neural plasticity are not well understood (Licht *et al.*, 2011). Previous studies of neural plasticity have mainly focused on contributors to neurogenesis in hippocampal neurons and cultured *Drosophila* neurons, such as neuronal stem cells (LaFerla, 2002). Here, we have defined the synaptic breakage and neurite rupture in neural plasticity in terms of membrane tension and calcium-induced retraction that will allow for predictable actin remodeling.

Calcium is a crucial component for the growth, differentiation, and survival of neurons (Rosenberg and Spitzer, 2011). Calcium helps to regulate the differentiation of specific neuronal types as well as their migration through the body, and calcium levels are directly liked to neurodegenerative diseases such as Alzheimer's (LaFerla, 2002). We followed neuronal cell response to extended calcium signals that may mimic dysfunctional states. Unexpectedly, we found that extended calcium levels resulted in complete neurite retraction, and this retraction can be seen by following the plasma membrane, by a GPCR coupled to Gαq, and by $PI(4,5)P_2$. These data show that the Gαq signaling pathways are intimately involved with the mechanical properties of the cell.

The connection between calcium signals from GPCR/Gαq and cell mechanics was supported using fluorescence-tagged actin and by measuring retraction when overexpressing cofilin, an actin depolymerizing protein, or drebrin, an actin monomer recruitment protein. Overexpressing cofilin at a level 6x higher than endogenous levels allows for much faster velocities of neurite retraction initiated by GPCR-Gαq/Ca^{2+} after an initial lag period. These observations correlate well with cofilin's ability to depolymerize actin, but shows that activation of the Gαq/$PI(4,5)P_2$/Ca^{2+} pathway is a necessary prerequisite. In contrast, cells

overexpressing drebrin show a similar retraction rate as endogenous which correlates to its ability to stabilize actin monomers (Mikati *et al.*, 2013). This observation indicates that the behavior we are viewing is due solely to actin depolymerization without contributions of the polymerization events. Thus, while Ca^{2+} signals drive retraction, actin plays a passive role.

There are other physiological events that might play a role in neurite retraction. PLCβ is the primary effector of Gαq, but we also note Gαq activates proteins that impact RhoA (see Sanchez-Fernandez *et al.*, 2014) potentially contributing to the mechanical changes associated with retraction. However, this contribution will be operative only for retraction that occurs in response to carbachol and not osmotic stress. Additionally, the loss of neurites during retraction shifts its associated plasma membrane population to the cytosol in the cell body. This net increase in the cytosolic PLCβ population will promote PLCβ's cytosolic roles in directing translation of specific mRNAs (see Scarlata *et al.*, 2018; Scarlata, 2019), which are typically not operative during Gαq stimulation. The net effect of cytosolic PLCβ would be shifting protein populations during longer times not probed in this study.

The coupling between calcium signaling and mechanical forces has been observed in cell motility and in dendritic spines during long-term potentiation, astrocyte calcium signaling, and neurite protrusion and formation (Mutalik *et al.*, 2018). On the basis of these studies, we postulated that neurite retraction results from changes in cortical tension brought about by receptor endocytosis, $PI(4,5)P_2$ hydrolysis and IP_3 generation, and an increase in intracellular calcium, and we formulated a mechanochemical pathway to test this idea. We found that, indeed, a force balance between cortical tension and actin-mediated forces, both of which are mediated by intracellular calcium levels, is sufficient to capture the dynamics of neurite retraction. This idea was explicitly tested by measuring changes in membrane stiffness with osmotic strength and by altering the effects of different actin remodeling proteins. We also found that the effects of actin and cortical tension could be uncoupled to a certain extent, pointing toward multiple mechanical pathways that could exquisitely regulate neurite retraction. We acknowledge that the proposed model is phenomenological, and while it captures the key physics of the processes underlying neurite retraction, future studies will focus on elaborating on some of the phenomenological relationships proposed here.

Our results show that acetylcholine-induced calcium signals may have a dramatic impact on neuronal morphology and synaptic connections, and this idea was demonstrated in *C. elegans*. Neurite formation and extension is essential to transition from neuroblast to mature neuron and *C. elegans* are an excellent model system to understand neurite formation and retraction. The site of nascent neurite outgrowth is determined by cell intrinsic factors that orchestrate the localized regulation of actin and microtubules, and in developing neurons, these factors are polarized at sites of neurite outgrowth in response to extracellular cues (Randlett, 2011). Our finding that the neural network of this organism can be modified by Gαq activation or increased mechanical tension may form a basis for studies that better describe neural rewiring paradigms.

In summary, our studies indicate the role of acetylcholine in facilitating neurite retraction. Further research on how this pathway interacts with other pathways to coordinate remodeling with such spatiotemporal precision will provide insights into the molecular basis of neurodegeneration.

MATERIALS AND METHODS

Cell culture, transfection, and differentiation

PC12 cells, which are derived from rat pheochromocytoma (ATCC CRL-1721), were cultured in 35-mm or 100-mm poly-D-lysine–coated Petri dishes using DMEM (Life Technologies) with 10% heat-inactivated horse serum (Life Technologies), 5% fetal bovine serum (Atlanta Biologicals), and 1% penicillin/streptomycin. The dishes were incubated with 5% CO_2 at 37°C. Cells were transfected using different amounts of plasmid based on the concentration as tested using a NanoDrop. Cells were transfected using Lipofectamine 3000 (Invitrogen) following the protocol of the manufacturer. The medium used in transfection was the same DMEM culture medium, with the exception of antibiotics to increase transfection efficiency, and the medium was changed back to normal culture medium after 24 h. Cells were differentiated using media that contained DMEM, 1% heat-inactivated horse serum, and 1% penicillin/streptomycin. Added to this would be a 1:1000 ratio of l00 ng/μl nerve growth factor (NGF) (Novoprotein). This medium is added to the cells for at least 48 h and up to 96 h to achieve long neurites.

Plasmids and maxi/min prep

Fluorescence-tagged plasmids were obtained and maxi/min prepped using a Qiagen kit and following the manufacturer's guidelines. The plasmids were obtained from Addgene. Actin #54967 was derived by Michael Davidson at Harvard Medical School, Drebrin #40359 was derived by Phillip Gordon-Weeks at King's College of London, Cofilin #51279 was derived by James Bamburg at Colorado State University, the Pleckstrin homology (PH)-domain of PLC8 #21179 was derived by Tobias Meyer at Stanford University, and the bradykinin type 2 receptor was modified from a construct provided by Fredrik Leed-Lundber, University of Texas, San Antonio.

Calcium green staining

Prior to imaging, cells were washed with Hanks' balanced salt solution (HBSS) with calcium, magnesium, no phenol red (Thermofisher), and then a 1:200 mixture of HBSS and Calcium Green (Thermofisher) was added and allowed to incubate for 1 h before imaging.

Preparation of carbachol

Carbachol in powdered form was obtained from Sigma Aldrich. It was dissolved in water to a final concentration of l mM at a volume of l0 ml and aliquoted into 500-μl portions to be used for each experiment. The solutions were kept at –20°C.

Fluorescence microscopy/stimulation of cells

Fluorescence imaging was done using a Zeiss LSM510 inverted confocal microscope. Imaging was carried out at least 48 h after transfection and differentiation. The cells were grown and imaged in a MAT-Tek 8 chamber glass-bottom plate or a MAT-Tek 35-mm glass-bottom dish. Once a single cell was found visually that expressed the plasmid or stain, the microscope was switched to the correct wavelength and laser intensity. A time series image was then started and stopped after 10 frames, the cells was manually stimulated by adding carbachol to the dish to achieve the desired final molarity, and the time series video was then started immediately after carbachol was added. Retraction velocities were determined by the software *Re-Track* (unpublished data).

Osmotic stress and EDTA studies

Osmotic stress studies were done using calcium-free isotonic media for imaging, with the addition of KCl at different concentrations to achieve osmotic stress. In studies that include EDTA (J.T. Baker),

cells were osmotically stressed and EDTA was added to the dish to give a final concentration of 0.5 µM for partial neurite retraction and 1 µM for full neurite retraction.

Plasmid-specific studies

Calcium Green and enhanced green fluorescent protein (eGFP) studies were imaged using an argon laser at 488 nm. Red fluorescent protein (RFP) and mCherry were imaged using argon ion and HeNe lasers at 543 nm. YFP and CFP were imaged using argon ion and HeNe lasers at a wavelength of 545 nm. Multitrack imaging can also be done combining of these setups. Images were taken by alternating between probes when data for more than one were being monitored, and these images were subsequently merged.

Atomic force microscopy stiffness measurements

Live cells were probed utilizing an MFP-3D-BIO atomic force microscope (Asylum Research) and a DNP cantilever (Bruker) with nominal spring constant 0.06 N/m. The cantilever was calibrated before each measurement to ensure accuracy. Cells were seeded on 60 mm poly-D-lysine–coated Petri dishes using DMEM (Life Technologies) with 10% heat-inactivated horse serum (Life Technologies), 5% fetal bovine serum (Atlanta Biologicals), and 1% penicillin/streptomycin. After 24 h of recovery, cells were differentiated using media containing DMEM, 1% heat-inactivated horse serum, and 1% penicillin/streptomycin. Added to this was a 1:1000 ratio of 100 ng/µl nerve growth factor (NGF) (Novoprotein). This was added to the cells a minimum of 24 h before measurements were taken.

Cells were viewed 2 d after plating and 1 d after treatment with nerve growth factor (NGF). Cells with minimal cell–cell contact were selected to reduce the mechanical impacts of cell communication. Three force curves in separate perinuclear regions with cantilever velocity of 2 µm/s and trigger point InN were taken for each selected cell. Measurements were taken within 30 min of removal from the incubator to facilitate cell viability.

The stiffness of the measured cells E was determined from the force curve data utilizing the Hertz model for conical cantilever tip geometry,

$$E = kd\pi\left(1-\nu^2\right)/2\Delta^2 \tan\phi$$

where k is the cantilever spring constant, d is the cantilever deflection, ν is the Poisson's ratio (0.5 used for an assumed incompressible material), Δ is the sample indentation depth, and ϕ is the half-angle of the conical cantilever tip (35°). The force curves were processed using a custom MATLAB code that fits the indentation curve over a 500 nm range after manual selection of the initial contact point.

Fluorescence imaging of *Caenorhabditis elegans*

Worms were transferred into a microcentrifuge tube containing l mM carbachol and were submerged in the tube for 30 min at room temperature or in 100 mM NaCl solution for 10 min. After 30 or 10 min, respectively, the worms were removed from solution and placed on a glass slide with a thin layer of agar for the worms to lie on. Excess carbachol was wicked up from the pad and the worms were paralyzed using 25 M levamisole, which does not affect our pathway of interest. The worms were then imaged on an inverted confocal microscope and were visually checked for neurite rupture and retraction.

Chemotaxis assay of *Caenorhabditis elegans*

Worms were transferred to a new seeded plate 24 h before the experiment. The day of the experiment an unseeded plate was marked with a dot in the center and two circles on either ends of the plate with the "C" for control of DI water and "D" for diacetyl, which is the attractant. Using approximately 1 ml of S Basal (5.85 g NaCl, 1 g K_2HPO_4, 6 g KH_2PO_4, 1 ml cholesterol [5 mg/ml in ethanol], H_2O to 1 liter; sterilize by autoclaving; see Stiernagle, 2006), the worms were washed into a microcentrifuge tube and allowed to pellet for 5–10 min. Once pelleted, the worms were washed with S Basal two more times and finally with water. Suspended worms (10 µl) were transferred to the experimental plate previously made and the excess water was removed by wicking. The plate was then incubated for 45 min at 20°C, and afterward, the worms that moved to either the attractant or control were counted.

ACKNOWLEDGMENTS

This work was supported by National Institutes of Health grant GM116187 (S.S.) and Air Force Office of Scientific Research (AFOSR) MURI FA9550-18-1-0051 (P.R.) and R01DC016058 (J.S.). We thank various members of the Rangamani and Scarlata labs for valuable discussion and manuscript review. We thank Sayed Iman Mousavi (Yale University) and Erkan Tuzel (Temple University) for writing the Re-Track program. We thank the UCSD Interfaces Graduate Training Program and the San Diego Fellowship for funding and support for M.B. M.B. was also supported by a National Defense Science and Engineering Graduate (NDSEG) Fellowship, AFOSR Multidisciplinary Research Program of the University Research Initiative (MURI) grant FA9550-18-1-0051 to P.R., and the National Institutes of Health (Grant T32EB009380).

REFERENCES

Berstein G, Blank JL, Jhon D-Y, Exton JH, Rhee SG, Ross EM (1992). Phospholipase C-β1 is a GTPase-activating protein for $G_{q/11}$, its physiologic regulator. Cell 70, 411–418.

Bittner MA, Holz RW (2005). Phosphatidylinositol-4,5-bisphosphate: actin dynamics and the regulation of ATP-dependent and -independent secretion. Mol Pharmacol 67, 1089–1098.

Bornschlogl T, Romero S, Vestergaard CL, Joanny JF, Van Nhieu GT, Bassereau P (2013). Filopodial retraction force is generated by cortical actin dynamics and controlled by reversible tethering at the tip. Proc Natl Acad Sci USA 110, 18928–18933.

Brini M, Cali T, Ottolini D, Carafoli E (2014). Neuronal calcium signaling: function and dysfunction. Cell Mol Life Sci 71, 2787–2814.

Calabrese B, Saffin JM, Halpain S (2014). Activity-dependent dendritic spine shrinkage and growth involve downregulation of cofilin via distinct mechanisms. PLoS One 9, e94787.

Clapham DE (2007). Calcium signaling. Cell 131, 1047–1058.

Datar A, Ameeramja J, Bhat A, Srivastava R, Bernal R, Prost J, Callan-Jones A, Pullarkat PA (2019). The roles of microtubules and membrane tension in axonal beading, retraction, and atrophy. Biophys J 117, 880–891.

Diz-Munoz A, Fletcher DA, Weiner OD (2013). Use the force: membrane tension as an organizer of cell shape and motility. Trends Cell Biol 23, 47–53.

Dohlman HG, Thorner J (1997). RGS proteins and signaling by heterotrimeric G proteins. J Biol Chem 272, 3871–3874.

Drubin DG, Feinstein SC, Shooter EM, Kirschner MW (1985). Nerve growth factor-induced neurite outgrowth in PC12 cells involves the coordinate induction of microtubule assembly and assembly-promoting factors. J Cell Biol 101, 1799–1807.

Franze K, Gerdelmann J, Weick M, Betz T, Pawlizak S, Lakadamyali M, Bayer J, Rillich K, Gogler M, Lu YB, *et al.* (2009). Neurite branch retraction is caused by a threshold-dependent mechanical impact. Biophys J 97, 1883–1890.

Freedman NJ, Lefkowitz RJ (1996). Desensitization of G protein-coupled receptors. Recent Prog Horm Res 51, 319–351; discussion 352–313.

Garcia P, Gupta R, Shah S, Morris AJ, Rudge SA, Scarlata S, Petrova V, McLaughlin S, Rebecchi MJ (1995). The pleckstrin homology domain of phospholipase C-delta 1 binds with high affinity to phosphatidylinositol 4,5-bisphosphate in bilayer membranes. Biochemistry 34, 16228–16234.

Getz M, Swanson L, Sahoo D, Ghosh P, Rangamani P (2019). A predictive computational model reveals that GIV/girdin serves as a tunable valve for EGFR-stimulated cyclic AMP signals. Mol Biol Cell 30, 1621–1633.
Gilbert J, Man H-Y (2017). Fundamental elements in autism: from neurogenesis and neurite growth to synaptic plasticity. Front Cell Neurosci 11, 359–359.
Goldberg DJ, Grabham PW (1999). Braking news: calcium in the growth cone. Neuron 22, 423–425.
Gomez TM, Spitzer NC (1999). In vivo regulation of axon extension and pathfinding by growth-cone calcium transients. Nature 397, 350–355.
Greene LA, Tischler AS (1976). Establishment of a noradrenergic clonal line of rat adrenal pheochromocytoma cells which respond to nerve growth factor. Proc Natl Acad Sci USA 73, 2424–2428.
Grintsevich EE, Reisler E (2014). Drebrin inhibits cofilin-induced severing of F-actin. Cytoskeleton (Hoboken) 71, 472–483.
Guo Y, Rebecchi M, Scarlata S (2005). Phospholipase Cbeta2 binds to and inhibits phospholipase Cdelta1. J Biol Chem 280, 1438–1447.
Hartzell CA, Jankowska KI, Burkhardt JK, Lewis RS (2016). Calcium influx through CRAC channels controls actin organization and dynamics at the immune synapse. Elife 5, e14850.
Hassinger JE, Oster G, Drubin DG, Rangamani P (2017). Design principles for robust vesiculation in clathrin-mediated endocytosis. Proc Natl Acad Sci USA 114, E1118–E1127.
He L, Tao J, Maity D, Si F, Wu Y, Wu T, Prasath V, Wirtz D, Sun SX (2018). Role of membrane-tension gated Ca(2+) flux in cell mechanosensation. J Cell Sci 131, jcs208470.
Kadamur G, Ross EM (2013). Mammalian phospholipase C. Annu Rev Physiol 75, 127–154.
Kerstein PC, Nichol RI, Gomez TM (2015). Mechanochemical regulation of growth cone motility. Front Cell Neurosci 9, 244.
King AE, Woodhouse A, Kirkcaldie MT, Vickers JC (2016). Excitotoxicity in ALS: overstimulation, or overreaction? Exp Neurol 275(Pt 1), 162–171.
LaFerla FM (2002). Calcium dyshomeostasis and intracellular signalling in Alzheimer's disease. Nat Rev Neurosci 3, 862–872.
Licht T, Goshen I, Avital A, Kreisel T, Zubedat S, Eavri R, Segal M, Yirmiya R, Keshet E (2011). Reversible modulations of neuronal plasticity by VEGF. Proc Natl Acad Sci USA 108, 5081–5086.
Logan MR, Mandato CA (2006). Regulation of the actin cytoskeleton by PIP2 in cytokinesis. Biol Cell 98, 377–388.
Lohmann C, Wong RO (2005). Regulation of dendritic growth and plasticity by local and global calcium dynamics. Cell Calcium 37, 403–409.
Mattson MP (2007). Calcium and neurodegeneration. Aging Cell 6, 337–350.
McCullough BR, Blanchoin L, Martiel JL, De la Cruz EM (2008). Cofilin increases the bending flexibility of actin filaments: implications for severing and cell mechanics. J Mol Biol 381, 550–558.
McKay SE, Purcell AL, Carew TJ (1999). Regulation of synaptic function by neurotrophic factors in vertebrates and invertebrates: implications for development and learning. Learn Mem 6, 193–215.
Mikati MA, Grintsevich EE, Reisler E (2013). Drebrin-induced stabilization of actin filaments. J Biol Chem 288, 19926–19938.
Mutalik SP, Joseph J, Pullarkat PA, Ghose A (2018). Cytoskeletal mechanisms of axonal contractility. Biophys J 115, 713–724.
Nair RR, Patil S, Tiron A, Kanhema T, Panja D, Schiro L, Parobczak K, Wilczynski G, Bramham CR (2017). Dynamic arc SUMOylation and selective interaction with F-actin-binding protein drebrin A in LTP consolidation in vivo. Front Synaptic Neurosci 9, 8.
Nourse JL, Pathak MM (2017). How cells channel their stress: interplay between Piezo1 and the cytoskeleton. Semin Cell Dev Biol 71, 3–12.
Pavlov D, Muhlrad A, Cooper J, Wear M, Reisler E (2007). Actin filament severing by cofilin. J Mol Biol 365, 1350–1358.
Randlett O, Poggi L, Zolessi FR, Harris WA (2011). The oriented emergence of axons from retinal ganglion cells is directed by laminin contact in vivo. Neuron 70, 266–280.
Rangamani P, Fardin MA, Xiong Y, Lipshtat A, Rossier O, Sheetz MP, Iyengar R (2011). Signaling network triggers and membrane physical properties control the actin cytoskeleton-driven isotropic phase of cell spreading. Biophys J 100, 845–857.
Raucher D, Stauffer T, Chen W, Shen K, Guo S, York JD, Sheetz MP, Meyer T (2000). Phosphatidylinositol 4,5-bisphosphate functions as a second messenger that regulates cytoskeleton-plasma membrane adhesion. Cell 100, 221–228.
Rosenberg SS, Spitzer NC (2011). Calcium signaling in neuronal development. Cold Spring Harb Perspect Biol 3, a004259.
Sanchez-Fernandez G, Cabezudo S, Garcia-Hoz C, Beninca C, Aragay AM, Mayor F Jr, Ribas C (2014). Galphaq signalling: the new and the old. Cell Signal 26, 833–848.
Scarlata S (2019). The role of phospholipase Cβ on the plasma membrane and in the cytosol: How modular domains enable novel functions. Adv Biol Regul 73, 100636.
Scarlata S, Singla A, Garwain O (2018). Phospholipase Cβ interacts with cytosolic partners to regulate cell proliferation. Adv Biol Regul 67, 7–12.
Sengupta P, Samuel ADT (2009). *Caenorhabditis elegans*: a model system for systems neuroscience. Curr Opin Neurobiol 19, 637–643.
Sharma S, Grintsevich EE, Phillips ML, Reisler E, Gimzewski JK (2011). Atomic force microscopy reveals drebrin induced remodeling of f-actin with subnanometer resolution. Nano Lett 11, 825–827.
Sheetz MP (2001). Cell control by membrane–cytoskeleton adhesion. Nat Rev Mol Cell Biol 2, 392–396.
Sheetz MP, Dai J (1996). Modulation of membrane dynamics and cell motility by membrane tension. Trends Cell Biol 6, 85–89.
Simunovic M, Manneville JB, Renard HF, Evergren E, Raghunathan K, Bhatia D, Kenworthy AK, Voth GA, Prost J, McMahon HT, *et al.* (2017). Friction mediates scission of tubular membranes scaffolded by BAR proteins. Cell 170, 172–184.e111.
Stiernagle T (2006, February 11). Maintenance of *C. elegans*. In: WormBook: The Online Review of *C. elegans* Biology [Internet], Pasadena, CA, 2005–2018.
Stuchlik A (2014). Dynamic learning and memory, synaptic plasticity and neurogenesis: an update. Front Behav Neurosci 8, 106–106.
Takeuchi T, Duszkiewicz AJ, Morris RGM (2014). The synaptic plasticity and memory hypothesis: encoding, storage and persistence. Philos Trans R Soc Lond B Biol Sci 369, 20130288.
van Rheenen J, Jalink K (2002). Agonist-induced PIP(2) hydrolysis inhibits cortical actin dynamics: regulation at a global but not at a micrometer scale. Mol Biol Cell 13, 3257–3267.
Voglis G, Tavernarakis N (2006). The role of synaptic ion channels in synaptic plasticity. EMBO Rep 7, 1104–1110.
West AE, Chen WG, Dalva MB, Dolmetsch RE, Kornhauser JM, Shaywitz AJ, Takasu MA, Tao X, Greenberg ME (2001). Calcium regulation of neuronal gene expression. Proc Natl Acad Sci USA 98, 11024–11031.
Zmurchok C, Bhaskar D, Edelstein-Keshet L (2018). Coupling mechanical tension and GTPase signaling to generate cell and tissue dynamics. Phys Biol 15, 046004.

Acknowledgement

Chapter 3, in full, is a reprint of the material as it appears in Gαq-mediated calcium dynamics and membrane tension modulate neurite plasticity in Molecular Biology of the Cell, 2020. Pearce, Katherine; Bell, Miriam; Linthicum, Will H.; Wen, Qi; Srinivasan, Jagan; Rangamani, Padmini; Scarlata, Suzanne, MBoC, 2020 [2]. The dissertation author was the co-primary investigator and co-author of this paper. For Chapter 3, I would like to acknowledge my coauthors Katherine Pearce, Will H. Linthicum, Professor Qi Wen, Professor Jagan Srinivasan, Professor Padmini Rangamani, and Professor Suzanne Scarlata. We thank various members of the Rangamani and Scarlata labs for valuable discussion and manuscript review. We thank Sayed Iman Mousavi (Yale University) and Erkan Tuzel (Temple University) for writing the Re-Track program. I would like to acknowledge my funding from the UCSD Interfaces Graduate Training Program and the San Diego Fellowship, from a National Defense Science and Engineering Graduate (NDSEG) Fellowship, AFOSR Multidisciplinary Research Program of the University Research Initiative (MURI) grant FA9550-18-1-0051 to P.R., and the National Institutes of Health (Grant T32EB009380).

Chapter 4

Does geometry influence membrane voltage propagation in dendritic spines and dendrites?

4.1 Introduction

Neurons use electrical signals to communicate quickly across multiple lengthscales. This was first observed in axons where an action potential, a change in membrane voltage, propagates down from the soma to trigger communication to its downstream neighbors. Historically, computational and mathematical models have been developed to describe these voltage dynamics, most notably the Hodgkin-Huxley model and cable equations [30,31]. Both these models can predict voltage depolarization as the sum of representative currents through voltage dependent channels, which mathematically are described through voltage dependent gating variables and reverse potentials. This approach was very successful and helped shepherd in the era of computational modeling into both the neuroscience community and the larger biophysics community [30].

Voltage propagation occurs on other portions of neurons as well, including along dendrites and within dendritic spines [32]. Studies have used cable equations and similar models to predict voltage in dendrites [33], but there are geometric constraints in some dendrites and in dendritic spines that begin to potentially violate the assumptions underlying those models. More specifically, we need to capture the small lengthscales, complex morphologies, and heterogeneous channel and receptor distributions of dendritic spines [7, 34, 35], and the cable equation has limitations to its spatial and biochemical representations and assumptions.

Therefore, we use a computational model to investigate how morphology influences membrane voltage propagation from a biochemical and electrical perspective. We want to investigate the propagation of voltage in both dendrites and dendritic spines [36–39]. Fundamentally membrane voltage refers to a difference in ion concentration across a membrane [40]; thus we propose the use of reaction-diffusion dynamics and Hodgkin-Huxley and Morris-Lecar inspired dynamics to model membrane potential explicitly as a function of spatial ion concentration [41]. In this way, we can directly relate membrane voltage to ion movement, neuronal morphology, and ion channel properties and localization.

4.2 Methods

4.2.1 Mathematical Model

To address membrane voltage change in response to receptor and channel activation, we developed 2D axisymmetric and 3D reaction-diffusion models in COMSOL with coupled membrane voltage and membrane fluxes for various ions. We explicitly model Na^+, K^+, Ca^{2+}, and Cl^- in the extracellular space (ECS), cytoplasm, and endoplasmic reticulum (ER) using reaction-diffusion dynamics. Each ion has boundary conditions corresponding

to ion influx or efflux through voltage-dependent channels, and the receptors AMPAR and NMDAR for the dendritic spine cases. We consider several different model geometries including a thin dendritic spine and dendrites.

4.2.2 Equations

Reaction diffusion dynamics

The various ion dynamics are given by reaction diffusion dynamics. For some ion Y, its volumetric dynamics are given by

$$\frac{\partial Y}{dt} = D_Y \nabla^2 Y - f(Y, ...), \tag{4.1}$$

where f(Y,...) are any volumetric reaction rates, and D_Y is the diffusion coefficient for ion Y. In this framework, membrane flux is given by

$$- D_Y \mathbf{n} \cdot \nabla Y = J_Y, \tag{4.2}$$

where J_Y captures any membrane flux reaction terms for the ion Y through specified boundaries.

Membrane voltage formulation

Membrane voltage is based on a combination of Hodgkin-Huxley and Morris-Lecar dynamics. For models of dendritic segments, several channels contribute to membrane dynamics including voltage-sensitive calcium channels, voltage-sensitive sodium channels, and voltage-sensitive potassium channels [42]. In dendritic spines, contributing currents come from AMPAR, SK channels, voltage-sensitive calcium channels, voltage-sensitive sodium channels, voltage-sensitive potassium channels, and NMDAR [31, 43]. Membrane

potential is given by

$$\frac{\partial V_m}{\partial t} = \frac{-1}{C_m}(\sum_x I_x), \tag{4.3}$$

where I_x is the current due to the respective channel x. Voltage dynamics are determined by the sum of all currents through the various channels. Voltage is defined as a partial differential equation because it is defined everywhere on the membrane, but it has no explicit diffusion term. Therefore, any change in voltage is due to ion movement that changes the currents, I_x, in the equation above.

The current equations are given in the form of

$$I_i = g_i m_i^n (V_m - E_i), \tag{4.4}$$

where i is the channel type, g is the channel conductance [pS], m is a gating parameter raised to the nth power, and E is the reverse potential of the channel. We explain these various components below.

Reverse potential formulation

The reverse potential, E, captures the difference in ion concentration across a membrane. When the membrane is in thermodynamic equilibrium (no net flux of ions), E for a specific ion is equal to the Nernst potential given by

$$E = \frac{RT}{zF} \ln \frac{Y_{EC}}{Y_{cyto}}, \tag{4.5}$$

where Y is the ion of interest, R is the universal gas constant, T is temperature in Kelvin, F is the Faraday constant, and z is the charge of the ion. For a postsynaptic neuron, the reverse potential for the neurotransmitter receptor's ion channel is the membrane

potential at which a given neurotransmitter causes no net current flow of ions. However, for the reverse potential when considering all ions that cross the membrane, the Goldman-Hodgkin-Katz equation is used [30]. The Goldman equation is used when there are active ion pumps and the cell is not in equilibrium, and is given by

$$E = \frac{RT}{F} \ln\left(\frac{\sum P^{+} Y^{+}_{EC} + \sum P^{-} Y^{-}_{EC}}{\sum P^{+} Y^{+}_{cyto} + \sum P^{-} Y^{-}_{cyto}}\right), \tag{4.6}$$

where P is permeability [m/s].

When considering voltage across an internal membrane such as the endoplasmic reticulum, we use the same formulation with $\frac{Y_{out}}{Y_{in}}$ now referring to $\frac{Y_{cyto}}{Y_{ER}}$. Therefore, the reverse potential for each channel current is defined at each location on the membrane and is dependent on the ion concentrations at that location.

Gating parameters formulation

The gating parameters are typically nonlinear functions of voltage, or calcium in the cause of SK channels. The two most common forms for the gating parameter equations are, for some gating parameter n,

$$\frac{dn}{dt} = \frac{n_\infty - n}{\tau_n} \tag{4.7}$$

or

$$\frac{dn}{dt} = \alpha(1 - n) - \beta n. \tag{4.8}$$

These two forms are related through

$$n_\infty = \frac{\alpha}{\alpha + \beta} \tag{4.9}$$

and

$$\tau_n = \frac{1}{\alpha + \beta}. \tag{4.10}$$

α and β are typically exponentials with voltage dependence [43], see Tables 4.1, 4.2, and 4.3 for their form and parameters. Channels will have specific gating variables with parameters tuned for that specific channel behavior.

4.2.3 Boundary Conditions

Each current terms in Eq. 4.3 corresponds to the total current through a channel or receptor. However the current, Eq. 4.4, can have contributions due to various ions. Therefore, membrane flux terms for each ion are defined as

$$J_y = \sum_x \eta\nu\mu I_x, \tag{4.11}$$

where η is some fraction that captures what percentage of the current through channel x is due to ion y, ν is a conversion factor between charge and ions, and μ is a conversion factor between ions and moles.

External stimulus of the system

Simplified models have an external current, I_{ext}, as the stimulus. For this spatial model, we consider this stimulus as a membrane source defined as

$$J_{ext} = \frac{I_{ext}}{C_m}, \tag{4.12}$$

which we apply over a specific membrane area. The magnitude of I_{ext} can vary and here we model the stimulus as a square wave lasting 10 ms.

4.2.4 Dendrite specific equations

The Hodgkin-Huxley and Morris-Lecar equations were designed for membrane voltage in axons, and here we first apply them to dendrites [43]. Therefore, voltage along the PM of the dendrite is given by

$$\frac{dV_m}{dt} = \frac{-1}{C_m}(I_{Ca} + I_{Na} + I_K + I_{Cl} - I_P), \tag{4.13}$$

where I_P is the current due to the sodium-potassium pump.

4.2.5 Dendritic spine specific equations

Dendritic spines have specialized receptors and channels compared to the dendrite. The exact composition and distribution of these channels and receptors are not well known. Considering some of these specialized channels and receptors, we write voltage along the PM of the dendritic spine as

$$\frac{dV_m}{dt} = \frac{-1}{C_m}(I_A + I_N + I_{SK} + I_L), \tag{4.14}$$

where I_A is the current due to AMPAR, I_N is the current due to NMDAR, I_{SK} is the current due to SK channels, and I_L is the current due to a leak term [44]. However, we can make additional changes to this equation to fully capture additional channels present in dendritic spines, such as those from voltage dependent calcium, sodium, and chloride channels. With these considerations, we get

$$\frac{dV_m}{dt} = \frac{-1}{C_m}(I_A + I_N + I_{SK} + I_{Ca} + I_{Na} + I_{Cl} - I_P). \tag{4.15}$$

For this model, instead of an artificial step function for the external current stim-

ulus, the stimulus is the activation of AMPAR and NMDAR due to glutamate binding. We implement the AMPAR and NMDAR currents only at the postsynaptic density (PSD) region at the top of the spine head.

4.3 Results

4.3.1 Simplified approach in dendrite segment shows effects of ultrastructure

We first implement a model for membrane voltage propagation in a dendrite with a combination of traditional Hodgkin-Huxley and Morris-Lecar channel dynamics. The spatial model generates a spike with characteristic dynamics seen in neurons, see Fig. 4.1. We model voltage in a cylindrical dendrite with a half micron radius and an oscillating ER structure acting as an excluded volume. We have an artificial external current as the input to the system, which we apply to the bottom half of the dendrite. An external current of 5 $\frac{\mu A}{cm^2}$ was applied over an area of 2.3562 μm^2. The membrane voltage propagates upward from the stimulated area, as seen in Fig. 4.2. The oscillating ER structure appears to alter the propagation of the membrane voltage depending on the distance between the ER and PM.

4.3.2 Simplified approach in toroid demonstrates halting of voltage propagation

Building on the results from the section of dendrite, a toroid with similar dimensions to the dendrite was constructed with the same governing voltage and ion equations as the dendrite model. We stimulate a quarter of this toroid with an external current, such that

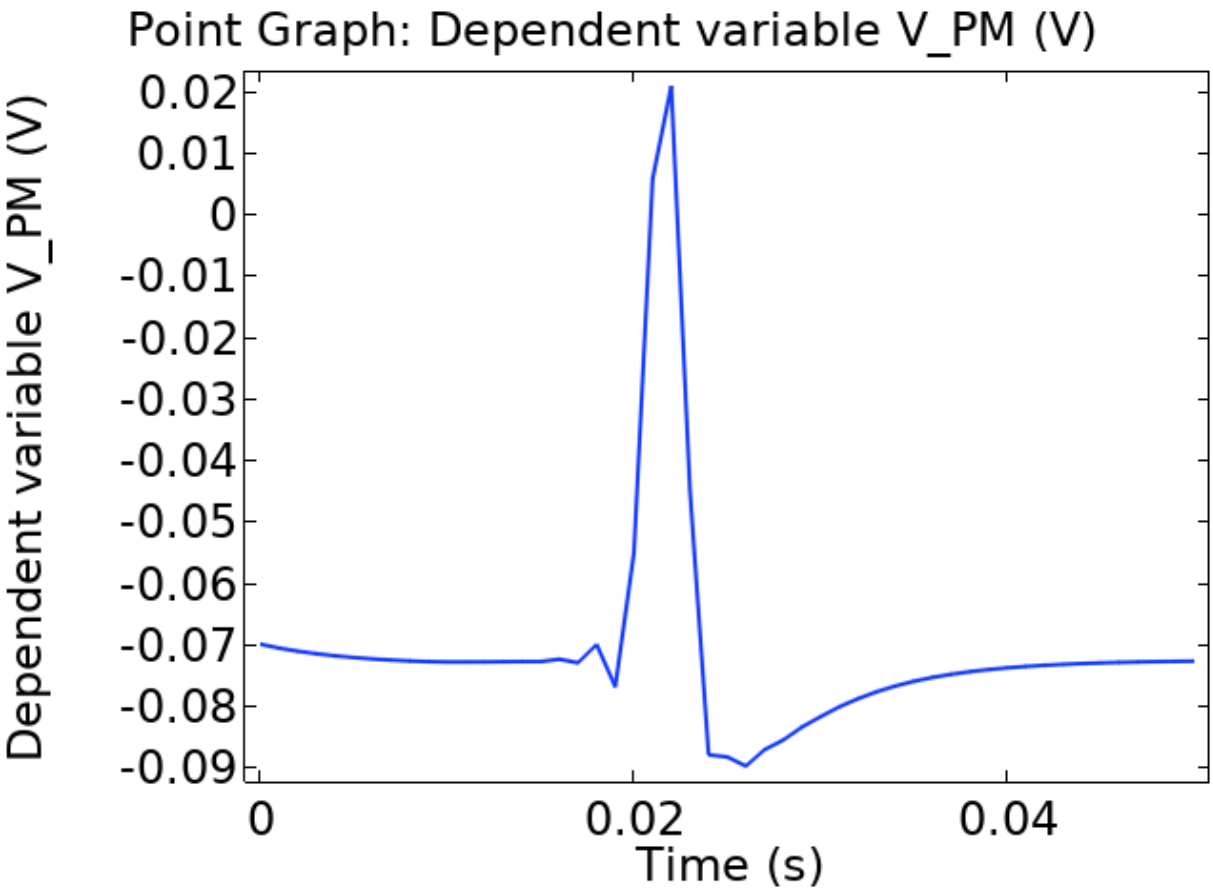

Figure 4.1: Temporal dynamics of membrane voltage propagation along the plasma membrane of a dendrite. The resting membrane voltage is ∼-70 mV while the maximum depolarization is ∼20 mV. The classic sections of an action potential in a neuron can be seen with depolarization, repolarization, hyperpolarization, and return to resting membrane voltage.

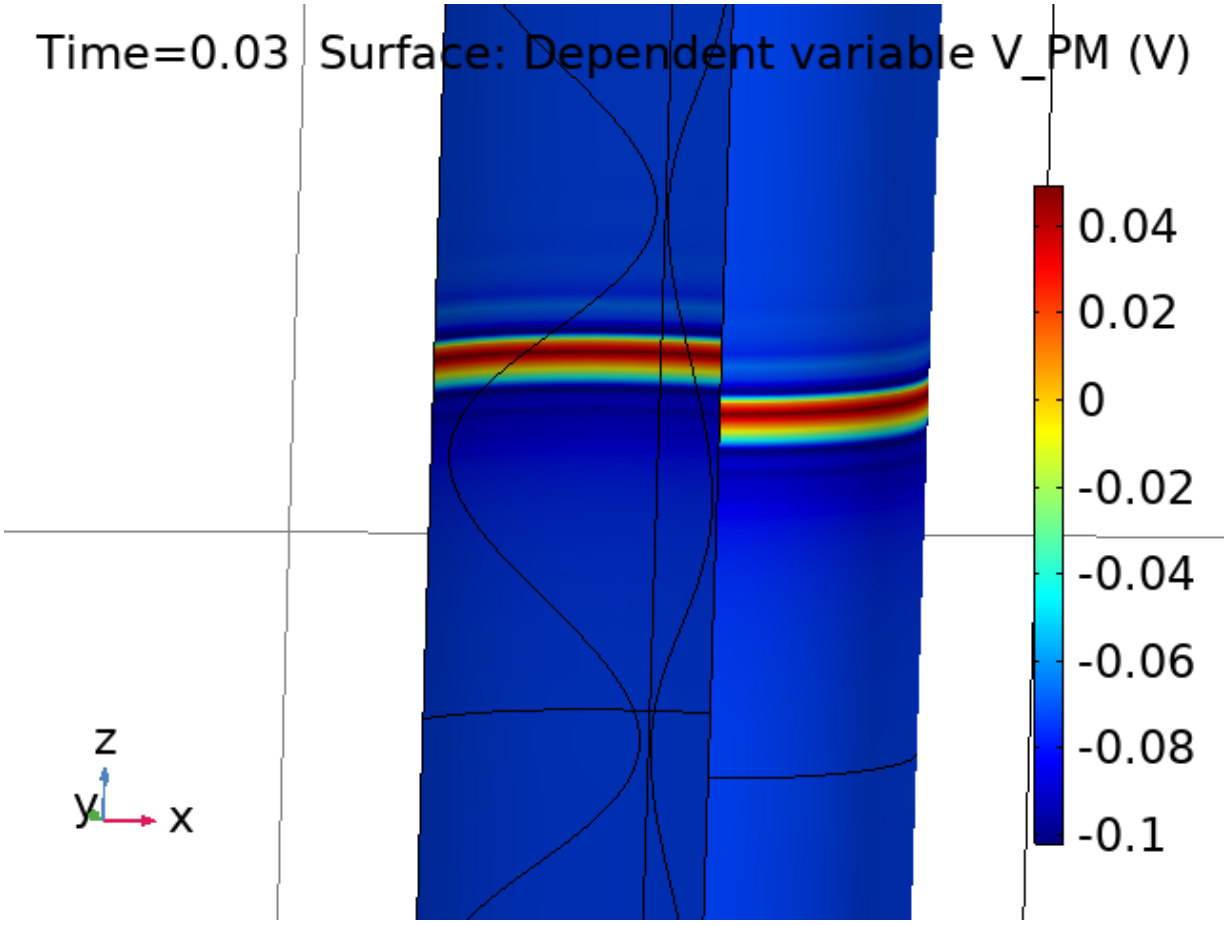

Figure 4.2: Spatial dynamics of membrane voltage propagation along the plasma membrane of a dendrite at 30 ms. The spike moves upwards from the stimulated lower half of the dendrite.

an area of 4.9342 µm^2 was stimulated with a current of 50 $\frac{\mu A}{cm^2}$. We see that due to the symmetry of the model, spiking propagates from both sides of the activated section, and interestingly, two spikes appear at both ends, separated by a certain length and time, see Fig. 4.3. Furthermore, as the spike propagates around the toroid, the difference between the perimeter on the inner and outer radius of the toroid becomes apparent as the spiking on the outer radius begins to lag behind the spiking at the inner membrane, see Fig. 4.4. Given enough time, in this case about 100 ms, the spikes meet at the other side of the toroid and annihilate each other.

4.3.3 Simplified approach in dendritic spines shows no spatial gradients

As a first step, we implement the same system as the dendrite and toroid model in a dendritic spine geometry taken from [3]. We localize the external stimulus to the post-synaptic density (PSD) region at the top of the spine head. We apply a stimulus of 41 $\frac{\mu A}{cm^2}$ over the PSD area of 0.076 µm^2. We see a similar temporal profile as the dendrite and toroid trials but with a more gradual depolarization section, see Fig. 4.5. However, the dendritic spine shows no spatial gradient for membrane voltage.

4.3.4 Specialized model in dendritic spines highlights numerical complexity of model

We then implement the full specialized system of equations in the dendritic spine geometry. We localize AMPAR and NMDAR currents and fluxes to the postsynaptic density (PSD) region at the top of the spine head. Using this set of equations, we found that our system is not properly tuned to generate realistic spiking dynamics. For instance, activation of the PSD region lead to numerous spikes with a larger membrane voltage range

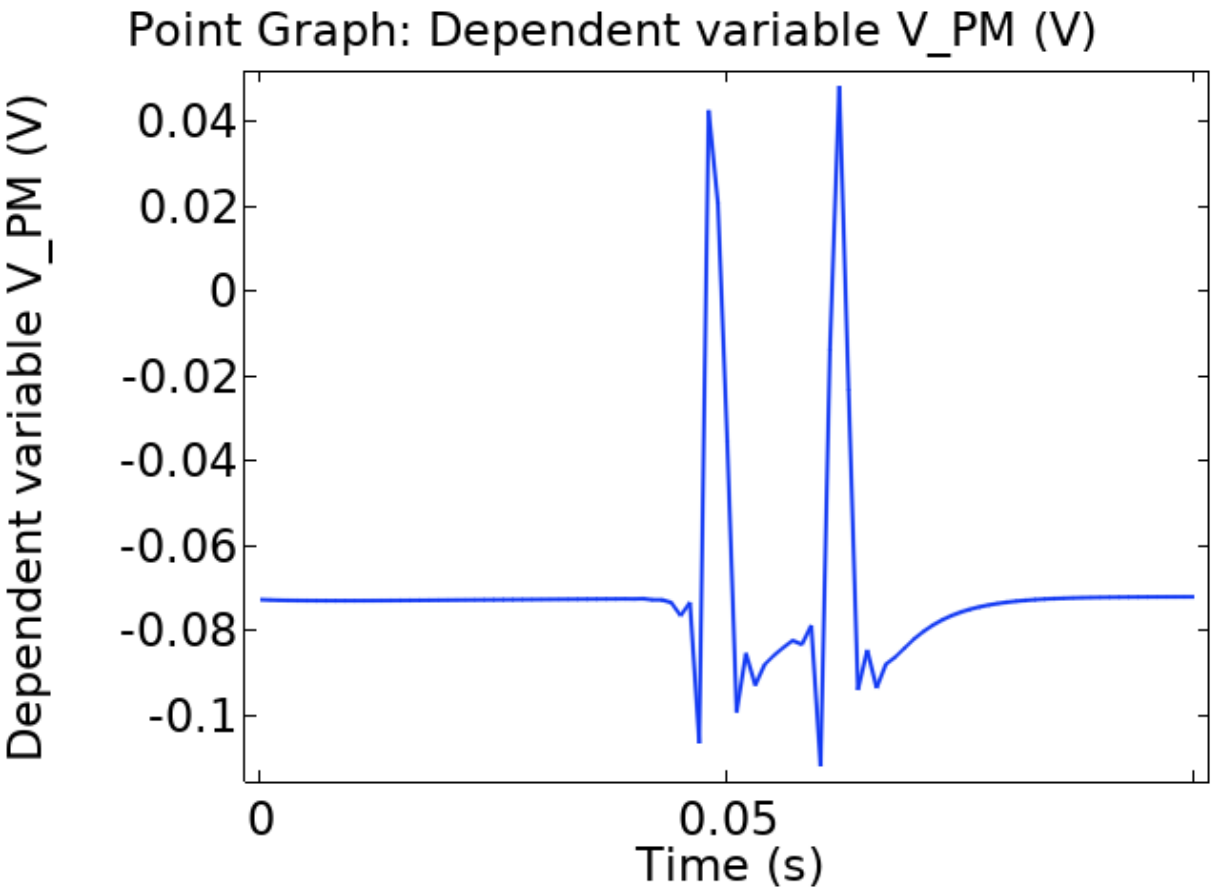

Figure 4.3: Temporal dynamics of membrane voltage propagation along the plasma membrane of a toroid. The resting membrane voltage is about -70 mV while the maximum depolarization is about 40 mV. There are two spikes emitting from both sides of the stimulated area and are separated by about 10 ms.

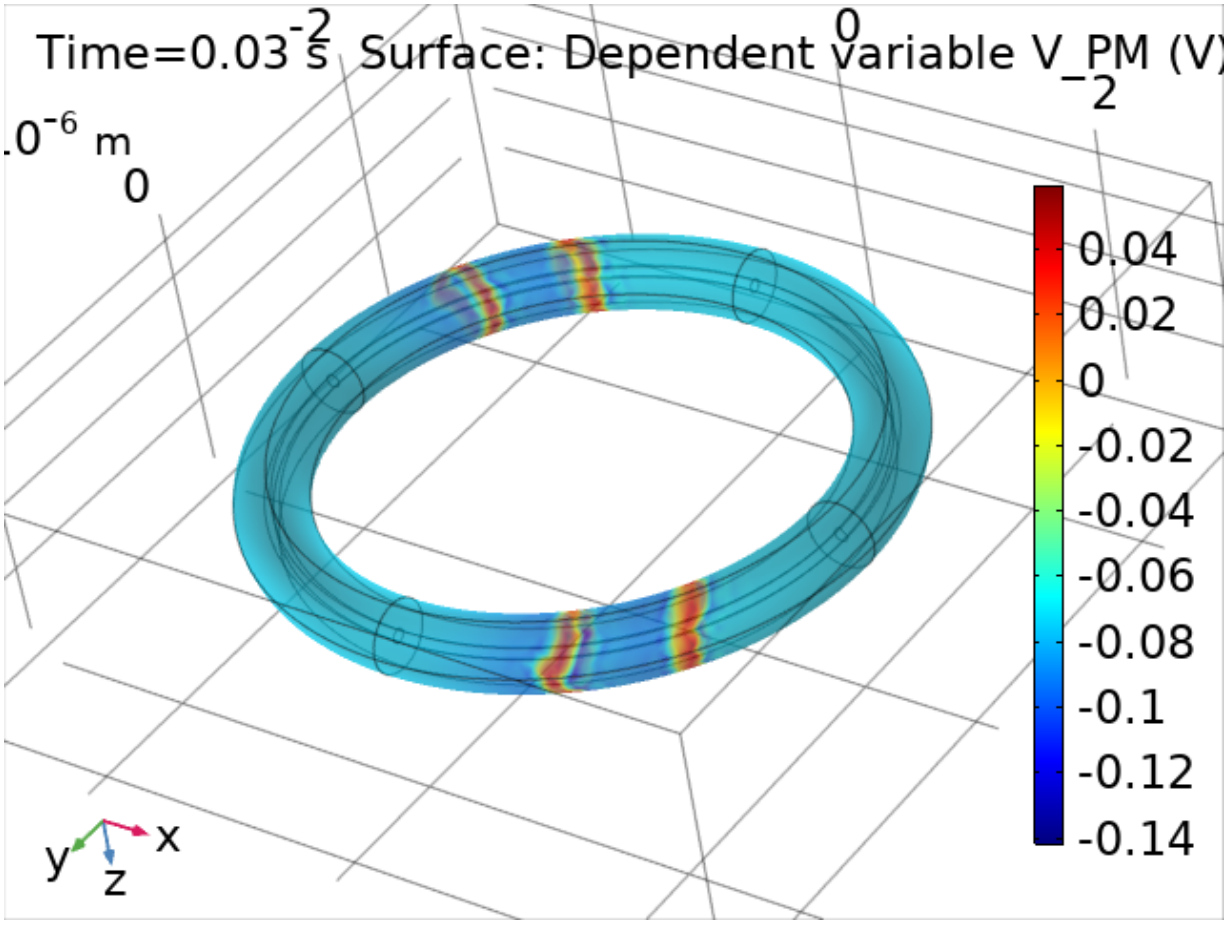

Figure 4.4: Spatial dynamics of membrane voltage propagation along the plasma membrane of a toroid. Two spikes initiate from both sides of the activated region and follow each other around the toroid.

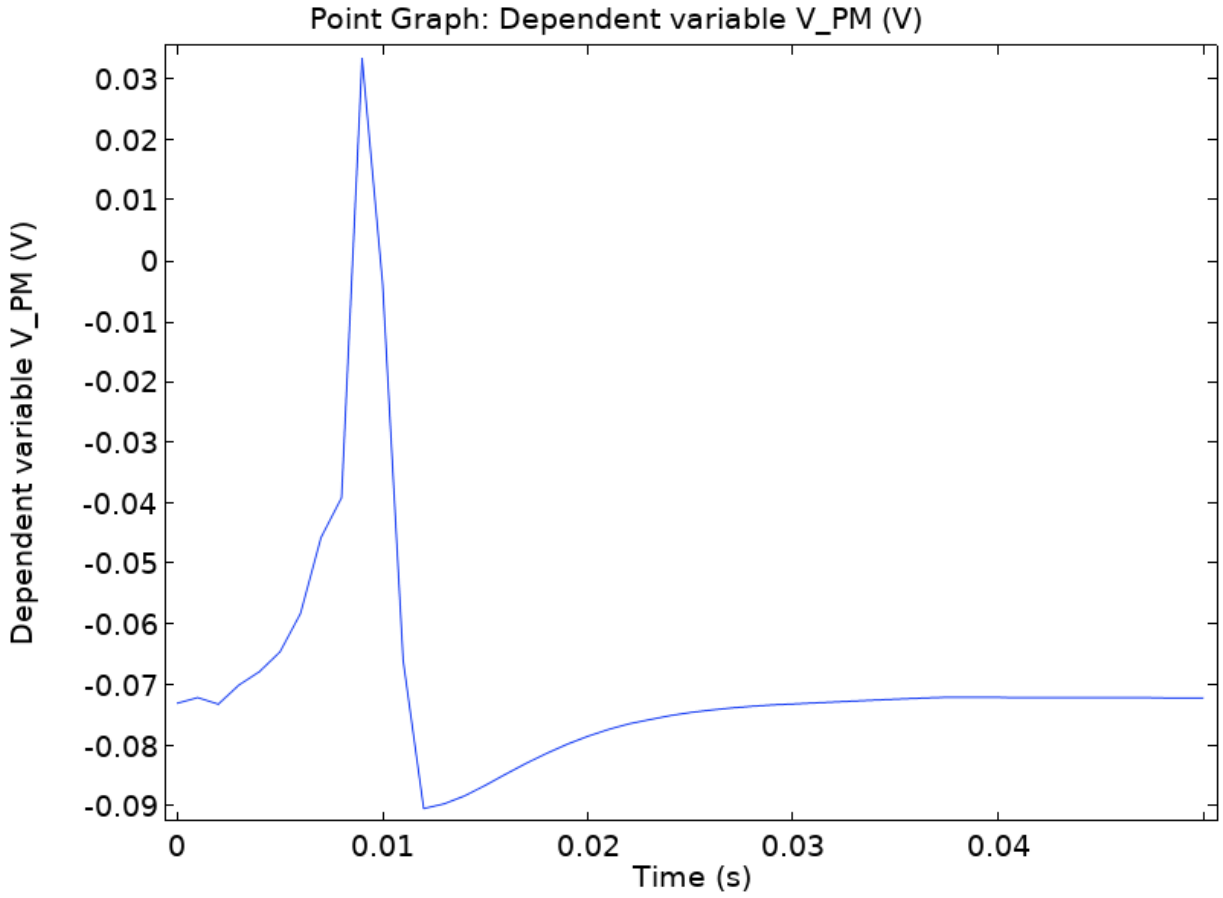

Figure 4.5: Temporal dynamics of membrane voltage in a dendritic spine with the simplified model. The dendritic spine shows similar temporal dynamics to the dendrite segment, but without any spatial gradient.

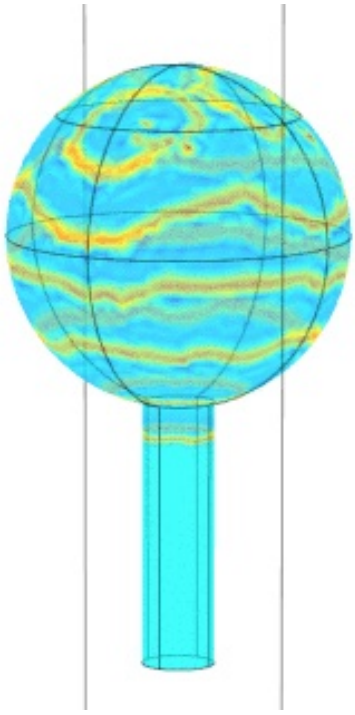

Figure 4.6: Membrane voltage in a dendritic spine with the more complex spiking model. Despite the spherical spine head being symmetric with respect to its PSD, voltage propagated non-symmetrically and feedback in the system lead to spiral formations.

than experimentally observed. Therefore, further tuning and parameter adjustments must be made to specialize the voltage model to the dendritic spine. Additionally, due to the coupled nature of the system, small numerical errors have severe consequences on the results and mesh quality can impact the results, as seen in Fig. 4.6 where mesh quality lead to voltage spirals.

4.4 Discussion

Based on these results, we can make several conclusions regarding membrane voltage propagation and membrane morphology. In particular, we expect that the area and magnitude of stimulation plays an important role in spiking frequency and amplitude. The

presence of two pairs of spikes in the toroid was most likely due to the large area of stimulation, while the multiple spikes in the dendritic spine was mostly likely due to extended activation time or magnitude. We predict that the subsequent annihilation of the spikes when they collided in the toroid was due to the deactivation of channels preventing further spiking behavior. We also predict that the time period of stimulation plays an important role as extended stimulation could cause deactivation of certain channels.

Ultrastructure also plays a role in membrane voltage propagation, with the ER structure altering the voltage dynamics in the dendrite section. Therefore, we predict that PM-ER contact sites could play important roles in modulating membrane voltage propagation. An outstanding question that remains is the potential role of membrane voltage propagation in the ER. It has recently been shown that the ER has a change in its membrane potential associated with the change in PM membrane voltage [45]. Therefore, it is possible that the ER, or spine apparatus, has a role in propagating electrical signals within neurons or influencing the electrical activity on the PM. Our collaborators explored this question and found that the ER might actually suppress its voltage propagation in neurons (Evan P. Campbell, Ahmed A. Abushawish, Miriam K. Bell, Melita Haryono, Padmini Rangamani, and Brenda L. Bloodgood. "Electrical signals in neuronal ER: large, linear, and spatially restricted." (in review)).

The dendritic spine shows no spatial gradient in membrane voltage when using the same equations as the dendrite model, which might be due to the short lengthscale and small volume of the dendritic spine. The cytoplasm of the dendritic spine is a crowded, actin-dense environment, potentially creating a slower effective diffusion coefficient for the cytosolic ions which might make a voltage gradient possible [46].

It should be noted that various parameters in this simplified model are actually variables with calcium-dependent properties; in particular, various channel permeabilities

are calcium-sensitive. Therefore, it is vital to consider the role of calcium influx on variable channel permeabilities. There are many additional factors to consider including the spatial distribution of ion channels and receptors, particularly in the dendritic spine; the identities and properties of channels and receptors; and the presence of a spine apparatus [3, 47].

Additionally, while not shown here, we also considered voltage propagation in tapered dendrites and between mother and daughter dendrites. Directionality of voltage propagation in dendrites has been shown to matter for voltage speed and propagation distance [33, 48], but the reasons for the asymmetry of propagation dynamics are not fully understood. We found that using our model, our voltage propagation speeds were consistently several orders of magnitude smaller than what has been experimentally recorded. There are several potential reasons for this: 1. The wave speed might be parameter dependent as was found for another pseudo-wave, a curvature wave due to bar protein recruitment [49, 50]; or 2. We are lacking a component of the model. In particular, it might be necessary to consider contributions due to electrodiffusion in this system due to the high concentrations of charged ions in small spaces [51, 52].

While we present a simplified signaling model, this work is a critical first step in coupling signaling, electrical activity, and morphology in dendrites and dendritic spines. Coupling reaction-diffusion dynamics and membrane flux boundary conditions with Hodgkin-Huxley and Morris-Lecar style voltage dynamics can generate realistic membrane potential spikes in both dendrites and dendritic spines. Much work remains to generate more specialized models that take into account biophysical and biochemical considerations such as specialized receptors and channels within dendritic spines, membrane flux distribution, and ultrastructure, and additional phenomena such as electrodiffusion.

Table 4.1: **Equations in model for all PM voltage.**

Equation	Expression	Meaning	Reference
I_{Na^+}	$(gNa_L + gNa * m^3 * h)(V_{PM} - ENa)$	Na^+ channel current	[43]
I_{K^+}	$(gK_L + gK * n^4)(V_{PM} - EK)$	K^+ channel current	[43]
I_{Cl^-}	$(gCl_L)(V_{PM} - ECl)$	Cl^- channel current	[43]
$I_{Ca^{2+}}$	$(gCa)r^2s(V_{PM} - ECa)$	Ca^{2+} channel current	[42]
r_m	$a_m(1-m) - b_m m$	$\frac{1}{s}$	[43]
a_m	$\frac{am1(V_{PM}+amV1)}{1-exp(\frac{-(V_{PM}+amV2)}{amV3})}$	$\frac{1}{s}$	[43]
b_m	$bm1 * exp(\frac{-(V_{PM}-bmV1)}{bmV2})$	$\frac{1}{s}$	[43]
r_h	$a_h(1-h) - b_h h$	$\frac{1}{s}$	[43]
a_h	$ah1 * exp(\frac{-(V_{PM}+ahV1)}{ahV2})$	$\frac{1}{s}$	[43]
b_h	$\frac{bh1}{1+exp(bhV1(V_{PM}-bhV2))}$	$\frac{1}{s}$	[43]
r_n	$a_n(1-n) - b_n n$	$\frac{1}{s}$	[43]
a_n	$\frac{an1(V_{PM}+anV1)}{1-exp(\frac{-(V_{PM}+anV2)}{anV3})}$	$\frac{1}{s}$	[43]
b_n	$bn1 * exp(\frac{-(V_{PM}+bnV1)}{bnV2})$	$\frac{1}{s}$	[43]
r_r	$\frac{dr}{dt} = \frac{r_\infty - r}{\tau_r}$	$\frac{1}{s}$	[42]
r_∞	$\frac{1}{1+exp(\frac{-(V_{PM}+rinfV1)}{rinfV2})}$	$\frac{1}{s}$	[42]
τ_r	$\frac{tr1+\frac{1}{exp(\frac{V_{PM}-trV1}{trV2})+exp(\frac{-(V_{PM}+trV3)}{trV4})}}{tr2}$	$\frac{1}{s}$	[42]
r˙s	$\frac{ds}{dt} = \frac{s_\infty - s}{\tau_s}$	$\frac{1}{s}$	[42]
s_∞	$\frac{1}{1+exp(\frac{-(V_{PM}+sinfV1)}{sinfV2})}$	$\frac{1}{s}$	[42]
τ_s	$\frac{ts1+\frac{1}{exp(\frac{V_{PM}+tsV1}{tsV2})+exp(\frac{-(V_{PM}+tsV3)}{tsV4})}}{ts2}$	$\frac{1}{s}$	[42]
Ip	$\rho(1+exp(\frac{A_{Na^+}-Na_{cyto}}{B_{Na^+}}))^{-1}(1+exp(\frac{A_{K^+}-K_{EC}}{B_{K^+}}))^{-1}$		

4.5 Acknowledgements

For Chapter 4, I wish to acknowledge Professor Brenda Bloodgood, Professor Padmini Rangamani, Evan Campbell, Jacqueline Griswold, Cuncheng Zhu, and Christopher Lee for valuable discussion.

Table 4.2: **Subset of parameters in model for all PM voltage.**

Parameter	Value	Units	Reference
C_m	1	$\frac{\mu F}{cm^2}$	[43]
gNa_L	0.0175	$\frac{mS}{cm^2}$	[43]
gNa	100	$\frac{mS}{cm^2}$	[43]
gK˙L	0.15	$\frac{mS}{cm^2}$	-
gK	40	$\frac{mS}{cm^2}$	[43]
gCl_L	0.05	$\frac{mS}{cm^2}$	[43]
gCa	1.1	$\frac{mS}{cm^2}$	-
am1	0.1	$\frac{1}{msmV}$	[43]
amV1	30	mV	[43]
amV2	30	mV	[43]
amV3	10	mV	[43]
bm1	4	$\frac{1}{ms}$	[43]
bmV1	55	mV	[43]
bmV2	18	mV	[43]
ah1	0.07	$\frac{1}{ms}$	[43]
ahV1	44	mV	[43]
ahV2	20	mV	[43]
bh1	1	$\frac{1}{ms}$	[43]
bhV1	-0.1	$\frac{1}{mV}$	[43]
bhV2	24	mV	[43]
an1	0.01	$\frac{1}{msmV}$	[43]
anV1	34	mV	[43]
anV2	34	mV	[43]
anV3	10	mV	[43]
bn1	0.125	$\frac{1}{ms}$	[43]
bnV1	44	mV	[43]
bnV2	80	mV	[43]

Table 4.3: **Rest of parameters in model for all PM voltage.**

Parameter	Value	Units	Reference
rinfV1	20	mV	[42]
rinfV2	7.4	mV	[42]
tr1	3	1	[42]
tr2	3	1	[42]
trV1	5	mV	[42]
trV2	10	mV	[42]
trV3	70	mV	[42]
trV4	15	mV	[42]
sinfV1	48	mV	[42]
sinfV2	5	mV	[42]
ts1	350	1	[42]
ts2	3	1	[42]
tsV1	16	mV	[42]
tsV2	4	mV	[42]
tsV3	375	mV	[42]
tsV4	50	mV	[42]
ρ	5.25	$\frac{\mu A}{cm^2}$	[43]
A_{Na^+}	25	mM	[43]
B_{Na^+}	3	mM	[43]
A_{K^+}	5.5	mM	[43]
B_{K^+}	1	mM	[43]

Chapter 5

Dendritic spine geometry and spine apparatus organization govern the spatiotemporal dynamics of calcium

Published Online: 19 July, 2019 | Supp Info: http://doi.org/10.1085/jgp.201812261

JGP Journal of General Physiology

RESEARCH ARTICLE

Dendritic spine geometry and spine apparatus organization govern the spatiotemporal dynamics of calcium

Miriam Bell[1], Tom Bartol[2], Terrence Sejnowski[2,3], and Padmini Rangamani[1]

Dendritic spines are small subcompartments that protrude from the dendrites of neurons and are important for signaling activity and synaptic communication. These subcompartments have been characterized to have different shapes. While it is known that these shapes are associated with spine function, the specific nature of these shape–function relationships is not well understood. In this work, we systematically investigated the relationship between the shape and size of both the spine head and spine apparatus, a specialized endoplasmic reticulum compartment within the spine head, in modulating rapid calcium dynamics using mathematical modeling. We developed a spatial multicompartment reaction–diffusion model of calcium dynamics in three dimensions with various flux sources, including N-methyl-D-aspartate receptors (NMDARs), voltage-sensitive calcium channels (VSCCs), and different ion pumps on the plasma membrane. Using this model, we make several important predictions. First, the volume to surface area ratio of the spine regulates calcium dynamics. Second, membrane fluxes impact calcium dynamics temporally and spatially in a nonlinear fashion. Finally, the spine apparatus can act as a physical buffer for calcium by acting as a sink and rescaling the calcium concentration. These predictions set the stage for future experimental investigations of calcium dynamics in dendritic spines.

Introduction

Dendritic spines, small protein- and actin-rich protrusions located on dendrites of neurons, have emerged as a critical hub for learning, memory, and synaptic plasticity in both short-term and long-term synaptic events (Bourne and Harris, 2008; Rangamani et al., 2016). These subcompartments provide valuable surface area for cell–cell interaction at synapses, and compartmentalization of signaling proteins to control and process incoming signals from the presynaptic terminal (Nishiyama and Yasuda, 2015; Yasuda, 2017). Thus, dendritic spines are hotbeds of electrical and chemical activity. Since calcium is the first incoming signal into the postsynaptic terminal, calcium temporal dynamics have been extensively studied experimentally and more recently computationally (Denk et al., 1996; Augustine et al., 2003; Bloodgood and Sabatini, 2005; Bartol et al., 2015b; Yasuda, 2017). In particular, calcium acts as a vital second messenger, triggering various signaling cascades that can lead to long-term potentiation, long-term depression, actin cytoskeleton rearrangements, and volume expansion, among other events (Holmes, 1990; Bourne and Harris, 2008; Rangamani et al., 2016).

Dendritic spine activity has numerous timescales, with signaling pathways operating on the millisecond to the hour timescale following spine activation (Yuste et al., 2000; Segal, 2005; Rangamani et al., 2016). Calcium dynamics are on the millisecond timescale, since calcium is the second messenger that floods the spine following the release of neurotransmitter from the presynaptic terminal. The temporal dynamics of calcium have provided valuable insight into the signaling dynamics in dendritic spines, and it is quite clear that calcium dynamics are influenced by a large number of factors. Multiple studies have connected the electrical activity of the plasma membrane (PM) voltage to calcium dynamics of N-methyl-D-aspartate receptors (NMDARs; Jahr and Stevens, 1993; Shouval et al., 2002; Rackham et al., 2010). The electrophysiology of dendritic spines influences many signaling dynamics through voltage-sensitive (or voltage-dependent) ion channels (Jaffe et al., 1994), and thus, models of these dynamics can be linked to downstream signaling.

Calcium is critical for almost all the reactions in the brain (Augustine et al., 2003) and is believed to accomplish a vast

[1]Department of Mechanical and Aerospace Engineering, University of California, San Diego, La Jolla, CA; [2]Howard Hughes Medical Institute, Salk Institute for Biological Studies, La Jolla, CA; [3]Division of Biological Sciences, University of California, San Diego, San Diego, CA.

Correspondence to Padmini Rangamani: padmini.rangamani@eng.ucsd.edu.

variety of functions through localization (Clapham, 1995, 2007; Yuste and Denk, 1995). One possible way to achieve localization is by restricting the distance between the calcium source (often a channel) and the sink (calcium sensors and buffers). Thus, the localization of calcium can result from the location and mobility of different buffers and sensors (Schmidt, 2012). Spatial models of calcium dynamics in dendritic spines that consider such effects have been proposed previously (Holcman et al., 2004; Means et al., 2006; Bartol et al., 2015b). Spatial-temporal models of calcium dynamics have highlighted the role of calcium-induced cytosolic flow and calcium influx regulation by Ca^{2+}-activated K^+ channels (SK channels; Holcman et al., 2004; Rackham et al., 2010). Computational studies using stochastic models of calcium transients have revealed that the readout of fluorescent probes can alter experimental readouts (Yuste et al., 2000; Higley and Sabatini, 2012; Bartol et al., 2015b). In particular, fluorescent probes can sequester calcium, effectively acting as calcium buffers and lowering the perceived calcium concentrations. Therefore, computational studies have already provided some insight into the spatiotemporal dynamics of calcium in both dendritic spines (Yuste et al., 2000; Segal, 2005; Rangamani et al., 2016) and whole neurons (Loewenstein and Sompolinsky, 2003). In this study, we specifically focus on the effect of spine geometry on calcium signals in the postsynaptic spine.

Recent advances in imaging and reconstruction techniques have shed light into the complex surface area of a single spine and the ultrastructure of the spine apparatus (SpApp; Kuwajima et al., 2013; Bartol et al., 2015a,b; Wu et al., 2017). Experimental evidence shows that calcium signals remain predominantly localized to single spines (Holmes, 1990; Koch and Zador, 1993; Sabatini et al., 2002). Dendritic spines have a unique set of shapes and recently the size and shape distribution of spines has been linked to their physiological function (Hering and Sheng, 2001; Berry and Nedivi, 2017). Additionally, only ∼14% of spines have a specialized ER known as the SpApp (Basnayake et al., 2018 *Preprint*; Jedlicka et al., 2008), which serves as a calcium store (Wuytack et al., 2002; Jedlicka et al., 2008). Indeed, calcium dynamics in dendritic spines are quite complex.

Given the importance of calcium dynamics in dendritic spines and the complexity of spine ultrastructure (Spacek and Harris, 1997; Holbro et al., 2009; Wu et al., 2017), we sought to use a computational approach to probe the role of spine geometry in modulating the spatiotemporal dynamics of calcium. Specifically, we seek to address the following questions: (i) How does the size and shape of both the spine head and SpApp affect calcium dynamics? (ii) How does the distribution of channels along the synaptic membrane modulate calcium dynamics within the spine? (iii) How do calcium buffers and calcium diffusion rates affect the spatiotemporal dynamics of calcium? To answer these questions, we develop a spatial 3-D reaction-diffusion model with multiple compartments. We chose a computational approach because it is not yet possible to manipulate spine size, shape, or SpApp location with precise control experimentally. However, the insights obtained from computational approaches can lay the groundwork for generating experimentally testable predictions (Kotaleski and Blackwell, 2010).

Materials and methods

Model assumptions

To interrogate the spatiotemporal dynamics of calcium in dendritic spines, we developed a reaction-diffusion model that accounts for the fluxes through the different sources and sinks shown in Fig. 1. We briefly discuss the assumptions made in developing this model and outline the key equations below. See Table 1 for common notation.

Time scale

We model a single dendritic spine of a rat hippocampal area CA1 pyramidal neuron as an isolated system, because we focus on the 10- to 100-ms timescale and the ability of the spine neck to act as a diffusion barrier for calcium (Yuste and Denk, 1995; Bloodgood and Sabatini, 2005; Byrne et al., 2011; Gallimore et al., 2016). As a result, we do not consider calcium dynamics due to the mitochondria. This assumption is valid in our model, because even though mitochondria are known to act as calcium stores, their dynamics are on a longer timescale (10–100 s; Wacquier et al., 2016) and mitochondria are located in the dendrite outside of the dendritic spine. Although, it is well known that the SpApp acts as a source for calcium, Ca^{2+} release from the SpApp occurs at longer timescales because of IP_3 receptors, RYR, and CICR (Jedlicka et al., 2008). It should also be noted that not all neurons have RYR and IP_3R on the SpApp (Mattson et al., 2000). Therefore, for the purpose and timescale of this study, we do not focus on CICR and therefore do not include RYR or IP_3R dynamics in this study.

Membrane voltage stimulus

We model membrane voltage as an algebraic equation based on the summation of an excitatory postsynaptic potential (EPSP) and a back-propagating action potential (BPAP) applied to the entire PM (Jahr and Stevens, 1993; Shouval et al., 2002; Griffith et al., 2016). The EPSP arrives 2 ms before the BPAP to stimulate the maximum possible membrane depolarization (Fig. 1 d; Hu et al., 2018). This stimulus triggers the influx of calcium into the spine head.

Spine head

The average spine head volume is ∼0.03 μm^3 (Spacek and Harris, 1997; Bartol et al., 2015b), but a large variation has been observed physiologically. The commonly observed shapes of dendritic spines include filopodia-like, stubby, short, and mushroom-shaped spines (Bourne and Harris, 2008; Berry and Nedivi, 2017). In this work, we consider two idealized geometries: a spherical spine head to represent a younger spine and an ellipsoidal spine head to represent a more mature mushroom spine (Spacek and Harris, 1997). The postsynaptic density (PSD) is modeled as a section of the membrane at the top of the spine head (Fig. 1 c). In simulations where the spine size is varied, we assume that the PSD changes surface area approximately proportionally to the spine head volume (Arellano et al., 2007).

SpApp

SpApps are found primarily in larger mushroom spines (Spacek and Harris, 1997), which hints at their role in potential

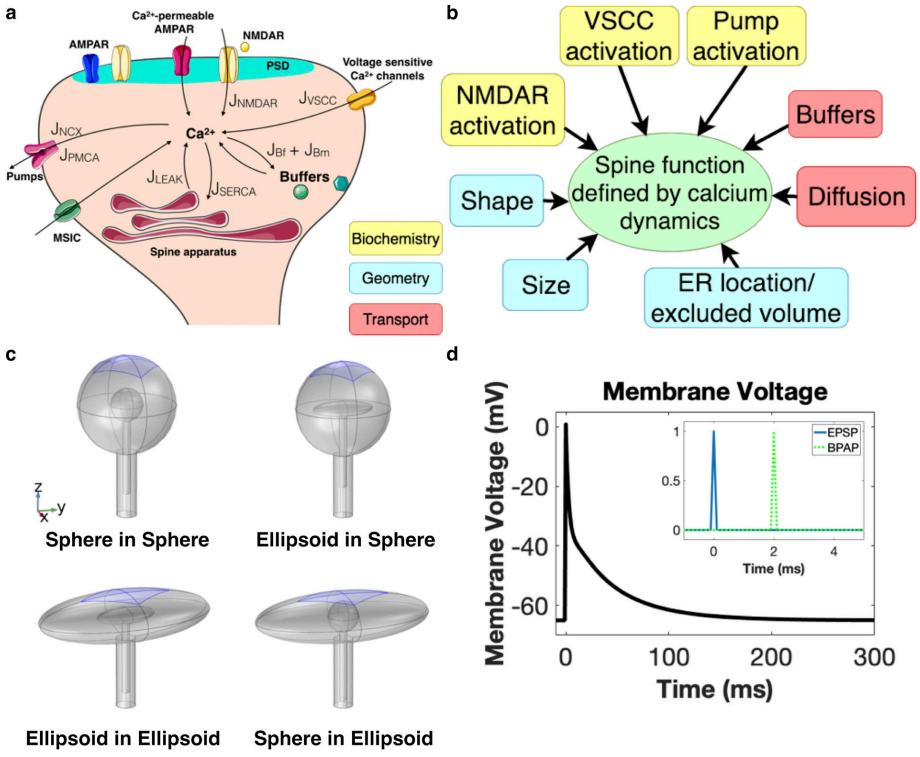

Figure 1. **Physical and chemical determinants of calcium influx in dendritic spines. (a)** Spatiotemporal dynamics of calcium in dendritic spines depend on multiple sources and sinks on both the spine membrane and the SpApp membrane. Fluxes are denoted as J_x, where x is the source or sink. These include receptors (NMDARs), channels (VSCCs), and pumps (PMCA and NCX). Calcium buffers are present both in the cytoplasm and on the PM. α-amino-3-hydroxy-5-methyl-4-isoxazolepropionic acid receptor (AMPAR) is another important receptor that is often used as a readout for long term potentiation and depression. We do not include its dynamics in this model. **(b)** A partial list of factors that can influence these dynamics include biochemical components (shown in panel a), geometry, and protein transport components, which are effectively coupled through transport phenomena. In this study, we focus on the effects of spine and SpApp size, spine and SpApp shape, flux through NMDAR and VSCC distribution on calcium spatiotemporal dynamics, and buffers. **(c)** Four different combinations of spine head and SpApp geometries are used as model geometries (spherical head with spherical apparatus, spherical head with ellipsoidal apparatus, ellipsoidal head with ellipsoidal apparatus, and ellipsoidal head with spherical apparatus) to study how spine geometry affects calcium dynamics. The coordinate axes correspond to 100 nm in the different geometries. The blue shaded regions denote the PSD for each geometry. **(d)** In our model, depolarization of the membrane is triggered by an EPSP followed closely by a BPAP to create a maximal depolarization according to STDP. This membrane voltage acts as the input to our model. Inset: Timing of the EPSP and the BPAP. We model the maximum possible membrane depolarization based on STDP with the EPSP arriving 2 ms before the BPAP.

regulation of sustained spine volume (Ostroff et al., 2017). We assume that the SpApp acts as a calcium sink within the timescale of interest (Segal et al., 2010). Another assumption is that the SpApp has the same shape as the spine head, a simplification of the more complicated and intricate SpApp geometry (Spacek and Harris, 1997).

PM fluxes

To maintain our focus on the short-timescale events associated with calcium dynamics, we include the following PM sources and sinks of calcium: voltage-sensitive calcium channels (VSCC), NMDARs, PM Ca^{2+}-ATPase (PMCA) pumps, and sodium–calcium exchanger (NCX) pumps. NMDARs are localized on the postsynaptic membrane adjacent to the PSD, designated at the top of the spine head. VSCC, PMCA, and NCX pumps are uniformly distributed along the PM, including at the base of the spine neck. Therefore, we model the dendritic spine as an isolated system with the spine neck base modeled in the same manner as the rest of the PM rather than explicitly modeling the base with an outward flux into the dendrite (see the following assumption).

Boundary condition at the base of the neck

We model the spine as an isolated system (Yuste and Denk, 1995; Sabatini et al., 2002; Bloodgood and Sabatini, 2005; Lee et al.,

Table 1. **Notation used in this study**

Variable/ parameter	Units	Definition/meaning
Ca^{2+}_{cyto}	μM	Calcium in the cytoplasm
Ca^{2+}_{ER}	μM	Calcium in the ER (SpApp)
D	$\frac{\mu m^2}{s}$	Diffusion rate
B_m	μM	Mobile buffers
B_f	Mol/ (μm^2 s)	Fixed buffers
PDE		Partial differential equation
ODE		Ordinary differential equation
J_x	Mol/ (μm^2 s)	Boundary flux due to x
CBP	μM	Calcium-binding proteins (calcium buffers)
^{V}cyto	μm^3	Volume of the cytoplasm excluding the SpApp volume
PM		Plasma membrane
SpApp		Spine apparatus
ECS		Extracellular space
n	μm	Scale factor to convert between volume reactions to boundary flux
^{n}PM	μm	Volume-to-surface area ratio of the cytoplasm to the PM
^{n}SpApp	μm	Volume-to-surface area ratio of the SpApp volume to the SpApp surface area
AUC	Ions/s	Area under the curve
EPSP	mV	Excitatory postsynaptic potential
BPAP	mV	Back-propagating action potential
NMDAR		N-methyl-D-aspartate receptor
VSCC		Voltage-sensitive calcium channel
PMCA		Plasma membrane calcium ATPase
NCX		Sodium–calcium exchanger

2009). Therefore, for most of our analyses, we use the same boundary conditions at the base of the spine neck as the rest of the PM. In the online supplemental material, we relax this assumption and test different boundary conditions, including a clamped calcium concentration at the base of the neck and an explicit effect of a dendritic shaft attached to the spine neck (Figs. S4 and S5).

Compartmental specific calcium ion concentration

We explicitly model calcium in the cytoplasm and in the SpApp. We assume that the calcium concentration in the extracellular space (ECS) is large enough (2 mM; Clapham, 1995; Bartol et al., 2015b) that the calcium influx into the spine has an insignificant effect on ECS calcium concentration. Therefore, ECS calcium concentration is assumed constant. We only solve the volumetric reactions in the cytoplasm. The ER calcium concentration is assumed to only affect the fluxes on the ER membrane.

Calcium-binding proteins (CBPs; buffers)

There are numerous CBPs present in the cytoplasm that act rapidly on any free calcium in the spine head (Yuste and Denk, 1995; Yuste et al., 2000; Sabatini et al., 2001, 2002; Bartol et al., 2015b). These CBPs are modeled as both mobile and fixed buffers in our system. Mobile buffers are modeled as volume components in the cytoplasm (Schmidt and Eilers, 2009; Schmidt, 2012), and they are modeled as a diffusive species with mass-action kinetics in the cytoplasm. We assume that the mobile buffers have a buffering capacity, κ, of 20, where $\kappa = [B_m]/K_d$ (Sabatini et al., 2002; Matthews and Dietrich, 2015; B_m is the mobile buffer concentration; K_d is the dissociation constant). Dendritic spines also have fixed or immobile buffers, but the molecular identity of fixed buffers remains more elusive. Studies suggest that they are primarily membrane-bound components (Matthews and Dietrich, 2015); therefore, we model fixed buffers as immobile species localized to the PM. As a result, the interactions of calcium with these fixed buffers are treated as flux boundary conditions for the surface reactions with mass-action kinetics. We assume fixed buffers have a K_d = 2 μM (Bartol et al., 2015b) and have a concentration of 78.7 μM (Bartol et al., 2015b). These values are converted to a membrane density by multiplying by the spine volume over PM surface area (n_{PMr}; see online supplemental material section S1.1 for more details.).

SpApp fluxes

In this model, the SpApp acts as a Ca^{2+} sink in the 10- to 100-ms timescale (Fifková et al., 1983; Fifková, 1985; Jedlicka et al., 2008). The implications of this assumption are discussed later in the paper. We assume that SERCA pumps are located uniformly on the SpApp membrane. SERCA pumps have been observed to buffer a large percentage of calcium within the spine, so we include SERCA pumps with a relatively large influx (Higley and Sabatini, 2012; Hu et al., 2018). We also include a small leak current from the SpApp to the cytoplasm and set this leak current to offset pump dynamics at basal calcium concentrations of 100 nM (Bartol et al., 2015b; Futagi and Kitano, 2015).

Based on these assumptions, we constructed a 3-D spatial model of Ca^{2+} dynamics in dendritic spines. Our control geometry is a medium-sized spine with volume of ∼0.06 μm^3 including the spine head and neck, with a SpApp of volume ∼0.003 μm^3. We use a spherical spine with spherical SpApp and ellipsoidal spine with ellipsoidal SpApp as our two control spines of interest. Most results are shown as a 2-D cross section for ease of interpretation (see Fig. S7 for examples of the full 3-D solutions).

Spatial model of Ca^{2+} influx

The spatiotemporal dynamics of calcium are determined by the combination of dynamics within the spine volume and boundary conditions at the PM and SpApp. Calcium dynamics in the spine volume are represented by a single reaction–diffusion equation:

$$\frac{\partial Ca^{2+}}{\partial t} = D\nabla^2 Ca^{2+} - f\left(Ca^{2+}_{cyto}, CBP\right). \quad (1)$$

Here, D is the diffusion coefficient of calcium and $f\left(Ca^{2+}_{cyto}, CDP\right)$ is a function that represents the reaction between cytosolic

calcium and mobile buffers in the cytoplasm; ∇^2 is the Laplacian operator in three dimensions. The stimulus to the system is the depolarization of the membrane based on an ESPS and BPAP separated by 2 ms (Fig. 1 d). The boundary conditions at the PM and the SpApp are given by time-dependent fluxes that represent the kinetics of different channels, pumps, and fixed buffers.

Boundary conditions at the PM

We model the calcium influx through activated NMDARs in response to glutamate release in the synaptic cleft and the calcium influx through VSCCs in response to membrane depolarization (Jahr and Stevens, 1993; Shouval et al., 2002; Bartol et al., 2015b). We should note that the majority of existing models for NMDAR and VSCC calcium influx assume well-mixed conditions. In this model, these species are restricted to the PM, which is the boundary of the geometry. This results in a time-dependent flux at the PM. Both the NMDAR and VSCC-mediated calcium influx depend on the membrane voltage (see Fig. 1 d); we prescribe this voltage as a set of biexponentials to capture a BPAP and EPSP based on previous studies (Jahr and Stevens, 1993; Shouval et al., 2002). On the PM, we also include PMCA and NCX that are activated in response to a change in cytosolic calcium concentration (Calizo et al., 2017 *Preprint*; Maurya and Subramaniam, 2007). We also localize fixed CBPs (fixed buffers) to the PM. Therefore, the binding of cytosolic calcium to fixed buffers (B_f) is modeled as a membrane flux, J_{Bf}. The flux boundary condition at the PM is then the sum of all these fluxes and is given by

$$-D(n \cdot \nabla Ca^{2+})\big|_{PM} = J_{NMDAR} + J_{VSCC} - J_{PMCA} - J_{NCX} - J_{Bf}. \quad (2)$$

The functions that define the flux terms in Eq. 2 are given in Table S1.

Boundary condition at the SpApp membrane

In the cases where we included a SpApp, we included SERCA pumps and a leak term along the SpApp membrane that are functions of the cytosolic calcium concentration. The boundary condition for the flux across the SpApp membrane is given by

$$-D(n \cdot \nabla Ca)\big|_{SpApp} = J_{SERCA} - J_{LEAK}. \quad (3)$$

The functions that define the flux term in Eq. 3 are given in Table S1.

To briefly summarize, these governing equations are simply the balance equations that keep track of the spatiotemporal dynamics of cytosolic calcium due to calcium diffusion and mobile buffers (Eq. 1), influx and efflux through the PM (Eq. 2), and influx and efflux through the SpApp membrane (Eq. 3). The coupled nature of this system of equations and time-dependent fluxes limits the possibility of obtaining analytical solutions even for simple geometries (Cugno et al., 2018 *Preprint*). Therefore, we use computational methods to solve these equations.

Parametric sensitivity analyses

Given the vast number of parameters in this model, we constrain the parameters in our model as follows: parameter values are chosen from experimental observations or existing computational models or to match overall experimental and computational observations with respect to pump or channel dynamics (section S1). Overall, we predict a high calcium concentration and relatively fast decay dynamics (Sabatini et al., 2002; Higley and Sabatini, 2012; Hu et al., 2018). See Fig. S2 for a comparison of temporal dynamics to existing literature. We conducted a kinetic parameter sensitivity analysis for our model using the open source software COPASI—a COmplex PAthway SImulator (Supplemental text). The sensitivity analysis was performed in COPASI by converting our spatial model into a compartmental ordinary differential equation (ODE) system. This conversion involves transforming boundary flux equations into volumetric reaction rate through the lengthscale factor n, the volume-to-surface area ratio.

Geometries used in the model

We modeled the dendritic spines using idealized geometries of spheres and ellipsoids; dendritic spines consist of a spine head attached to a neck, with a similarly structured SpApp within the spine, see Fig. 1 c for the different model geometries used in this study. These geometries were inspired by reconstructions (Bartol et al., 2015a; Griffith et al., 2016; Paulin et al., 2016) and were idealized for ease of computation. For the variations of the base of the neck, we also include a condition with an explicit dendrite modeled as a cylinder attached to the spine neck, Figs. S4 and S5. The geometric parameters, including volume and surface area, are given in Table S8.

Numerical methods

Simulations for calcium dynamics were conducted using commercial finite-element software (COMSOL Multiphysics 5.4). Specifically, the general form and boundary partial differential equations (PDEs) interface were used and time-dependent flux boundary conditions were prescribed. A user-defined tetrahedral mesh with a maximum and minimum element size of 0.0574 µm and 0.00717 µm, respectively, was used. Due to the time-dependent, nonlinear boundary conditions used in this model, we also prescribed four boundary layers (prism mesh elements) on all membranes in COMSOL. A time-dependent solver was used to solve the system, specifically a MUMPS (MUltifrontal Massively Parallel sparse direct Solver) solver with backward differentiation formula time-stepping method with a free time stepper. Results were exported to MATLAB for further analysis. All COMSOL files will be posted on the Rangamani Lab website for public dissemination.

Online supplemental material

All model equations and parameters and geometric parameters can be found in the online supplemental material. Fig. S1 shows the effects due to using a different lengthscale, n. Fig. S2 shows temporal comparison with other existing models. Fig. S3 is a sensitivity analysis of model parameters. Figs. S4 and S5 show the case when the neck base has different boundary conditions in spherical and ellipsoidal spines, respectively. Fig. S6 shows the effect of spine neck radius. Fig. S7 shows calcium spatial dynamics in 3D for spherical and ellipsoidal spines. Fig. S8 shows temporal dynamics and peak concentrations for spines of

various shapes. Fig. S9 shows the effects of different calcium buffers in ellipsoidal spines. Table S1 lists the main equations in the model. Table S2 lists parameters used in the model for the volumes. Table S3 lists parameters for NMDAR. Table S4 lists parameters for membrane voltage. Table S5 lists parameters for VSCC. Table S6 lists parameters for PMCA and NCX pumps. Table S7 lists parameters for SERCA. Table S8 lists the size and shape parameters of the different geometries. Table S9 lists size variations for the spherical spine head with spherical SpApp. Table S10 lists size variations for the ellipsoidal spine head with ellipsoidal SpApp. Table S11 lists size variations for the spherical spine head with spherical SpApp when varying SpApp volume. Table S12 lists size variations for the ellipsoidal spine head with ellipsoidal SpApp when varying SpApp volume.

Results

Using the model developed above (Eqs. 1–3), we investigated how different geometric factors of the spine head and SpApp affect calcium dynamics. Because of the coupling between the volume dynamics (Eq. 1) and the fluxes on the membranes due to biochemical components (Eqs. 2 and 3), the effect of spine geometry on calcium dynamics is quite complex. To parse the coupled effects, we have categorized and organized our simulations as follows and discuss each case in detail. First, we investigated the effect of spine volume to surface area ratio. This parameter can be changed in multiple ways: by changing the shape of the spine head and the shape or presence of the SpApp (Figs. 2 and 3), by changing the size of the spine head alone (Fig. 4), or by changing the size of the SpApp alone (Fig. 5). Next, we investigated the effect of spatial distribution of the fluxes on the PM (Fig. 6). Finally, we demonstrate the effect of buffer types and their location (Figs. 7 and 8). We describe each of these results in detail below.

Effect of spine volume to surface area on calcium dynamics

Effects of shape of the spine head and the shape of the SpApp on calcium dynamics

We first analyzed how the volume to surface area ratio of the spine affects the spatiotemporal dynamics of calcium by simulating calcium dynamics in the different geometries shown in Fig. 1 c. All of these geometries were constructed such that they have the same volume of the spine cytosol but the surface area of the PM and SpApp vary because of the shape (Table S8). We note that in all the geometries, the temporal dynamics of calcium shows a rapid increase in the first 2–3 ms and a decay over ∼50 ms (Fig. S8). This time course is consistent with experimentally observed and computationally modeled calcium dynamics (Ngo-Anh et al., 2005; Matthews et al., 2013; Hu et al., 2018; Figs. 2 d and S2, respectively). The spatial profiles of calcium in spheres and ellipsoids (Fig. 2, a and b) show that spine shape can alter the spatial gradients and decay profiles of calcium. In particular, we observe that while at 5 ms all shapes demonstrate a gradient from the PSD region to the spine neck, because of the localized influx of calcium through the NMDAR in the PSD, at 10 ms, the ellipsoidal spine heads have almost no gradient within the spine head. Instead, they have a more pronounced difference between the spine head and spine neck. We also changed the shape of the SpApp to get different combinations of spine head and SpApp geometries (Fig. 2). Since the apparatus acts as a sink, we find that the reduction in surface area to volume ratio of the spherical apparatus leads to less influx into the SpApp, compared with the ellipsoidal SpApp (Fig. 2 c). This result emphasizes the nonintuitive relationships between organelle shape and spine shape.

In addition to the transient response of calcium, the cumulative calcium (total calcium) also carries information with respect to synaptic plasticity (Bourne and Harris, 2008; Rangamani et al., 2016; Basak and Narayanan, 2018). Therefore, we calculated the integrated calcium over the entire spine volume (area under the curve [AUC]; Gorman and Sejnowski, 1988; Heinrich et al., 2002; Atay and Skotheim, 2017) over 300 ms. Calcium AUC at 300 ms (Fig. 2 c) shows that all spines have slightly different accumulated calcium. Upon closer examination of the membrane fluxes of the sphere and ellipsoid spines (Fig. 2, e–m), we see that there is a complex relationship between the calcium ion concentration and nonlinear flux terms. In particular, the higher calcium influx in the ellipsoids due to the larger surface area leads to a higher efflux of calcium through the PMCA, NCX, and SERCA pumps and increased binding to fixed buffers on the PM. Therefore, the nonlinear effects of the fluxes associated with the pumps reduces the difference in calcium between spines of different shapes.

Effects of the presence/absence of the SpApp on volume to surface area

Another way to modulate the volume to surface area ratio is to consider spines with and without the SpApp. In our model, the SpApp serves both as a calcium sink through SERCA pumps and as an excluded volume. We observe that the presence of the SpApp in both spheres and ellipsoids (Fig. 3, a and d, top row) results in a steeper gradient from the PSD to the neck when compared with the spines without a SpApp (Fig. 3, a and d, bottom row). Additionally, at 10 ms, spines without a SpApp have a higher calcium concentration than spines with a SpApp. This is because the dynamics of calcium are altered in the presence of the SpApp by the SERCA fluxes, Eq. 3. As a result, regardless of the shape, spines with a SpApp have a faster decay of cytosolic calcium (Fig. 3, b and e). We found that in both geometries, the AUC of spines with a SpApp was lower at different time points when compared with spines without a SpApp (Fig. 3, c and f). At 300 ms, the spine without a SpApp has 47.75% more total calcium for the spherical geometry and 49.09% more for the ellipsoidal geometry. Thus the flux due to SERCA plays a significant role in altering the decay dynamics of calcium in spines with SpApp and as a result alters the total calcium.

Effect of spine volume on calcium dynamics

In addition to spine shape, spine size (volume) is also known to change during development and plasticity related events (Knott et al., 2006; Kasai et al., 2010; Rangamani et al., 2016). How does changing the volume of the spine, while maintaining the same shape, affect calcium dynamics? To answer this question, we conducted simulations in spherical and ellipsoidal spines of

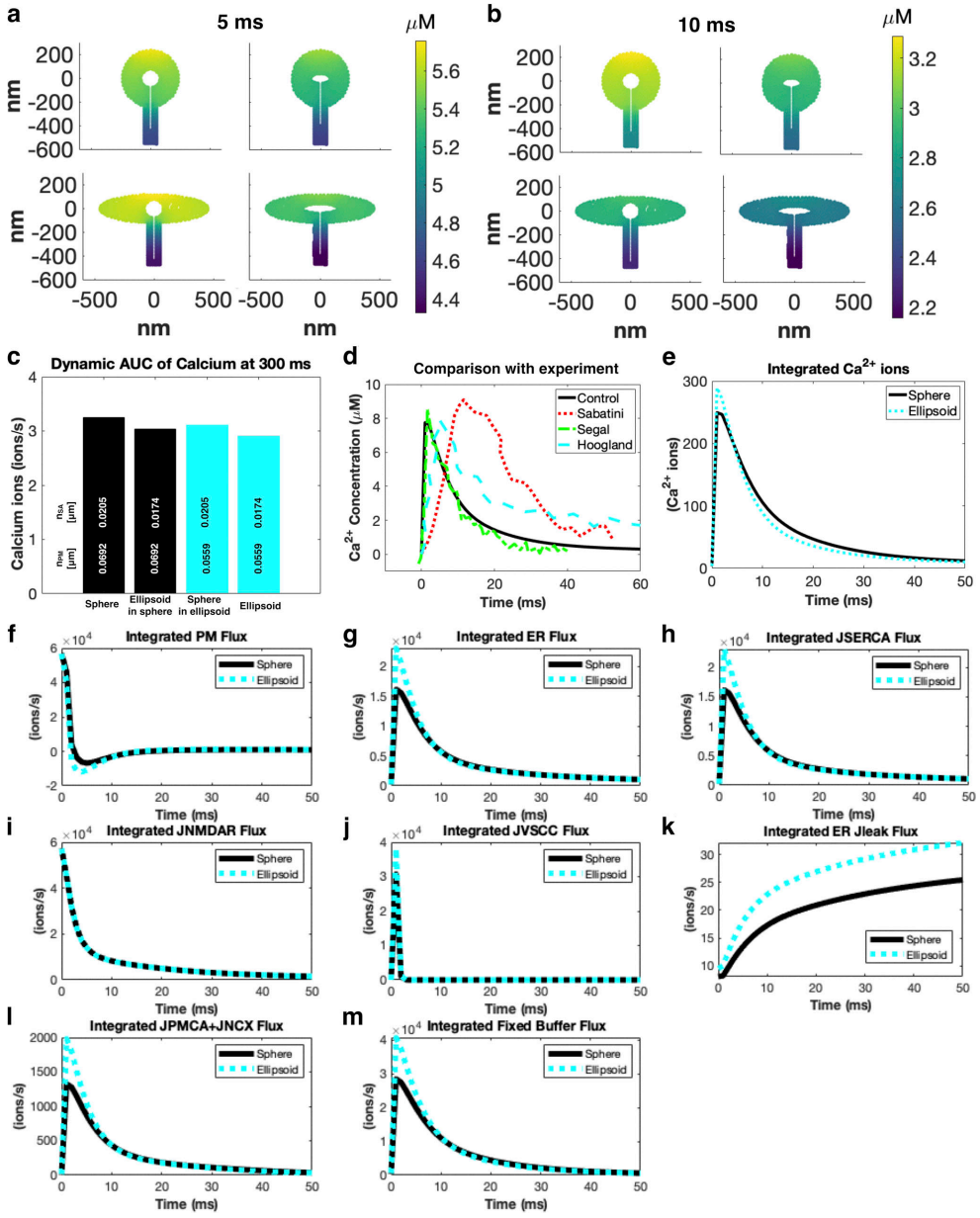

Figure 2. **Spine head volume-to-surface area ratio modifies calcium dynamics through membrane flux contributions. (a and b)** Spatial distribution of calcium in spines at two different time points (5 ms [a] and 10 ms [b]). The instantaneous gradient of calcium ions depends on the shape of the spine head and the shape of the SpApp. **(c)** Calcium accumulation at 300 ms was calculated using the AUC of the spatial and temporal dynamics of calcium throughout the volume; the differences between the shapes are small, with the most pronounced difference being a 12% increase in AUC between the sphere and ellipsoid

spines. **(d)** We plot the temporal dynamics at the top of the spherical control spine versus reported experimental calcium transients from previous studies (Sabatini et al., 2002; Hoogland and Saggau, 2004; Segal and Korkotian, 2014). The experimental transients are reported in terms of fluorescence, which we assume are linearly proportional to concentration (Yasuda et al., 2004). We plot Fig. 1 F from Sabatini et al. (2002), Fig. 1 from Segal and Korkotian (2014), and Fig. 2 D from Hoogland and Saggau (2004). PlotDigitizer was used to trace the temporal profiles that were then plotted in MATLAB. We more closely compared the spherical and ellipsoidal spines by integrating total calcium ions over time (e) and considering the integrated fluxes for both shapes (f–m). We see that the ellipsoid has more calcium ions than the sphere (e), because despite having more calcium influx due to VSCC (j), the subsequent higher calcium concentration leads to higher efflux due to pumps (h and l) and buffers (m). Note the timescale in panels e–m is shortened to 50 ms for clarity.

different volumes. Recall that the control spine has a cytosolic volume, V_{cyto}, of 0.06 μm³ (Table S8). For each geometry (sphere and ellipsoid), we maintained the same size and shape of the SpApp as before and only changed the spine cytoplasm volume in the range of 0.5 V_{cyto} to 1.5 V_{cyto} (Tables S9 and S10). We found that the relationship between spine volume and calcium

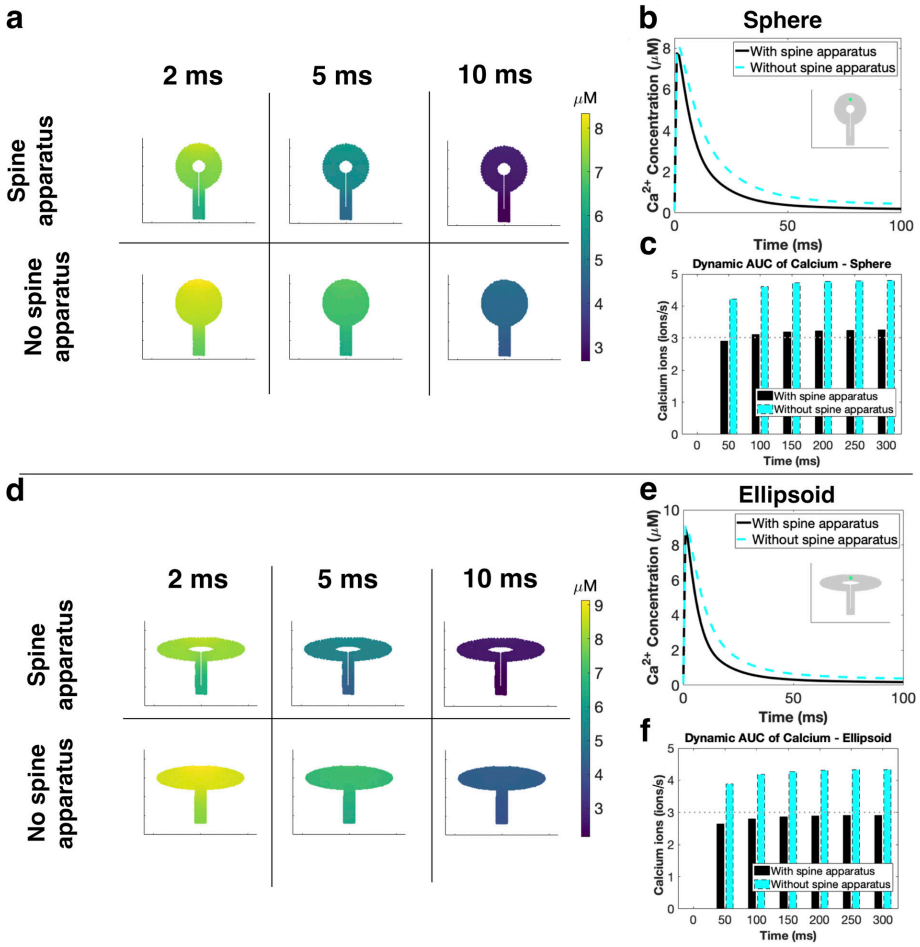

Figure 3. **The presence of a SpApp, acting as a sink, modulates calcium dynamics.** Spines without SpApp have higher and more sustained calcium activity despite their increased volume in both spherical (a) and ellipsoidal (d) spines. Temporal dynamics (b and e) and AUC (c and f) plots show that the absence of a SpApp (no SERCA flux, denoted as J_{SERCA}) leads to a prolonged calcium transient and higher total calcium levels for both spherical and ellipsoidal shapes. Insets in panels b and e show the location in the spine from where the time courses were plotted.

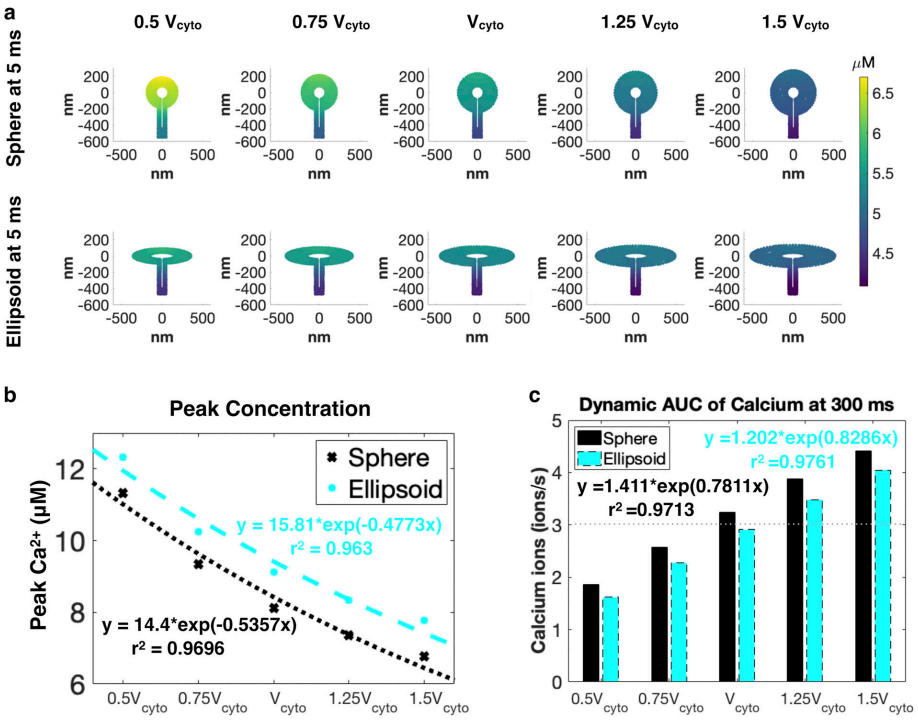

Figure 4. **Accumulated calcium scales inversely proportional to the spine head volume. (a)** Calcium dynamics in spines of different sizes show that as spine volume increases, calcium concentration in the spine decreases. The effect of spine size on the temporal dynamics of calcium is seen in the peak values (b) and AUCs of calcium (c). Increasing spine volume decreases the peak calcium concentration but increases overall AUC in the spine irrespective of the spine shape. cyto, cytoplasm.

concentration is inversely proportional. For spine volumes smaller than the control, we observed an increase in calcium concentration for both geometries, whereas for larger volumes, calcium concentration decreases (Fig. 4, a and b). As expected, we found that for both geometries, an increase in spine volume resulted in an increase in cumulative calcium (Fig. 4 c). Furthermore, we found that the change in cumulative calcium has a direct but nonlinear relationship with the change in spine volume. For the range of volumes investigated, the peak calcium concentration and AUC show an exponential relationship with respect to volume. We see at all sizes the ellipsoid has higher peak concentrations but lower AUC compared with the sphere.

Effect of SpApp size and geometry

The complex architecture of the SpApp was recently elucidated in a focused ion beam scanning electron microscopy study by Wu et al. (2017). Since we cannot yet manipulate the shape of the SpApp in vivo, we varied the geometric features of the SpApp in silico to see how they affect calcium dynamics. Previously, we showed that SpApp shape and spine volume separately can alter the AUC and peak calcium. Here, for a given spine shape, we varied the volume of the SpApp to modulate the cytosolic volume to SpApp volume ratio. In this case, by varying the SpApp volume, we altered the spine volume to be 50% and 75% of V_{cyto}, the control spine volume. Here, we change the spine volume by the changing SpApp size (Fig. 5). We found that a larger SpApp leads to a decrease in calcium concentrations and AUC (Fig. 5, a and c) but an increase in peak concentration (Fig. 5 b). We note that as SpApp volume increases, AUC drops in a nonlinear manner in both geometries. The spherical spine has a 55.4% and 77.8% reduction in AUC from control for the 75% and 50% spines, while the ellipsoidal spine has a 57.2% and 79.4% reduction from control. For all sizes, the ellipsoid shows higher peak concentrations but lower AUC compared with the sphere. This effect is in part due to the shortened distance between the PSD and SpApp in the ellipsoid. The distance between the PSD and SpApp is an important lengthscale in the spine, since it controls the distance between the sources and sinks of calcium. Therefore, changing this lengthscale, as happens when changing the SpApp volume, influences calcium dynamics in nonlinear ways. From these observations, we conclude that spine volume coupled with SpApp volume and surface area is an important regulator of calcium dynamics in dendritic spines.

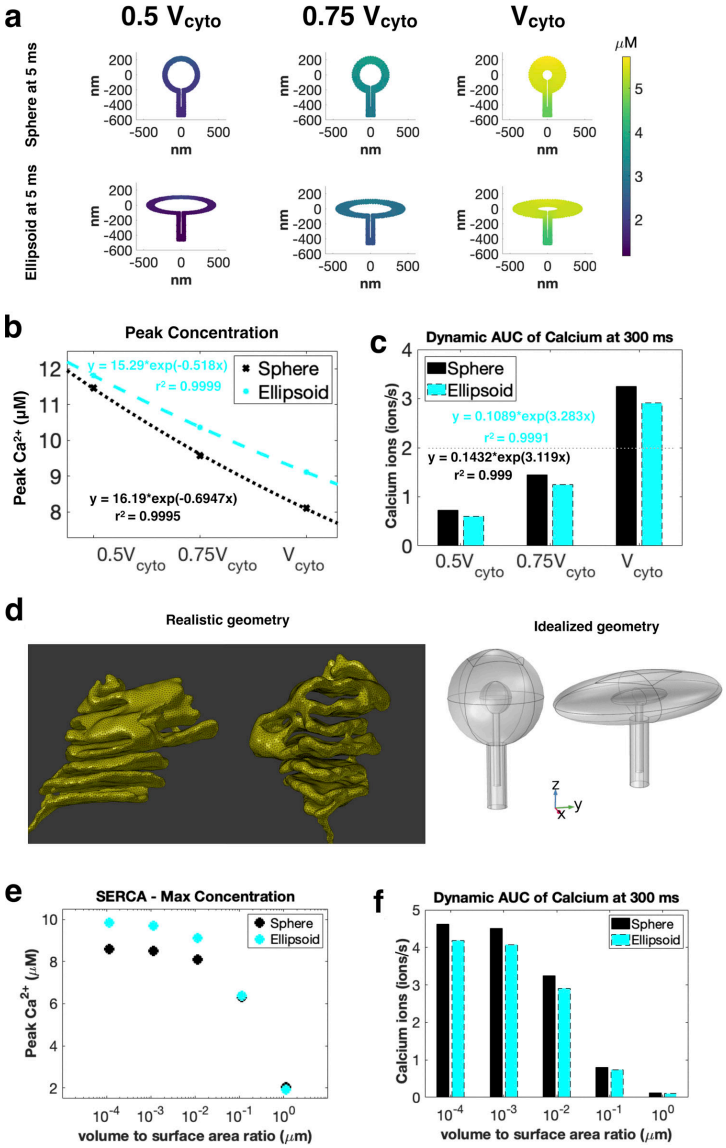

Figure 5. **Increasing SpApp volume reduces accumulated calcium and SpApp volume-to-surface area modulates its ability to act as a sink. (a)** Calcium dynamics depends on the size of SpApp; decreasing cytoplasmic volume by increasing SpApp size results in a smaller calcium concentration when compared with a larger spine volume with smaller SpApp. The effect of SpApp size on the temporal dynamics of calcium is seen in the (b) peak values and (c) AUCs of calcium. Increasing SpApp volume (decreasing spine volume) decreases calcium concentration in the spine (a and c) but leads to higher peak concentrations (b). For both geometries, the peak calcium concentration increases for decreasing volume, and can be fit to exponential curves. **(d)** While we are used idealized geometries for both the spine and SpApp, in reality, the SpApp has a complex, helicoidal structure. We investigate this realistic geometry by changing the n_{SpApp} contribution in the SERCA flux equation. We see that increasing n_{SpApp} makes SERCA more effective, leading to lower peak concentrations (e) and lower AUC (f). However, we see that as we decrease n_{SpApp}, the change in peak concentration and AUC plateaus, representing highly inefficient SERCA pumps. cyto, cytoplasm.

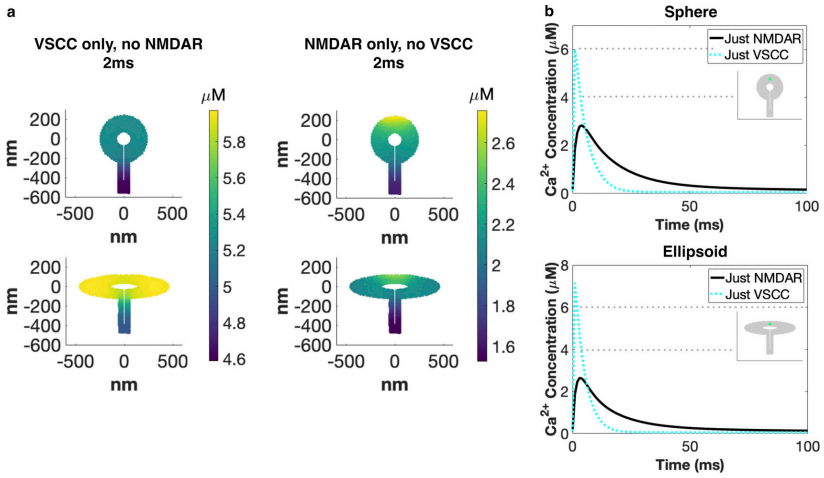

Figure 6. **Localization of membrane fluxes alters the spatiotemporal dynamics of calcium. (a)** Spatial dynamics at 2 ms for spherical and ellipsoidal spines with only one of VSCC or NMDAR as the calcium source. When the main calcium source is the VSCC, we see a more uniform concentration with the main gradient between the spine head and spine neck. When the NMDAR is the main calcium source, we see a large spatial gradient with a higher concentration at the PSD, because the NMDAR is localized to the PSD. **(b)** Temporal dynamics for spherical and ellipsoidal spines with either the VSCC or NMDAR as the calcium source. Temporal dynamics clearly show that VSCCs act on a faster timescale and have a higher peak calcium when compared with the NMDARs. However, NMDAR influx leads to a more prolonged calcium transient.

An intriguing feature of the SpApp in particular (Fig. 5 d; Wu et al., 2017) and the ER in general (Nixon-Abell et al., 2016) is the large surface-to-volume ratio occupied by this organelle. Therefore, we next considered the effect of the volume-to-surface area ratio (n; given in units of length) of the SpApp (Fig. 5, d–f). We modeled the boundary flux on the SpApp membrane such that this flux is proportional to n_{SpApp} (volume-to-surface area ratio for the SpApp). As a result, when we increase the "volume" of the SpApp by increasing n_{SpApp}, calcium flux into the SpApp will increase. We noticed that at lower n_{SpApp} values, the peak calcium concentration and to a less obvious extent the AUC (Fig. 5, e and f) plateau but decrease substantially at larger n_{SpApp} values.

From these observations, we conclude that the SpApp acts as a physical and spatial buffer for calcium dynamics by regulating the timescale through surface to volume regulation in the interior of the spine. The SpApp acts as a calcium sink in the timescale of interest (Fifková et al., 1983; Fifková, 1985; Jedlicka et al., 2008), and in the absence of the SpApp, the only way to remove calcium from this system is through CBPs and pumps. Furthermore, since the SpApp has been known to grow and retract from the dendritic spine in response to stimuli (Deller et al., 2006), regulation of SpApp surface area can also allow for rescaling calcium dynamics in the spine (Wilson et al., 1983).

Spatial distribution of membrane fluxes governs calcium dynamics supralinearly in dendritic spines

The density of VSCCs and number of NMDARs that open in response to stimuli in dendritic spines varies (Sabatini and Svoboda, 2000). One of the primary determinants of calcium dynamics in the spine is the various membrane fluxes, because these fluxes serve as sources and sinks at the PM and sinks at the SpApp membrane. We investigated the effect of the spatial distribution of membrane fluxes on calcium dynamics in the dendritic spine by considering either only NMDARs or VSCCs as the calcium source (Fig. 6). We observed that if only NMDAR activity was present, then calcium concentration was high in the PSD region due to the localization of NMDARs to the PSD but the overall calcium concentration was small regardless of the spine head shape (Fig. 6 a). However, if only VSCCs were active, then the spatial gradient of calcium is mainly between the spine head and spine neck (Fig. 6 a). The temporal dynamics are also affected by the receptor and channel distributions (Fig. 6 b). With only VSCC present, there is a larger calcium peak, but with faster decay. With only NMDARs, we observe a lower calcium peak concentration but a prolonged transient. Therefore, membrane flux distribution can impact the spatial and temporal dynamics of calcium in a nonlinear manner. This agrees with experimental results stating that the various calcium sources behave supralinearly (Yuste and Denk, 1995) and a balance between various calcium fluxes is required for tightly regulating calcium concentrations in these small volumes.

Calcium buffers and diffusion couple to alter calcium spatiotemporal dynamics

Due to the vast number of buffers that are known to affect calcium dynamics, we investigated the effect of four different buffer conditions: (i) both fixed membrane-bound buffers and

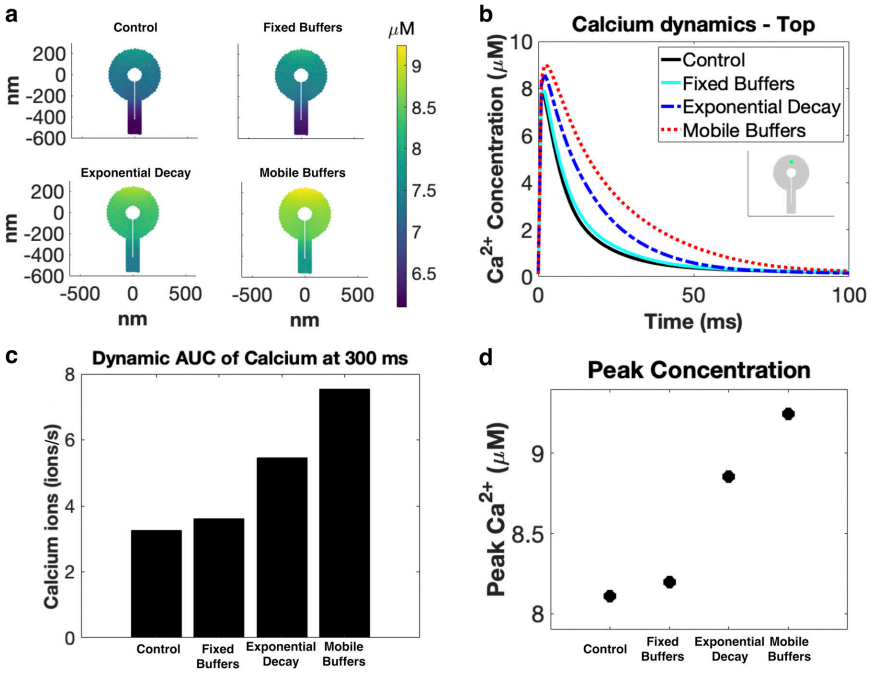

Figure 7. **Calcium buffers and CBPs modify all aspects of calcium dynamics. (a)** Spatial dynamics at 2 ms for spherical spines with different buffer conditions: control (with both fixed and mobile buffers), only fixed buffers, only mobile buffers, and a lumped exponential decay. While all buffer cases show relatively similar peak concentrations (d), all other quantifications show that buffer type greatly impacts the calcium transient decay time (a–c). Temporal dynamics (b) show that the control and fixed buffer cases have much faster decay, which translates into lower AUC values (c).

mobile cytosolic buffers (control), (ii) fixed buffers localized to the membrane, (iii) mobile buffers in the cytoplasm, and (iv) a uniform exponential decay applied across the whole cytoplasm (Figs. 7 and S9). We observe similar spatial dynamics for all buffer types (Fig. 7 a), but temporal dynamics differ greatly (Fig. 7 b) and, as a result, alter accumulated calcium (Fig. 7 c). We see that the decay behavior of calcium, and therefore total calcium, is highly dependent on buffer type. Peak calcium follows the same trend as AUC, with mobile buffers having the highest calcium concentrations and total calcium, then exponential decay, fixed buffers, and finally the control. We also consider how reaction dynamics versus diffusion rate govern calcium dynamics because buffer dynamics and diffusion rates of calcium are coupled (Yuste et al., 2000). We varied the diffusion rate of calcium and the concentration of mobile buffers to quantify how calcium dynamics are reaction or diffusion controlled (Fig. 8). We see that diffusion controls the spatial gradient seen within the spine (Fig. 8 a), while mobile buffer concentration controls the lifetime of the calcium transient (Fig. 8 b). Combining these effects, we see that the buffer concentration variation has the greatest effect at lower diffusion rates (bottom row of Fig. 8, a and b, and Fig. 8 c). The peak concentration of calcium is almost entirely dependent on the diffusion rate (Fig. 8 d). Therefore, based on the high diffusion rate of Ca^{2+} reported in the literature, we expect the system to be in a diffusion-dominated regimen.

Discussion

Calcium is a fundamental player in both neuronal (cellular) and neural (systems) functionality (Siesjö, 1990; Keener and Sneyd, 1998; Yuste, 2010). Compartmentalized by dendritic spines, calcium has a vital role in triggering signaling pathways for long-term potentiation, long-term depression, synaptic plasticity, and other processes associated with learning and memory formation (Rangamani et al., 2016). However, while dendritic spines are known to form functional subcompartments, it is less understood how this specialized compartmentalization impacts calcium dynamics (Yuste et al., 2000). In this study, we explored the intricate relationship between calcium dynamics and the shape and size of dendritic spine structures. We found that while the relationship between spine geometry and calcium dynamics is quite complicated (Hering and Sheng, 2001; Rochefort and Konnerth, 2012; Berry and Nedivi, 2017), some general conclusions can be drawn from our study.

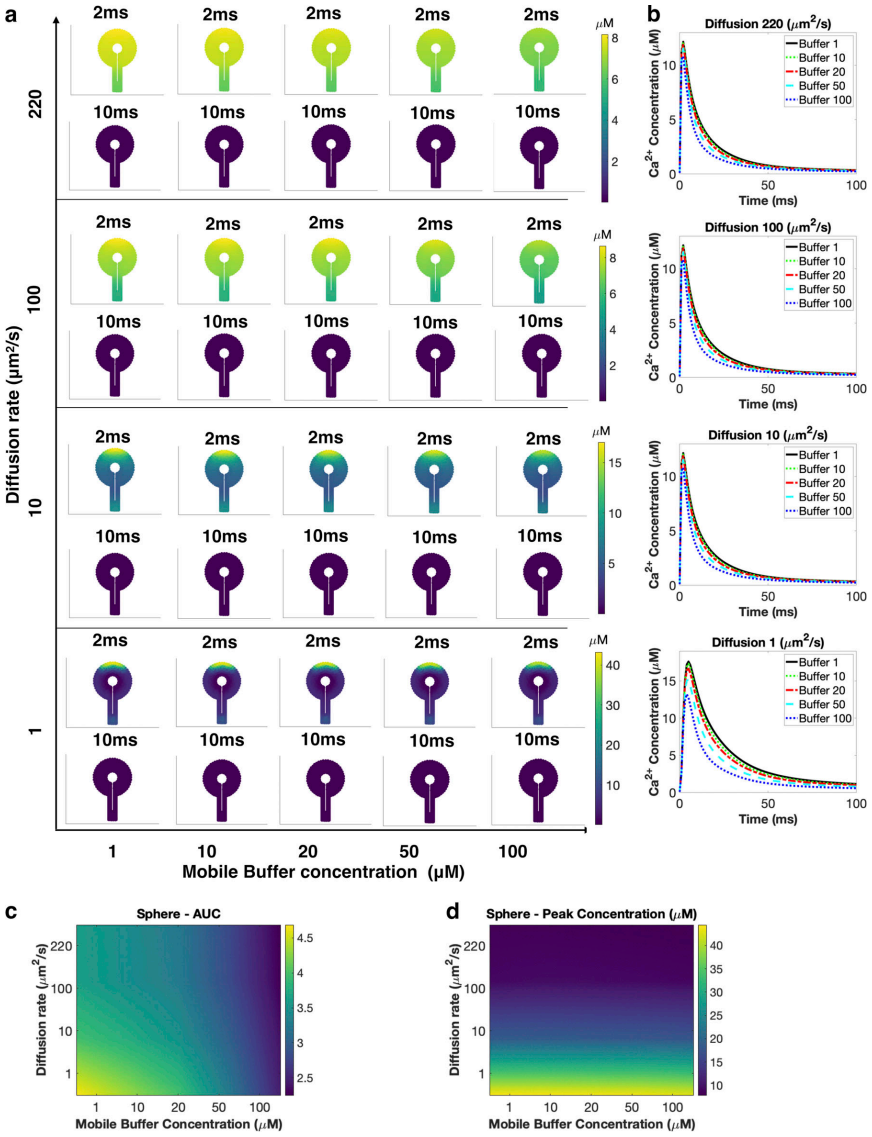

Figure 8. **Calcium diffusion rates control spatial gradients of calcium while buffer concentrations control transient decay dynamics. (a)** Spatial dynamics at 2 ms and 10 ms for a spherical spine. We varied the diffusion coefficient and the mobile buffer concentration. Based on this phase diagram, the diffusion coefficient dictates the range of the spatial gradient of calcium, while buffer binding rate influences the lifetime of the spatial gradient. **(b)** Temporal calcium dynamics at the top of the spherical spine. The temporal dynamics show that the concentration of mobile buffer affects the lifetime of the calcium transient, as expected. **(c)** AUC shows that lower mobile buffer concentration and lower diffusion rates leads to higher levels of total calcium. **(d)** Peak concentration is primarily determined by the diffusion rate of calcium and is almost independent of mobile buffer concentration.

First, the volume-to-surface ratio, rather than the shape and size itself, seems to have a dramatic effect on spine calcium (Figs. 2, 3, 4, and 5). Of course, the volume-to-surface ratio itself can be dramatically altered by size, shape, and internal organization as a many-to-one function. Then, we can think of the ultrastructural organization of the dendritic spine (Spacek and Harris, 1997) as perhaps "optimized" to not only increase contacts with neighboring axons and neural circuit connection (Yuste and Denk, 1995; Yuste et al., 2000; Yuste, 2010) but also tune this volume-to-surface ratio dynamically (Murakoshi and Yasuda, 2012). This volume-to-surface ratio coupling further highlights the complex relationship between spatial sources and sinks of calcium, which becomes apparent when the distance between the spine PM and internal organelle becomes quite small. We note that in our model, we assume constant pump density, which highlights the volume-to-surface area ratios between various shapes (Matsuzaki et al., 2001; Noguchi et al., 2005). Experimental results have already shown different behavior in large versus small dendritic spines (Paulin et al., 2016), and additional studies on dendritic spine geometry have shown that stable, mature spines are usually larger spines that tend toward mushroom shapes as they grow around adjoining axons and are more likely to have a SpApp (Spacek and Harris, 1997). In comparison, younger, less stable spines tend to be smaller and more spherical (Spacek and Harris, 1997; Berry and Nedivi, 2017). Therefore, we predict that spine size and SpApp presence are coupled to control calcium dynamics. This result should be investigated further, in particular to make predictions on why stable spines tend to be larger and mushroom shaped. The inverse relationship between the volume-to-surface ratio that we found and a possible exponential relationship suggest a potential limiting mechanism for maintaining homeostasis of synaptic potentiation (Lee et al., 2010, 2012; Béïque et al., 2011; Turrigiano, 2011). By altering the spine size dynamically (Murakoshi and Yasuda, 2012) and the presence and absence of the SpApp dynamically (Deller et al., 2006), spines could maintain their optimal range of synaptic function (Lee et al., 2010, 2012; Béïque et al., 2011; Turrigiano, 2011).

Second, localization of membrane fluxes alters calcium transients (Figs. 5 and 6). These fluxes, which serve as boundary conditions, can be altered by changing the density and distribution of calcium sources and sinks. This idea is consistent with how calcium signal localization is a result of tuning the distance between sources and sinks (Augustine et al., 2003). We show here that in addition to distance, the strength of the fluxes is important. Thus, in various disease states that impact the distribution or strength of membrane components, we predict atypical spatial calcium gradients are possible that could impact downstream signaling pathways. For example, NMDAR dysfunction, whether leading to increased or decreased functionality, can potentially lead to central nervous system diseases such as stroke, Huntington's disease, or schizophrenia (Zhou and Sheng, 2013).

Finally, the role buffers play in modulating calcium transients is not only by changing the decay time as previously thought but also by tuning the membrane fluxes, especially in the case of fixed buffers (Figs. 7 and 8; Higley and Sabatini, 2012; Matthews and Dietrich, 2015). Again, the timescale that we see is a combination of rate alterations at the membrane and rate alterations in the volume resulting in broader control of calcium dynamics. The crowded environment within the spine head also has consequences for calcium diffusion, and while it is possible for calcium to diffuse through a crowded space, particularly in the PSD, the exact mechanisms of such transport remain unclear (Santamaria et al., 2006; Hotulainen and Hoogenraad, 2010; Byrne et al., 2011). Thus, our study highlights the need for connecting biophysical features of the spine and molecule localization to the dynamics of calcium (Fig. 1).

We also note that our model has certain limitations. In particular, within the crowded environment of the dendritic spine cytoplasm is an abundance of actin, which has previously been shown to have the potential to create cytosolic flow through contraction following spine activation, leading to faster calcium diffusion (Holcman et al., 2004). We do not address this spine contraction in this model, but actin contributions are a focus of ongoing research in our group. While we touched upon the role of diffusion and CBPs, we also acknowledge that much work remains to be done on the true impact of the dense actin network and crowded environment within dendritic spines in regulating these processes (Ouyang et al., 2005). In addition, we modeled isolated spines, but the width of the spine neck has been showed as an important determinant of calcium dynamics when comparing larger and smaller spines (Noguchi et al., 2005; Arellano et al., 2007; Araya et al., 2014) and could play into communication to the dendrite. It is also possible that stochastic modeling will give better quantitative insights without altering the underlying physics (Kotaleski and Blackwell, 2010; Bartol et al., 2015b; Voorsluijs et al., 2019). The development of a combined stochastic–deterministic model can help combine these two regimes to address the fundamental physics that occurs in these small systems with complex membrane dynamics and few molecule situations.

Despite these shortcomings, we have identified several key features of the relationship between dendritic spine geometry and calcium dynamics. Current models of synaptic weight updates use calcium as the determinant for the synaptic weight vector and the learning rate (Malenka et al., 1988; Cummings et al., 1996; Shouval et al., 2002; Yeung et al., 2004). Here, we show that calcium in a spine, even in short timescales, is a function of geometry, ultrastructure, and buffers. Based on these insights, we speculate on what the biophysical features of the spine mean for neural systems-level functionality. It has long been considered that a neural circuit level model of synaptic weight updates can be informed by the calcium transients in the synapse. As a result, weighting functions have been proposed that consider calcium dynamics (Cummings et al., 1996; Shouval et al., 2002; Yeung et al., 2004), and these functions have been used to connect biophysical features of NMDARs to synaptic weight updates in models of spike time-dependent plasticity (STDP; Sejnowski, 1977; Song et al., 2000; Izhikevich, 2007; Bush and Jin, 2012; Standage et al., 2014). We now propose that the calcium transient is explicitly a function of the spine volume-to-surface area, ultrastructure, and buffers, and that the calcium functions that inform the synaptic weight vectors and synaptic

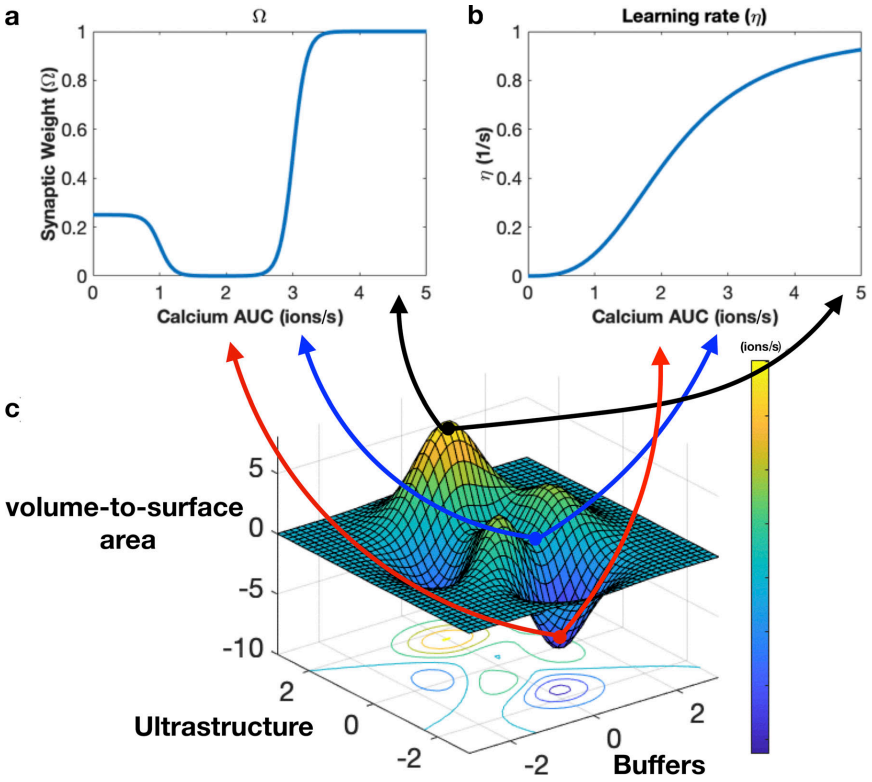

Figure 9. **Biophysical factors can impact synaptic weights through calcium dynamics. (a)** Synaptic weight can be calculated from calcium dynamics (Shouval et al., 2002). We plot changes in synaptic weight due to calcium quantified through accumulated calcium. **(b)** Calcium dynamics also dictate the learning rate of the spine. **(c)** Qualitative representation of the effects of calcium AUC on synaptic weight and learning rate. Using our model, we can map how various factors governing calcium dynamics influence both synaptic weights and learning rates of dendritic spines. This surface plot visualizes how three different factors (volume to surface area ratio, ultrastructure, and calcium buffers) couple to influence calcium AUC (color bar) that feeds back into synaptic weight changes and learning rates.

learning rate (Fig. 9) must be updated to consider such geometric information. We anticipate that such new models can give us better insight into the neural circuitry of the brain and also better inform bioinspired engineering of neuromorphic circuits (Cruz-Albrecht et al., 2012). We also acknowledge that much work remains to be done in connecting the spatial signaling aspects in postsynaptic spines with neural circuit behavior but hope that this work will inspire more multiscale modeling efforts in this field. The spatial aspects of calcium dynamics are also fundamental toward understanding the downstream dynamics of critical molecules such as calcium/calmodulin-dependent protein kinase II (CaMKII), the small RhoGTPases (Cdc42, Rho, and Rac), and subsequently actin dynamics in dendritic spine remodeling (Oertner and Matus, 2005; Murakoshi and Yasuda, 2012; Miermans et al., 2017; Ohadi and Rangamani, 2019 *Preprint*; Ohadi et al., 2019 *Preprint*; Yasuda et al., 2003; Rangamani et al., 2016; Yasuda, 2017). Going beyond single spine dynamics, the propagation of the downstream mechanochemical activity to neighboring spines is a key step toward integrating single spine behavior to multiple spines, across the dendrite, and ultimately the whole cell (Majewska et al., 2000; Bloodgood and Sabatini, 2005; Herz et al., 2006; Schmidt et al., 2007; Yasuda, 2017). Thus, we posit that accounting for the spatial and physical aspects of calcium dynamics is the first step toward deciphering the complex shape–function relationships of dendritic spines.

Acknowledgments

We thank various members of the Rangamani Lab for valuable discussion, Mariam Ordyan for manuscript review, and Professor Brenda Bloodgood and Evan Campbell for their expertise. We thank Professor Pietro De Camilli and his laboratory for supplying images used to construct the mesh seen in Fig. 5 d.

This work was supported by the University of California, San Diego Interfaces Graduate Training Program and a San Diego Fellowship, Air Force Office of Scientific Research (AFOSR) Multidisciplinary University Research Initiative (MURI) grant FA9550-18-1-0051 (M. Bell, P. Rangamani, and T. Sejnowski), and the National Institutes of Health (grant T32EB009380).

The authors declare no competing financial interests.

Author contributions: M. Bell and P. Rangamani conceived the project. M. Bell conducted all the simulations. All authors conducted data analysis and contributed to writing the manuscript. M. Bell made all the figures.

José D. Faraldo-Gómez served as editor.

Submitted: 26 September 2018
Revised: 10 May 2019
Accepted: 17 June 2019

References

Araya, R., T.P. Vogels, and R. Yuste. 2014. Activity-dependent dendritic spine neck changes are correlated with synaptic strength. *Proc. Natl. Acad. Sci. USA.* 111:E2895–E2904. https://doi.org/10.1073/pnas.1321869111

Arellano, J.I., R. Benavides-Piccione, J. Defelipe, and R. Yuste. 2007. Ultrastructure of dendritic spines: correlation between synaptic and spine morphologies. *Front. Neurosci.* 1:131–143. https://doi.org/10.3389/neuro.01.1.1.010.2007

Atay, O., and J.M. Skotheim. 2017. Spatial and temporal signal processing and decision making by MAPK pathways. *J. Cell Biol.* 216:317–330. https://doi.org/10.1083/jcb.201609124

Augustine, G.J., F. Santamaria, and K. Tanaka. 2003. Local calcium signaling in neurons. *Neuron.* 40:331–346. https://doi.org/10.1016/S0896-6273(03)00639-1

Bartol, T.M. Jr., C. Bromer, J. Kinney, M.A. Chirillo, J.N. Bourne, K.M. Harris, and T.J. Sejnowski. 2015a. Nanoconnectomic upper bound on the variability of synaptic plasticity. *eLife.* 4:e10778. https://doi.org/10.7554/eLife.10778

Bartol, T.M., D.X. Keller, J.P. Kinney, C.L. Bajaj, K.M. Harris, T.J. Sejnowski, and M.B. Kennedy. 2015b. Computational reconstitution of spine calcium transients from individual proteins. *Front. Synaptic Neurosci.* 7:17. https://doi.org/10.3389/fnsyn.2015.00017

Basak, R., and R. Narayanan. 2018. Active dendrites regulate the spatiotemporal spread of signaling microdomains. *PLOS Comput. Biol.* 14:e1006485. https://doi.org/10.1371/journal.pcbi.1006485

Basnayake, K., E. Korkotian, and D. Holcman. 2018. Fast calcium transients in neuronal spines driven by extreme statistics. *bioRxiv.* doi:10.1101/290734 (Preprint posted April 8, 2018)

Béïque, J.-C., Y. Na, D. Kuhl, P.F. Worley, and R.L. Huganir. 2011. Arc-dependent synapse-specific homeostatic plasticity. *Proc. Natl. Acad. Sci. USA.* 108:816–821. https://doi.org/10.1073/pnas.1017914108

Berry, K.P., and E. Nedivi. 2017. Spine dynamics: are they all the same? *Neuron.* 96:43–55. https://doi.org/10.1016/j.neuron.2017.08.008

Bloodgood, B.L., and B.L. Sabatini. 2005. Neuronal activity regulates diffusion across the neck of dendritic spines. *Science.* 310:866–869. https://doi.org/10.1126/science.1114816

Bourne, J.N., and K.M. Harris. 2008. Balancing structure and function at hippocampal dendritic spines. *Annu. Rev. Neurosci.* 31:47–67. https://doi.org/10.1146/annurev.neuro.31.060407.125646

Bush, D., and Y. Jin. 2012. Calcium control of triphasic hippocampal STDP. *J. Comput. Neurosci.* 33:495–514. https://doi.org/10.1007/s10827-012-0397-5

Byrne, M.J., M.N. Waxham, and Y. Kubota. 2011. The impacts of geometry and binding on CaMKII diffusion and retention in dendritic spines. *J. Comput. Neurosci.* 31:1–12. https://doi.org/10.1007/s10827-010-0293-9

Calizo, R.C., A. Ron, M. Hu, S. Bhattacya, W.G.M. Janssen, J. Hone, S. Scarlata, P. Rangamani, and R. Iyengar. 2017. Curvature regulates subcellular organelle location to control intracellular signal propagation. *bioRxiv.* doi:10.1101/161950 (Preprint posted July 11, 2017)

Clapham, D.E. 1995. Calcium signaling. *Cell.* 80:259–268. https://doi.org/10.1016/0092-8674(95)90408-5

Clapham, D.E. 2007. Calcium signaling. *Cell.* 131:1047–1058. https://doi.org/10.1016/j.cell.2007.11.028

Cruz-Albrecht, J.M., M.W. Yung, and N. Srinivasa. 2012. Energy-efficient neuron, synapse and STDP integrated circuits. *IEEE Trans. Biomed. Circuits Syst.* 6:246–256. https://doi.org/10.1109/TBCAS.2011.2174152

Cugno, A., T.M. Bartol, T.J. Sejnowski, R. Iyengar, and P. Rangamani. 2018. Geometric principles of second messenger dynamics in dendritic spines. *bioRxiv.* doi:10.1101/444489 (Preprint posted October 20, 2018)

Cummings, J.A., R.M. Mulkey, R.A. Nicoll, and R.C. Malenka. 1996. Ca2+ signaling requirements for long-term depression in the hippocampus. *Neuron.* 16:825–833. https://doi.org/10.1016/S0896-6273(00)80102-6

Deller, T., C. Bas Orth, A. Vlachos, T. Merten, D. Del Turco, D. Dehn, P. Mundel, and M. Frotscher. 2006. Plasticity of synaptopodin and the spine apparatus organelle in the rat fascia dentata following entorhinal cortex lesion. *J. Comp. Neurol.* 499:471–484. https://doi.org/10.1002/cne.21103

Denk, W., R. Yuste, K. Svoboda, and D.W. Tank. 1996. Imaging calcium dynamics in dendritic spines. *Curr. Opin. Neurobiol.* 6:372–378. https://doi.org/10.1016/S0959-4388(96)80122-X

Fifková, E. 1985. A possible mechanism of morphometric changes in dendritic spines induced by stimulation. *Cell. Mol. Neurobiol.* 5:47–63. https://doi.org/10.1007/BF00711085

Fifková, E., J.A. Markham, and R.J. Delay. 1983. Calcium in the spine apparatus of dendritic spines in the dentate molecular layer. *Brain Res.* 266:163–168. https://doi.org/10.1016/0006-8993(83)91322-7

Futagi, D., and K. Kitano. 2015. Ryanodine-receptor-driven intracellular calcium dynamics underlying spatial association of synaptic plasticity. *J. Comput. Neurosci.* 39:329–347. https://doi.org/10.1007/s10827-015-0579-z

Gallimore, A.R., A.R. Aricescu, M. Yuzaki, and R. Calinescu. 2016. A computational model for the ampa receptor phosphorylation master switch regulating cerebellar long-term depression. *PLOS Comput. Biol.* 12:e1004664. https://doi.org/10.1371/journal.pcbi.1004664

Gorman, R.P., and T.J. Sejnowski. 1988. Analysis of hidden units in a layered network trained to classify sonar targets. *Neural Netw.* 1:75–89. https://doi.org/10.1016/0893-6080(88)90023-8

Griffith, T., K. Tsaneva-Atanasova, and J.R. Mellor. 2016. Control of ca2+ influx and calmodulin activation by sk-channels in dendritic spines. *PLOS Comput. Biol.* 12:e1004949. https://doi.org/10.1371/journal.pcbi.1004949

Heinrich, R., B.G. Neel, and T.A. Rapoport. 2002. Mathematical models of protein kinase signal transduction. *Mol. Cell.* 9:957–970. https://doi.org/10.1016/S1097-2765(02)00528-2

Hering, H., and M. Sheng. 2001. Dendritic spines: structure, dynamics and regulation. *Nat. Rev. Neurosci.* 2:880–888. https://doi.org/10.1038/35104061

Herz, A.V., T. Gollisch, C.K. Machens, and D. Jaeger. 2006. Modeling single-neuron dynamics and computations: a balance of detail and abstraction. *Science.* 314:80–85. https://doi.org/10.1126/science.1127240

Higley, M.J., and B.L. Sabatini. 2012. Calcium signaling in dendritic spines. *Cold Spring Harb. Perspect. Biol.* 4:a005686. https://doi.org/10.1101/cshperspect.a005686

Holbro, N., A. Grunditz, and T.G. Oertner. 2009. Differential distribution of endoplasmic reticulum controls metabotropic signaling and plasticity at hippocampal synapses. *Proc. Natl. Acad. Sci. USA.* 106:15055–15060. https://doi.org/10.1073/pnas.0905110106

Holcman, D., Z. Schuss, and E. Korkotian. 2004. Calcium dynamics in dendritic spines and spine motility. *Biophys. J.* 87:81–91. https://doi.org/10.1529/biophysj.103.035972

Holmes, W.R. 1990. Is the function of dendritic spines to concentrate calcium? *Brain Res.* 519:338–342. https://doi.org/10.1016/0006-8993(90)90098-V

Hoogland, T.M., and P. Saggau. 2004. Facilitation of L-type Ca2+ channels in dendritic spines by activation of β2 adrenergic receptors. *J. Neurosci.* 24:8416–8427. https://doi.org/10.1523/JNEUROSCI.1677-04.2004

Hotulainen, P., and C.C. Hoogenraad. 2010. Actin in dendritic spines: connecting dynamics to function. *J. Cell Biol.* 189:619–629. https://doi.org/10.1083/jcb.201003008

Hu, E., A. Mergenthal, C.S. Bingham, D. Song, J.-M. Bouteiller, and T.W. Berger. 2018. A glutamatergic spine model to enable multi-scale modeling of nonlinear calcium dynamics. *Front. Comput. Neurosci.* 12:58. https://doi.org/10.3389/fncom.2018.00058

Izhikevich, E.M. 2007. Solving the distal reward problem through linkage of STDP and dopamine signaling. *Cereb. Cortex.* 17:2443–2452. https://doi.org/10.1093/cercor/bhl152

Jaffe, D.B., S.A. Fisher, and T.H. Brown. 1994. Confocal laser scanning microscopy reveals voltage-gated calcium signals within hippocampal dendritic spines. *J. Neurobiol.* 25:220–233. https://doi.org/10.1002/neu.480250303

Jahr, C.E., and C.F. Stevens. 1993. Calcium permeability of the N-methyl-D-aspartate receptor channel in hippocampal neurons in culture. *Proc. Natl. Acad. Sci. USA.* 90:11573–11577. https://doi.org/10.1073/pnas.90.24.11573

Jedlicka, P., A. Vlachos, S.W. Schwarzacher, and T. Deller. 2008. A role for the spine apparatus in LTP and spatial learning. *Behav. Brain Res.* 192:12–19. https://doi.org/10.1016/j.bbr.2008.02.033

Kasai, H., M. Fukuda, S. Watanabe, A. Hayashi-Takagi, and J. Noguchi. 2010. Structural dynamics of dendritic spines in memory and cognition. *Trends Neurosci.* 33:121–129. https://doi.org/10.1016/j.tins.2010.01.001

Keener, J.P., and J. Sneyd. 1998. *Mathematical Physiology.* Vol. 1. Springer-Verlag, New York. https://doi.org/10.1007/b98841

Knott, G.W., A. Holtmaat, L. Wilbrecht, E. Welker, and K. Svoboda. 2006. Spine growth precedes synapse formation in the adult neocortex in vivo. *Nat. Neurosci.* 9:1117–1124. https://doi.org/10.1038/nn1747

Koch, C., and A. Zador. 1993. The function of dendritic spines: devices subserving biochemical rather than electrical compartmentalization. *J. Neurosci.* 13:413–422. https://doi.org/10.1523/JNEUROSCI.13-02-00413.1993

Kotaleski, J.H., and K.T. Blackwell. 2010. Modelling the molecular mechanisms of synaptic plasticity using systems biology approaches. *Nat. Rev. Neurosci.* 11:239–251. https://doi.org/10.1038/nrn2807

Kuwajima, M., J. Spacek, and K.M. Harris. 2013. Beyond counts and shapes: studying pathology of dendritic spines in the context of the surrounding neuropil through serial section electron microscopy. *Neuroscience.* 251:75–89. https://doi.org/10.1016/j.neuroscience.2012.04.061

Lee, K.F., C. Soares, and J.-C. Béïque. 2012. Examining form and function of dendritic spines. *Neural Plast.* 2012:704103. https://doi.org/10.1155/2012/704103

Lee, M.-C., R. Yasuda, and M.D. Ehlers. 2010. Metaplasticity at single glutamatergic synapses. *Neuron.* 66:859–870. https://doi.org/10.1016/j.neuron.2010.05.015

Lee, S.-J.R., Y. Escobedo-Lozoya, E.M. Szatmari, and R. Yasuda. 2009. Activation of CaMKII in single dendritic spines during long-term potentiation. *Nature.* 458:299–304. https://doi.org/10.1038/nature07842

Loewenstein, Y., and H. Sompolinsky. 2003. Temporal integration by calcium dynamics in a model neuron. *Nat. Neurosci.* 6:961–967. https://doi.org/10.1038/nn1109

Majewska, A., A. Tashiro, and R. Yuste. 2000. Regulation of spine calcium dynamics by rapid spine motility. *J. Neurosci.* 20:8262–8268. https://doi.org/10.1523/JNEUROSCI.20-22-08262.2000

Malenka, R.C., J.A. Kauer, R.S. Zucker, and R.A. Nicoll. 1988. Postsynaptic calcium is sufficient for potentiation of hippocampal synaptic transmission. *Science.* 242:81–84. https://doi.org/10.1126/science.2845577

Matsuzaki, M., G.C. Ellis-Davies, T. Nemoto, Y. Miyashita, M. Iino, and H. Kasai. 2001. Dendritic spine geometry is critical for AMPA receptor expression in hippocampal CA1 pyramidal neurons. *Nat. Neurosci.* 4:1086–1092. https://doi.org/10.1038/nn736

Matthews, E.A., and D. Dietrich. 2015. Buffer mobility and the regulation of neuronal calcium domains. *Front. Cell. Neurosci.* 9:48. https://doi.org/10.3389/fncel.2015.00048

Matthews, E.A., S. Schoch, and D. Dietrich. 2013. Tuning local calcium availability: cell-type-specific immobile calcium buffer capacity in hippocampal neurons. *J. Neurosci.* 33:14431–14445. https://doi.org/10.1523/JNEUROSCI.4118-12.2013

Mattson, M.P., F.M. LaFerla, S.L. Chan, M.A. Leissring, P.N. Shepel, and J.D. Geiger. 2000. Calcium signaling in the ER: its role in neuronal plasticity and neurodegenerative disorders. *Trends Neurosci.* 23:222–229. https://doi.org/10.1016/S0166-2236(00)01548-4

Maurya, M.R., and S. Subramaniam. 2007. A kinetic model for calcium dynamics in RAW 264.7 cells: 1. Mechanisms, parameters, and subpopulational variability. *Biophys. J.* 93:709–728. https://doi.org/10.1529/biophysj.106.097469

Means, S., A.J. Smith, J. Shepherd, J. Shadid, J. Fowler, R.J. Wojcikiewicz, T. Mazel, G.D. Smith, and B.S. Wilson. 2006. Reaction diffusion modeling of calcium dynamics with realistic ER geometry. *Biophys. J.* 91:537–557. https://doi.org/10.1529/biophysj.105.075036

Miermans, C.A., R.P. Kusters, C.C. Hoogenraad, and C. Storm. 2017. Biophysical model of the role of actin remodeling on dendritic spine morphology. *PLoS One.* 12:e0170113. https://doi.org/10.1371/journal.pone.0170113

Murakoshi, H., and R. Yasuda. 2012. Postsynaptic signaling during plasticity of dendritic spines. *Trends Neurosci.* 35:135–143. https://doi.org/10.1016/j.tins.2011.12.002

Ngo-Anh, T.J., B.L. Bloodgood, M. Lin, B.L. Sabatini, J. Maylie, and J.P. Adelman. 2005. SK channels and NMDA receptors form a Ca2+-mediated feedback loop in dendritic spines. *Nat. Neurosci.* 8:642–649. https://doi.org/10.1038/nn1449

Nishiyama, J., and R. Yasuda. 2015. Biochemical computation for spine structural plasticity. *Neuron.* 87:63–75. https://doi.org/10.1016/j.neuron.2015.05.043

Nixon-Abell, J., C.J. Obara, A.V. Weigel, D. Li, W.R. Legant, C.S. Xu, H.A. Pasolli, K. Harvey, H.F. Hess, E. Betzig, et al. 2016. Increased spatiotemporal resolution reveals highly dynamic dense tubular matrices in the peripheral ER. *Science.* 354:aaf3928. https://doi.org/10.1126/science.aaf3928

Noguchi, J., M. Matsuzaki, G.C. Ellis-Davies, and H. Kasai. 2005. Spine-neck geometry determines NMDA receptor-dependent Ca2+ signaling in dendrites. *Neuron.* 46:609–622. https://doi.org/10.1016/j.neuron.2005.03.015

Oertner, T.G., and A. Matus. 2005. Calcium regulation of actin dynamics in dendritic spines. *Cell Calcium.* 37:477–482. https://doi.org/10.1016/j.ceca.2005.01.016

Ohadi, D., and P. Rangamani. 2019. Geometric control of frequency modulation of camp oscillations due to ca2+-bursts in dendritic spines. *bioRxiv.* doi:10.1101/520643 (Preprint posted January 15, 2019)

Ohadi, D., D.L. Schmitt, B. Calabrese, S. Halpain, J. Zhang, and P. Rangamani. 2019. Computational modeling reveals frequency modulation of calcium-camp/pka pathway in dendritic spines. *bioRxiv.* doi:10.1101521740 (Preprint posted January 16, 2019)

Ostroff, L.E., B. Botsford, S. Gindina, K.K. Cowansage, J.E. LeDoux, E. Klann, and C. Hoeffer. 2017. Accumulation of polyribosomes in dendritic spine heads, but not bases and necks, during memory consolidation depends on cap-dependent translation initiation. *J. Neurosci.* 37:1862–1872. https://doi.org/10.1523/JNEUROSCI.3301-16.2017

Ouyang, Y., M. Wong, F. Capani, N. Rensing, C.-S. Lee, Q. Liu, C. Neusch, M.E. Martone, J.Y. Wu, K. Yamada, et al. 2005. Transient decrease in F-actin may be necessary for translocation of proteins into dendritic spines. *Eur. J. Neurosci.* 22:2995–3005. https://doi.org/10.1111/j.1460-9568.2005.04521.x

Paulin, J.J., P. Haslehurst, A.D. Fellows, W. Liu, J.D. Jackson, Z. Joel, D.M. Cummings, and F.A. Edwards. 2016. Large and small dendritic spines serve different interacting functions in hippocampal synaptic plasticity and homeostasis. *Neural Plast.* 2016:6170509. https://doi.org/10.1155/2016/6170509

Rackham, O.J., K. Tsaneva-Atanasova, A. Ganesh, and J.R. Mellor. 2010. A ca2+-based computational model for nmda receptor-dependent synaptic plasticity at individual post-synaptic spines in the hippocampus. *Front. Synaptic Neurosci.* 2:31.

Rangamani, P., M.G. Levy, S. Khan, and G. Oster. 2016. Paradoxical signaling regulates structural plasticity in dendritic spines. *Proc. Natl. Acad. Sci. USA.* 113:E5298–E5307. https://doi.org/10.1073/pnas.1610391113

Rochefort, N.L., and A. Konnerth. 2012. Dendritic spines: from structure to in vivo function. *EMBO Rep.* 13:699–708. https://doi.org/10.1038/embor.2012.102

Sabatini, B.L., and K. Svoboda. 2000. Analysis of calcium channels in single spines using optical fluctuation analysis. *Nature.* 408:589–593. https://doi.org/10.1038/35046076

Sabatini, B.L., M. Maravall, and K. Svoboda. 2001. Ca(2+) signaling in dendritic spines. *Curr. Opin. Neurobiol.* 11:349–356. https://doi.org/10.1016/S0959-4388(00)00218-X

Sabatini, B.L., T.G. Oertner, and K. Svoboda. 2002. The life cycle of Ca(2+) ions in dendritic spines. *Neuron.* 33:439–452. https://doi.org/10.1016/S0896-6273(02)00573-1

Santamaria, F., S. Wils, E. De Schutter, and G.J. Augustine. 2006. Anomalous diffusion in Purkinje cell dendrites caused by spines. *Neuron.* 52:635–648. https://doi.org/10.1016/j.neuron.2006.10.025

Schmidt, H. 2012. Three functional facets of calbindin D-28k. *Front. Mol. Neurosci.* 5:25. https://doi.org/10.3389/fnmol.2012.00025

Schmidt, H., and J. Eilers. 2009. Spine neck geometry determines spino-dendritic cross-talk in the presence of mobile endogenous calcium binding proteins. *J. Comput. Neurosci.* 27:229–243. https://doi.org/10.1007/s10827-009-0139-5

Schmidt, H., S. Kunerth, C. Wilms, R. Strotmann, and J. Eilers. 2007. Spino-dendritic cross-talk in rodent Purkinje neurons mediated by endogenous Ca2+-binding proteins. *J. Physiol.* 581:619–629. https://doi.org/10.1113/jphysiol.2007.127860

Segal, M. 2005. Dendritic spines and long-term plasticity. *Nat. Rev. Neurosci.* 6:277–284. https://doi.org/10.1038/nrn1649

Segal, M., and E. Korkotian. 2014. Endoplasmic reticulum calcium stores in dendritic spines. *Front. Neuroanat.* 8:64. https://doi.org/10.3389/fnana.2014.00064

Segal, M., A. Vlachos, and E. Korkotian. 2010. The spine apparatus, synaptopodin, and dendritic spine plasticity. *Neuroscientist.* 16:125–131. https://doi.org/10.1177/1073858409355829

Sejnowski, T.J. 1977. Statistical constraints on synaptic plasticity. *J. Theor. Biol.* 69:385–389. https://doi.org/10.1016/0022-5193(77)90146-1

Shouval, H.Z., M.F. Bear, and L.N. Cooper. 2002. A unified model of NMDA receptor-dependent bidirectional synaptic plasticity. *Proc. Natl. Acad. Sci. USA.* 99:10831–10836. https://doi.org/10.1073/pnas.152343099

Siesjö, B.K. 1990. Calcium in the brain under physiological and pathological conditions. *Eur. Neurol.* 30(Suppl 2):3–9, discussion:39–41. https://doi.org/10.1159/000117184

Song, S., K.D. Miller, and L.F. Abbott. 2000. Competitive Hebbian learning through spike-timing-dependent synaptic plasticity. *Nat. Neurosci.* 3: 919–926. https://doi.org/10.1038/78829

Spacek, J., and K.M. Harris. 1997. Three-dimensional organization of smooth endoplasmic reticulum in hippocampal CA1 dendrites and dendritic spines of the immature and mature rat. *J. Neurosci.* 17:190–203. https://doi.org/10.1523/JNEUROSCI.17-01-00190.1997

Standage, D., T. Trappenberg, and G. Blohm. 2014. Calcium-dependent calcium decay explains STDP in a dynamic model of hippocampal synapses. *PLoS One.* 9:e86248. https://doi.org/10.1371/journal.pone.0086248

Turrigiano, G. 2011. Too many cooks? Intrinsic and synaptic homeostatic mechanisms in cortical circuit refinement. *Annu. Rev. Neurosci.* 34: 89–103. https://doi.org/10.1146/annurev-neuro-060909-153238

Voorsluijs, V., S.P. Dawson, Y. De Decker, and G. Dupont. 2019. Deterministic limit of intracellular calcium spikes. *Phys. Rev. Lett.* 122:088101. https://doi.org/10.1103/PhysRevLett.122.088101

Wacquier, B., L. Combettes, G.T. Van Nhieu, and G. Dupont. 2016. Interplay between intracellular ca 2+ oscillations and ca 2+-stimulated mitochondrial metabolism. *Sci. Rep.* 6:19316. https://doi.org/10.1038/srep19316

Wilson, C.J., P.M. Groves, S.T. Kitai, and J.C. Linder. 1983. Three-dimensional structure of dendritic spines in the rat neostriatum. *J. Neurosci.* 3: 383–388. https://doi.org/10.1523/JNEUROSCI.03-02-00383.1983

Wu, Y., C. Whiteus, C.S. Xu, K.J. Hayworth, R.J. Weinberg, H.F. Hess, and P. De Camilli. 2017. Contacts between the endoplasmic reticulum and other membranes in neurons. *Proc. Natl. Acad. Sci. USA.* 114:E4859–E4867. https://doi.org/10.1073/pnas.1701078114

Wuytack, F., L. Raeymaekers, and L. Missiaen. 2002. Molecular physiology of the SERCA and SPCA pumps. *Cell Calcium.* 32:279–305. https://doi.org/10.1016/S0143416002001847

Yasuda, R. 2017. Biophysics of biochemical signaling in dendritic spines: Implications in synaptic plasticity. *Biophys. J.* 113:2152–2159. https://doi.org/10.1016/j.bpj.2017.07.029

Yasuda, H., A.L. Barth, D. Stellwagen, and R.C. Malenka. 2003. A developmental switch in the signaling cascades for LTP induction. *Nat. Neurosci.* 6:15–16. https://doi.org/10.1038/nn985

Yasuda, R., E.A. Nimchinsky, V. Scheuss, T.A. Pologruto, T.G. Oertner, B.L. Sabatini, and K. Svoboda. 2004. Imaging calcium concentration dynamics in small neuronal compartments. *Sci. STKE.* 2004:pl5.

Yeung, L.C., H.Z. Shouval, B.S. Blais, and L.N. Cooper. 2004. Synaptic homeostasis and input selectivity follow from a calcium-dependent plasticity model. *Proc. Natl. Acad. Sci. USA.* 101:14943–14948. https://doi.org/10.1073/pnas.0405555101

Yuste, R. 2010. *Dendritic Spines.* MIT Press, Cambridge, MA. https://doi.org/10.7551/mitpress/9780262013505.001.0001

Yuste, R., and W. Denk. 1995. Dendritic spines as basic functional units of neuronal integration. *Nature.* 375:682–684. https://doi.org/10.1038/375682a0

Yuste, R., A. Majewska, and K. Holthoff. 2000. From form to function: calcium compartmentalization in dendritic spines. *Nat. Neurosci.* 3: 653–659. https://doi.org/10.1038/76609

Zhou, Q., and M. Sheng. 2013. NMDA receptors in nervous system diseases. *Neuropharmacology.* 74:69–75. https://doi.org/10.1016/j.neuropharm.2013.03.030

Acknowledgement

Chapter 5, in full, is a reprint of the material as it appears in Dendritic spine geometry and spine apparatus organization govern the spatiotemporal dynamics of calcium in Journal of General Physiology, 2019. Bell, Miriam; Bartol, Tom; Sejnowski, Terrence; Rangamani, Padmini, JGP, 2019 [3]. The dissertation author was the primary investigator and author of this material. For Chapter 5, I would like to acknowledge my coauthors Dr. Tom Bartol, Professor Terrence Sejnowski, and Professor Padmini Rangamani. I would like to thank various members of the Rangamani Lab for valuable discussion, Mariam Ordyan for manuscript review, and Professor Brenda Bloodgood and Evan Campbell for their expertise. We thank Professor Pietro De Camilli and his laboratory for supplying images used to construct the mesh seen in Figure 5.5d. I would like to acknowledge my funding from the UCSD Interfaces Graduate Training Program and the San Diego Fellowship, AFOSR Multidisciplinary Research Program of the University Research Initiative (MURI) grant FA9550-18-1-0051 to P.R., and the National Institutes of Health (Grant T32EB009380).

Chapter 6

Stochastic simulations reveal that dendritic spine morphology regulates synaptic plasticity in a deterministic manner

6.1 Introduction

Dendritic spines are small protrusions along the dendrites of neurons that compartmentalize postsynaptic biochemical, electrical, and mechanical responses. These subcompartments house the majority of excitatory synapses and are key for neuronal communication and function [6, 53]. Because of their unique biochemical compartmentation capabilities, spines are thought of as computational units that can modify their synaptic strength through a process called synaptic plasticity [53, 54].

Calcium plays a key role as a second messenger in biochemical and physical modi-

fications during synaptic plasticity, triggering downstream signaling cascades within dendritic spines, and the entire neuron [54–56]. Efforts have also linked calcium levels to synaptic weight change [13, 57–59]. Synaptic weight update refers to the change in the strength of the postsynaptic response in the event of neurotransmitter release from the presynapse. Calcium levels have often been used as an indicator of the early events preceding the complex downstream signaling [12, 13, 60, 61], specifically the modulation of α-amino-3-hydroxy-5-methyl-4-isoxazolepropionic Acid Receptor (AMPAR) density [7], and thus inform the synaptic weight update. An increase in synaptic weight is associated with Long Term Potentiation (LTP), while a decrease in synaptic weight is associated with Long Term Depression (LTD) [62, 63]. While synaptic weight update requires a host of downstream signaling and mechanical interactions, the level of calcium can be thought of as an indicator of synaptic plasticity and weight [13, 64].

Dendritic spines have characteristic sizes and shapes that dynamically change over time in response to stimulus, and are associated with their function and synaptic plasticity [65]. Just as whole cell shape is known to influence signaling dynamics [66–69], studies have specifically probed the interplay between calcium dynamics and dendritic spine morphology [3, 55, 70, 71]. Due to the historical significance of dendritic spines as electrical subcompartments, the morphology of the spine neck has been implicated in regulating calcium signaling and longer spine necks were found to decouple spine-dendrite calcium signaling [72]. Additional modeling work coupled actin-myosin contractions to cytoplasmic flow to identify two timescales of calcium motion, driven by flow and diffusion respectively, that depend on spine geometry [73]. A combined analytical and numerical study showed how geometry and curvature gives rise to pseudo-harmonic functions that can predict the locations of maximum and minimum calcium concentration [70]. More recently, we used a deterministic reaction-diffusion model to investigate dendritic spine morphology and ultra-

structure, and found that dendritic spine volume-to-surface area ratios and the presence of spine apparatus modulate calcium levels [3]. As we have shown before, the natural length scale that emerges for reaction-diffusion systems with boundary conditions that have influx and efflux rates is the volume-to-surface area ratio [66, 70]. What remains unclear is whether the trends from dimensional analysis of deterministic models continue to hold despite the stochastic nature of calcium influx and efflux across the wide range of spine shapes.

Due the small volume of dendritic spines, stochastic calculations are important to gain insight into the spatiotemporal dynamics of spine calcium; there are approximately seven ions of calcium in a resting spine [71, 74]. Due to their probabilistic nature and discrete number, calcium channels and receptors appear to behave stochastically [75–77]. This indicates that the system leans towards stochasticity and it has been suggested that synaptic plasticity itself relies on stochasticity for robustness [75, 78, 79]. In this work, using idealized and realistic spine geometries, we investigate the impact of shape and stochasticity on calcium dynamics and synaptic weight change. We seek to answer the following specific question: How do specific geometric parameters – namely shape and size of dendritic spines – influence calcium dynamics? To address these questions, we built a spatial, stochastic model of calcium dynamics in various dendritic spines geometries. We used idealized geometries to control for various geometric parameters and then extended our calculations to realistic geometries. We probed the influence of spine shape, volume, and volume-to-surface area ratio on calcium influx, variance of calcium dynamics, and the robustness of synaptic weight. We show that although calcium dynamics in individual spines is stochastic, the key readouts from the model, including mean calcium and synaptic weight update, behave deterministically with respect to the variation of geometric parameters.

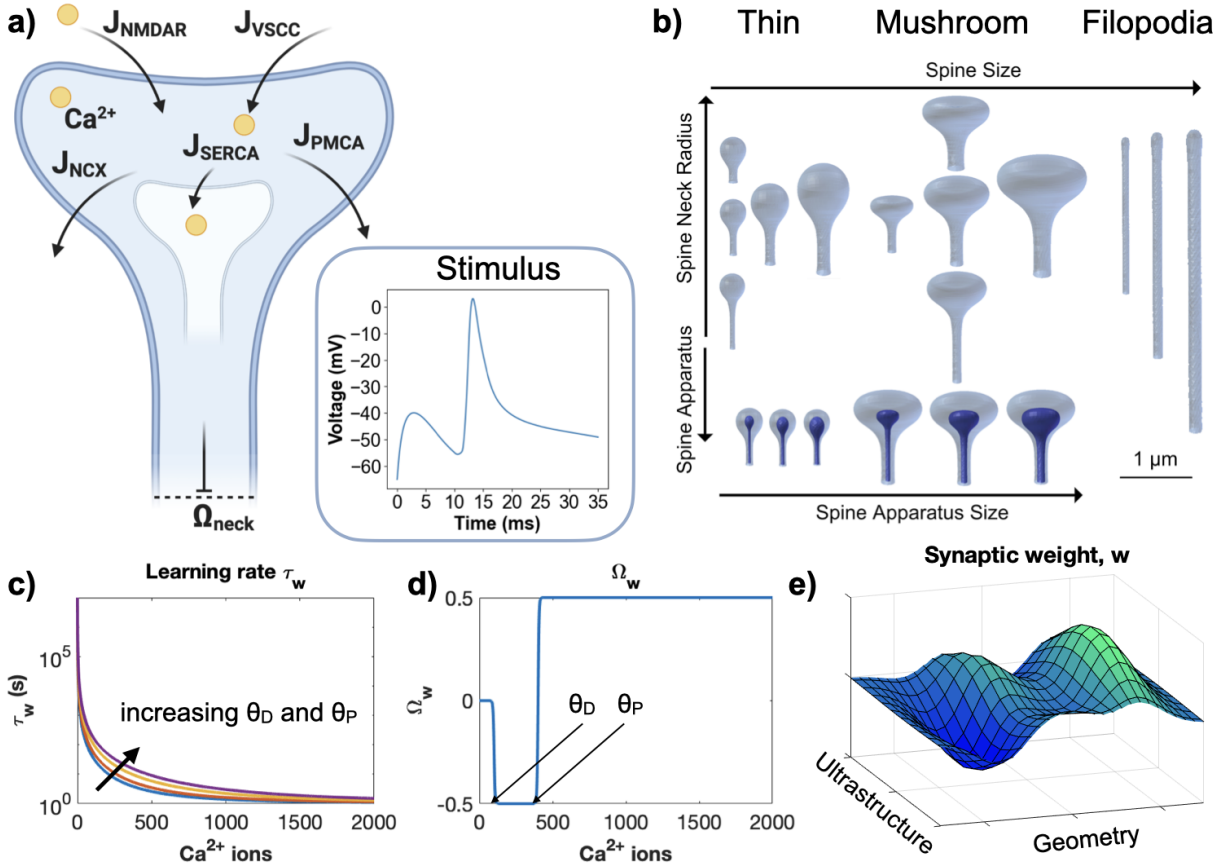

Figure 6.1: **Model overview.** a) Our stochastic model includes calcium influx through NMDAR and VSCC, calcium efflux to the extracellular space through PMCA and NCX pumps, and to the Spine Apparatus through SERCA pumps. Arrows indicate the movement of Ca^{2+} through the labeled pump, channel, or receptor. Ω_{neck} represents the Dirichlet boundary condition at the base of the spine neck, at which the concentration of calcium ions is clamped to zero. Cytosolic calcium is buffered using mobile and immobile calcium buffers. Inset: A change in membrane potential triggered by an excitatory postsynaptic action potential (EPSP) and back propagating action potential (BPAP) acts as the model stimulus. b) The geometric factors considered in our model include spine shape, spine size, neck radius and length, and SpApp size. We investigate three spine shapes: thin, mushroom, and filopodia-shaped. Calcium levels determine the learning rate τ_w, (c), and function Ω_w, (d), that in turn determine synaptic weight, (e). The influence of geometry and ultrastructure on calcium signaling thus has an influence on synaptic weight. θ_D and θ_P represent the thresholds for long term depression and potentiation, respectively. Panel a) was generated using `biorender.com`.

6.2 Results

In this work, we sought to decipher the contributions of spine size and shape to synaptic weight change. We briefly summarize our model development strategy here as shown in Figure 6.1. We conducted stochastic simulations of calcium influx through *N*-methyl-D-aspartate Receptor (NMDAR) and Voltage Sensitive Calcium Channels (VSCCs) based on [71]. The system stimulus is a Excitatory Postsynaptic Potential (EPSP) and Back Propagating Action Potential (BPAP) offset by 10 ms [71]. Calcium ions leave the spine volume through the pumps on the plasma membrane, Plasma Membrane Ca^{2+}-ATPase (PMCA) and Sodium-Calcium Exchanger (NCX), and into the Spine Apparatus (SpApp) (if present) through Sarco/Endoplasmic Reticulum Ca^{2+}-ATPase (SERCA). In addition, the base of the spine neck has a Dirichlet boundary condition of calcium clamped to zero. Mobile and immobile buffers are present in the cytoplasm to reversibly bind calcium, and there is an additional exponential decay throughout the cytoplasm. All simulations were performed using MCell [80–82] to capture the stochastic nature of calcium dynamics in the small spine volumes and each simulation condition was run with 50 random seeds. System configuration and analysis scripts are all available on Github `https://github.com/RangamaniLabUCSD/StochasticSpineSimulations`. Synaptic weight was calculated using an ordinary differential equation dependent on the total number of calcium ions in the cytoplasm at each time point, see supplement of [4].The rate of synaptic weight update depends on a learning rate, τ_w, and a thresholding function, Ω_w, that are both dependent on calcium ion levels, Figure 6.1c-d. We investigate how spine geometry and ultrastructure can influence synaptic weight change (Figure 6.1e). Model geometries were selected as follows: idealized geometries of thin, mushroom, and filopodia-shaped geometries from [27], see supplemental figures in [4].For each geometry, the Postsynaptic Density (PSD) area was set as a fixed proportion of the spine volume. We first investi-

gate whether spine size has any effect on filopodia-shaped spines (Figure 6.2), thin spines (Figure 6.3), and mushroom spines (Figure 6.4). Next we consider the role of spine apparatus (Figure 6.5). Last we test the trends we find in idealized spines on realistic spine geometries (Figure 6.6). Our results predict that synaptic weight change through calcium dynamics is a deterministic function of geometric parameters of the spines (Figure 6.7). We note that our goal is not to provide a function fit but to demonstrate trends. We discuss these results in detail below.

6.2.1 Synaptic weight change depends on spine volume-to-surface ratio in filopodia-shaped spines

We begin our analysis with a simple question – does spine size alter synaptic weight change? To answer this question, we first examined filopodia-shaped spines. Dendritic filopodia are precursors of dendritic spines and serve to bridge the gap between the dendrite and an axon that is passing by during synapse formation [83]. These are highly motile elongated structures that resemble tubules (lengths of 2–20 µm and neck diameters smaller than 0.3 µm). The simplicity of this geometry allows us to focus on the role of size alone in a simple spine geometry. We used spine geometries of three different volumes (0.017, 0.058 and 0.138 μm^3). Simulations revealed that the calcium dynamics in these tubule-shaped spines appeared to follow a 'plug-flow' behavior where at 15 ms, all the calcium is localized to one region (Figure 6.2a). This behavior is because of the narrow geometry of the spine, preventing dispersion of the calcium. Next, we look at the temporal dynamics of calcium and note that the larger spines have larger numbers of calcium ions (Figure 6.2b) but also have a larger variance of calcium ions (Figure 6.2c). We further characterized the dynamics by considering the peak calcium values and decay time constants of the calcium transients versus the spine volume-to-surface area ratio. We chose the volume-to-surface area ratio as

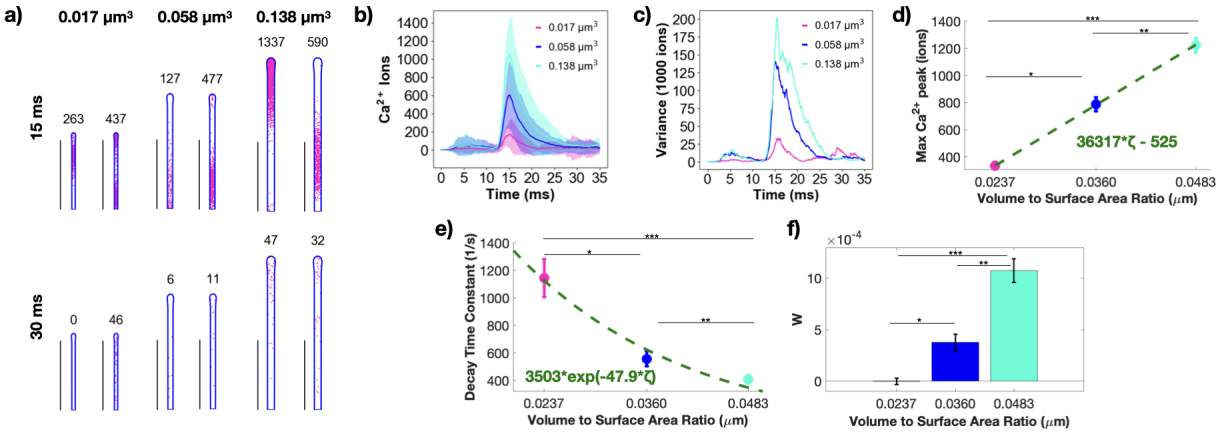

Figure 6.2: **Calcium dynamics and synaptic weight change in filopodia-shaped spines depend on spine size.** a) Spatial plots illustrating Ca^{2+} localization at 15 and 30 ms for filopodia-shaped spines with different volumes (0.017, 0.058 and 0.138 µm^3). The number above each geometry corresponds to the number of Ca^{2+} in that frame. Scale bars: 2 µm. b) Mean (solid) and standard deviation (shaded area) of Ca^{2+} transients across 50 simulations for each of the three filopodia-shaped spine sizes. c) Variance of Ca^{2+} over time. d) The mean and standard error (n=50) of the peak number of Ca^{2+} in different filopodia-shaped spine sizes shows statistically significant differences; p* = 2.0262×10^{-11}; p** = 9.898×10^{-8}; p*** = 4.362×10^{-26} using a two-tailed t-test. We fit the trend in peak Ca^{2+} as a linear function of volume-to-surface area ratio, ζ; $r^2 = 0.5521$ for the linear fit. e) The decay timescales of each Ca^{2+} transient are estimated by fitting with an exponential decay function $c \cdot \exp(-kt)$. The mean and standard error (n=50) of the decay time constant, k, shows statistically significant differences across filopodia-shaped spine sizes; p* = 1.6331×10^{-4}; p** = 0.0209; p*** = 1.3381×10^{-6} from a two-tailed t-test. The mean decay time constants as a function of volume-to-surface area ratio, ζ, was fit with an exponential $a \cdot \exp(-b\zeta)$; $r^2 = 0.203$ for the exponential fit. f) The mean and standard error (n=50) of the calculated synaptic weight change at the last time point in the simulation for all filopodia-shaped spine sizes, plotted against the volume-to-surface area ratio, shows statistically significant differences between all cases; p* = 2.7290×10^{-5}; p** = 2.8626×10^{-6}; p*** = 1.6321×10^{-14} from two-tailed t-test.

a geometric metric of spine morphology because it encompasses both the cytosolic volume through which calcium diffuses and the surface area of the spine membrane through which calcium can enter and leave the system. Additional analyses with respect to spine volume are shown in the supplement of [4].

We note that, indeed, increasing spine size and therefore the volume-to-surface ratio, causes a linearly proportional and significant increase in peak calcium ions (Figure 6.2d). We also found that the decay time of calcium from the peak decreased with increasing volume-to-surface area ratios and satisfied an exponential dependence (Figure 6.2e). As spine size increases, the decay time constant decreases, showing that it takes longer for calcium to clear out of the larger spines and spines with larger volume-to-surface area ratios. Finally, we calculated the synaptic weight change (see Supplemental Section in [4]) and compared this value at 35 ms across volume-to-surface area ratios for the filopodia-shaped spines (Figure 6.2f).We observed that while the smallest spine had no observable weight change presumably because of the net low calcium influx, the weight change increases with increase in spine volume-to-surface-area ratio (Figure 6.2f). Thus, we find that even for a shape as simple as a filopodia-shaped spine, changes in spine volume-to-surface area ratio can dramatically alter calcium dynamics and synaptic weight change even in stochastic conditions suggesting a close coupling between spinogenesis and calcium handling.

6.2.2 Thin and mushroom-shaped spines modulate synaptic weight changes as a function of volume-to-surface area ratio

We next asked if the relationships of spine size and synaptic weight change observed for filopodia-shaped spines (Figure 6.2) also holds for thin and mushroom-shaped spines.

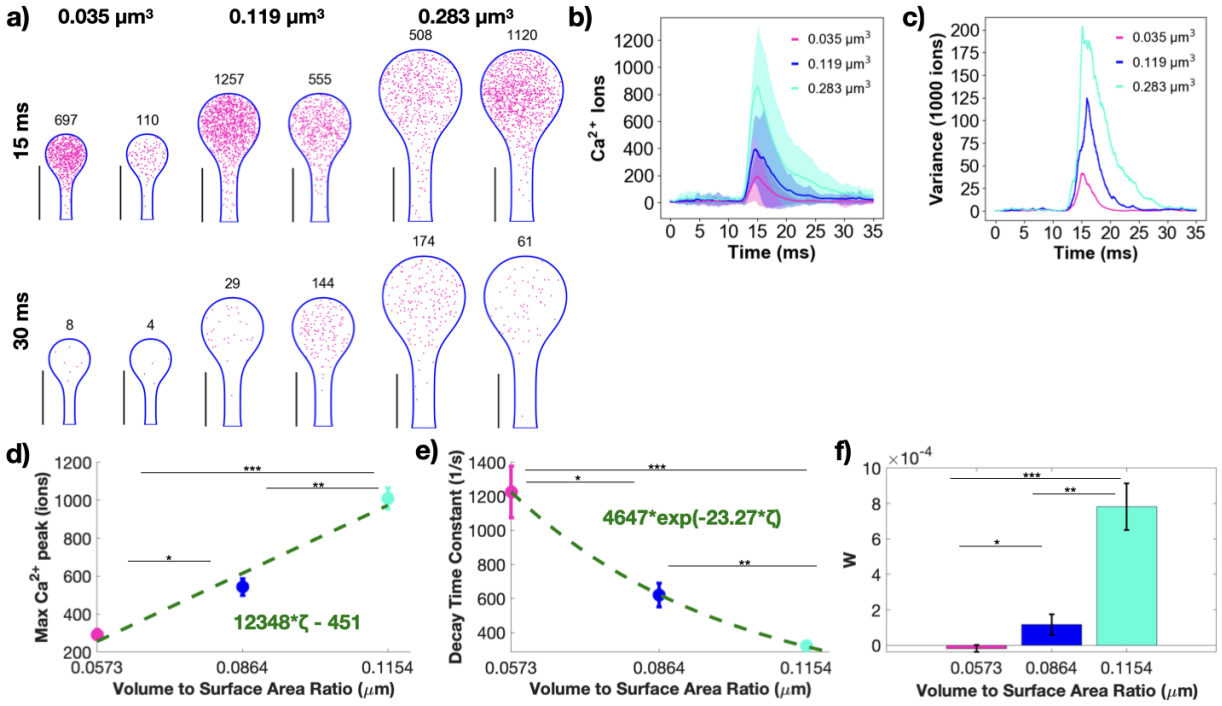

Figure 6.3: **Changing thin spine size modulates calcium dynamics and synaptic weight change.** a) Spatial plots illustrating Ca^{2+} localization at 15 and 30 ms for thin spines with different volumes 0.035, 0.119 and 0.283 µm^3). The number above each geometry corresponds to the number of Ca^{2+} in the frame. Scale bars: 0.5 µm. b) Mean (solid) and standard deviation (shaded area) of Ca^{2+} transients across 50 simulations for each of the three thin spine sizes. c) Variance of Ca^{2+} over time. d) The mean and standard error (n=50) of the peak number of Ca^{2+} in different thin spine sizes shows statistically significant differences; p* = 5.2641×10^{-6}; p** = 2.7377×10^{-9}; p*** = 5.0036×10^{-20} from two-tailed t-test. We fit the trend in peak Ca^{2+} as a linear function of volume-to-surface area ratio, ζ; $r^2 = 0.4676$ for the linear fit. e) The decay timescales of each Ca^{2+} transient are estimated by fitting with an exponential decay function $c \cdot \exp(-kt)$. The mean and standard error (n = 50) of the decay time constant, k, shows statistically significant differences across thin spine sizes; p* = 4.3976×10^{-4}; p** = 1.1541×10^{-4}; p*** = 5.4590×10^{-8} from two-tailed t-test. The mean decay time constants as a function of volume-to-surface area ratio, ζ, was fit with an exponential $a\cdot\exp(-b\zeta)$; $r^2 = 0.2285$ for the exponential fit. f) The mean and standard error (n = 50) of the calculated synaptic weight change at the last time point in the simulation for all thin spine sizes, plotted against the volume-to-surface area ratio, shows statistically significant differences between all cases; p* = 0.0315; p** = 1.0661×10^{-5}; p*** = 2.5751×10^{-8} from two-tailed t-test.

Thin and mushroom-shaped spines emerge from filopodia-shaped spines as spinogenesis progresses [83, 84]. While it has been proposed that spines exist in a continuum of shapes [85], historically it has been useful to categorize spines into specific categories of shapes [34]. Thin spines, with small heads and thin necks, have been classified as 'write-enabled' or learning spines due to their high motility. Mushroom spines, on the other hand, with bulbous heads and relatively wider necks, are termed 'write-protected' or memory spines due to their stability [86]. Thin spines are characterized by a spherical head and we repeated the calcium influx simulations in thin spines of three different volumes (0.035, 0.119 and 0.283 μm^3) that were informed by the ranges found in the literature, Figure 6.3. We observe that, in thin spines, the calcium ions are concentrated in the head at 15 ms but disperse more uniformly by 30 ms (Figure 6.3a).We do not observe a plug-flow like behavior as we did for filopodia-shaped spines likely because of the differences in both shape and volume of the thin spines. Calcium dynamics in thin spines follows the expected temporal dynamics (Figure 6.3b), with larger spines having larger peak calcium and increased time to decay. Larger thin spines also have larger variance in the calcium ion concentration over time (Figure 6.3c). Next, we found that the maximum calcium ions per spine was significantly larger in larger spines with statistically different values for the different sized spines. The peak calcium increased linearly compared to spine volume-to-surface area but with a smaller slope when compared to the filopodia-shaped spines (max peak values in filopodia-shaped spines increased three times faster than those in thin spines), (Figure 6.3d). This suggests that the size dependence of calcium grows slower in thin spines than in filopodia-shaped spines. The decay time also showed an exponential decay in thin spines with increasing volume-to-surface area ratio (Figure 6.3e). The exponent was smaller for thin spines when compared to filopodia-shaped spines (47.9 versus 23.27) suggesting that the decay rate with respect to volume-to-surface area ratio

was slower in thin spines. Finally, the synaptic weight change showed an increase with volume-to-surface area ratio in thin spines (Figure 6.3f) indicating that larger spines are capable of stronger learning outcomes.

Finally, we repeated our analysis for mushroom-shaped spines of increasing volume (0.080, 0.271 and 0.643 μm^3), (Figure 6.4). The effect of the shape of the spines is evident in the spatial dynamics of calcium (Figure 6.4a).Even at 15 ms, we note that while a vast majority of calcium ions are localized in the spine head, there is spillover of calcium into the neck; this is particularly evident in the spines of larger volume in (Figure 6.4a). We further investigated the role of the spine neck in both thin and mushroom spines in the supplement of [4].

The effect of increases in volume, and therefore increases in volume-to-surface area on the temporal dynamics of calcium is an increase in peak calcium (Figure 6.4b,d) and variance (Figure 6.4c), and a decrease in the decay time constant (Figure 6.4e). The synaptic weight change in mushroom spines increases with spine volume-to-surface area and is larger for these mushroom spines than the filopodia-shaped and thin spines (Figure 6.4f). We observe that the peak calcium shows a linear increase with volume-to-surface area ratio with a slope that lies between the thin spines and filopodia-shaped spines. Finally, the decay time constant decreases with spine volume-to-surface area ratio but with a smaller exponential decay when compared to thin spines and filopodia-shaped spines. These two results point to the following conclusions – first, an increase in spine volume results in an increase in critical readouts of synaptic plasticity and second, the shape of the spine alters the quantitative relationships of synaptic plasticity by allowing access to different volume-to-surface area ratios.

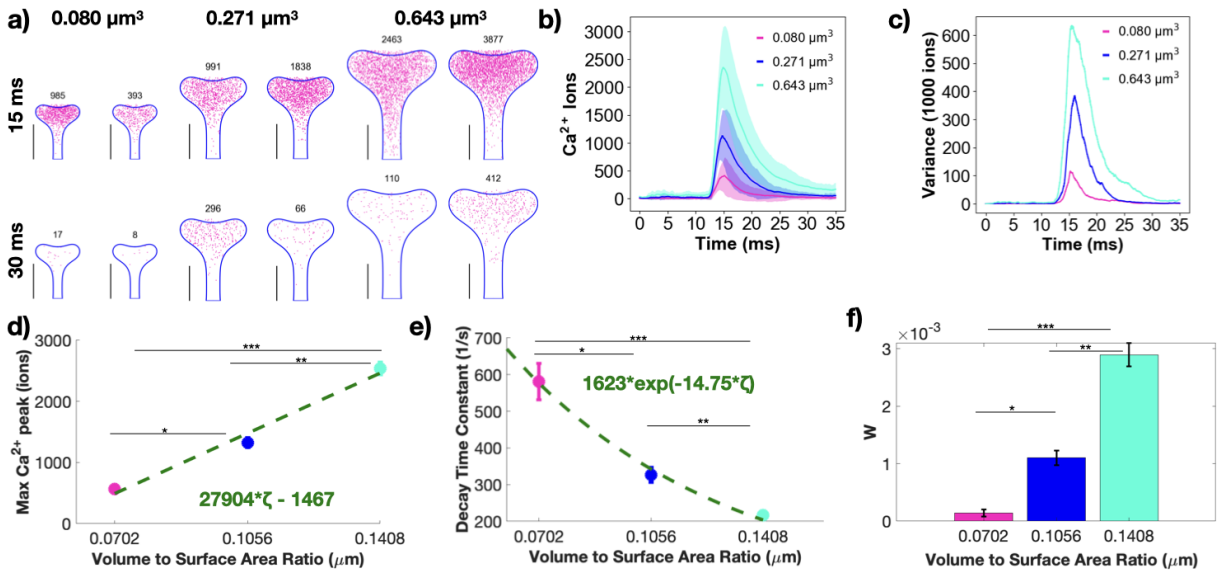

Figure 6.4: **Changing mushroom spine size modulates calcium dynamics and synaptic weight change.** a) Spatial plots illustrating Ca^{2+} localization at 15 and 30 ms for mushroom spines with different volumes (0.080, 0.271 and 0.643 µm^3). The number above each geometry corresponds to the number of Ca^{2+} in the frame. Scale bars: 0.5 µm. b) Mean (solid) and standard deviation (shaded area) of Ca^{2+} transients across 50 simulations for each of the three mushroom spine sizes. c) Variance of Ca^{2+} over time. d) The mean and standard error (n=50) of the peak number of Ca^{2+} in different mushroom spine sizes shows statistically significant differences; p* = 4.1244×10^{-13}; p** = 6.6467×10^{-15}; p*** = 7.8934×10^{-32} from two-tailed t-test. We fit the trend in peak Ca^{2+} as a linear function of volume-to-surface area ratio, ζ; $r^2 = 0.6655$ for the linear fit. e) The decay timescales of each Ca^{2+} transient are estimated by fitting with an exponential decay function $c \cdot \exp(-kt)$. The mean and standard error (n=50) of the decay time constant, k, shows statistically significant differences across mushroom spine sizes; p* = 6.8175×10^{-6}; p** = 6.4075×10^{-6}; p*** = 1.1118×10^{-10} from two-tailed t-test. The mean decay time constants as a function of volume-to-surface area ratio, ζ, was fit with an exponential $a \cdot \exp(-b\zeta)$; $r^2 = 0.3223$ for the exponential fit. f) The mean and standard error (n=50) of the calculated synaptic weight change at the last time point in the simulation for all mushroom spine sizes, plotted against the volume-to-surface area ratio, shows statistically significant differences between all cases; p* = 5.1012×10^{-10}; p** = 2.0097×10^{-11}; p*** = 2.1447×10^{-23} from two-tailed t-test.

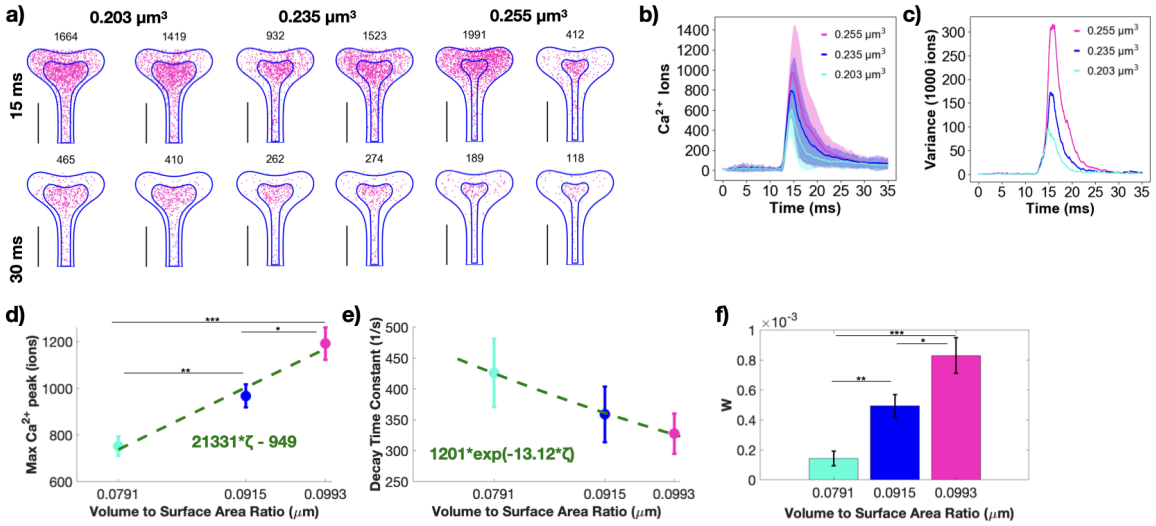

Figure 6.5: **Spine apparatus size modulates synaptic weight change in mushroom spines.** a) Spatial plots at 15 and 30 ms for mushroom spines with spine apparatus of different volumes (net spine volumes of 0.203, 0.235 and 0.255 µm^3). The numbers on top of the shape indicate the total number of calcium ions at that instant in both the spine apparatus and cytoplasm. Scale bars: 0.5 µm. Calcium ions over time as mean and standard deviation (b) and variance (c) for all three mushroom spines with different spine apparatus sizes. Shaded regions in (b) denote standard deviation. d) Peak calcium ion number for each mushroom spine with a spine apparatus, with the mean and standard error (n=50), show statistically significant differences; p* = 0.0101; p** = 0.0010; p*** = 4.0801×10^{-7} from two-tailed t-test. We fit the trend in peak values with a linear function against the volume-to-surface area ratio; r^2=0.1768 for the linear fit. e) We fit the decay dynamics of each calcium transient with $c \cdot \exp(-kt)$ and report the decay time constant, k, as a mean and standard error (n = 50) against volume-to-surface area ratio. The decay time constants were not statistically different. We fit the trend in decay time constants as a function of volume-to-surface area ratio with an exponential $a \cdot \exp(-b\zeta)$, where ζ is the volume-to-surface area ratio; r^2 = 0.0166 for the fit. f) Calculated synaptic weight change mean and standard error (n = 50) at the last time point for all three mushroom spines with spine apparatus show statistically significant differences between all cases; p* = 0.0198; p** = 2.0977×10^{-4}; p*** = 6.0097×10^{-7} from two-tailed t-test.

6.2.3 Spine apparatus size tunes synaptic weight changes by altering the volume-to-surface area relationships

Approximately 14 % of dendritic spines have specialized endoplasmic reticulum called spine apparatus which are preferentially present in larger, mature spines [3, 87, 88]. Furthermore, recent studies have shown that the spine apparatus and the ER are dynamic structures in the dendrite and dendritic spines [89]. Previously, we showed that the spine apparatus modulates calcium transients in deterministic models of calcium influx [3] by altering the net fluxes [70]. Here, we investigate how these relationships are altered in stochastic models in mushroom spines, Figure 6.5 (See [4] for the consideration of thin spines with spine apparatus).When a spine apparatus is present in the spine head, it effectively reduces the volume of the spine cytosol and in the time frame of our consideration, acts as a calcium sink (by the action of the SERCA pumps) [90]. We also varied spine apparatus size in the medium-sized mushroom spine, see Figure 6.5a and supplement of [4].Calcium transients and variance showed much smoother dynamics for the mushroom spines compared to the thin spines, compare Figure 6.5b-c versus figures in the supplement of [4].Peak calcium values were all statistically different for the different spine apparatus sizes and followed a linear relationship with respect to the volume-to-surface area ratio, Figure 6.5d. Decay time constants were fit with an exponential relationship but there were no statistical differences across different spines (Figure 6.5e). All different spine apparatus sizes produce synaptic weight changes that are statistically different, such that increases in spine apparatus size result in smaller spine volume (and smaller volume-to-surface area ratio) and therefore produce smaller weight changes, Figure 6.5f. Thus, the presence of spine apparatus alters the volume-to-surface area ratio for spines and therefore tunes calcium levels and synaptic weight updates in the large mushroom spines with an inverse relationship to the spine apparatus size.

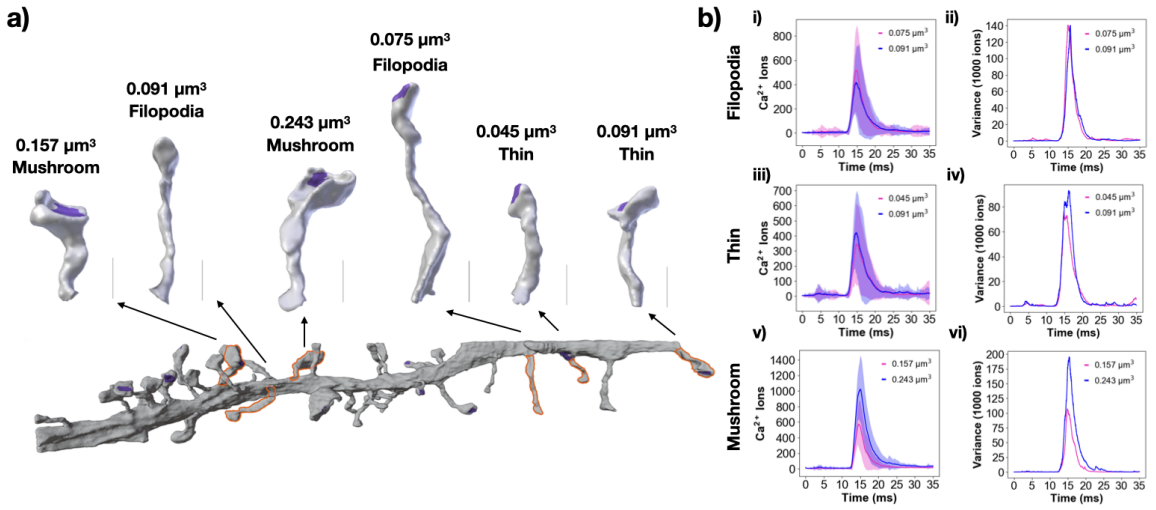

Figure 6.6: **Real spine geometries show size dependence for calcium dynamics.** a) Spines similar to the idealized geometries were selected from a reconstructed dendrite [29]. Representative filopodia-shaped spines, thin spines, and mushroom spines were selected and labelled with their volume and shape. Scale bars: 0.5 µm. b) Calcium transients as means and standard deviation, along with variance over time for the realistic spines of different shapes; i-ii) filopodia-shaped spines, iii-iv) thin spines, and v-vi) mushroom spines. The realistic spines are labeled with their volumes.

6.2.4 Simulations in realistic geometries reveals that synaptic weight change depends on spine volume and volume-to-surface area

Thus far, we focused on idealized geometries of spines, to identify relationships between key synaptic variables and key geometric variables. We found that the peak calcium concentration, decay time constant, and synaptic weight depend on the volume-to-surface area ratio within each shape classification. Do these relationships hold for realistic geometries as well? To answer this question, we selected realistic geometries from mesh models [91] informed by electron micrographs from Wu et al [29].

Realistic spines have more complex geometries that do not fall into the exact morphological categories that we used for idealized spines. To test the significance of these variations, we selected two spines of each shape (thin, mushroom, and filopodia-shaped) and conducted simulations with the exact same parameters as the idealized simulations (Figure 6.6a). We chose realistic geometries that were within the range of sizes of the idealized geometries. The PSDs in the realistic spines were annotated during the segmentation process and no modifications were made to the PSD marked regions. To capture filopodia-shaped protrusions, we selected long, thin spines (with minimal differentiation between the head and neck) that had marked PSD, because we did not include dendritic filopodia in the section. Details on how to use realistic geometries in these simulation modalities can be found in the Supplemental Material.

For filopodia-shaped spines, we found that peak calcium and variance varied with volume but the variance was not appreciably different for the two spines that we used to conduct simulations (Figure 6.6b(i-ii)). The realistic thin spines we chose had volumes similar to the filopodia-shaped spines and they also exhibited calcium dynamics proportional to their volume (Figure 6.6b(iii-iv)).Mushroom spines had larger volumes and larger PSD

areas when compared to the thin or filopodia-shaped spines (Figure 6.6b(v, vi)).Again, the calcium dynamics was proportional to the volume and showed that larger spines have higher peak calcium concentrations. Thus, the relationships of spine geometry and calcium dynamics hold in realistic geometries as well.

6.3 Discussion

Dendritic spines have been studied extensively as biochemical signaling compartments and their role in calcium sequestration has been theorized extensively [3,6,55,70,92–94]. Their unique morphological features and the classification of spine sizes and shapes with respect to function suggests possible structure-function relationships at the level of individual spines. In this work, we used stochastic modeling of calcium transients in dendritic spines of different geometries to understand how spine size and shape affect synaptic weight change. Using a stochastic simulation is important to investigate variance amongst spine shape and size as dendritic spines have small volumes and probabilistic channel dynamics. Using idealized and select realistic geometries we found that geometric properties, specifically, the volume-to-surface area affected key properties of calcium transients including peak calcium, decay time constants, and synaptic weight change. We discuss these findings in the context of different aspects of synaptic plasticity.

Our models predict despite the individual calcium transients being stochastic, there is a predictive deterministic trend that appears to carry through the different sizes and shapes of spines used in our model (Figure 6.7). We highlight that our goal is to demonstrate a trend in the data as opposed to building numerical functions. Although we fit the various data, we note that the r^2 is often weak, indicative of the complexities that underlie such efforts. With this in mind, one of the advantages of our modeling approach here is that we can directly compare across the entire range of idealized and realistic ge-

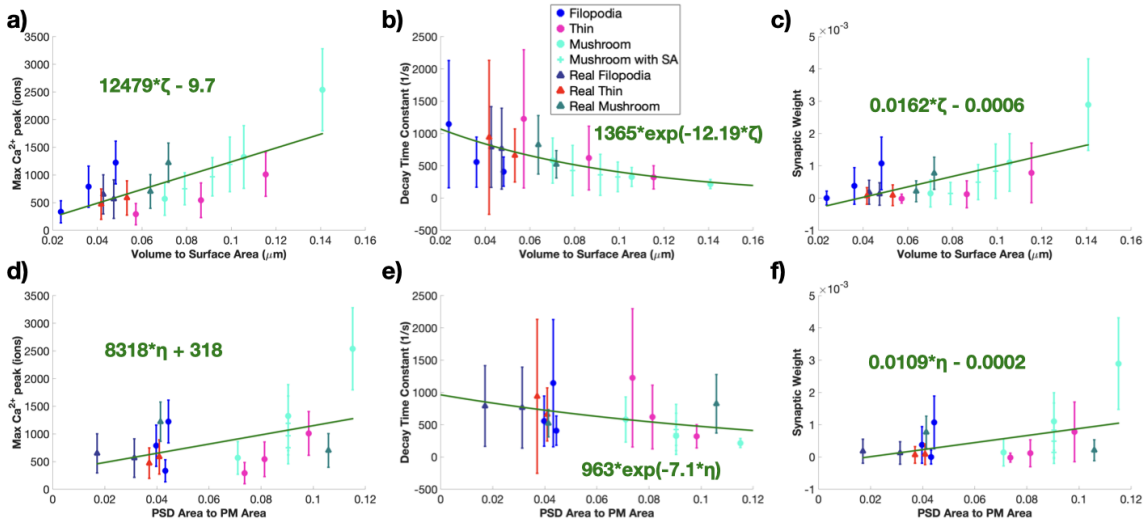

Figure 6.7: **Idealized and realistic spines show overall trends in peak calcium, decay rates, and synaptic weight change with respect to volume-to-surface area ratios.** a) All calcium peaks as mean and standard error (n=50) across volume to surface area ratio show an overall increasing trend. We fit the trend in peak values with a linear function against the volume-to-surface area ratio; $r^2 = 0.351$ for the linear fit. b) We fit the decay dynamics of each calcium transient with $c \cdot \exp(-kt)$ and report the decay time constant, k, as a mean and standard error (n = 50) against volume-to-surface area ratio. We fit the trend in decay time constants as a function of volume-to-surface area ratio with an exponential $a \cdot \exp(-b\zeta)$, where ζ is the volume-to-surface area ratio; $r^2 = 0.1114$ for the fit. c) Calculated synaptic weight change mean and standard error (n = 50) at the last time point for all idealized and realistic spines shows an increasing trend. We fit the trend in synaptic weight change with a linear function against the volume-to-surface area ratio; $r^2 = 0.2815$ for the linear fit. d) All calcium peaks as mean and standard error (n=50) across PSD surface area to plasma membrane surface area ratio show an overall increasing trend. We fit the trend in peak values with a linear function against the PSD-to-surface area ratio; $r^2 = 0.1441$ for the linear fit. e) We fit the decay dynamics of each calcium transient with $c \cdot \exp(-kt)$ and report the decay time constant, k, as a mean and standard error (n = 50) against PSD-to-surface area ratio. We fit the trend in decay time constants as a function of PSD-to-surface area ratio with an exponential $a \cdot \exp(-b\eta)$, where η is the volume-to-surface area ratio; $r^2 = 0.0428$ for the fit. f) Calculated synaptic weight change mean and standard error (n = 50) at the last time point for all idealized and realistic spines shows an increasing trend. We fit the trend in synaptic weight change with a linear function against the PSD-to-surface area ratio; $r^2 = 0.1186$ for the linear fit.

ometries. By considering all the data from our models, for a total of 18 geometries with 50 simulations in each, we find that the peak calcium density is more-or-less linear with the volume-to-surface area ratio (Figure 6.7a). The decay time constant for calcium transients shows an exponential decay for larger volume-to-surface ratios with quite a bit of variability for smaller ratios (Figure 6.7b). And finally, the synaptic weight change increases as volume-to-surface area increases (Figure 6.7c).

In the idealized geometries, the PSD area is a manually-fixed proportion of the spine volume but realistic geometries do not have this artificial constraint. Therefore, we redid our analysis using PSD area-to-surface area ratios (PSD to Plasma Membrane (PM) ratio). We still found the same relationships overall (Figure 6.7d-f) but this time with clustering of data around some ratios. This indicates that the PSD area is an important additional degree of freedom for synaptic weight change that must be considered for interpretation of geometric features and using realistic geometries with boundary markings allows us to investigate this. It is important to note that there is a lot more variability in the smaller volume-to-surface area ratios suggesting the response of smaller spines may be more erratic than larger spines. This feature can work as a double-edged sword – it may provide an advantage during the development of spines or be an disadvantage in the case of loss of spines [95, 96].

Finally, we interpret our predictions in the context of spine shapes. Filopodia are prevalent during early synaptogenesis and can transition into dendritic spines based on synaptic activity [83]. Additionally, various disease states produce modified dendritic spines that appear more like filopodia [97]. The lack of significant weight changes for the smallest filopodia-shaped spine indicates that there is a volume threshold at which filopodia receive enough stimulus trigger synaptic weight change and transition towards more stable, mature dendritic spines. Importantly, the early synaptic weight changes

emphasize how the increase in spine volume changes the weight outcome from LTD to LTP. This increase in synaptic weight emphasizes how an increase in spine size can push a thin spine to transition into a stable, larger mushroom spine.

The difference in peak calcium level, decay dynamics, and synaptic weight changes as different spine shapes are scanned across different sizes can also provide insight on spine shape transitions during development and maturation. Filopodia-shaped spines have larger increases in peak calcium levels and synaptic weight updates and faster decreases in decay time constants as their volume-to-surface area ratios and volumes increase, compared to both thin and mushroom spines; Figure 6.2, Figure 6.3, and Figure 6.4. This suggests that filopodia can very quickly alter their calcium levels, and therefore are well-suited for initially identifying possible synaptic partners and subsequently directing resources to those filopodia that are good candidates to transition to dendritic spines [98]. Once filopodia are established, their linear calcium increase with volume might be unsustainable and might lead to the reduced levels of increase for thin spines of comparable volume-to-surface area (and volume). This suggests that larger stimuli might be necessary to push thin spines towards more excitation, perhaps prevent excessive numbers of thin spines from maturing and leading to resource depletion and excess neural connectivity [99]. Mushroom spines once again show more of an increase in synaptic weight as they increase in volume-to-surface area ratio (and volume) but at volumes shifted from the filopodia-shaped spines, perhaps highlighting their role as key communication hubs [99]. The volume shift seen in mushroom spines versus filopodia-shaped spines might serve to limit the number of mature, highly excitable dendritic spines as both a key neuronal network and resource regulation feature. When the spine apparatus acts as a sink, its presence dampens synaptic weight changes in mushroom spines, potentially acting to stabilize the spine from future changes as suggested by others [86, 100].

We note that our study is only a small piece of the puzzle with respect to synaptic plasticity. For instance, whether one should use total number of calcium ions or use calcium concentration in evaluating synaptic weight change requires additional exploration. For instance, we find that when calcium results are converted from total ions to average concentration along with the phenomenological synaptic weight equations, we get different trends in synaptic weight update results, see Supplement of [4].However, converting our previous results [3] into total ions shows the same trends for max Ca^{2+} peak and decay time constants as this current study, see Supplement of [4].Thus, a simple unit issue can lead to conflicting results in spatial models and indicates that we need further discussion and investigation on the structure of phenomenological equations for synaptic weight to understand which factors of calcium dynamics matter and to what degree. An additional limitation of this study is the usage of traditional p-values for statistical analysis of the data (see Supplement of [4] for details on h and p-values), since the statistics field has suggested moving away from null-hypothesis significance testing [101]. We also note that our current focus is on very early events and these models must be extended to longer time scale events to explore the biochemical and geometric interplay for downstream signaling [102–105].

In summary, our computational models using idealized and realistic geometries of dendritic spines have identified potential relationships between spine geometry and synaptic weight change that emerge despite the inherent stochasticity of calcium transients. The advances in computational modeling and techniques have set the stage for a detailed exploration of biophysical processes in dendritic spines [11, 102, 106]. Such efforts are critical for identifying emergent properties of systems behavior and also eliminating hypotheses that are physically infeasible [1, 107]. Models such as this and others can set the stage for investigating longer time scale events in spines including the downstream effectors of calcium [64, 103, 108, 109], and actin remodeling for structural plasticity [23, 28].

6.4 Methods

We constructed a system of stochastic partial differential equations to describe calcium dynamics in the postsynaptic spine following glutamate release from the presynaptic terminal. The signaling model was developed from prior art from Refs. [3, 71]. The equations for estimating synaptic weight update were modified from Refs. [13, 100]. Simulations were carried out in MCell [80, 81] and analyzed in MATLAB. Idealized dendritic spine geometries were adapted from geometries obtained from the mechanical equilibrium of membranes described by thin-shell mechanics in Ref. [27]. Electron microscopy images taken from [29] were meshed and curated using techniques from [91] to generate realistic dendritic spine geometries. Additional details regarding the signaling model, simulation parameters, and analysis can be found in the Supplement of [4].

6.5 Acknowledgements

Chapter 6, in full, is a reprint of the submitted material Stochastic simulations reveal that dendritic spine morphology regulates synaptic plasticity in a deterministic manner, 2021. Holst, Maven; Bell, Miriam; Lee, Christopher T.; Rangamani, Padmini, 2021 [4]. The dissertation author was the co-primary investigator and co-author of this material. For Chapter 6, I would like to acknowledge my coauthors Maven Holst, Dr. Christopher T. Lee, and Professor Padmini Rangamani. I would like to acknowledge my funding from a National Defense Science and Engineering Graduate (NDSEG) Fellowship.

Chapter 7

Crosstalk between biochemical signaling & trafficking governs AMPAR dynamics in synaptic plasticity

Introduction

A vast majority of the excitatory postsynaptic sites of synapses are housed in dendritic spines. Dendritic spines are small protrusions, 0.01 to 0.8 µm^3 in volume, along the dendrites of neurons and act as signaling subcompartments, generating biochemical, electrical, and mechanical responses in response to stimuli from the presynaptic terminal [6]. Despite their small size, dendritic spines undergo complex biochemical signal transduction, spanning multiple timescales and pathways involving many protein kinases and phosphatases [93,110]. Integration of these different pathways into a readout for learn-

ing and memory formation is the basis of synaptic plasticity, which refers to the ability of a synapse to regulate its connection strength through both biochemical and structural components [93].

A widely accepted and functional readout of synaptic plasticity is the density of the glutamatergic receptor, AMPAR (α -amino-3-hydroxy-5-methyl-4-isoxazolepropionic acid receptor), at the postsynaptic density (PSD) on the spine head [10]. Due to the importance of AMPAR for proper synaptic plasticity and neural function, dysregulation in either the underlying biochemical signaling or trafficking mechanisms of AMPAR can lead to severe consequences on learning, memory formation, and neural function, see Figure 7.1a.

Even though the processes associated with accumulation of AMPAR at the PSD are quite complex, to understand the events leading to the modification of AMPAR density on the spine head, we first provide a brief summary of the upstream signaling events organized by timescales, see Figure 7.1b for a schematic of these event timescales. The timescale of AMPAR increase/decrease at PSD after a stimulus varies from 10s [110–112] to a longer timescale of 60 minutes associated with long-term potentiation/depression (LTP/LTD) [24, 113, 114]. The main events occurring within these timescales are listed below.

- In response to a glutamate release event coupled with a voltage stimulus (primarily, an excitatory postsynaptic potential (EPSP) and a backpropagating action potential (BPAP)), N-methyl-D-aspartate receptors (NMDAR) and voltage sensitive calcium channels (VSCC) open on the spine membrane, resulting in an influx of Ca^{2+} into the spine. Calcium influx into the spine is the first step in numerous different signaling pathways important for synaptic function and from a modeling perspective is one of the most studied event in spines [11, 70, 71, 100, 102, 115, 116]. This voltage depolarization and subsequent calcium influx occurs over the millisecond timescale

and is the fastest timescale considered in our model.

- Cytosolic Ca^{2+} rapidly binds a variety of different species over the millisecond to second timescale, notably calmodulin (CaM) [117], which in turn triggers various kinases and phosphatases including Calcium/calmodulin-dependent protein kinase II (CaMKII) and protein phosphatase 1 (PP1) [103,110,118]. Free cytosolic Ca^{2+} is also bound to various calcium buffers both in the cytoplasm and located on the membrane [115,119]. CaM additionally binds to scaffolding proteins such as neurogranin (Ng) which impacts the available CaM for CaMKII activation [109].

- CaMKII is one of the most abundant proteins in the brain and its dynamics are vital for neural processes like synaptic plasticity, specifically LTP and LTD [14,15]. CaMKII is known to increase the exocytosis rate of AMPAR to the surface of the spine head [112], promoting the idea that it is a molecular marker of memory [120, 121]. CaMKII is activated rapidly by Ca^{2+}-bound CaM but its activity can remain elevated in the minute timescale due to its autophosphorylation dynamics (discussed more below) [122,123]. CaMKII is also known to deactivate different phosphatases, including PP1 [124,125]. In light of the critical role played by CaMKII in synaptic plasticity, a brief history of modeling is warranted.

  In [126], the idea that CaMKII activation exhibited bistability was proposed as a model to explain the long-time activation of CaMKII even after the stimulus was removed. In particular, [110] proposed a bistable model that included mutual inhibition and autoactivation of CaMKII and PP1 through Michaelis-Menten style dynamics [110,126–128], see Figure 7.1c for a model of these bistable dynamics. This achieved multiple steady states of CaMKII and PP1 dependent on the level of Ca^{2+} input. While this system provided a switch that was protected from stochastic fluctuations and provided sustained CaMKII activity to model either LTP or

LTD, experiments at the time only showed transient CaMKII activity [122, 129] and failed to find a hysteresis in the CaMKII-PP1 system [130, 131]. However, more recently, [132] experimentally showed the presence of CaMKII-PP1 hysteresis and bistability within individual holoenzymes in the presence of an NMDAR-derived peptide. They concluded that the CaMKII-PP1 system can act as a memory switch with bistability but only in the presence of NMDAR [132]. Other experiments showed that the observed bistability features required higher than relevant concentrations of Ca^{2+} suggesting that (a) bistability could exist at basal conditions if there are additional, currently unknown, signaling interactions that alter CaMKII dynamics [131], or (b) bistability might exist within localized domains such as within the PSD versus the spine cytoplasm [133], or (c) the observed hysteresis is not from true bistable dynamics but rather just a delayed return to a monostable state [132], which was supported by other models [134].

The temporal dynamics of CaMKII have also been extensively investigated experimentally. CaMKII was initially thought to have sustained activation because of its elevated levels following a brief stimulus and the necessity of CaMKII autophosphorylation for LTP [135]. However, more recent experiments show that CaMKII activation is actually transient and that LTP is associated with only transient CaMKII activity [129], see Figure 7.1d for a model of transient CaMKII and PP1 dynamics. Experimentally measured CaMKII dynamics are often fit with a biexponential decay with a fast and slow timescale [136]. While phosphastases are known to be involved in CaMKII inactivation, it was shown that phosphatases do not affect the fast decay dynamics of CaMKII [136]. Recently, we developed a multiscale model of CaMKII activation that considered monomer kinetics and holoenzyme kinetics and showed that CaMKII acts as a leaky integrator of Ca^{2+} pulses in the presence of Ng and

PP1 [109], as seen experimentally in sLTP [137]. Another model also suggests that CaMKII is a leaky integrator of Ca^{2+} when in a PP1-rich environment [133].

- In addition to CaMKII, different phosphatases are also activated by Ca^{2+}-bound CaM and play important roles in signaling control loops for synaptic plasticity [124, 130, 138]. PP1 in particular is enriched in dendritic spines and is implicated in the regulation of LTD [118, 138, 139] and its activation is thought to increase the rate of endocytosis of AMPAR [126, 140]. PP1 has been hypothesized to deactivate CaMKII [124]; CaMKII is ultrasensitive in the presence of phosphatases and CaMKII within PSD was mainly dephosphorylated by PP1 [118]. Inhibiting protein phosphatases could convert short-term potentiation (STD) induced by exposure to K^+ into LTP [129].

- CaMKII and PP1 influence AMPAR dynamics at the PSD by regulating exocytosis to the membrane and endocytosis from the membrane, respectively [140]. Specifically when CaMKII levels are high, AMPAR trafficking to the PSD is increased through exocytosis [141] and these conditions support the induction of LTP [121]. In contrast, when PP1 dominates the system, AMPAR density at the PSD decreases through endocytosis, supporting the induction of LTD [118, 142, 143]. Beyond endo- and exocytosis, there are other sources of AMPAR that can interact with AMPAR at the PSD. Pools of AMPAR exist on both the perisynaptic region and extrasynaptic regions both in the spine and on the dendrite, and laterally diffuse across the membrane into the PSD [25]. Synaptic activity, particularly CaMKII activation, can trigger movement of these AMPAR sources into the dendritic spine and towards the PSD region [15, 16, 144]. Therefore, AMPAR dynamics during this early synaptic plasticity phase occur over the 5-10 minute timescale [103]. Retention of the AMPAR at the PSD can occur through scaffolding molecules. TARPS (e.g. stargazin)

binds to AMPAR very early on in the AMPAR lifecycle [16]. AMPAR also binds to scaffolding proteins, such as PSD95, to form bound AMPAR and this binding interaction plays a key role in determining AMPAR dynamics and localization in the PSD [14, 145].

Given the complexity of AMPAR density at the PSD, we seek to answer the following questions using computational modeling. How do the timescales of upstream biochemical signaling affect AMPAR dynamics? Specifically, how does the choice of biochemical signaling (bistable versus monostable model, Figure 7.1c versus d) of CaMKII/PP1 influence bound AMPAR dynamics? What is the role played by the trafficking modalities and influx of AMPAR on these dynamics? And finally, how do these response change with frequency of stimulus? To answer these questions, we developed a system of coupled compartmental ordinary differential equations. While we fully acknowledge that our model makes significant simplifications of the complex signaling processes [103], our focus is on understanding how these different timescales and contributions play an important role, see Figure 7.1. Using this model, we demonstrate that AMPAR dynamics depends in an expected manner on upstream signaling but unexpectedly on trafficking.

Model development

To study the dynamics of AMPAR during synaptic plasticity, we constructed a system of compartmental deterministic ordinary differential equations (ODEs) that describes the influx of calcium, activation of CaMKII and PP1, and AMPAR dynamics on the membrane. We note that the pathways involved are quite complex and we make simplifying assumptions to probe the timescales of AMPAR dynamics on the membrane. Here we list these model assumptions, describe the key components of the model, and provide the governing equations.

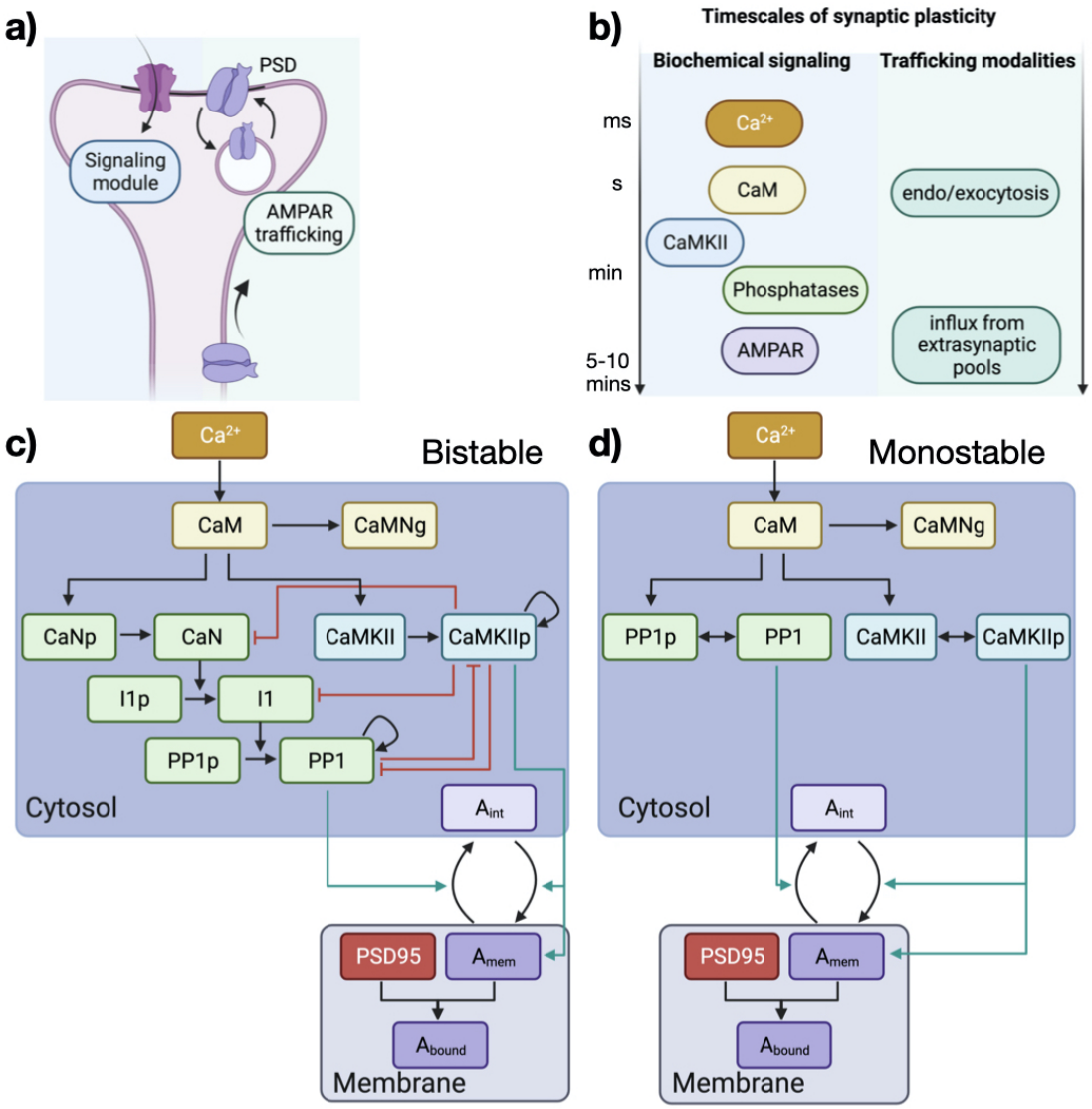

Figure 7.1: Schematic of AMPAR signaling and trafficking. a) AMPAR dynamics depend on a combination of signaling dynamics triggered through synaptic communication and movement of AMPAR through different trafficking mechanisms. b) Synaptic plasticity and specifically AMPAR modifications span several timescales from fast calcium influx to receptor trafficking into the dendritic spine. Although the signaling underlying synaptic plasticity is very complex, here we present two simplified biochemical signaling pathways to investigate the effects of both biochemical and trafficking variations on bound AMPAR at the PSD. The bistable model (c) and monostable model (d) represent two different mathematical formulations to describe how CaMKII and PP1 interact in dendritic spines. Black lines represent activation, red lines represent inhibition, and teal lines highlight biochemical influences on trafficking mechanisms. Made with Biorender.com.

Model assumptions

- **Compartments:** We model a dendritic spine in the hippocampus as an two compartment system with a cytoplasm and plasma membrane. The cytoplasm has a volume of 0.06 μm^3 based on the average dendritic spine volume [115, 146, 147]. The plasma membrane has a surface area of 0.8 μm^2, which is the approximately surface area for an idealized spherical spine with a volume of 0.06 μm^3 [115]. When converting between the volumetric cytoplasm and 2D plasma membrane compartments, we use a length scale conversion (n) of 0.1011 µm to convert units [148]. All species are well mixed within their compartment. We model the spine as an isolated compartment besides the initial Ca^{2+} influx and the influx of CaMKII-dependent membrane AMPAR [54, 122].

- **Timescales:** We focus on AMPAR dynamics associated with synaptic plasticity on the 10 minute timescale [103].

- **Reaction types:** A vast majority of the reactions are modeled as either mass action dynamics or enzymatic Hill function reactions (See Tables 7.1, 7.2, 7.3, 7.4, 7.5, 7.6). Several components, including the dynamics of NMDAR and VSCC, are custom equations that describe how their activation depends on voltage [57, 115]. AMPAR endocytosis and exocytosis are taken as modified mass action dynamics with additional dependence on activated CaMKII and PP1 [110, 126]. AMPAR influx from extrasynaptic pools outside of the dendritic spine is modeled as a time-dependent and activated CaMKII-dependent process to represent activity-dependent diffusion of membrane AMPAR into the system [144,149]. This AMPAR influx term means that the system does not have mass conservation for the membrane AMPAR (Amem) species.

- **Kinetic parameters:** Reaction rates were taken from previous studies [115, 124] or approximately fit to experimental data. In particular, the rates for CaMKII and PP1 decay dynamics for the monostable model were fit to experimental data [116,136,137], see Figure 7.2j-k.

Key components

The goal of this model is to investigate AMPAR dynamics during spine activation and the key upstream kinase and phosphatase activity. We highlight the key model components below.

- **Stimulus and Ca^{2+} influx:** We simulate the activation of a dendritic spine due to voltage depolarization so the model stimulus is a time dependence voltage profile representing an EPSP and a BPAP offset by 2 ms [115]. The voltage depolarization is assumed to accompany a glutamate release, such that both NMDARs and VSCCs are activated, allowing for calcium influx into the spine. We do not explicitly model the glutamate release from the presynapse or the diffusion of glutamate in the extracellular space. We also do not explicitly model extracellular calcium, as we assume it has such a high concentration that the calcium influx into the dendritic spine has negligible effects [115]. After Ca^{2+} floods into the spine through NMDAR and VSCC, it is pumped out of the spine through PM Ca^{2+}-ATPase (PMCA) pumps and sodium–calcium exchanger (NCX) pumps [115]. Ca^{2+} influx into the spine is also rapidly buffered by downstream signaling species, and here we explicitly model Ca^{2+} binding to Calmodulin (CaM) [124]. We do not consider additional buffers here due to explicit modeling of binding to CaM.

- **Calmodulin activation:** Calmodulin (CaM) is quickly bound to Ca^{2+} in dendritic spines and we simplify Ca^{2+}/CaM binding in a single mass action equation. We

note that Ca^{2+}/CaM binding is a multistate process with different intermediates [105,109]; we simplify the process to focus on key timescales of CaM. We denote the activated CaM complex (CaM bound to 4 Ca^{2+}, $Ca^{2+}{}_4$CaM) as Ca^{2+}CaM.

- **Activation of downstream components by calmodulin:** CaM acts as a key propagating signal by binding with the scaffolding protein neurogranin (Ng) [109], and activated CaM activates both CaMKII and the phosphatase cascade [124].

- **CaMKII and phosphatase dynamics:** We investigate two different models for CaMKII and phosphatase dynamics, shown in Fig. 7.1c and d.

  - **Bistable model:** In the bistable model, activated CaM triggers the phosphorylation of CaMKII, which can then autophosphorylate itself [110,124,127,150]. Activated CaM triggers the dephosphorylation of calneurin (CaN), which is the first step in a phosphatase cascade involving inhibitor-1 (I1) and PP1, where CaN activates I1 and I1 activates PP1 [124,151], see Supplemental Material for a comment on I1. Activated PP1 can then autodephosphorylate itself [124,152]. Active CaMKII can deactivate each of the active phosphatases. Activated PP1 can dephosphorylate CaMKII, while activated CaMKII can phosphorylate PP1, so the active species of both CaMKII and PP1 deactivate the other species [132,152]. We refer to this model as the bistable model because this system can achieve different steady state behavior of CaMKII and PP1 dependent on different stimulus, initial conditions, and other factors [110].

  - **Monostable model:** In the monostable model, activated CaM triggers the phosphorylation of CaMKII, but CaMKII deactivates over time proportionally to its activated concentration [122,153]. Similarly, activated CaM triggers the activation of PP1, which then decays to its inactive state proportionally to its

active concentration. We refer to this model as the monostable model because the rate of decrease for both active CaMKII and active PP1 is linearly proportional to their concentrations and therefore only produce a single steady state.

- **AMPAR trafficking and signaling:** AMPAR is a membrane-bound protein; it is located on the plasma membrane and on endosomal membranes, and undergoes both basal and activity dependent endocytosis and exocytosis [154, 155]. In our model, we incorporate CaMKII-dependent exocytosis [141] and PP1-dependent endocytosis [110]. AMPARs also diffuses into the spine in response to CaMKII activity through lateral membrane diffusion from extrasynaptic pools on the dendrite [25,141]. On the membrane, AMPAR binds to scaffolding proteins, such as PSD95, to stabilize at the PSD [156]. We assume that there is a pool of PSD95 available to bind with membrane AMPAR. This bound AMPAR/PSD95 complex, denoted as bound AMPAR, is the model readout.

Governing equations

We construct a compartmental system of ordinary differential equations that represent signaling species in the two different compartments, the cytoplasm and the plasma membrane. The temporal dynamics of each signaling species, c_i, is given by

$$\frac{dc_i}{dt} = R_i, \tag{7.1}$$

where R_i represents the net flux of the species i. The reactions governing the dynamics of each species are the sum of sources and sinks such that $R_i = R_{i,source} - R_{i,sink}$. For membrane AMPAR, this coupled system can be understood through a series of CaMKII and

PP1 dependent sources and sinks for AMPAR on the membrane. Unbound AMPAR on the membrane increases through CaMKII-dependent exocytosis and influx, and decreases through PP1-dependent endocytosis. Free AMPAR on the membrane can bind to scaffolding proteins such as PSD95 to become bound in the PSD region. As mentioned above, the exact dynamics of CaMKII and phosphatase cascades in dendritic spines remain unknown. How those CaMKII and phosphastase dynamics in turn then affect AMPAR dynamics is also unclear.

The various species and their reactions can be found in Tables 7.1, 7.2, and 7.3 for the bistable model, and Tables 7.4, 7.5, and 7.6 for the monostable model.

Variations of different parameters

To investigate the role of upstream kinase and phosphatase cascades on AMPAR dynamics, we compare two different signaling networks – the bistable and monostable models described above. Additionally, due to the coupling of CaMKII and PP1 and their opposing effects on AMPAR, we also varied the initial conditions of CaMKII and PP1, specifically their inactive species' initial condition. This initial concentration variation is meant to represent variations in spine size along with different cytosolic conditions such as variations that occur after synaptic activation or in different regions such as the PSD. Next, we vary the relative contributions of endocytosis/exocytosis and AMPAR influx to investigate the role of signaling on different trafficking mechanisms. This variation of trafficking also accounts for differences in dendritic spine geometry, such as differences in spine surface area and volume that would influence speed or magnitude of the trafficking mechanism. We also specifically vary the contributions of endocytosis and exocytosis separately in two different manners - 1. where we scale the contributions of the activity dependent terms, and 2. where we scale the contributions of the whole endocytosis and

Table 7.1: **AMPAR pathway reactions, reaction types, and reaction rates used in the bistable model**

	List of Reactions	Reaction Type	Reaction Rate
Module 0:	Ca^{2+} Influx		
0	$Ca^{2+}_{ECS} \rightleftharpoons Ca^{2+}_{cyto}$	Custom[0]	$R_0 = J_{influx} - J_{efflux}$
Module 1:	Ca^{2+}/CaM Complex Formation		
1	$3\,Ca^{2+} + CaM \underset{kb1}{\overset{kf1}{\rightleftharpoons}} Ca^{2+}CaM$	MA[1]	$R_1 = k_{f1}[Ca^{2+}]^3[CaM] - k_{b1}[Ca^{2+}CaM]$
Module 2:	CaM/Ng Complex Formation		
2	$CaM + Ng \underset{kb2}{\overset{kf2}{\rightleftharpoons}} CaMNg$	MA	$R_2 = k_{f2}[CaM][Ng] - k_{b2}[CaMNg]$
Module 3:	CaMKII activation and deactivation		
3	$CaMKII + \mathbf{Ca^{2+}CaM} \xrightarrow{Kcat3} CaMKIIp$	CB[2,3]	$R_3 = \frac{K_{cat3}[Ca^{2+}CaM]^4[CaMKII]}{K^4_{m3}+[Ca^{2+}CaM]^4}$
4	$CaMKII + \mathbf{CaMKIIp} \xrightarrow{Kcat4} CaMKIIp$	CB	$R_4 = \frac{K_{cat4}[CaMKIIp][CaMKII]}{K_{m4}+[CaMKII]}$
5	$CaMKIIp + \mathbf{PP1} \xrightarrow{Kcat5} CaMKII$	CB	$R_5 = \frac{K_{cat5}[PP1][CaMKIIp]}{K_{m5}+[CaMKIIp]}$
Module 4:	Phosphatase cascade activation and deactivation		
6	$CaNp + \mathbf{Ca^{2+}CaM} \xrightarrow{Kcat6} CaN$	CB	$R_6 = \frac{K_{cat6}[Ca^{2+}CaM]^4[CaNp]}{K^4_{m6}+[Ca^{2+}CaM]^4}$
7	$CaN + \mathbf{CaMKIIp} \xrightarrow{Kcat7} CaNp$	CB	$R_7 = \frac{K_{cat7}[CaMKIIp][CaMKII]}{K_{m7}+[CaMKII]}$
8	$I1p + \mathbf{CaN} \xrightarrow{Kcat8} I1$	CB	$R_8 = \frac{K_{cat8}[CaN][I1p]}{K_{m8}+[I1p]}$
9	$I1 + \mathbf{CaMKIIp} \xrightarrow{Kcat9} I1p$	CB	$R_9 = \frac{K_{cat9}[CaMKIIp][I1]}{K_{m9}+[I1]}$
10	$PP1p + \mathbf{I1} \xrightarrow{Kcat10} PP1$	CB	$R_{10} = \frac{K_{cat10}[I1][PP1p]}{K_{m10}+[PP1p]}$
11	$PP1p + \mathbf{PP1} \xrightarrow{Kcat11} PP1$	CB	$R_{11} = \frac{K_{cat11}[PP1][PP1p]}{K_{m11}+[PP1p]}$
12	$PP1 + \mathbf{CaMKIIp} \xrightarrow{Kcat12} PP1p$	CB	$R_{12} = \frac{K_{cat12}[CaMKIIp][PP1]}{K_{m12}+[PP1]}$
Module 5:	AMPAR trafficking		
13	$Aint \underset{kb13(PP1)}{\overset{kf13(CaMKIIp)}{\rightleftharpoons}} Amem$	MA	$R_{13} = (c_1[CaMKIIp] + c_3)[Aint] - (c_2[PP1] + c_4)[Amem]$
14	$\varnothing \xrightarrow{kf14(CaMKIIp)} Amem$	Custom[4]	$R_{14} = (k_{f14}(t)[CaMKIIp])$
Module 6:	AMPAR/Scaffolding Complex		
15	$Amem + PSD95 \underset{kb15}{\overset{kf15}{\rightleftharpoons}} ABound$	MA	$R_{15} = k_{f15}[Amem][PSD95] - k_{b15}[ABound]$

1 [0] Custom taken from [115]: see Supplemental material for details. $J_{influx} = J_{NMDAR} + J_{VSCC} + J_{leak}$ and $J_{efflux} = J_{PMCA} + J_{NCX}$.; [1] MA: Mass Action; [2] CB: Cooperative Binding; [3] Enzyme is in bold type. [4] Custom is given in Supplemental material.

exocytosis terms. These trafficking variations can represent disease states where AMPAR influx, or endocytosis and exocytosis are hindered or upregulated. Finally, we vary the model stimulus by supplying active CaM pulses of different frequencies and magnitudes.

Table 7.2: **Reaction parameters calculated for the bistable model**

Reaction rate	$\mathbf{k_f}$	unit	$\mathbf{k_b}$	unit	$\mathbf{K_{cat}}$	unit	$\mathbf{K_m}$	unit	$\mathbf{K_r}$	unit
R_1	7.75	$\mu M^{-3} \cdot s^{-1}$	1	s^{-1}	-	-	-	-	-	-
R_2	5	$\mu M^{1} \cdot s^{-1}$	1	s^{-1}	-	-	-	-	-	-
R_3	-	-	-	-	120	s^{-1}	4	µM	-	-
R_4	-	-	-	-	1	s^{-1}	10	µM	-	-
R_5	-	-	-	-	15	s^{-1}	3	µM	-	-
R_6	-	-	-	-	127	s^{-1}	0.34	µM	-	-
R_7	-	-	-	-	0.34	s^{-1}	127	µM	-	-
R_8	-	-	-	-	0.034	s^{-1}	4.97	µM	-	-
R_9	-	-	-	-	0.0688	s^{-1}	127	µM	-	-
R_{10}	-	-	-	-	50	s^{-1}	80	µM	-	-
R_{11}	-	-	-	-	2	s^{-1}	80	µM	-	-
R_{12}	-	-	-	-	0.07166	s^{-1}	4.97	µM	-	-
R^{*}_{13}	1,6	$\mu M^{-1} \cdot s^{-1}$, s^{-1}	1,8	$\mu M^{-1} \cdot s^{-1}$, s^{-1}	-	-	-	-	-	-
R^{**}_{14}	-	-	-	-	-	-	-	-	-	-
R_{15}	0.0349	$\mu m^2 \cdot molecules^{-1} \cdot s^{-1}$	1	s^{-1}	-	-	-	-	-	-

1 * This reaction represents a membrane flux so there is a reaction between species of different compartments. The units here represent the base reaction without unit conversion between species. Please see Supplemental material for more detail.

2 ** This reaction represents a CaMKIIp-dependent influx of membrane AMPAR and is a custom reaction. Please see Supplemental material for more detail on this reaction and R_0.

Numerical methods

The system of deterministic ordinary differential equations was coded and solved in MATLAB R2018b and R2020b. The solver ode23s was used for all numerical simulations. The model was run for 500 s with outputs every 0.01 s. Time stepping was set up automatically in MATLAB. Time-to-peak (TTP) and peak values were found using the MATLAB function max() for a precise numerical value. Steady state was determined when the rate of change of the species was determined to be small (approximately 1×10^{-3}) or for simplicity at the end of the simulation time range, see Supplemental Material for more information. A sensitivity analysis was run for both signaling models in COPASI. The model files can be found on GitHub under RangamaniLabUCSD.

Table 7.3: **Initial concentrations and ordinary differential equations for bistable model**

Species	Initial condition	Units	ODE
Ca^{2+}	0.1	µM	$\frac{d[Ca^{2+}]}{dt} = R_0 - 3R_1$
CaM	10	µM	$\frac{d[CaM]}{dt} = -R_1$
Ca^{2+}CaM	0	µM	$\frac{d[Ca^{2+}CaM]}{dt} = R_1$
Ng	20	µM	$\frac{d[Ng]}{dt} = -R_2$
CaMNg	0	µM	$\frac{d[CaMNg]}{dt} = R_2$
CaMKII	20[1]	µM	$\frac{d[CaMKII]}{dt} = -R_3 - R_4 + R_5$
CaMKIIp	0	µM	$\frac{d[CaMKIIp]}{dt} = R_3 + R_4 - R_5$
CaNp	1	µM	$\frac{d[CaNp]}{dt} = -R_6 + R_7$
CaN	0	µM	$\frac{d[CaN]}{dt} = R_6 - R_7$
I1p	1.8	µM	$\frac{d[I1p]}{dt} = -R_8 + R_9$
I1	0	µM	$\frac{d[CaN]}{dt} = R_8 - R_9$
PP1p	0.25[1]	µM	$\frac{d[PP1p]}{dt} = -R_{10} - R_{11} + R_{12}$
PP1	0	µM	$\frac{d[PP1]}{dt} = R_{10} + R_{11} - R_{12}$
Aint	0.1597	µM	$\frac{d[Aint]}{dt} = -R_{13}$
Amem	7.288	$\frac{molecules}{\mu m^2}$	$\frac{d[Amem]}{dt} = R_{13} + R_{14} - R_{15}$
PSD95	4000	$\frac{molecules}{\mu m^2}$	$\frac{d[PSD95]}{dt} = -R_{15}$
ABound	1000	$\frac{molecules}{\mu m^2}$	$\frac{d[ABound]}{dt} = R_{15}$

[1] Initial condition is varied in some of the simulations.
In simulations, membrane components are converted to moles per meter squared.

Results

Using a compartmental ODE model, we investigated the timescales of different biochemical signaling events underlying AMPAR dynamics during synaptic plasticity. We use the following metrics to generate quantitative comparisons between the different conditions tested in the model: peak concentration, time to peak, steady state concentration, and time to steady state. Bound AMPAR (membrane AMPAR bound to PSD95) is the ultimate model readout for synaptic plasticity.

Table 7.4: **AMPAR pathway reactions, reaction types, and reaction rates used in the monostable model**

	List of Reactions	Reaction Type	Reaction Rate
Module 0:	Ca^{2+} Influx		
0	$Ca^{2+}_{ECS} \rightleftharpoons Ca^{2+}_{cyto}$	Custom$^{(0)}$	$R_0 = J_{influx} - J_{efflux}$
Module 1:	Ca^{2+}/CaM Complex Formation		
1	$3\,Ca^{2+} + CaM \underset{kb1}{\overset{kf1}{\rightleftharpoons}} Ca^{2+}CaM$	MA$^{(1)}$	$R_1 = k_{f1}[Ca^{2+}]^3[CaM] - k_{b1}[Ca^{2+}CaM]$
Module 2:	CaM/Ng Complex Formation		
2	$CaM + Ng \underset{kb2}{\overset{kf2}{\rightleftharpoons}} CaMNg$	MA	$R_2 = k_{f2}[CaM][Ng] - k_{b2}[CaMNg]$
Module 3:	CaMKII activation and deactivation		
3	$CaMKII + \mathbf{Ca^{2+}CaM} \xrightarrow{Kcat3} CaMKIIp$	CB$^{(2,3)}$	$R_3 = \frac{K_{cat3}[Ca^{2+}CaM]^4[CaMKII]}{K^4_{m3}+[Ca^{2+}CaM]^4}$
4	$CaMKIIp \xrightarrow{kf4} CaMKII$	MA	$R_4 = k_{f4}[CaMKIIp]$
Module 4:	Phosphatase cascade activation and deactivation		
5	$PP1p + \mathbf{Ca^{2+}CaM} \xrightarrow{Kcat5} PP_1$	CB	$R_5 = \frac{K_{cat5}[Ca^{2+}CaM]^4[PP1p]}{K^4_{m5}+[Ca^{2+}CaM]^4}$
6	$PP_1 \xrightarrow{kf6} PP1p$	MA	$R_6 = k_{f6}[PP1]$
Module 5:	AMPAR trafficking		
7	$Aint \underset{kb7(PP1)}{\overset{kf7(CaMKIIp)}{\rightleftharpoons}} Amem$	MA	$R_7 = (c_1[CaMKIIp] + c_3)[Aint] - (c_2[PP1] + c_4)[Amem]$
8	$\varnothing \xrightarrow{kf8(CaMKIIp)} Amem$	Custom$^{(4)}$	$R_8 = (k_{f8}(t)[CaMKIIp])$
Module 6:	AMPAR/Scaffolding Complex		
9	$Amem + PSD95 \underset{kb9}{\overset{kf9}{\rightleftharpoons}} ABound$	MA	$R_9 = k_{f9}[Amem][PSD95] - k_{b9}[ABound]$

1 $^{(0)}$ Custom taken from [115]: see Supplemental material for details. $J_{influx} = J_{NMDAR} + J_{VSCC} + J_{leak}$ and $J_{efflux} = J_{PMCA} + J_{NCX}$.; $^{(1)}$ MA: Mass Action; $^{(2)}$ CB: Cooperative Binding; $^{(3)}$ Enzyme is in bold type. $^{(4)}$ Custom is given in Supplemental material.

Ca^{2+} influx dynamics are the same for both the monostable and the bistable models

We first focus on the early events in the spine in response to Ca^{2+} influx (Figure 7.2; bistable in blue, monostable in red). When Ca^{2+} floods into the spine, it is rapidly bound by CaM and effluxes through various pumps; see Module 0 and 1 in Table 7.1 and Table 7.4. In response to the voltage stimulus (Figure 7.2a, inset; see Key Components of model), Ca^{2+} influx is rapid and decays within 10 s (Figure 7.2a), consistent with previous models [71, 109, 115] and experiments [157, 158]. Ca^{2+} bound CaM, denoted as Ca^{2+}CaM, shows a slightly slower increase to peak value compared to Ca^{2+} (290 ms for

Table 7.5: **Reaction parameters calculated for the monostable model**

Reaction rate	$\mathbf{k_f}$	unit	$\mathbf{k_b}$	unit	$\mathbf{K_{cat}}$	unit	$\mathbf{K_m}$	unit	$\mathbf{K_r}$	unit
R_1	7.75	$\mu M^{-3} \cdot s^{-1}$	1	s^{-1}	-	-	-	-	-	-
R_2	5	$\mu M^{1} \cdot s^{-1}$	1	s^{-1}	-	-	-	-	-	-
R_3	-	-	-	-	120	s^{-1}	4	µM	-	-
R_4	-	-	-	-	-	-	-	-	0.05	s^{-1}
R_5	-	-	-	-	127	s^{-1}	0.34	µM	-	-
R_6	-	-	-	-	-	-	-	-	0.025	s^{-1}
R_7^*	1,6	$\mu M^{-1} \cdot s^{-1}$, s^{-1}	1,8	$\mu M^{-1} \cdot s^{-1}$, s^{-1}	-	-	-	-	-	-
R_8^{**}	-	-	-	-	-	-	-	-	-	-
R_9	0.0349	$\mu m^2 \cdot molecules^{-1} \cdot s^{-1}$	1	s^{-1}	-	-	-	-	-	-

1 * This reaction represents a membrane flux so there is a reaction between species of different compartments. The units here represent the base reaction without unit conversion between species. Please see Supplemental material for more detail.

2 ** This reaction represents a CaMKIIp-dependent influx of membrane AMPAR and is a custom reaction. Please see Supplemental material for more detail on this reaction and R_0.

Ca^{2+}CaM versus 90 ms for Ca^{2+}) and also decays within the approximately 10 s timescale (Figure 7.2b). Free CaM can also bind to the scaffolding protein neurogranin [109, 159]. Our model is a closed system for all species except A_{mem} and begins with no CaM·Ng, so this model only considers Ng as a CaM sink. In our simulations, the CaM·Ng complex attains a high value at steady state (9.8 µM) in that same time frame of 10 s (Figure 7.2c).

Because of the upstream nature of these modules, both the bistable and monostable model show very similar dynamics and model readouts for these species, see Figure 7.2d-e. We note that the CaM·Ng complex reaches an ultimate peak value after achieving steady state because we define steady state as when the rate of change of the species is small (see Supplemental material). We also see that the time to peak for CaM·Ng in the monostable model is longer than the time to peak for the bistable model ($\sim$ 37 s vs $\sim$ 27 s); however the concentrations for peak value and steady state value for both models are all the same (9.81 µM) so the differences in time to peak and steady state time are not of significance in the model (Figure 7.2d-e). Thus, the influx of Ca^{2+} and buffering by CaM are not affected

Table 7.6: **Initial concentrations and ordinary differential equations for bistable model**

Species	Initial condition	Units	ODE
Ca^{2+}	0.1	µM	$\frac{d[Ca^{2+}]}{dt} = R_0 - 3R_1$
CaM	10	µM	$\frac{d[CaM]}{dt} = -R_1$
Ca^{2+}CaM	0	µM	$\frac{d[Ca^{2+}CaM]}{dt} = R_1$
Ng	20	µM	$\frac{d[Ng]}{dt} = -R_2$
CaMNg	0	µM	$\frac{d[CaMNg]}{dt} = R_2$
CaMKII	20[1]	µM	$\frac{d[CaMKII]}{dt} = -R_3 + R_4$
CaMKIIp	0	µM	$\frac{d[CaMKIIp]}{dt} = R_3 - R_4$
PP1p	0.25[1]	µM	$\frac{d[PP1p]}{dt} = -R_5 + R_6$
PP1	0	µM	$\frac{d[PP1]}{dt} = R_5 - R_6$
Aint	0.1597	µM	$\frac{d[Aint]}{dt} = -R_7$
Amem	7.288	$\frac{molecules}{\mu m^2}$	$\frac{d[Amem]}{dt} = R_7 + R_8 - R_9$
PSD95	4000	$\frac{molecules}{\mu m^2}$	$\frac{d[PSD95]}{dt} = -R_9$
ABound	1000	$\frac{molecules}{\mu m^2}$	$\frac{d[ABound]}{dt} = R_9$

[1] Initial condition is varied in some of the simulations.
In simulations, membrane components are converted to moles per meter squared.

by the choice of the model for CaMKII/AMPAR dynamics as expected, establishing the proof-of-principle that the early time scale dynamics, particularly for Ca^{2+} influx, are unaffected by model choice.

Kinase and phosphatase dynamics differ between the monostable and the bistable models as expected

We next describe the dynamics of the kinases and phosphatases in the cascade for one particular choice of initial conditions (IC) (inactive CaMKII IC of 20 µM and inactive PP1 IC of 0.25 µM; see Table 7.3 and Table 7.6). Given the differences in the models used to describe CaMKII activation and phosphatase dynamics, we see substantial differences

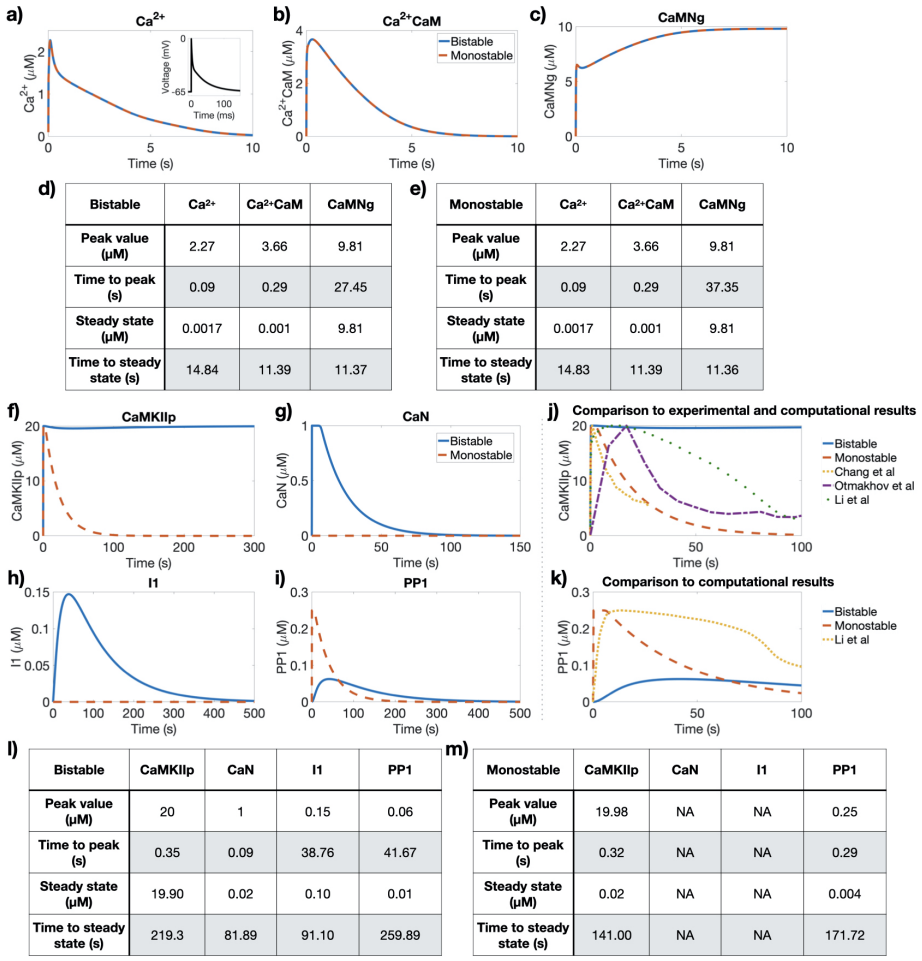

Bistable	Ca²⁺	Ca²⁺CaM	CaMNg
Peak value (μM)	2.27	3.66	9.81
Time to peak (s)	0.09	0.29	27.45
Steady state (μM)	0.0017	0.001	9.81
Time to steady state (s)	14.84	11.39	11.37

Monostable	Ca²⁺	Ca²⁺CaM	CaMNg
Peak value (μM)	2.27	3.66	9.81
Time to peak (s)	0.09	0.29	37.35
Steady state (μM)	0.0017	0.001	9.81
Time to steady state (s)	14.83	11.39	11.36

Bistable	CaMKIIp	CaN	I1	PP1
Peak value (μM)	20	1	0.15	0.06
Time to peak (s)	0.35	0.09	38.76	41.67
Steady state (μM)	19.90	0.02	0.10	0.01
Time to steady state (s)	219.3	81.89	91.10	259.89

Monostable	CaMKIIp	CaN	I1	PP1
Peak value (μM)	19.98	NA	NA	0.25
Time to peak (s)	0.32	NA	NA	0.29
Steady state (μM)	0.02	NA	NA	0.004
Time to steady state (s)	141.00	NA	NA	171.72

Figure 7.2: Early and intermediate timescale events. Temporal dynamics of cytosolic Ca^{2+} (a), activated Ca^{2+}/CaM complex (b), and CaM/Ng complex (c) all show similar dynamics for both the bistable (blue line) and monostable models (red line). Black inset in (a) is the voltage stimulus that represents a EPSP and BPAP separated by 2 ms. Peak and steady state values and times for Ca^{2+}, Ca^{2+}/CaM complex, and CaM/Ng complex for the bistable (d) and monostable (e) models show similar dynamics for early timescale events. Temporal dynamics of activated CaMKII (f), activated CaN (g), activated I1 (h), and activated PP1 (i) for both the bistable and monostable models show very different results. Note that the monostable model does not involve CaN and I1. j) Comparison of CaMKII dynamics between the bistable (blue) and monostable (red) models, experimental observations [136, 137], and other models [116]. k) Comparison of PP1 dynamics between both the bistable (blue) and monostable (red) models and another model [116]. Peak and steady state values and times for activated CaMKII, activated CaN, activated I1, and activated PP1 for the bistable (l) and monostable (m) models show different dynamics.

in the kinetics when comparing the two signaling models (Figure 7.2). In both models, Ca^{2+}CaM activates CaMKII rapidly to its maximum value (20 µM). However, in the bistable model, CaMKII remains elevated at its maximum value while in the monostable model CaMKII decays towards zero, see Figure 7.2f. In the bistable model, Ca^{2+}CaM activates CaN as the first step of the phosphatase cascade, see Figure 7.2g-i, blue line. The bistable phosphatase cascade shows rapid activation of CaN to its maximum concentration (1 µM), which then triggers activation of I1 and then PP1 (Figure 7.2g-i). I1 and PP1 have larger peak times than CaN in the bistable model because of the temporal relay of information ($\sim$ 40 s versus less than 1 s for CaN peak), see Figure 7.2l,m. The monostable model has a different activation pathway for PP1; PP1 is directly activated by Ca^{2+}CaM such that it operates on the same timescale as CaMKII [116]. As a result, PP1 and CaMKII have very similar kinetics in the monostable model with a rapid rise followed by a decay to zero (Figure 7.2f, i, red line).

We compare our computational model results to other experimental [136, 137] and computational results [116] (Figure 7.2j-k). We note that our goal is not to match the exact dynamics of CaMKII or PP1 dynamics from experiments but to provide estimates for different timescales based on experimental conditions. [137] studies CaMKII dynamics in dendritic spines using fast-framing two-photon fluorescence lifetime imaging of hippocampal slices. Similarly [136] studies CaMKII and various mutants in hippocampal slices using two photon glutamate uncaging. To compare timescales, we scale all other results to our maximum CaMKII and PP1 concentrations. We see that across all published data CaMKII concentration increases rapidly, but there is variation in decay time (17.6 s for [137], 38.1 s for [136], 61.5 s for [116]). The monostable model decays with a rate of 20 s which resembles the rate of [137], while the various other CaMKII results all decay within approximately 100 s except the bistable model which remains elevated (Figure 7.2j), for this choice of IC.

Phosphatase temporal dynamics are harder to compare against experiments because many studies do not capture these dynamics; however PP1 decay parameters appear slower than CaMKII decay [116,124] so we include these dynamics in our monostable model. Observations of PP1 temporal dynamics from [116] show a longer elevated period compared to our monostable results (decay time of 85.7 s from [116]) but have rise dynamics intermediate between our bistable and monostable dynamics (Figure 7.2k).

To more directly compare our CaMKII and PP1 temporal dynamics, we compare the decay times across experimental and model results. CaMKII decay dynamics have been estimated experimentally as having two timescales of delay τ_{fast} = 6.4 ± 0.7 s and τ_{slow} = 92.6 ± 50.7 s with different fractions of fast and slow decay (74% vs 26%) [137] ([136] shows similar decay values). Equivalent parameters for PP1 could not be immediately found for this system. Our time constants for CaMKII and PP1 decay were τ = 20 s and τ = 40 s, respectively (See Table 7.2 and Table 7.5).

A direct comparison of model readouts for the bistable and the monostable model are shown in Figure 7.2l-m, respectively. The main differences in the CaMKII dynamics are in the steady state values in the bistable and the monostable model (19.9 µM versus 0.02 µM respectively) and the time to steady state (∼ 219 s versus ∼ 141 s), where the bistable model takes longer to reach steady state but hovers near maximal value. When comparing PP1 dynamics for both the models, we note that the bistable model has a lower peak value (0.06 µM) when compared to the monostable model (0.25 µM). While PP1 steady state goes to zero for both models for this choice of initial conditions, the time it takes for steady state is different (∼ 260 s for the bistable model compared to ∼172 s for the monostable model) suggesting that these differences in timescales may have an impact on downstream events.

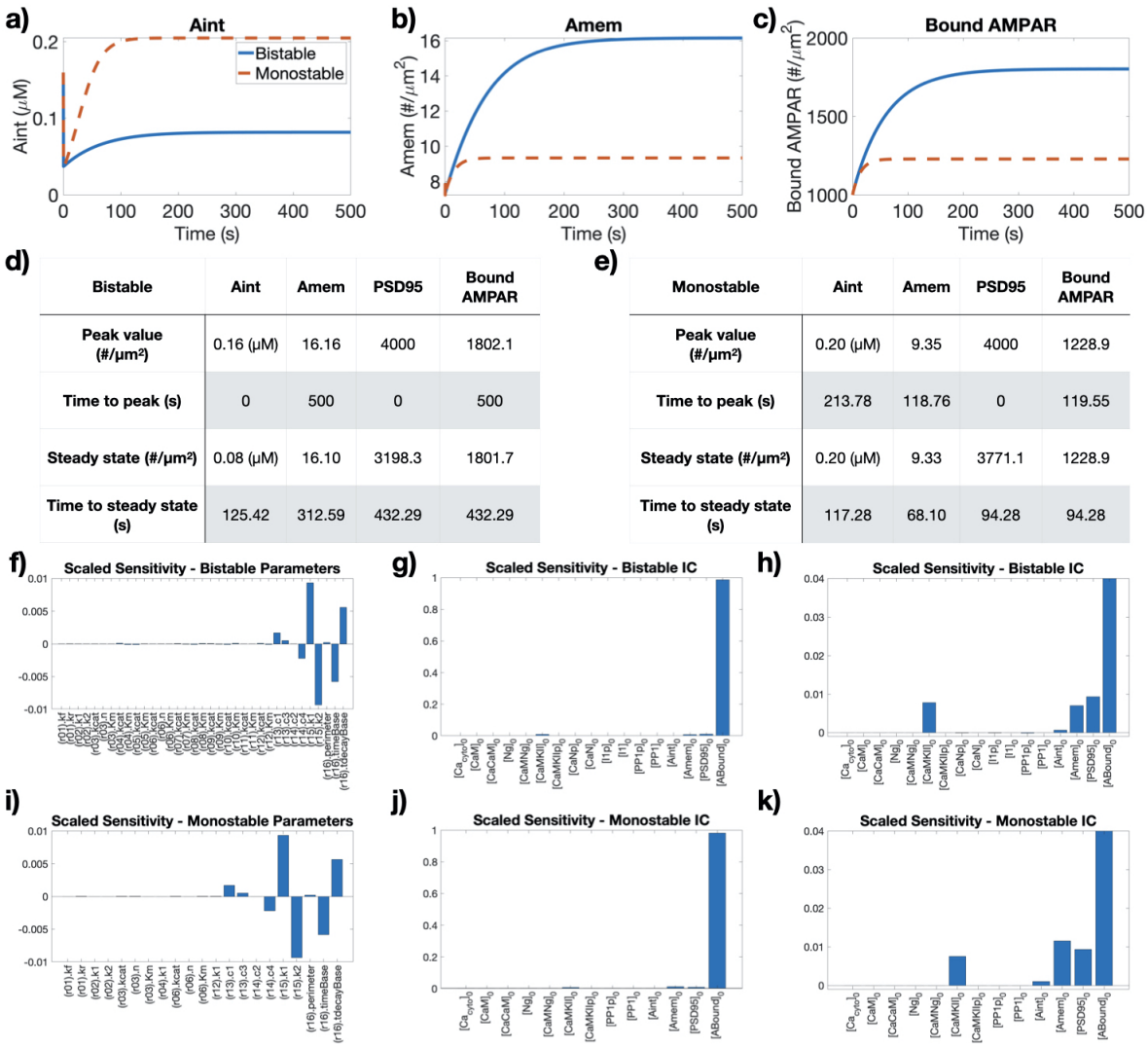

d)

Bistable	Aint	Amem	PSD95	Bound AMPAR
Peak value (#/μm²)	0.16 (μM)	16.16	4000	1802.1
Time to peak (s)	0	500	0	500
Steady state (#/μm²)	0.08 (μM)	16.10	3198.3	1801.7
Time to steady state (s)	125.42	312.59	432.29	432.29

e)

Monostable	Aint	Amem	PSD95	Bound AMPAR
Peak value (#/μm²)	0.20 (μM)	9.35	4000	1228.9
Time to peak (s)	213.78	118.76	0	119.55
Steady state (#/μm²)	0.20 (μM)	9.33	3771.1	1228.9
Time to steady state (s)	117.28	68.10	94.28	94.28

Figure 7.3: Late timescale dynamics. a) Temporal dynamics of internal AMPAR in endosomes (Aint, a), free AMPAR on the membrane (Amem, b), and bound AMPAR (c) for both the bistable and monostable models show similar general trends. Peak and steady state values and times for Aint, Amem, PSD95, and bound AMPAR for the bistable (d) and monostable (e) models show key differences in dynamics. Scaled sensitivity analysis results with respect to the bound AMPAR readout for the bistable parameters (f), bistable initial conditions (g), and a zoomed view of the bistable IC results (h). Scaled sensitivity analysis results with respect to the bound AMPAR readout for the monostable parameters (i), monostable initial conditions (j), and a zoomed view of the monostable IC results (k).

AMPAR dynamics are dependent on model choice for CaMKII/PP1 balance

We next investigated how the differences in kinase and phosphatase dynamics might influence the dynamics of AMPAR for a single set of initial conditions (20 µM for CaMKII and 0.25 µM for PP1). Given that downstream signaling can integrate the details of upstream signaling kinetics [160] and can integrate out the effect of upstream timescales [105], we wondered if the differences in the two models would make a difference in AMPAR dynamics. We track three populations of AMPAR in our model – AMPAR in endosomes (Aint, modeled as a volume component), free AMPAR on the synaptic membrane (Amem), and AMPAR bound to PSD95 (bound AMPAR). Internalized AMPAR can become membrane-bound as a result of CaMKII-dependent exocytosis; membrane bound AMPAR is endocytosed in a PP1-dependent manner (R13 in Table 7.1 and R7 in Table 7.4). Membrane AMPAR increases through a CaMKII-dependent influx that represents AMPAR diffusing laterally into the spine from extrasynaptic pools of membrane AMPAR outside of the spine [25, 141] (R14 in Table 7.1 and R8 in Table 7.4). Membrane bound AMPAR can be immobilized by binding to PSD95 among other PSD proteins (R15 in Table 7.1 and R9 in Table 7.4). AMPAR is known to interact with a plethora of cytosolic and membrane bound species at the PSD, often with complex phosphorylation or other activation dynamics [16, 145, 161]; however in our system we chose to model PSD95 and Amem binding through simple mass action kinetics (Module 6 in Table 7.1 and Table 7.4). Despite simple reaction kinetics, this scaffold interaction significantly influences the system, demonstrating how simple signaling components can dominate more complex signaling motifs [162]. Our simulations show that internal AMPAR (Aint) is quickly exocytosed but then gradually increases again due to endocytosis, with the monostable model having a larger increase in internal AMPAR steady state compared to the bistable model

(0.20 µM versus 0.08 µM; Figure 7.3a). Free AMPAR on the membrane increases to a new steady state with the bistable model having a significantly higher density than the monostable model (Figure 7.3b). The higher Amem density in the bistable model is because the bistable model has a higher steady state value of CaMKII for the ICs (20 µM for CaMKII and 0.25 µM for PP1) than the monostable model and even though the PP1 peak is higher in the monostable model, the impact of CaMKII is stronger on the balance between Aint and Amem. Naturally, the unbounded scaffolding protein PSD95 decreases to a new steady state value as it binds to free membrane AMPAR (Amem) to form bound AMPAR (Figure B.4a) in both cases. We note that membrane AMPAR has rapid binding to form bound AMPAR, but also has a rapid increase in endocytosis/exocytosis and influx rates (Figure B.4b-c). Bound AMPAR increases in both models to new steady states but reaches a much higher density in the bistable model compared to the monostable model ($\sim$ 1802 receptors per micron squared versus $\sim$ 1229 receptors per micron squared; Figure 7.3c), again because of the stronger effect of CaMKII. These densities of bound AMPAR are within the range of AMPAR densities observed in experiments [146,163–168]. The monostable model achieves steady state for all AMPAR species and PSD95 within $\sim$ 117 s, faster than the bistable model whose fastest component, Aint, took $\sim$ 125 s to reach steady state (Figure 7.3d-e).

Next, we conducted a sensitivity analysis to better understand the significant parameters and initial conditions that influenced bound AMPAR in both models (Figure 7.3f-k). The sensitivity analysis was run in COPASI [169] and the influence of each parameter and initial condition was considered on the final readout of bound AMPAR, see Supplemental material sensitivity analysis section for more details. We find similar trends for both the bistable and monostable models – bound AMPAR is most sensitive to the kinetic parameters that govern endo/exocytosis, CaMKII-mediated AMPAR influx, PSD95

binding rates, and to the initial conditions of CaMKII, PSD95, and the subpopulations of different AMPAR species. As expected, the bound AMPAR readout was highly sensitive to the IC of bound AMPAR, but was also sensitive to parameters and species associated with the scaffold binding reactions. Thus, CaMKII-mediated AMPAR influx and AMPAR binding to PSD95 both greatly influence bound AMPAR dynamics as compared to CaMKII and PP1-mediated exocytosis and endocytosis. The slower timescale and higher steady state density for bound AMPAR associated with the bistable model can be explained by the elevated CaMKII steady state that leads to a higher influx of membrane AMPAR. Thus, because of the nature of the upstream kinase (prolonged activation versus finite time activation), the density of bound AMPAR on the membrane can be significantly impacted.

Effect of CaMKII and PP1 initial conditions on model-dependent AMPAR readout

One of the key differences between a bistable model formulation for CaMKII (in this case coupled with a phosphatase cascade) and the monostable model is the dependence of steady state values for CaMKII and PP1 on the initial conditions (IC) [124, 128]. To understand how bound AMPAR depends on the initial condition of inactive CaMKII and PP1, we conducted a parameter sweep (Figure 7.4) and focus on the steady state behavior. For temporal dynamics of all active PP1 and active CaMKII for both the bistable and monostable models across the explored IC regimes, see Figure B.1. Temporal dynamics of bound AMPAR for both the bistable and monostable models can be found in Figure B.3. For the bistable model, active CaMKII, active PP1, and bound AMPAR steady states all show dependence on both CaMKII and PP1 initial conditions, with the higher CaMKII IC leading to higher bound AMPAR density, and higher PP1 IC leading

to lower bound AMPAR density (Figure 7.4a). It is useful to recall that an increase in bound AMPAR density is associated with LTP, while a decrease is associated with LTD. In these cases, despite PP1 IC having a strong influence on the bistable system, all cases either display LTP or no change (NC). High CaMKII IC and low PP1 IC leads to high active CaMKII at steady state in the bistable model and therefore high bound AMPAR, whereas low CaMKII IC with high PP1 IC will lead to low active CaMKII at steady state and therefore low bound AMPAR (Figure 7.4b). We also see that for two different PP1 concentrations, CaMKII can achieve two different steady state values for the same CaMKII IC, the hallmark of bistability, Figure 7.4b. Similarly, for two different CaMKII ICs, PP1 can also achieve two different steady state values for the same PP1 IC. Considering bound AMPAR across CaMKII ICs for two different PP1 ICs, for a small PP1 IC (0.1 µM), bound AMPAR at steady state is linear with respect to CaMKII IC; for the higher PP1 IC (0.5 µM), bound AMPAR shows a non-linear dependence on CaMKII ICs. When we vary PP1 ICs for two different CaMKII ICs, we observe that for a small CaMKII IC (12 µM), bound AMPAR steady state decreases with respect to PP1 IC; for the higher CaMKII IC (20 µM), bound AMPAR shows only slight dependence on PP1 IC, slightly decreasing for high PP1 IC.

We conducted a similar parameter sweep with the monostable model (Figure 7.4c-d). The monostable model only has one steady state for both CaMKII and PP1 which is zero (Figure 7.4c). Therefore, the initial condition only determines the peak value of the model without any coupling between CaMKII and PP1, as seen in Figure B.2. Bound AMPAR shows dependence on CaMKII IC but none on PP1 IC in this case (Figure 7.4c,d). Overall the monostable model did not demonstrate a strong dependence on ICs as compared to the bistable model. The steady state heatmaps clearly show that the monostable model has no coupling between CaMKII and PP1 dynamics and the bound AMPAR steady

state depends on the CaMKII IC (Figure 7.4c, d, right column).

Effect of varying trafficking conditions on AMPAR dynamics

Thus far, we have focused only on the signaling dynamics of CaMKII and PP1 on AMPAR. Next, we investigated how the coupling between signaling dynamics and trafficking dynamics can affect bound AMPAR. As described in Table 7.1 and Table 7.4, bound AMPAR also depends on endo- and exocytosis and influx of AMPAR from the extrasynaptic pool (see Figure B.4).

The dynamics of A_{mem} are given by the following equation

$$\begin{aligned}\frac{dA_{mem}}{dt} = & \underbrace{(c_1[CaMKIIp]+c_3)[A_{int}]n}_{\text{Basal and CaMKII-dependent exocytosis}} - \underbrace{(c_2[PP1]+c_4)[A_{mem}]}_{\text{Basal and PP1-dependent endocytosis}} \\ & - \underbrace{(k_{bind}[PSD95][A_{mem}]) - k_{release}[A_{Bound}])}_{\text{scaffolding}} \\ & + \underbrace{\frac{P_{base}e^{\frac{-t}{\tau_{decay}}}[CaMKIIp]}{\tau_{base}}}_{\text{CaMKII-mediated influx from extrasynaptic space}} .\end{aligned} \tag{7.2}$$

The new terms introduced here are the following: $P_{base} = 0.9069\ \mu m$, $\tau_{base} = 800$ s, $\tau_{decay} = 60$ s, and n $= 0.1011\ \mu m$. P_{base} is the spine neck base perimeter and we approximate it from an average thin spine in [115]. Endocytosis and exocytosis rates were taken from [110]. τ_{base} is the timescale of influx and can be though of as the timescale at which AMPAR moves into the dendritic spine [114]. τ_{decay} is the timescale of CaMKII activity and captures the timescale over which active CaMKII triggers the influx of membrane AMPAR into the spine [141]. n is the lengthscale conversion factor and captures the spine volume to surface area ratio. The CaMKII-mediated influx is inspired by [141] and captures how elevated CaMKII levels can trigger the movement of AMPAR into the activated spine, but the signal must turn off to prevent excessive AMPAR influx. We note that mathematically the

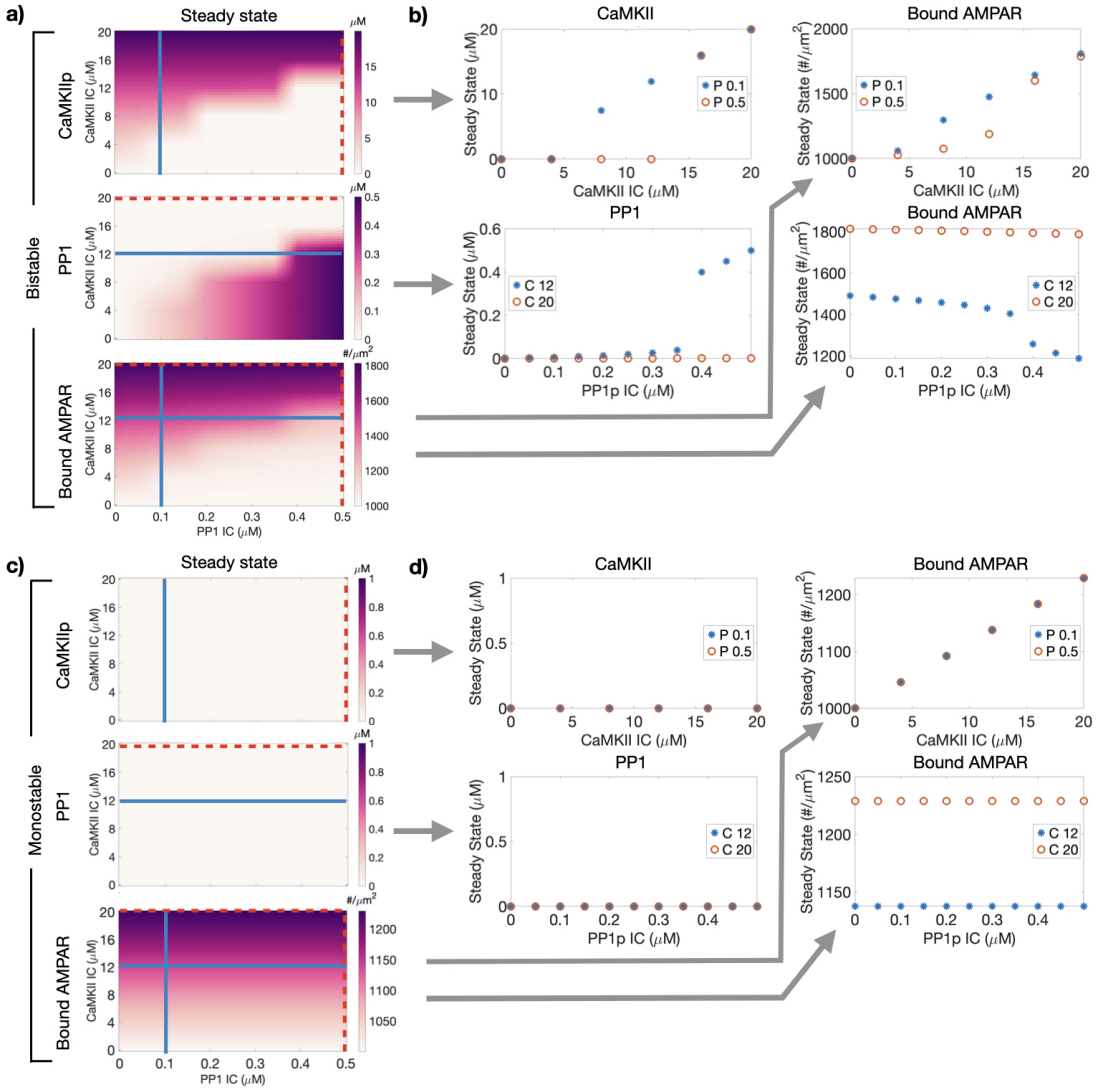

Figure 7.4: Variations in initial conditions for inactive CaMKII and PP1 influences active CaMKII, active PP1, and bound AMPAR dynamics in a model-dependent manner. a) Steady state values for active CaMKII, active PP1, and bound AMPAR (top to bottom row, respectively) for the bistable model. b) Steady state value of CaMKII, PP1, and bound AMPAR for two set PP1 ICs and varied CaMKII IC and for two set CaMKII IC and varied PP1 ICs for the bistable model. c) Steady state values for active CaMKII, active PP1, and bound AMPAR (top to bottom row, respectively) for the monostable model. d) Steady state value of CaMKII, PP1, and bound AMPAR for two set PP1 ICs and varied CaMKII IC and for two set CaMKII IC and varied PP1 ICs for the monostable model.

presence of the influx term results in an open system for AMPAR mass conservation since the total number of receptors in the simulation can change because of external sources.

The dynamics of bound AMPAR are given by

$$\frac{dA_{bound}}{dt} = \underbrace{(k_{bind}[PSD95][A_{mem}]) - k_{release}[A_{Bound}])}_{\text{scaffolding}}, \tag{7.3}$$

which describes the binding and unbinding of free AMPAR and PSD95, a scaffolding molecule, to form bound AMPAR. We assume that there is a pool of free PSD95 ready to bind membrane AMPAR.

Using this framework, we asked how the different trafficking conditions impact bound AMPAR. In what follows, we compare all the parameter variations to a control, which is defined as the simulation in which all forms of trafficking (PP1-dependent endocytosis, CaMKII-dependent exocytosis, and a CaMKII-dependent influx source of AMPAR) are present (Figure 7.4a, bottom row for bistable and (Figure 7.4c, bottom row for monostable). Recall that, for the control cases, bound AMPAR reached a maximum of 1802 per square micron for the bistable case versus 1229 per square micron for the monostable case.

We considered the steady state value (value at 500 s) of all AMPAR species for two *in silico* knockout trafficking conditions - no CaMKII-mediated influx (Figure 7.5a) and no endocytosis/exocytosis (Figure 7.5b) for different CaMKII and PP1 ICs. Temporal dynamics of bound AMPAR with different CaMKII and PP1 initial conditions for the various trafficking knockout cases can be found in Figure B.3 and heatmaps showing PSD95 steady state dynamics for different CaMKII and PP1 initial conditions for the various trafficking cases are in Figure B.5.

We first asked what happens if influx is removed as a source of AMPAR but endocytosis and exocytosis are retained? We found that the contribution of endocytosis and exocytosis were smaller compared to the influx from extrasynaptic regions (Figure 7.5a). The bistable model shows dependence on both CaMKII/PP1 IC, while the monostable

case leads to homogeneous results for all species (Figure 7.5a).Thus, in the absence of influx but in the presence of endocytosis and exocytosis, we find that bound AMPAR readout mimics the upstream signaling pathway. The steady state for both Amem and bound AMPAR was lower in the monostable case versus the bistable case, highlighting how the elevated CaMKII levels in the bistable case contribute to both free and bound AMPAR pools even in the absence of endo and exocytosis. However, if we retain influx but turn off endocytosis/exocytosis, internal AMPAR cannot be trafficked onto the membrane, so there is no change in Aint concentration for either choice of upstream signaling (Figure 7.5b, first column). Additionally, there is a coupled dependence on IC for Amem and bound AMPAR for the bistable case but only CaMKII IC dependence for Amem and bound AMPAR for the monostable case (Figure 7.5b). Because there was no direct impact of PP1 and CaMKII on Amem levels through endocytosis and exocytosis, the coupled PP1/CaMKII effect in the bistable model is due to the upstream interactions between CaMKII and PP1 that then influence steady state CaMKII levels that mediate AMPAR influx. In the parameter space of varying CaMKII and PP1 ICs, in the bistable model, we observe a smooth dependence of Amem and bound AMPAR; this is different from the case without influx but with endo/exocytosis where the bound AMPAR demonstrate a step-like response. This suggests that influx of AMPAR term takes a bistable cascade as an input and produces a proportional mapping as an output.

Is it possible that the conclusion that influx of AMPAR is a dominant contributor to bound AMPAR dynamics is a result of the choice of parameters for the endo/exocytosis terms (obtained from [126])? And can we investigate the endocytosis and exocytosis contributions separately as suggested by [7]? Recall that the exocytosis and endocytosis term is given as

$$J_{exo/endo} = \underbrace{(c_1[CaMKIIp] + c_3)[A_{int}]n}_{\text{Basal and CaMKII-dependent exocytosis}} - \underbrace{(c_2[PP1] + c_4)[A_{mem}]}_{\text{Basal and PP1-dependent endocytosis}} , \qquad (7.4)$$

where both exocytosis and endocytosis have a species dependent component and a basal contribution. To answer the questions raised above, we varied the relative contributions of CaMKII-mediated exocytosis and PP1-mediated endocytosis in two different ways. In the first method, we scale the c_1 and c_2 terms, such that

$$J_{exo/endo} = \underbrace{(c_1 Exo[CaMKIIp] + c_3)[A_{int}]n}_{\text{Basal and CaMKII-dependent exocytosis}} - \underbrace{(c_2 Endo[PP1] + c_4)[A_{mem}]}_{\text{Basal and PP1-dependent endocytosis}}, \quad (7.5)$$

where Exo and Endo are scaling factors that range from 0 to 500 and essentially modify the rate of activity-dependent endocytosis or exocytosis and can be attributed to other biophysical factors that affect trafficking [149, 170]. A maximum value of 500 was chosen to ensure that given the control initial conditions of CaMKII and PP1, the endocytosis term could achieve the same magnitude as the original exocytosis term (Figure 7.6a and c). In this case, the stimulus was applied at t = 0, since the system was already at steady state.

In the second method, we scale the entire exocytosis and endocytosis terms, such that

$$J_{exo/endo} = \underbrace{Exo(c_1[CaMKIIp] + c_3)[A_{int}]n}_{\text{Basal and CaMKII-dependent exocytosis}} - \underbrace{Endo(c_2[PP1] + c_4)[A_{mem}]}_{\text{Basal and PP1-dependent endocytosis}}, \quad (7.6)$$

where Exo and Endo are scaling factors that range from 0 to 1 and modify the cumulative rate of endocytosis or exocytosis. This scaling essentially alters the steady state of the system in the absence of stimulus and so we first simulated the system to steady state and then added the stimulus at t = 500 s (gray dashed line in Figure 7.6b and d).

We considered four different cases for both the bistable and monostable models, Figure 7.6. First we considered the models with and without influx (Figure 7.6, top and bottom rows, respectively). Second we considered two different initial conditions for CaMKII, 10 and 20 µM, but only one IC for PP1 (0.25 µM). Recall that for the bistable model, the first condition (10 µM CaMKII and 0.25µM PP1) leads to an elevated PP1 concentration, while the second condition (20 µM CaMKII and 0.25 µM PP1) leads to

an elevated CaMKII concentration. We plot bound AMPAR over time for four different endocytosis (En) and exocytosis (Ex) scaling sets (En 0, Ex 0; En 0, Ex Max; En Max, Ex 0; En Max, Ex Max) for both scaling methods, Figure 7.6. For temporal plots of bound AMPAR for each of these various conditions, see Figure B.8. For a closer analysis of AMPAR dynamics for the c_1 and c_2 approach, see Figure B.7. For steady state values of bound AMPAR for both approaches, see Figure B.6.

In the absence of influx of AMPAR, we find that bound AMPAR can achieve a new steady state after stimulus if there is a constant elevated concentration for CaMKII or PP1 that drives either endocytosis or exocytosis, Figure 7.6a,b. The monostable case does not have sustained CaMKII and PP1 activation (Figure 7.2f,i) and therefore, in all variations the monostable model returns bound AMPAR to its initial condition. In contrast, the bistable model has elevated PP1 for the 10 µM CaMKII IC, and elevated CaMKII for the 20 µM CaMKII IC; depending on the dominant contribution between active endocytosis and exocytosis, bound AMPAR can attain a new increased or decreased steady state. When the entire terms are scaled, for the case when the relative contribution of endocytosis is maximized for both values of CaMKII IC, bound AMPAR steady state even before stimulus goes to zero (Figure 7.6b; red lines). This suggests that in the absence of influx, even for situations where CaMKII is active at high concentrations at steady state, it is possible to get low bound AMPAR because of the contributions of trafficking.

When AMPAR influx is present, bound AMPAR demonstrates a dose-dependence on CaMKII as opposed to a switch-like response, Figure 7.6c,d. When the entire trafficking terms are scaled and endocytosis is maximized for either CaMKII IC, we see that with an influx the system has a transient increase in bound AMPAR after stimulation at t = 500 s before it returns back to its previous zero steady state (Figure 7.6d,red lines). Thus, we find that even when influx is present, a balance between endocytosis and exocytosis is

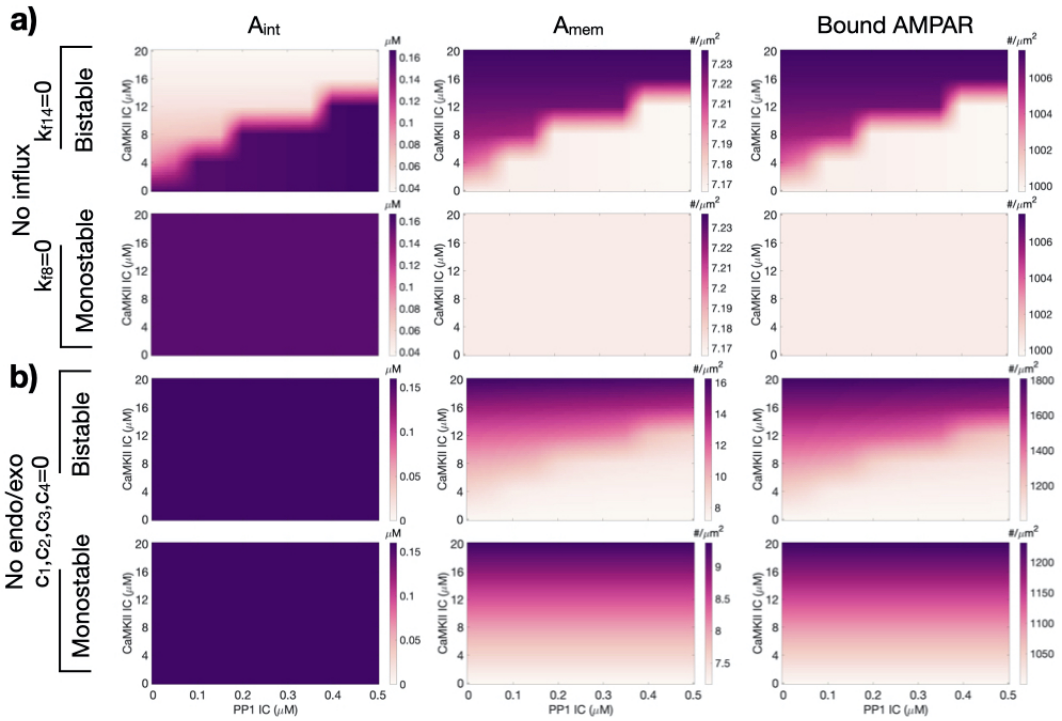

Figure 7.5: Effect of CaMKII and PP1 initial condition on trafficking mechanisms. a) Species value at 500 s for internal AMPAR (Aint), membrane AMPAR (Amem), and bound AMPAR for the bistable (top row) and monostable (bottom row) models in the trafficking case without an external AMPAR source for different CaMKII and PP1 ICs. b) Species value at 500 s for the bistable (top row) and monostable (bottom row) models in the trafficking case without endocytosis and exocytosis for different CaMKII and PP1 ICs.

necessary to elevate bound AMPAR on the membrane.

Bound AMPAR as a function of time-dependent stimuli

Thus far, we have focused on model choices and variations for a single stimulus, see Figure 7.2a, inset. In reality, dendritic spines receive a sequence of stimuli in a frequency-dependent manner [105, 116, 123]. Here we consider the effect of a train of elevated Ca^{2+}CaM activity at different spiking frequencies (0.5 Hz, 0.1 Hz, 0.05 Hz, [171]), for two different stimulus strengths and two different CaMKII ICs, see Figure 7.7a. Pre-

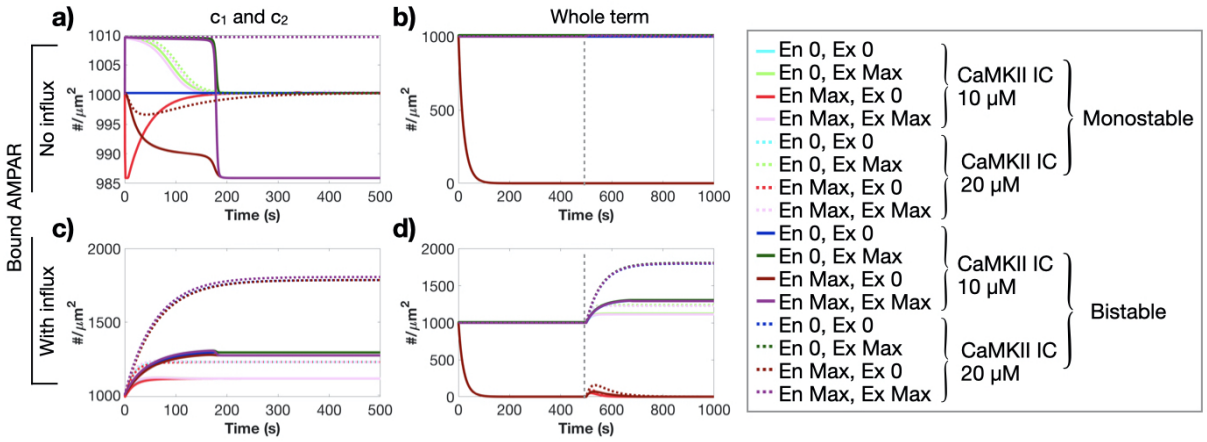

Figure 7.6: Variation of different trafficking conditions on bound AMPAR. Temporal dynamics of bound AMPAR without AMPAR influx for two different CaMKII initial conditions (10 µM and 20 µM), different contributions of endocytosis and exocytosis, for the bistable and monostable models, for the scaling method that scales c_1 and c_2 (a) and the whole endocytosis and exocytosis terms (b). Temporal dynamics of bound AMPAR with AMPAR influx for two different CaMKII initial conditions (10 µM and 20 µM), different contributions of endocytosis and exocytosis, for the bistable and monostable models, for the scaling method that scales c_1 and c_2 (c) and the whole endocytosis and exocytosis terms (d). Endocytosis and exocytosis were varied in two different ways: a,c) (c_1 and c_2): the species dependent rates of c_1 and c_2 were scaled; and b,d) (Whole term): the entire exocytosis and endocytosis term was scaled (c_1, c_3 and c_2, c_4). The dashed gray line in b and d indicates when the stimulus was applied to the system at t = 500 s. Gray inset: Legend where general color corresponds to a predetermined endocytosis (En)/exocytosis (Ex) scaling in this order (En 0, Ex 0; En 0, Ex Max; En Max, Ex 0; En Max, Ex Max), solid and dashed lines indicate the 10 µM and 20 µM CaMKII IC, respectively; and the lighter colors indicate the monostable model and dark colors indicate the bistable model. Note Max is 500 for a and c, and 1 for b and d.

vious studies have shown that CaMKII can integrate calcium/calmodulin activity as a leaky integrator [109, 137], so we consider how stimulus magnitude and frequency affect CaMKII and bound AMPAR dynamics. We note that for the bistable model, there was no noticeable difference in CaMKII and bound AMPAR dynamics for the different combinations of conditions, see Figure B.9. This is because the activation of CaMKII and bound AMPAR is already maxed out due to the first activation spike so subsequent spikes have no effect. In the case of the monostable model, we observe that CaMKII behaves as a leaky integrator as the stimulus frequency increases (Figure 7.7b) and the peak values are proportional to the CaMKII IC. Bound AMPAR correspondingly shows a frequency and CaMKII IC-dependent response (Figure 7.7c). When we look at the steady state values of bound AMPAR, we observe that for 1X stimulus, the value of bound AMPAR decreases as the frequency increases for both values of CaMKII IC (Figure 7.7d). When we increase the stimulus amplitude by 10-fold (blue line in Figure 7.7a), the monostable model shows similar temporal dependencies for CaMKII (Figure 7.7e) with the peak values maxing out the available CaMKII. Bound AMPAR integrates these temporal dynamics and shows higher values than the 1x stimulus (Figure 7.7f). The value of bound AMPAR, in this case of 10X stimulus, increases as the stimulus frequency increases for both values of CaMKII IC (Figure 7.7g).

Discussion

The choice of model formulation is critical for the interpretation of results in computational and systems biophysics. In the case of synaptic plasticity and learning models, the idea that CaMKII can act as a molecular marker for learning and that a bistable model could be interpreted as a molecular switch has received a lot of attention [150]. Indeed, the idea of a bistable switch has the appeal of making direct associations with LTP and

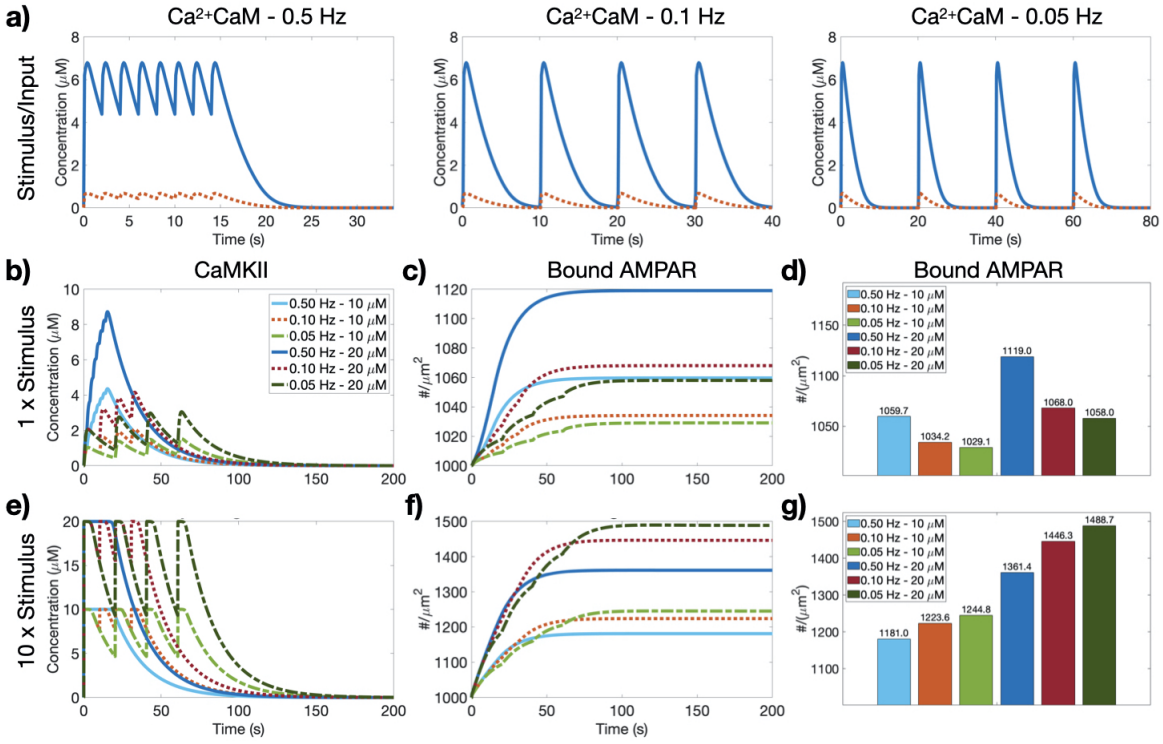

Figure 7.7: Effect of multiple active Calmodulin spikes on CaMKII and bound AMPAR dynamics in the monostable model. a) Multiple spikes of active CaM were input into the different model systems at different frequencies (0.5 Hz, 0.1 Hz, 0.05 Hz; left, middle, and right, respectively) at two different amplitudes (large - blue, small - red). The large stimulus is 10 times the smaller stimulus. Active CaMKII (b) and bound AMPAR (c) temporal dynamics for the monostable model for the small Ca^{2+}CaM stimulus for all three frequencies and both CaMKII IC. d) Steady state bound AMPAR for the small stimulus for each frequency and CaMKII IC. Active CaMKII (e) and bound AMPAR (f) temporal dynamics for the monostable model for the large Ca^{2+}CaM stimulus for all three frequencies and both CaMKII IC. g) Steady state bound AMPAR for the large stimulus for each frequency and CaMKII IC.

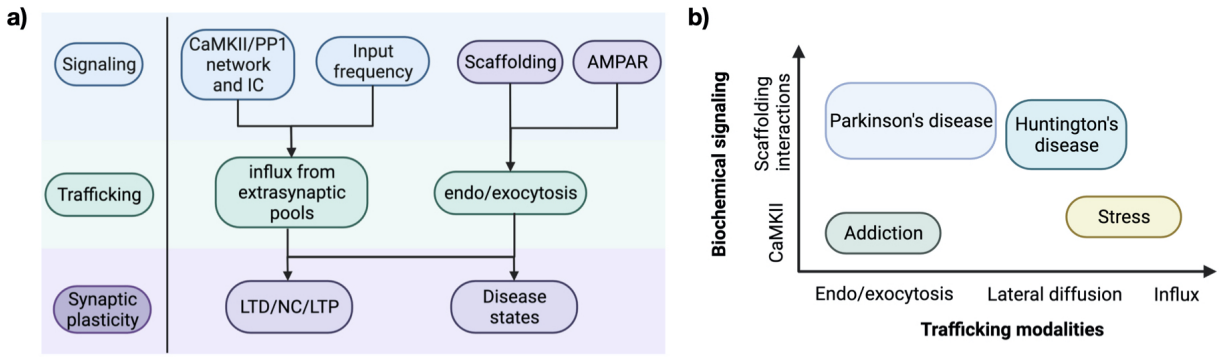

Figure 7.8: Synaptic consequences of coupling between AMPAR signaling and trafficking. a) Signaling and trafficking components interact to determine changes in synaptic plasticity, whether LTD, NC, LTP, or disease states. b) Dysfunction within either the AMPAR signaling or trafficking mechanisms can lead to various disease states, including Parkinson's disease, Huntington's disease, addiction, and stress. Figure made in Biorender.com.

LTD – high stable CaMKII can be interpreted as LTP and low stable CaMKII can be interpreted as LTD [14]. There are two scenarios that complicate this simple picture. First, detailed kinetic models of CaMKII monomers and holoenzymes and experiments have not shown evidence of CaMKII bistability [109, 122, 129]. Second, in recent years, it has become clearer that the increase of AMPAR density at the PSD is perhaps a better molecular marker for learning [26, 172–174] and the net increase in AMPAR depends on various trafficking modalities which in turn depend on upstream signaling pathways. Therefore, here, we chose to investigate how the model choice for upstream signaling could affect the predictions of the model for bound AMPAR, Figure 7.8a. Additionally, many neurological disorders and diseases include a component of AMPAR dysregulation, Figure 7.8b. For example, Huntington's disease involves a disruption in the binding between AMPAR and scaffolding molecules such as PSD-95; both Alzheimer's Disease and Parkinson's Disease related dementia involve an increase in AMPAR endocytosis in response to Aβ oligomers, while Parkinson's Disease also involves an impairment in scaffold binding and AMPAR endocytosis; and mental stress is believed to cause increases in AMPAR

lateral diffusion [175]. Therefore, it is clear that the regulation and dynamics of AMPAR have significant neurological consequences. By considering two different signaling model candidates and performing signaling and trafficking variations Figure 7.1, we can provide the following predictive insights from our model.

The first insight is that bound AMPAR mimics the dynamics of the upstream model (bistable or monostable) with respect to endo/exocytosis rates as well as ICs in the absence of AMPAR influx. We found that the different signaling models (Figure 7.2) translated to different AMPAR timescales (Figure 7.3), primarily through their CaMKII dynamics which informed the influx of AMPAR. Indeed, variations of different parameters and coupling within each model showed that by construction, the bistable model had a stronger coupling between bound AMPAR and upstream signaling than the monostable model at steady state, Figure 7.4. These pattern held when considering each signaling model with endocytosis and exocytosis or with the AMPAR influx, separately, Figure 7.5. Thus, careful dissection of the upstream signaling pathways and crosstalk is necessary for building predictive models.

Second, by changing the relative contributions of trafficking, we predict that effects of trafficking can dominate the signaling effects. Specifically, our model predicts that influx of AMPAR from the extrasynaptic space serves to partially override the impact of upstream signaling and trafficking, Figure 7.6. In some cases but not all, where endocytosis dominates, where one would expect LTD-like behavior, influx of receptors allows for bound AMPAR to either increase or remain unchanged, thereby preventing LTD. Additionally in Figure 7.6d, when bound AMPAR started at zero but had an AMPAR influx, bound AMPAR transiently increased due to this AMPAR influx but the large endocytosis term drove the system back to zero steady state, (Figure 7.6d, red lines). This is the only condition that does not show an increase in bound AMPAR steady state when there is

an influx term, and could be representative of a disease state where the spine remains silent despite AMPAR influx [7]. Coupling of trafficking with signaling is critical to build mechanochemical models of complex biological processes. Even though we use simple rate representations of trafficking, these rates can be interpreted as factors outside of the signaling pathway such as membrane tension [27, 176, 177], lipid composition [178], and other mechanical factors [23, 179]. The third prediction, related to the previous insight, is that in high CaMKII conditions, the system can lose dependence on endo/exocytosis levels because CaMKII can determine the AMPAR outcome through its influence on the influx term or maxing out the exocytosis term, demonstrating how signaling can drive overall dynamics, as seen in the bistable model with high CaMKII IC (see Figure B.6a, left column).

The fourth prediction from the models is that for bound AMPAR to achieve a new steady state value, it requires one of two things. Option 1 – seen best through the with influx cases in Figure 7.6 – is an increase in the total AMPAR in the system (increased membrane AMPAR through a source term, an open system). Option 2 – The presence of a constantly driving term in the endo/exocytosis rates - either elevated PP1 or elevated CaMKII. These can be seen through the difference in bistable and monostable model behavior in Figure 7.6. The monostable model showed no dependence on endo/exocytosis when there was no influx; instead, it needed an influx of membrane AMPAR to shift the system to a new steady state value. This is why the bistable case can achieve new steady state values despite no influx, while the monostable case cannot.

Finally, we found that the monostable and bistable models had different effects on integrating time-dependent Ca^{2+} influx (Figure 7.7). For example, the bistable model was not very sensitive to temporal changes to the stimulus (Figure B.9). This is because once CaMKII reached a high steady state, it remained at that value. The monostable model

on the other hand demonstrated the ability to (a) integrate input frequency and filter out the high frequency effects while retaining sensitivity and (b) show a stimulus-dependent bound AMPAR response. Thus, we predict that while bistable models of CaMKII have appeal in terms of 'on' and 'off' switches, a monostable model has a distinct advantage of being able to respond proportionally to time-dependent input. This is a desirable trait in synaptic plasticity since frequency dependence is a huge part of learning and memory formation [180]. It has been known that frequency of stimulation can play important roles in CaMKII activation and induction of different synaptic plasticity forms [123, 181]. Historically, many models of synaptic plasticity have relied on the integration of fast variables by slower parameters [92,102,103,105,181]. Therefore, we found that integration of fast parameters by slow species in synaptic plasticity is actually model dependent. This indicates that there can be more nuance to synaptic plasticity depending on its underlying signaling network dynamics [181]. Therefore, a key takeaway from these results is that the underlying parameters and model architecture can influence not just synaptic plasticity readouts but their dependence on upstream signaling.

Here we used a simplified signaling network to investigate a complex biological process, a method that has successfully explained complex signaling dynamics in dendritic spines before [182]. We acknowledge that our model has many simplifying assumptions and adding biochemical details at various levels is required to build more confidence in these approaches. In addition to biochemical complexity, we will also need to consider other factors that are known to affect synaptic plasticity into the computational models. For instance, signaling nanodomains exist within dendritic spines [183]. Often driven by Ca^{2+} influx, these regions of activation can trigger localized events and it is hypothesized that CaMKII could behave differently in localized domains versus whole dendritic spines [133, 184]. The PSD region also acts as a protein dense, membraneless compartment that

can localize signaling processes due to enriched protein concentrations [185]. The effects of this localization and crowding are not clear; for example, while PP1 is enriched in the PSD, it is possible that crowding and additional molecular binding partners can shield CaMKII from dephosphorylation from PP1 in this region [139, 152]. Neurogranin (Ng) plays a seemingly contradictory role in dendritic spines in that despite binding CaM and thus reducing the amount of free CaM available in the system, its presence is known to lower the threshold of LTP through the NMDAR/CaMKII pathway [159, 186]. This contradiction has been explained as follows – Ng-mediated CaM sequestration in the dendritic spine effectively increases the available CaM during spine activation [109, 159]. Specifically Ng can localize CaM close to the plasma membrane of spines to enhance CaMKII activation over CaN activation, leading to enhanced synaptic strength [109, 159, 186]. Additionally, PSD95 itself gets phosphorylated and that affects accumulation at the PSD, but this signaling occurs through a different pathway [145] compared to the signaling considered in this model; therefore, we do not include PSD95 phosphorylation in this study. However, activation and localization of PSD95 and other important scaffolding species could play important roles in AMPAR dynamics at the PSD. Therefore, the localization of these subdomains can play key roles in regulating synaptic plasticity and can actually help explain some of the conflicting experimental evidence on CaMKII dynamics [187].

Trafficking also complicates matters for signaling as both PP1 and CaMKII are recruited into the spine in response to NMDAR activity [15, 139]. While we have considered some trafficking of AMPAR into the synapse through either CaMKII-mediated membrane influx or endocytosis and exocytosis, there is spatial complexity associated with trafficking of AMPAR because of lateral membrane diffusion of AMPAR from the perisynaptic region and from extrasynaptic pools both in the spine and on the dendrite, because of cytosolic influx of endosomes outside of the spine, and because of specific locations of endocyto-

sis/exocytosis [16, 188, 189]. A complication of AMPAR trafficking is that dendritic spine geometry has been found to alter AMPAR diffusion into dendritic spines, making spine geometry another important factor to investigate [114]. An important assumption in this work is that in increase in AMPAR is from AMPAR on the membrane diffusing laterally into the spine or PSD. This analysis would be different if the influx term instead affect internal AMPAR (Aint) which can only become bound AMPAR by exocytosing onto the membrane; or if there was a combination of influx through endosomes in the cytosol and laterally diffusing membrane AMPAR. Thus, spatial models that take these effects into account would be important to fully explore these details.

In summary, we have demonstrated how two different simple biochemical signaling pathways of CaMKII and PP1 can lead to different AMPAR dynamics downstream, Figure 7.8a. From a signaling perspective, our results highlight the importance of network architecture, the strength of molecular interactions, and the reaction dynamics. With regards to synaptic plasticity, our results highlight the nuances to LTP induction and how modeling efforts of LTP need to be cognizant of the many dependencies of synaptic plasticity (e.g. stimulus magnitude and frequency, upstream signaling dynamics and concentrations, signaling nanodomains, geometric considerations, etc). Both of the CaMKII/PP1 models investigated in this work are possible candidates for what occurs in dendritic spines and from our results, both probably exist as the monostable model acts as a CaMKII leaky integrator [109, 137] but CaMKII is known to autophosphorylate as in the bistable model [121]. The two different signaling dynamics might be differentiated between spatially in nanodomains of activity where conditions favor one versus the other, or they might have different triggers [190]. Nonetheless, these results indicate that the induction and regulation of synaptic plasticity, in this case LTP, might be much more nuanced than previously assumed, and will require a more thorough investigation to parse out the

different signaling, spatial, and temporal influences behind synaptic plasticity.

Acknowledgements

Chapter 7, in full, is a reprint of the submitted material Crosstalk between biochemical signaling & trafficking governs AMPAR dynamics in synaptic plasticity, 2022. Bell, Miriam; Rangamani, Padmini, 2022 [5]. The dissertation author was the primary investigator and author of this material. For Chapter 7, I would like to acknowledge my coauthor Professor Padmini Rangamani, and my funding from a National Defense Science and Engineering Graduate (NDSEG) Fellowship. We thank members of the Rangamani Lab for their comments and support.

Chapter 8

Mechanochemical modeling of AMPAR trafficking

Introduction

Dendritic spines are small protrusions along dendrites that serve as signaling subcompartments and have characteristic shapes associated with their development state, learning, memory formation, and disease states [6, 191]. Most excitatory synapses are housed in dendritic spines and regulate the strength of their connections through biochemical and structural modifications in a process called synaptic plasticity. In particular, the number of AMPARs, α-amino-3-hydroxy-5-methyl-4-isoxazolepropionic acid receptors, at the postsynaptic density (PSD) at the synapse modulates the sensitivity of the synapse to presynaptic glutamate release, effectively tuning the synaptic connection strength [172,173]. Since AMPAR density is an important indicator of synaptic plasticity, specifically long-term potentiation (LTP) and long-term depression (LTD), it is vital to understand the role played by different factors that regulate AMPAR density [192, 193].

The factors that influence AMPAR can be classified into biophysical and biochem-

ical features. Key among these factors are the (a) upstream signaling network [103], (b) trafficking mechanisms and their location specificity [154, 155, 189], (c) lateral diffusion in the plane of the spine membrane [16, 194], and (d) size and shape of the spine [195]. We briefly summarize the key experimental observations and open questions in the literature with respect to AMPAR dynamics at the PSD with a specific focus on LTP.

- **AMPAR density increases during LTP**

  AMPAR interacts with a variety of membrane bound and cytosolic proteins [118]. In particular, it binds to PSD-95 (SAP90) at the PSD where it colocalizes into clusters [161,196–198]. AMPAR density at the PSD is used as a readout for synaptic plasticity, with long term potentiation (LTP) associated with an increase in AMPAR bound to PSD95 at the synapse [156]. During LTP induction, AMPAR density is expected to increase up to 200% at the PSD within a few minutes [6, 142, 154, 199].

- **Role of CaMKII in AMPAR dynamics in LTP**

  CaMKII is an abundant, vital protein that interacts with AMPAR, along with a plethora of other proteins, molecules, and species in dendritic spines. CaMKII is implicated in controlling the level of AMPAR in spines through exocytosis rates [141], various binding/signaling interactions [200], and by triggering AMPAR influx into the spine [144, 149]. While CaMKII is known to autophosphorylate, its exact dynamics after phosphorylation have been debated as either a bistable switch with sustained elevated activity (bistable model) [135] or a transient increase followed by exponential decay (monostable model) [122, 137]. Since CaMKII is a key signaling species underlying synaptic plasticity, its spatiotemporal dynamics are of particular interest as they can significantly influence downstream AMPAR dynamics [15, 121, 152, 180, 201].

- **Role of spine size and shape**

  Dendritic spines have characteristic shapes and sizes related to their developmental stage, activation history, and function [19, 20]. Spines are typically categorized into four subtypes - filopodial, stubby, thin, and mushroom. Thin and mushroom spines tend to be more prevalent in the adult brain, where mushroom spines tend to be larger and more stable compared to the smaller and more adaptive thin spines [65, 202]. It has been experimentally observed that PSD size correlates to spine volume [203], and that AMPAR number at the PSD is proportional to synaptic area and spine head volume [21, 164, 204]. However, more recent analysis have brought these exact relationships under question [205]. Furthermore, dendritic spines' shapes and sizes are known to influence signaling [70, 102, 115], but it is unknown how spine geometry couples with trafficking mechanisms and signaling to regulate AMPAR dynamics at the PSD.

- **Role of trafficking**

  AMPARs are packaged in endosomes inside the cytoplasm which can exchange with the membrane via endocytosis and exocytosis [154, 155]. Kinase and phosphatase activity appear to influence these rates, with CaMKII and PP1 dynamics leading to exocytosis and endocytosis, respectively [110, 118, 206]. The exact location of endo/exocytosis remains unclear with evidence indicating near the PSD [154, 207], on the dendrite [199], or at various sites regulated by synaptic activity [24, 208].

- **Role of lateral diffusion and extrasynaptic pool**

  AMPAR undergoes lateral membrane diffusion at different rates in various regions of the spine membrane, depending on its biochemical interactions [16, 26, 194, 209]. Extrasynaptic pools of AMPAR on the membrane have been observed on dendritic

spines and along the dendrite [25]. It has been proposed that CaMKII signaling can influence the trafficking of AMPAR from these pools into activated dendritic spines [141, 144, 200].

While these different aspects have been studied experimentally [24, 25, 93, 111, 196, 210] and computationally [103, 110, 113, 124, 193, 201], a comprehensive spatiotemporal model that accounts for these different factors is missing in the literature. In particular, the spatial localization of these biochemical interactions and the role of dendritic spine morphology in these processes are not well-known. Dendritic spines are extremely small (femtoliter volumes) and remain challenging to probe experimentally. Therefore, we strive to address some of the open questions mentioned above through a spatial model in which we can systematically vary biophysical features and components such as spine size and shape, trafficking, and localization of membrane boundary fluxes. Here we present a computational model linking dendritic spine morphology, LTP signaling networks, AMPAR trafficking, and synaptic plasticity. Using a spatial, deterministic reaction-diffusion model, we sought to answer the following fundamental questions: How does spine morphology influence different underlying biochemical signaling pathways that determine AMPAR dynamics? What role do different trafficking modalities play in determining AMPAR dynamics? And finally, how do signaling dynamics, spine morphology, and trafficking modalities couple to regulate AMPAR density at the PSD in realistic spine geometries?

Given the multiple aspects of AMPAR regulation as noted above, we use a computational model in idealized and realistic geometries to predict the effects of biochemical and biophysical factors on AMPAR dynamics during LTP. We investigate the dynamics of two biochemical CaMKII models – a bistable model and a monostable model – on CaMKII and AMPAR behavior. We find that i) both CaMKII models produce elevated but different steady states for AMPAR levels with the monostable model capable of acting as a

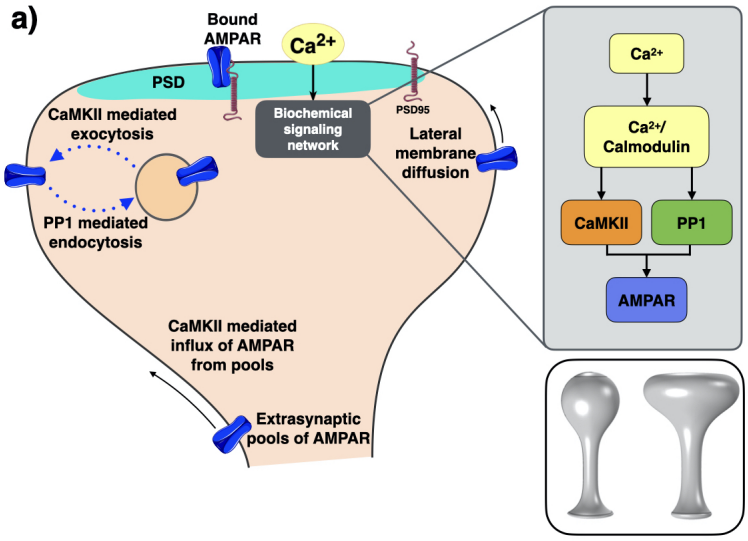

Figure 8.1: a) A combination of geometric, biochemical, and transport phenomenon factors influence AMPAR dynamics at the PSD during LTP. A biochemical network triggered by calcium influx into the spine head leads to changes in AMPAR density at the PSD. Various mechanisms govern AMPAR trafficking to the PSD, including CaMKII mediated exocytosis, PP1 mediated endocytosis, lateral membrane diffusion, and an extrasynaptic pool of AMPAR located at the base of the spine neck. Endo/exocytosis can take place anywhere on the plasma membrane. PSD95 binds AMPAR in the PSD region to form bound AMPAR. Grey inset: Biochemical signaling involves the mutual activation of CaMKII and phosphatases that compete to influence AMPAR. Bottom inset: Idealized dendritic spines represent thin (left) and mushroom (right) spines.

leaky integrator, ii) the different trafficking factors modulate AMPAR steady state values and AMPAR temporal dynamics at three key timescales, and iii) both idealized and real spine geometries show a positive correlation between total receptor number at the PSD and spine volume to surface area ratio, while exhibiting a size dependent resetting of percent change in AMPAR at the PSD which could act to optimize resources and prevent excessive synaptic plasticity in spines of certain sizes.

Model Development

To investigate AMPAR spatiotemporal dynamics, we construct a simplified biochemical signaling network describing AMPAR dynamics on the timescale of minutes in hippocampal pyramidal CA1 neurons with deterministic reaction diffusion equations, see Fig. 8.1a. Here we list various model assumptions, describe the key steps in the biochemical signaling cascade, provide the general governing equations, and characterize the idealized and realistic spine morphologies.

Model assumptions

- **Geometries:** We utilize both idealized and realistic geometries of thin and mushroom spines. Idealized geometries were taken from [27] and scaled to different volumes representative of average dendritic spine volumes [115, 146]. Realistic geometries were meshed from EM image stacks of a hippocampal dendritic segment [29,148].

- **Timescales:** We focus on AMPAR dynamics on the 5 minute timescale.

- **Reaction types:** The majority of the signaling reactions are either mass action or enzymatic Hill functions. Some reactions are custom and have explicit time dependent components such as the equations for Ca^{2+} influx through NMDAR and VSCC, and CaMKII-mediated AMPAR influx. The CaMKII-mediated AMPAR influx through the spine neck base is a flux boundary condition so there is not mass conservation for AMPAR in the system with influx. The model reactions are the same as those presented in [201] but translated to a spatial reaction-diffusion systems from a compartmental model.

- **Kinetic parameters:** Reaction rates are taken from previous studies or approximated from experimental data when possible.

- **Boundary conditions:** The stimulus to the system involves a Ca^{2+} influx through the plasma membrane as a membrane boundary condition [115]. Cytosolic AMPAR can be exchanged with membrane AMPAR through a flux boundary condition on the whole plasma membrane except the bottom of the spine neck. All other volumetric species have no flux boundary conditions on the plasma membrane. All membrane species have no flux boundary conditions at the base of the spine neck except for membrane AMPAR which has a Dirichlet boundary condition that is dependent on both active CaMKII concentration and time. Therefore, there is no mass conservation for the AMPAR species when there is a boundary flux at the spine neck base representing influx from an extrasynaptic pool of AMPAR. This AMPAR influx at the spine neck is dependent on the concentration of active CaMKII at that location and is time dependent, with a decaying exponential that acts to deactivate the term to prevent constant influx. See supplemental material for more information.

Modular construction of biochemical signaling network

To investigate AMPAR spatiotemporal dynamics, we construct a simplified biochemical signaling network describing AMPAR dynamics on the timescale of minutes in hippocampal pyramidal CA1 neurons with deterministic reaction diffusion equations, see Fig. 8.1a. We highlight the key signaling components below.

- **Model stimulus and Ca^{2+} Module:** The dendritic spine is activated by a voltage depolarization at the membrane that represents an excitatory postsynaptic potential (EPSP) and a backpropagating action potential (BPAP) offset by 2 ms. This voltage spike activates NMDAR localized at the PSD, and VSCC across the whole dendritic spine membrane. Ca^{2+} is then pumped out of the spine through PMCA and NCX pumps or is bound to other signaling species. All calcium influx and efflux reactions

are taken from [115].

- **Calmodulin Module:** Ca^{2+} activates calmodulin (CaM) to form a Ca^{2+}/CaM complex [124]. We model this binding as a single mass action reaction. Free CaM can also bind to Neurogranin (Ng), so Ng acts as a CaM sink in this system.

- **CaMKII and phosphatase Module:** To investigate the controversy surrounding CaMKII dynamics [110, 137], we consider two different CaMKII and PP1 models (orange and green in Fig. 8.1).

  - **Bistable model:** The bistable CaMKII model is designed to show bistable behavior dependent on the level of calcium influx and the relative concentrations of CaMKII and PP1 [124]. CaMKII is activated by the Ca^{2+}/CaM complex, can autophosphorylate itself, and is deactivated by active PP1. For the phosphatase cascade, calneurin (CaN) is activated by the Ca^{2+}/CaM complex, and subsequently activates inhibitory-1 (I1), which then activates protein phosphatase 1 (PP1) that can autoactivate itself. All the phosphatases are deactivated by active CaMKII. For our selected calcium influx and initial conditions of CaMKII and PP1, we expect a sustained high concentration of activated CaMKII following activation for this bistable model.

  - **Monostable model:** The monostable model is designed to show exponential decay of both CaMKII and PP1, due to their rate change being linearly dependent on their own concentration. In this way, CaMKII exhibits transient activation and always has a single steady state of zero concentration. Both CaMKII and PP1 are directly activated by Ca^{2+}/CaM. We fit CaMKII and PP1 decay dynamics to both experimental and other modeling results [116, 136, 137].

- **AMPAR signaling and trafficking Module:** The last module (blue in Fig. 8.1)

captures AMPAR dynamics. Free AMPAR is modeled on the whole plasma membrane and can be bound by PSD95 in the PSD region to become bound AMPAR with a slower diffusion coefficient. Thus, bound AMPAR is localized to the prescribed PSD membrane. Endocytosis and exocytosis can occur throughout the whole plasma membrane as boundary conditions that exchange membrane AMPAR and cytosolic AMPAR through CaMKII mediated exocytosis and PP1 mediated endocytosis [110]. We note that this is an important assumption since existing literature predicts that there is limited or no exocytosis and endocytosis in the PSD region due to the crowded environment [154, 207]. Active CaMKII also mediates the influx of membrane AMPAR from an extrasynaptic pool modeled as a membrane flux at the base of the spine neck [141, 200].

The signaling networks used in this model can be found in [201] and are described in more detail in the Supplemental Material.

Governing equations

We construct a system of partial differential equations representing the reaction-diffusion dynamics of signaling species in three different spatial compartments. The spatial regions include the cytoplasm (3D volume), plasma membrane (2D surface), and the PSD membrane (a subset of the plasma membrane, 2D surface). The reaction diffusion dynamics of each signaling species, c_i, are given by

$$\frac{\partial c_i}{\partial t} = D_{c_i} \nabla^2 c_i + R_i, \tag{8.1}$$

with the boundary condition given as

$$- D_{c_i}(\mathbf{n} \cdot \nabla c_i)|_{\partial\Omega} = J_i. \tag{8.2}$$

R_i is the reactions for species c_i in its respective compartment. J_i is the boundary condition for species c_i on boundary $\partial\Omega$. For a volumetric species, its reaction diffusion dynamics occur within the 3D volume and boundary conditions are on its encompassing 2D surface. For a membrane species, its reaction diffusion dynamics occur on its 2D surface and boundary conditions are on any encompassing 1D line. All signaling species can diffuse unless specifically stated, such as in the trafficking knockout case with no diffusion for membrane AMPAR. All volumetric species have no flux boundary conditions except for Ca^{2+}, and cytosolic AMPAR (Aint) which exchanges with membrane AMPAR (Amem). All volumetric species have a no flux boundary condition at the bottom of the spine neck. For the membrane bound species, PSD95 and bound AMPAR are localized to the PSD and have no flux boundary conditions along the PSD perimeter, while Amem is on the whole plasma membrane and has a flux boundary condition at the perimeter of the spine neck base. All species have homogeneous initial conditions within their respective compartments. Ca^{2+} influx acts as the stimulus to the signaling cascade and involves localized membrane fluxes at the PSD and along the plasma membrane.

The specific equations, boundary conditions, initial conditions, and parameters can be found in the Supplemental Material.

Spine model geometry

We modeled both 2D axisymmetric idealized spines and 3D realistic spines reconstructed from EM images [29], as isolated compartments. Idealized spines were modeled after characteristic thin and mushroom spines, see inset in Fig. 8.1 and [27], and realistic spines were selected from the dendritic segment shown in Fig. 8.6a. A range of spine sizes

were explored for both idealized and realistic geometries, with care taken to select a variety of realistic spine morphologies. The plasma membrane was modeled as the whole spine surface except for the bottom base of the spine neck, and the PSD regions were labelled at the top of the spine head for idealized geometries and as denoted during segmentation for the realistic spines. We quantify the various spine morphologies in terms of their volumes (vol) and their volume to surface area (SA) ratio (VSA ratio).

Simulation variations

To investigate the role of biochemical signaling, we consider two different biochemical signaling networks for CaMKII and PP1 - the bistable and monostable models described above. We also consider different trafficking knockout conditions. Specifically, we vary the presence of endocytosis and exocytosis, an extrasynaptic AMPAR influx, and membrane diffusion of free membrane AMPAR. Computationally, this involves turning on and off the terms for these various components. We also consider stimulus frequency by using active Calmodulin pulses directly as input into the system. For the realistic spine geometries, a simplified model was utilized with the temporal dynamics of active CaMKII and active PP1 acting as the stimulus for a reduced biochemical network of Aint, Amem, PSD95, and bound AMPAR. Due to geometric complexity and thus numerical complexity, endocytosis and exocytosis were localized to the PSD for the realistic spine simulations.

Numerical methods

All simulations were run in COMSOL Multiphysics, a commercial finite-element software. The general form and boundary partial differential equations (PDEs) interface was used. For the various simulations, a COMSOL generated mesh of “extra fine” or “extremely fine” elements was selected with several boundary layers added to the membrane.

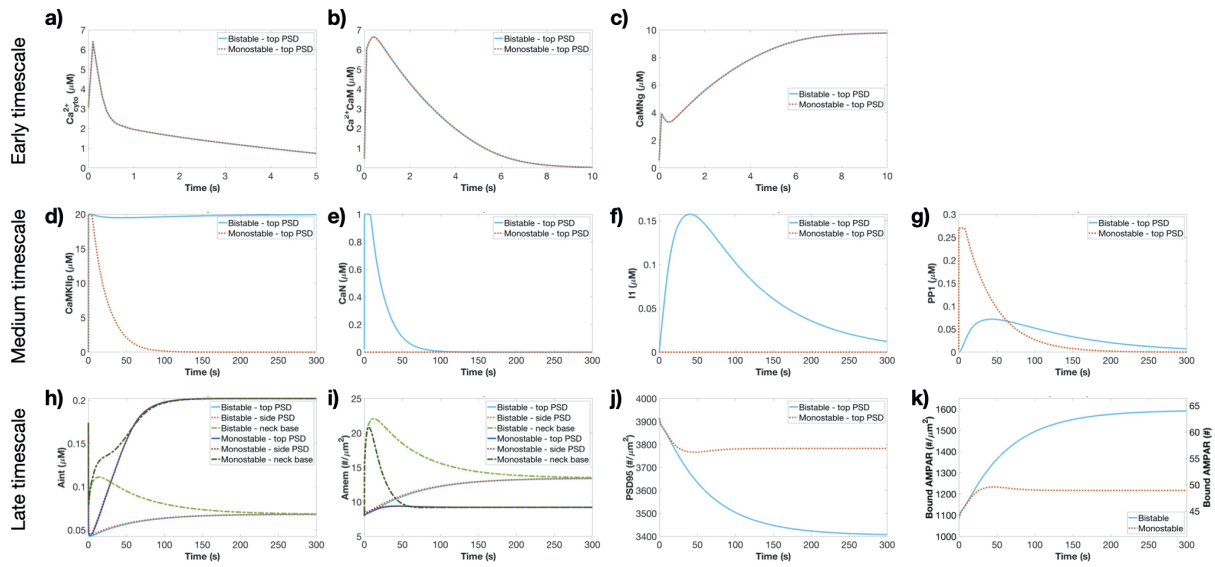

Figure 8.2: **Temporal dynamics of key species in both biochemical models in a control thin spine.** Temporal dynamics of the early timescale species Ca^{2+} (a), active calmodulin (Ca^{2+}/CaM; b), and CaM bound Neurogranin (CaMNg; c). Temporal dynamics of medium timescale species active CaMKII (d), CaN (e), I1 (f), and PP1 (g). Temporal dynamics of late timescale species cytosolic AMPAR (Aint; h), membrane AMPAR (Amem; i), PSD95 (j), and bound AMPAR plotted as density and total receptor number (k).

Boundary layers were added due to the complex boundary conditions and geometry in the simulations. The absolute tolerance was lowered to 0.0001 for all simulations.

Analysis and plotting were performed in MATLAB.

Results

We develop two separate models of CaMKII and PP1 dynamics to explore both bistable dynamics that lead to elevated activated CaMKII concentration and monostable dynamics that lead to transient CaMKII dynamics, see Figure 8.2 for both CaMKII and PP1 temporal dynamics. We consider bound AMPAR dynamics at the PSD as both a receptor density and total receptor number as the readout of the model. Total receptor

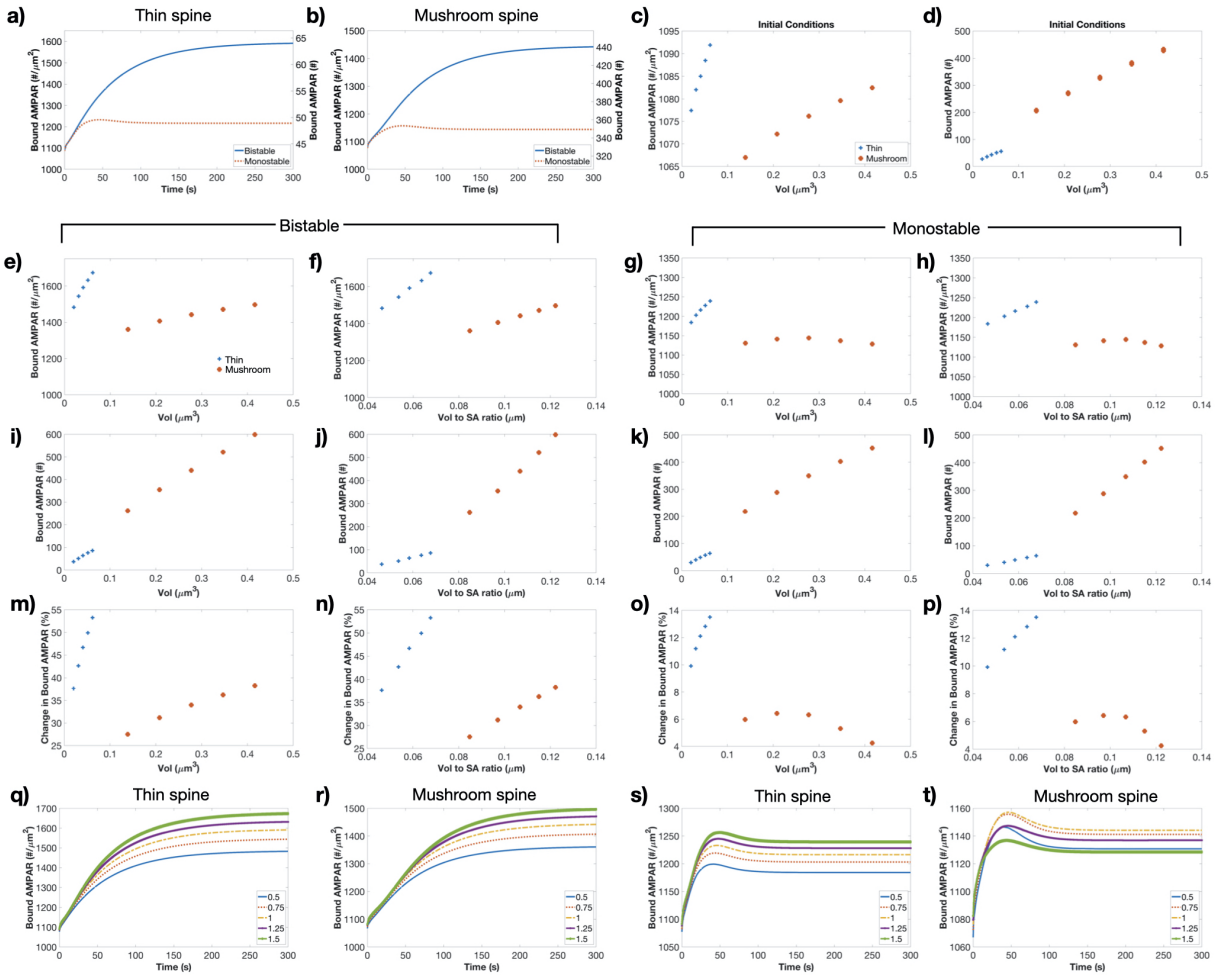

Figure 8.3: **Bound AMPAR dynamics for thin and mushroom spines of different sizes.** Temporal dynamics of bound AMPAR for both the bistable and monostable models (blue and red lines, respectively) for a control thin spine (a) and for a control mushroom spine (b). Each simulation is run to its steady state in the absence of a stimulus. Initial conditions of bound AMPAR for each spine is given as a density (c) and total receptor number (d). Blue points denote the thin spines and red points denote the mushroom spines. We consider the steady state of bound AMPAR at 300 s for each spine for both the bistable and monostable models versus volume and volume to SA ratio as a receptor density (e-h), total receptor number (i-l), and percent change from steady state (m-p). We plot the temporal dynamics of bound AMPAR at the top of the PSD for each size of spine for the thin (q) and mushroom (r) spines for the bistable model and the thin (s) and mushroom (t) spines for the monostable model.

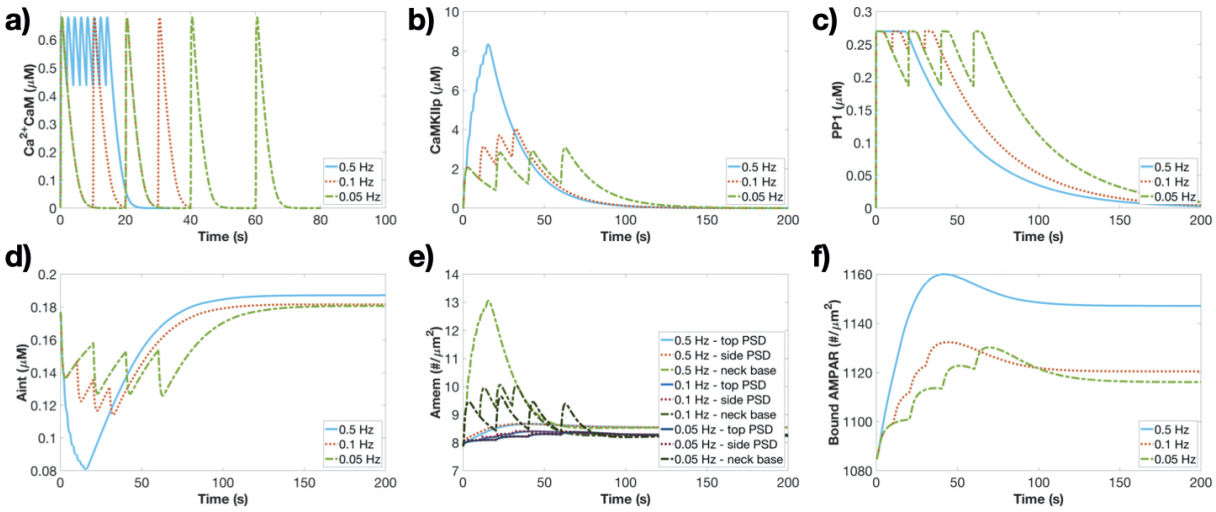

Figure 8.4: **Temporal dynamics of monostable model in a thin control spine for Ca^{2+}CaM pulses of different frequencies.** a) Ca^{2+}CaM temporal dynamics at three different frequencies (0.5, 0.1, and 0.05 Hz) at the top of the PSD region for the monostable model. Temporal dynamics of active CaMKII (b), active PP1 (c), cytosolic AMPAR (d), membrane AMPAR (e), and bound AMPAR (f) for three different frequencies for the monostable model.

number is obtained by integrating receptor density over the PSD membrane area. We investigate three different trafficking mechanisms as shown in Fig. 8.1a - a CaMKII-mediated influx of membrane AMPAR from extrasynaptic pool of membrane-bound AMPAR at the base of the spine neck (influx term), lateral membrane diffusion of AMPAR, and CaMKII and PP1 mediated exocytosis and endocytosis of AMPAR, respectively. We vary these trafficking conditions in five cases - 1. a control case with all trafficking conditions, 2. no influx at the spine neck base (no influx), 3. no influx and no endo/exocytosis of AMPAR (only diffusion), 4. no endocytosis/exocytosis (no En/Ex), and 5. no lateral membrane diffusion of AMPAR (no diffusion).

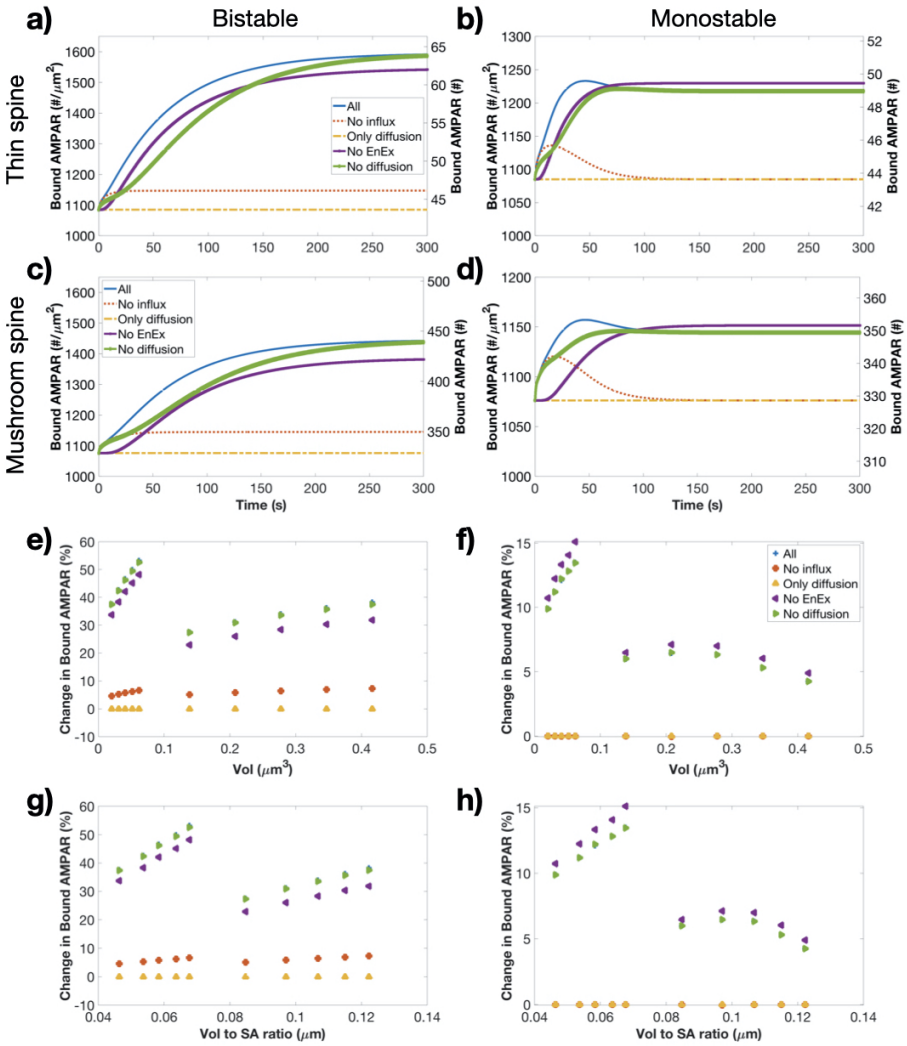

Figure 8.5: **Bound AMPAR dynamics and steady state behavior for different trafficking knockout conditions.** Temporal dynamics of bound AMPAR at the top of the PSD for the thin control spine for different trafficking knockout cases for the bistable (a) and monostable (b) models. Temporal dynamics of bound AMPAR at the top of the PSD for the mushroom control spine for different trafficking knockout cases for the bistable (c) and monostable (d) models. Percent change in bound AMPAR steady state from initial condition for all spine volumes for the different trafficking knockout cases for the bistable (e) and monostable (f) models. Percent change in bound AMPAR steady state from initial condition for all spine volume to SA ratios for the different trafficking knockout cases for the bistable (g) and monostable (h) models.

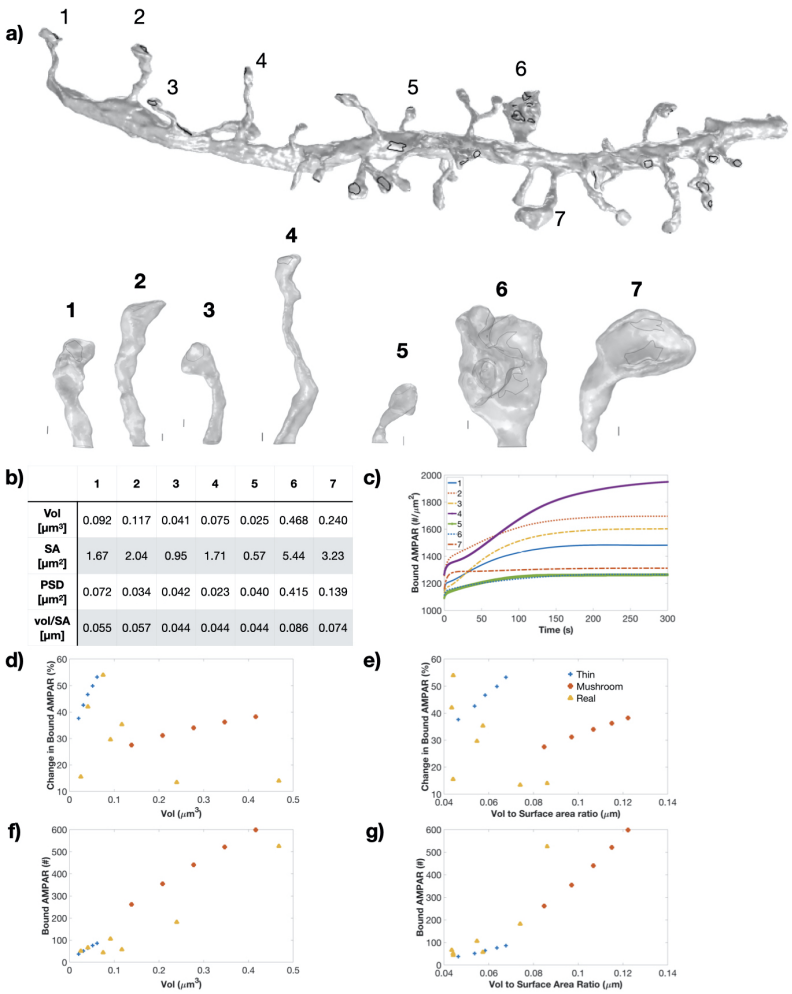

	1	2	3	4	5	6	7
Vol [μm³]	0.092	0.117	0.041	0.075	0.025	0.468	0.240
SA [μm²]	1.67	2.04	0.95	1.71	0.57	5.44	3.23
PSD [μm²]	0.072	0.034	0.042	0.023	0.040	0.415	0.139
vol/SA [μm]	0.055	0.057	0.044	0.044	0.044	0.086	0.074

Figure 8.6: **Bound AMPAR dynamics and steady state behavior for the bistable model in realistic geometries.** a) Dendritic segment reconstructed from EM data stacks in [29]. We conduct simulations for the bistable model in all the numbered spines, shown below the segment. Scale bars next to each individual spine correspond to 100 nm. PSDs are denoted by black lines on the dendritic segment and light grey lines on the individual spines. b) Geometric parameters including volume, surface area, PSD surface area, and volume to surface area ratio for the various realistic spines. c) Temporal dynamics of bound AMPAR at the top of a PSD for the 7 different realistic spines. Percent change in bound AMPAR steady state at 300s for idealized and realistic spines versus spine volume (d) and volume to SA ratio (e). The thin spines are in blue, mushroom spines are in red, and realistic spines are in yellow. Steady state at 300s of total number of bound AMPAR at the PSD for idealized and realistic spines versus spine volume (f) and volume to SA ratio (g).

Temporal dynamics are primarily homogeneous except for AMPAR species

We consider the temporal dynamics of key species for a thin spine of average volume, Figure 8.2. The temporal dynamics of key species show similar dynamics to our previous compartmental ODE model [201]. Most species showed homogeneous spatial dynamics due to homogeneous initial conditions for all species and fast Ca^{2+} diffusion. Ca^{2+} acts on a fast timescale to activate downstream species such as calmodulin (CaM), to produce Ca^{2+}CaM. Calmodulin also activates Neurogranin (Ng) which acts as a CaM sink. Both models show similar early timescale dynamics (Figure 8.2a-c) but the different CaMKII and phosphatase models translate to very different medium timescale events (Figure 8.2d-g). In the bistable model, CaMKII remains elevated while CaMKII in the monostable model activates and decays exponentially. For both models, PP1 activates and decreases, with the bistable model showing a delayed activation due to the temporal delay in the phosphatase cascade. AMPAR dynamics in the cytosol (Aint) and on the membrane (Amem) show spatial heterogeneity during early timescales but eventually reach a homogeneous steady state, Figure 8.2h-i. Both models show elevated Amem at the base of the spine neck (light and dark green lines) due to the Amem boundary condition that is dependent on active CaMKII activity. Cytosolic AMPAR initially rapidly decreases for both models but then increases for both at the neck base as membrane AMPAR is endocytosed due to its high density. PSD95 and bound AMPAR dynamics show opposite decreasing and increasing dynamics as expected, since PSD95 binds to membrane AMPAR to form bound AMPAR, Figure 8.2j-k. The bistable model produces a higher steady state of bound AMPAR and membrane AMPAR compared to the monostable model, but the monostable model has higher cytosolic AMPAR compared to the bistable steady state. Interestingly, the monostable model actually increases its cytosolic store of AMPAR after activation.

Bound AMPAR shows clear trends across both spine size and shape

We consider an idealized thin spine and mushroom spine with volumes representative of average thin and mushroom spines, respectively. Typically thin spines tend to be smaller in volume than mushroom spines, so the control thin spine is approximately 7 times smaller than the control mushroom spine. The thin spine and mushroom spine show similar temporal dynamics for both the monostable and bistable models, Figure 8.3a,b. We note that while the bound AMPAR densities are within similar ranges, these densities translate to larger total number of receptors for the mushroom spine as it has a larger PSD surface area. We vary the control thin and mushroom spines volume by increasing and decreasing them by 50% to explore the dendritic spine size space. As noted above, each simulation is run to steady state before applying the model stimulus, resulting in slightly different bound AMPAR steady states for each spine geometry. We plot the initial conditions for bound AMPAR for all spine geometries as a receptor density and total receptor number (Figure 8.3c-d) and we see that while the thin spines tend to have higher initial receptor densities, those densities translate to much smaller total receptor numbers compared to the mushroom spines.

We run simulations in these various spine geometries and consider the steady state value for bound AMPAR as a receptor density, total receptor number, and percent change from steady state, and plot them against both volume and volume to surface area ratio for the different spines geometries and two different biochemical models Figure 8.3e-p. For the bistable model, plots of bound AMPAR density and percent change versus volume and volume to surface area ratio showed similar trends; as the thin spines (smaller, blue dots) and mushroom spines (larger, red dots) increase in volume or vol to SA ratio within their shape group, the steady state bound AMPAR density increases Figure 8.3e-f; m-n.

However, when transitioning from the thin spines to the larger mushroom spines, the bound AMPAR density (or percent change) drops, resetting to a lower density (or percent change) that then increases as the mushroom spines gets larger. For the monostable model, plots of bound AMPAR density and percent change versus volume and volume to surface area ratio show a similar reset between the thin and mushroom spines (Figure 8.3g-h; o-p); however within the mushroom spines (red dots), there is a nonmonotonic change in receptor density and percent change as the volume (or vol/SA) increases. When considering total receptor number (Figure 8.3i-l), both the bistable and monostable models show similar trends with increasing receptor numbers for increasing vol (and vol/SA) which is to be expected from the initial conditions. There is a discontinuity of the trend between the different spine shapes which is accentuated in the volume to SA ratio plots.

To get a better understand of the range of values accessed by changing spine volume, we plot the temporal dynamics of each spine shape for the two different models (Figure 8.3q-t). We clearly see that for both shapes in the bistable model and for the thin spine in the monostable model, a larger spine leads to a larger increase in bound AMPAR; while in contrast, the mushroom spine with the monostable model shows a maximal increase in bound AMPAR for the control volume spine.

Considering all these various metrics, there is a resetting of the bound AMPAR density (or percent change in bound AMPAR) between the two spine shapes seen across spine volume (and vol to SA ratio). This trend matches the pattern found for synaptic weight updates based on Ca^{2+} influx into dendritic spines of different sizes and geometries [211]. Thin spines are able to increase the density of bound AMPAR more rapidly for increases in their volume; while in comparison, mushroom spines have a slower increase in density with respect to volume. This supports previous reports that thin spines are more adaptive compared to mushroom spines [65, 202]. This resetting of bound AMPAR for

larger mushroom spines can act to optimize biochemical resources, preventing excessive bound AMPAR density increases for larger spines which would translate to much higher total receptor numbers.

It is important to note that each geometry started with the same initial conditions but was run to steady state in the absence of stimulus. The only species that reached new steady states were the AMPAR species and PSD95. The new bound AMPAR initial conditions range approximately 30 ($\#/\mu m_2$) across the different sized spines. Therefore, to verify that the stimulus causes the trend in bound AMPAR within each spine shape, we consider a variety of metrics for AMPAR. Clearly, the trend in bound AMPAR density still holds within each spine shape for different spine sizes when we factor in each simulations' initial conditions by considering percent change. However, when considering change in bound AMPAR in terms of total receptor number, we see a discontinuity in the transition between thin and mushroom spines as the spine vol (or vol/SA ratio) increases, Figure 8.3i-l.

Therefore, when factoring in the differences between initial steady state values across spine sizes and shapes, the difference between the thin and mushroom spines is emphasized. It appears that transitioning between a thin spine and a mushroom spine serves as a beneficial means to reduce the increase in AMPAR density as the same increase for a larger spine would correspond to a larger total number of receptors, which could strain dendritic spine resources.

The biochemical models also show important differences with the bistable model leading to much larger percent increases in bound AMPAR compared to the monostable model ($\sim$ 55% increase vs $\sim$ 14 % increase, respectively). Additionally, the mushroom spines with the monostable model show the only dynamics that are not a monotonic increase in bound AMPAR density or percent change (Figure 8.3h,p,t). It is possible that

as the mushroom spines increased in volume, there was a trade off between how quickly AMPAR could flood into the spine due to the CaMKII-dependent influx and subsequently diffuse to the PSD, versus how far the AMPAR must travel and how quickly CaMKII deactivates in the monostable model.

The monostable model integrates calmodulin stimulus as a leaky integrator

We next consider how stimulus frequency can influence bound AMPAR readout. We applied active CaM pulses at different frequencies throughout the whole spine as the model stimulus instead of calcium influx, Figure 8.4a. We note that we use a much smaller active calmodulin magnitude for these pulses compared to our model (see Figure 8.2b) to prevent rapid activation of CaMKII which would prevent us from seeing any temporal nuances. The bistable model shows no dependence on frequency, with all stimulus activating CaMKII to its maximum concentration and bound AMPAR showing similar dynamics, Figure C.1. For the monostable model, CaMKII acts as a leaky integrator for all frequencies and this integration behavior translates into bound AMPAR dynamics for the 0.1 Hz and 0.05 Hz stimulus that show the integration effects, Figure 8.4b-f. Free AMPAR (Amem) show location dependent behavior as the influx at the spine neck base is dependent on active CaMKII, Figure 8.4e.

Trafficking knockout cases mimic trends in the control trafficking cases

We next considered the contributions of different trafficking mechanisms by systematically knocking out various terms. Specifically, we consider five different cases - 1. a control case with all trafficking conditions (all), 2. a case with no influx at the spine

neck base (no influx), 3. a case with no influx and no endo/exocytosis of AMPAR (only diffusion), 4. a case with no endocytosis/exocytosis (no EnEx), and 5. a case with no lateral membrane diffusion of AMPAR (no diffusion). We consider the temporal dynamics of the thin and mushroom control spines for the bistable and monostable model for these various trafficking variations, Figure 8.5a-d. Both spine shapes show similar bound AMPAR temporal dynamics within each biochemical model.

We will review the bistable model temporal behavior first, Figure 8.5a,c. Bound AMPAR in the all trafficking (all, blue) condition increases quickly and plateaus gradually as the CaMKII-mediated influx continues since CaMKII remains activated in the bistable model for these initial conditions. When there is no influx (red), we see a similar rapid increase like the control case but then a quick plateau to a lower steady state value. In the only diffusion case (yellow), there is no change in bound AMPAR, verifying that the system begins at steady state. In the no endo/exocytosis case (purple), we see a clear temporal delay in bound AMPAR increase before it plateaus in the same manner as the control case but at a slightly reduced steady state. In the no membrane diffusion case (green), we see a fast initial increase but then slower increase dynamics before the system eventually reaches the same steady state as the control case.

The monostable model leads to different behavior compared to the bistable model, Figure 8.5b,d. The control case (blue) rapidly increases to a peak, slightly decreases and then plateaus to a steady state that is significantly lower than the bistable model. This is due to the transient CaMKII dynamics which means that there is a significantly smaller influx of extrasynaptic AMPAR at the spine neck for the monostable model. The no influx case transiently increases and then returns to its initial steady state (red). This supports the concept that bound AMPAR requires a consistent forcing term (sustained elevated CaMKII to force exocytosis) or a change in available AMPAR to reach a new

steady state [201]. Similar to the bistable model, the only diffusion case (yellow) shows no change from initial condition. The no endocytosis/exocytosis case (purple) shows a delayed increase in bound AMPAR but smoothly reaches a new steady state value that exceeds the steady state for the control case. In the no membrane diffusion case (green), similar to the bistable model, we get an initial increase like the control case but then a slower gradual increase to the same level as the control case.

Interestingly, the no endocytosis/exocytosis case in the monostable model has a higher steady state than the control case. In the control case, the monostable model has an increase in internal AMPAR following stimulus, with Aint steady state increasing from its initial condition (compared to the bistable model decreasing from its initial condition). Without the ability to undergo endocytosis, the system has more available membrane AMPAR to convert to bound AMPAR, leading to the elevated steady state compared to the control case.

Therefore considering these knockout cases, we conclude that the initial rapid increase in bound AMPAR is due to endocytosis and exocytosis. We also predict that the rate of increase of bound AMPAR after approximately 25 seconds is membrane diffusion dependent and therefore modifications to AMPAR membrane diffusion could modulate the later stage dynamics of AMPAR increase. Additionally, the steady state of bound AMPAR depends on the total amount of AMPAR available to the system, including membrane AMPAR from the influx and cytosolic AMPAR from exocytosis and endocytosis. Assuming available endocytosis and exocytosis locations, even without membrane diffusion, bound AMPAR can increase to the same steady state as the control case.

Next, we want to understand how changing spine size can affect these trafficking trends. We consider the percent change in bound AMPAR steady state versus both volume and vol to SA ratio for spines of different sizes for all trafficking cases, Figure 8.5e-h. We

find that the patterns versus vol and vol to SA ratio observed previously for the control case hold for the various knockout cases. In particular, the no influx case showed no change from initial density for the monostable model but marginal increases in the bistable model (red dots). The only diffusion case showed no change in bound AMPAR for both models and all geometries (yellow dots). The no endo/exocytosis case mimicked trends with respect to geometry found in the control case, but with a slight decrease in the bistable model and slight increase in the monostable case (purple dots). The no diffusion case had the same changes in bound AMPAR steady states as the control case (green dots that overlap the blue dots). Therefore, it is important to consider both temporal and steady state dynamics of bound AMPAR to fully understand the consequences of trafficking mechanisms.

Realistic spines show a similar trend as idealized spines for the bistable model

We next want to consider if these geometric trends held for realistic spines which have much more variability and complexity to their morphologies [18]. We used spine geometries reconstructed from EM images [29] and meshed to a sufficient quality to run simulations [148]. However, due to the complexity of the geometries and thus numerical complexity, we considered a simplified model setup. Specifically, due to the spatial homogeneity of upstream signaling species, we only simulate the AMPAR species and PSD95, with a temporal input of spatially homogeneous active CaMKII and PP1 dynamics taken from the thin control spine simulation results. We also localize AMPAR endocytosis and exocytosis to the PSD membrane, which should act to delay the rise to steady state but we predict should achieve similar steady state as if endocytosis and exocytosis existed everywhere. We acknowledge that experimental evidence suggests that endocytosis and exocytosis is most likely localized at the perisynaptic membrane adjacent to the PSD

rather than at the PSD itself [154, 207], but we make this computational assumption because we are focusing on steady state as opposed to spatiotemporal dynamics for this specific analysis.

We consider the bistable model in these realistic spine geometries because the idealized bistable model spines showed fairly large percent increases and clear trends, Figure 8.3. We pick seven reconstructed spines of different volumes from a single dendritic segment, Figure 8.6a. The different spines had a variety of morphologies with different volumes, surface areas, and PSD surface areas, Figure 8.6b. The various realistic spines were run to an initial steady state, and with the CaMKII and PP1 stimulus all show increasing bound AMPAR dynamics, Figure 8.6c.

We compare the percent increase to bound AMPAR steady state in the realistic spines to the ideal thin and mushroom spines, and observe a noisier trend Figure 8.6d-e. Specifically, when plotted against volume or volume to SA ratio, in the smaller vol (or vol to SA) regime, there was an faster increase in percent increase as the spines increased in volume (or vol/SA). The percent increase then reset around a particular value for volume or vol/SA, before increasing again for larger volumes (or vol/SA). Therefore, it appears that realistic spines follow a similar trend to the idealized spines; within a smaller volume (or vol to SA ratio) regime (below 0.1 μm^3 or 0.07 μm), percent increase in bound AMPAR increases quickly as the geometric parameter increases. There is then some resetting regime where the percent change falls, and then the percent change increases with increasing geometric parameter again but at a slower rate. However the realistic spines have a less clean trend and instead show more variability. For example, comparing realistic spines 3, 4, and 5, these spines have different morphologies and volumes, but almost exactly the same volume to surface area ratio. Therefore, what geometric parameter we consider will show a different trend for bound AMPAR increase Figure 8.6d-e.

We last consider the total receptor number by integrating receptor density across PSD surface area for the realistic spines and idealized spines versus volume and volume to SA ratio, Figure 8.6f-g. We see that similar to the idealized spines, the realistic spines show an increasing trend in total receptor number versus both volume and volume to SA ratio.

Discussion

AMPAR dynamics are vital for synaptic plasticity, synaptic transmission, and proper neuronal function. The importance of AMPAR in LTP is well established and much work has been done to investigate the signaling pathways and trafficking modalities related to AMPAR behavior. However, how all these various factors interact to modulate AMPAR dynamics remains unknown. In this work, we propose that AMPAR dynamics depend on a combination of trafficking modalities and a complex interplay between spine morphology and signaling networks. We investigated these dynamics by considering two different biochemical models for the underlying kinase and phosphatase interactions (bistable and monostable) in idealized spines of two different shapes (thin and mushroom). We systematically varied the volumes of these two idealized shapes to explore the geometric parameter regime (Figure 8.3) and varied the biochemical stimulus frequencies to consider biochemical filtering (Figure 8.4). We then performed knockout simulations of the different trafficking mechanisms in the idealized spines of different volumes, Figure 8.5. Finally, we compared our predictions for the bistable model in idealized spines with realistic spine morphologies, Figure 8.6. We found several predictions based on these simulations which we will discuss below.

The first insight is that upstream cytosolic signaling species show homogeneous spatial dynamics at these extended timescales (Figure 8.2) and mimic the dynamics seen

in our previous compartmental model results [201]. This is due to the homogeneous initial conditions for all cytosolic species and the fast diffusion of Ca^{2+} that activates the system, such that Ca^{2+} itself achieves a uniform spatial distribution within seconds of its influx. However, we did see spatial heterogeneity in the membrane bound species. For the AMPAR species, we found that the influx of membrane AMPAR at the spine neck leads to a transient elevation in cytosolic and membrane AMPAR at that location, but given enough time, both species return to a single steady state Figure 8.2h-i. However, if more specific localization of cytosolic species is considered, the role of cytosolic nanodomains might come into play.

The second insight is that, similar to the previous compartmental model results, the monostable model exhibits leaky integrator dynamics in a full spatial system while the bistable model did not, see Figure 8.4 and Figure C.1; compare to compartmental model in [201]. In this spatial system, there are more distinct integration steps with the lower frequency pulses compared to previous ODE model results, which could be attributed to diffusive effects as the system has to equilibrate across the whole spine geometry. The time needed to spatially equilibrate can also been seen in the overlap between the 0.1 Hz and 0.05 Hz cases, where the the lower frequency cases causes a higher delayed peak of bound AMPAR that is comparable to the 0.1 Hz case, but then drops to a lower steady state. Both these first two insights show the importance of spatial modeling where reaction-diffusion coupling and localization of membrane fluxes and boundary conditions can alter signaling dynamics.

The third insight is that idealized and realistic spines showed clear trends in regards to geometric parameters for both models, with a reset regime where percent increase drops, Figure 8.3. Both the bistable and monostable models displayed this resetting dynamics, and the trend held in both idealized and realistic spines. There were however model de-

pendent trends with receptor density and percent change within idealized spine shape, volume, and vol to SA ratio. The bistable model showed increasing percent change within idealized shapes as the spine size got larger; however the monostable model showed an increasing trend for the small thin spines but a nonmonotonic trend for the larger mushroom spines. Additionally, the percent changes in the bistable model are much larger than the percent changes in the monostable model, which is consistent with previous studies of the system [201]. The realistic morphologies emphasized the resetting between smaller and larger spines but did not show as clear trends within those volume regimes, Figure 8.6. Therefore, the bound AMPAR response can be thought of as three geometric regimes; the first at small volumes (or vol to SA ratio) shows large percent increases in bound AMPAR, the intermediate regime shows a suppressed response, and the large vol (vol to SA ratio) regime shows increases but at a slower rate. It is still unclear why these resetting behavior occurs at these particular volume or vol to SA ratio regime, and further investigation is needed to pinpoint the significance of those regimes.

These complex realistic spines also demonstrate how spine morphologies have various geometric parameters that can modulate their dynamics and it is still unclear what parameters matter and how they affect the system dynamics. It is important to note that we consider percent increase in bound AMPAR because bound AMPAR can be read as a density or in terms of total receptors at the PSD. It is highly likely that it is important to consider both readouts since density could capture what the local environment at the spine experiences while total receptor number can capture the importance of the synapse to the overall neural system. This is particularly important because small thin spines showed a larger biochemical increase in bound AMPAR and therefore an ability to dynamically adapt; while large mushroom spines showed a smaller percent increase in bound AMPAR but represent more receptors at their PSDs, which shows their biochem-

ical stability. Therefore, we hypothesize that dendritic spines utilize different geometric parameters to modulate their responses during synaptic plasticity. In particular, we believe the division between smaller and larger spines serves to optimize resources where the geometric features of larger spines lead them to be biochemically conservative or stable compared to smaller spines. Additionally, it might be advantageous to prevent excessive bound AMPAR increase in some intermediate spine volume regime to prevent too many medium sized spines from utilizing too many resources. This supports the idea of resource optimization amongst spine clusters, where important large spines must have enough resources to uphold the neural network architecture and fundamental communication, while smaller spines need resources to form new connections; which leads to medium spines restricting their synaptic response [87]. It is highly likely that additional geometric features, such as PSD area, PSD number, spine neck geometry, and internal ultrastructure such as spine apparatus could also serve to tune the synaptic response, as has been hypothesized by others [205]. Therefore, the control of these morphological features effectively tunes the response of a spine during structural plasticity, highlighting the importance of structure-function feedback.

Finally, the fourth insight is that different trafficking modalities impact different aspects of the bound AMPAR response. In particular, breaking the AMPAR response at the PSD down into three temporal regimes, the fast timescale dynamics (0-20s) appear to be due to endocytosis and exocytosis, the intermediate timescale dynamics (20-200s) appear to be due to diffusion, and finally the late timescale steady state dynamics are governed by the availability of total AMPAR (cytosolic, membrane bound, bound to PSD95, and influx from extrasynaptic pools), Figure 8.5. Similar to previous findings [201], the system needs either a constant forcing term (such as elevated CaMKII or PP1) or AMPAR influx to change steady state bound AMPAR. There various trafficking trends held for different

spine geometries.

While we have been able to couple biochemical signaling, trafficking, and spine morphology, there are limitations to this model and many extensions to this work. Below, we discuss some next steps based on key findings in our work.

We found that endocytosis and exocytosis of AMPAR play key roles in short timescale AMPAR dynamics; however, we do not account for the timescales of the physical mechanisms of endosome fusion or fission, or the physical obstacles that could impede endosome movement within the spine. In particular, the PSD region is extremely dense and it has been hypothesized that endo/exocytosis would be hindered in this region [189,207,212]. In our model, we allowed AMPAR endo/exocytosis along the whole plasma membrane, including the PSD area; therefore, it would be valuable to investigate the consequences of restricted endocytosis and exocytosis. Regarding timescales, the discovery of ultrafast endocytosis provides optimism that AMPAR exocytosis could potentially occur over the short timescales that we propose here [177].

AMPAR is also known to form distinct clusters with a variety of different proteins and scaffolding molecules [14, 16, 161], and the dynamics of cluster formation and stability remains debated [197, 213]. We treat the PSD as a single large homogeneous cluster, so the consequences of these clusters have not been investigated. We found that the role of endo/exocytosis, membrane lateral diffusion, and extrasynaptic pools all appear to play important but temporally segregated roles in AMPAR increase at the PSD. This might suggest that these various AMPAR trafficking mechanisms act as duplicate pathways for AMPAR increase. Closer examination of the locations of both endo/exocytosis and extrasynaptic pools, and clarification on cytosolic and membrane diffusion rates would provide valuable insight into this prediction.

Varying spine size shows an interesting trade-off between signal resilience and max-

imum increases for bound AMPAR density. Smaller thin spines, that also tend to have smaller volume to surface area ratio, show a wider range in AMPAR density increase compared to the larger mushroom spines, which was also seen in the realistic spines (Figure 8.3 and Figure 8.6). This suggests that thin spines have more variability and can access a wider range of AMPAR density values, perhaps tying into their higher instability [86]. Conversely, mushroom spines have a more constant range of AMPAR density values, perhaps emphasizing their stability [86]. This observation is complicated by an inversion of this relationship with regards to total AMPAR number, where smaller spines show a smaller range in total AMPAR number compared to larger spines. It is experimentally observed that total AMPAR number is correlated to spine head volume and synaptic area [21, 164, 204], but since AMPAR dynamics depend on its local environment, we do believe that considering AMPAR density is a valuable metric. Further investigation into the significance of AMPAR density versus total receptor number would be extremely insightful.

The presence of an extrasynaptic pool of membrane AMPAR, which was modeled as a source at the base of the spine neck, complicated the system as there was no longer mass balance for AMPAR. With an extrasynaptic pool, the bistable models took much longer to reach steady state than the monostable models, since active CaMKII remained elevated in the bistable model versus transient in the monostable model. Therefore, it is important to consider the role of the dendritic spine as an isolated subcompartment, but we also need to consider its role within a spine cluster along a dendrite [87].

While we observe the same trends for AMPAR density and total AMPAR for the realistic spines as seen for the idealized spines (Figure 8.6), the trend is not as clean which emphasizes the nuances of spine morphologies, particularly how trying to classify spines via a single morphological feature, in this case volume or volume to surface area ratio, is not

sufficient to fully explain the consequential AMPAR dynamics. Furthermore, the averaging of observed dendritic spine geometries, which are often used to construct idealized spines, could eliminate important outlier cases with significant biological purposes [18]. Therefore, considering realistic spine morphologies provides insight into these unique geometric cases that would otherwise be overlooked.

Thus, there remain many opportunities to expand on this work to address the complexity found within dendritic spines biochemically and geometrically.

Dendritic spine geometry is known to be important for synaptic function, yet the exact consequences of spine morphology on synaptic plasticity remain unknown. Using a systems-biology approach, we have investigated various components that influence AMPAR increase at the PSD during LTP. We find that two different CaMKII models both produce stable increases in AMPAR levels, but display different steady state values and temporal dynamics. We show that AMPAR endo/exocytosis, membrane diffusion, and extrasynaptic pools affect different aspects of AMPAR increase; endo/exocytosis modulate the initial increase in bound AMPAR; membrane diffusion influences intermediate timescale effects and can alter the time to achieve steady state; and steady state values depend on the total amount of accessible AMPAR through both endo/exocytosis and the extrasynaptic pool. We identified different geometric regimes that displayed different trends in bound AMPAR increase with smaller spines showing higher percent increases, an intermediate regime of low response, and then a moderate percent increase at larger spines. We predict that these regimes act to optimize resource usage while supporting a dendrite's ability to maintain large, resource-intensive spines while investing in small, adaptive spines needed for future connections. Lastly, comparisons between ideal and real spines highlight how morphological complexity prevents correlations to a single geometric factor.

Although we have focused specifically on AMPAR dynamics in excitatory synapses on dendritic spines, we believe that this model combination of signaling dynamics and realistic cellular geometries along with knockout trafficking cases is a powerful tool to explore biochemical and morphological coupling in general. Well-mixed models and compartmental models can provide great insight into the signaling dynamics within dendritic spines [103, 124], but cannot address the inherently spatial questions associated with protein trafficking and spine geometry. As imaging techniques, image segmentation, and meshing technologies advance [148], the ability to computationally model realistic cellular geometries improves, providing more insight into the consequences of complex cellular structure and ultrastructure. Our results highlight the need to consider more biological complexity in terms of spatial modeling both by considering realistic spine morphologies [18, 214] and by considering the localization of proteins and microenvironments [102]. We hypothesize that AMPAR dynamics depend on a combination of trafficking mechanisms to provide robust responses to synaptic stimuli. However, more complex models will be needed to investigate this hypothesis and test when these various trafficking mechanisms could fail. In addition, additional work is needed to consider a variety of other biochemical signaling interactions, particularly in microenvironments like the PSD, and other biophysical interactions, such as crowding, confinement, and liquid liquid phase separation, that could influence AMPAR dynamics during LTP.

Acknowledgements

Chapter 8 contains material from Mechanochemical modeling of AMPAR trafficking by Miriam Bell, Christopher T. Lee, and Padmini Rangamani, which is being prepared for submission. This dissertation author was the primary investigator and author of this paper. For Chapter 8, I would like to acknowledge my coauthors Dr. Christopher T.

Lee, and Professor Padmini Rangamani. We thank Dr. Mayte Bonilla Quintana and Dr. Sage Malingen for manuscript feedback. This work was supported by a National Defense Science and Engineering Graduate (NDSEG) Fellowship to M.K.B., a Hartwell Foundation Postdoctoral Fellowship to C.T.L., and Air Force Office of Scientific Research FA9550-18-1-0051 to P.R..

Chapter 9

Concluding remarks and future directions

9.1 Summary and future work

Structural plasticity is a clear example of the coupling between structure and function. Neurons must be able to adapt at dendritic spines to modify their synaptic strength to ensure proper neural function. At synapses, embedded feedback loops cause biochemical signaling to constantly update determinents of future signaling dynamics, including biochemical and structural factors. Additionally, morphology can influence signaling dynamics, closing the structure-function feedback loop. Improvements in biosensor development and imaging techniques continue to shed light on the complex inner workings of dendritic spines and the process of structural plasticity. However, it remains challenging to experimentally parse out the exact roles, dynamics, and contributions of individual signaling motifs and species, and biophysical features such as morphology and ultrastructure.

In this dissertation, we construct and utilize mathematical and computational models (Chapter 2, [1]) to investigate the coupling between structure and function underlying

synaptic and structural plasticity. We propose (i) a mechanochemical model which captures extreme structural plasticity in neurites (Chapter 3, [2]), (ii) an attempt to rectify membrane voltage propagation as ion flux and diffusion in dendritic spines and dendrites (Chapter 4), (iii) an investigation of the influence of spine morphology and ultrastructure on fast Ca^{2+} dynamics in deterministic and stochastic systems (Chapters 5 and 6, [3,4]), and (iv) a model of how coupling between biochemical signaling at different timescales, receptor trafficking, and spine morphology governs synaptic plasticity (Chapters 7 and 8, [5]). In the remaining chapter, I will summarize the contributions of this dissertation and address some future directions to build on these findings.

9.1.1 Thesis summary

Biochemical signaling influences morphology

Structural plasticity refers to a synapse's ability to morphologically change in response to a biochemical stimulus. Therefore, signaling dynamics clearly can trigger mechanical and morphological changes in synapses. This is a hallmark of dendritic spines and neurons. However, we considered an example of structural plasticity that involved an extreme form of neuronal remodeling. In Chapter 3, we investigated how a biochemical stimulus could trigger the rupture and retraction of neurites on PC12 cells [2]. Based on a series of experimental investigations by our collaborators, we constructed a biochemical signaling pathway that we hypothesized to be activated following acetylcholine application. We then coupled the signaling network as the input to a mechanics model of neurite retraction based on actin dynamics and membrane tension. With this framework, we could then predict neurite retraction rates during different overexpression experiments on actin modifying proteins. We found that the Gαq/PLCβ /PI(4,5)P2 pathway couples calcium responses to neurite remodeling and ultimately neural plasticity.

Morphology influences biochemical signaling

It is known that structure can influence function, but the exact manner in which neuronal morphology across different lengthscales and timescales influences biochemical signaling during synaptic plasticity is not well understood. We sought to investigate this coupling between morphology and signaling through a series of computational models. In Chapter 4, we investigated how dendritic spine and dendrite morphology influences voltage propagation by considering membrane depolarization as ion influx and diffusion. We found that while this was a realistic interpretation of membrane voltage as ion movement, our current model lacks either fundamental physics components such as electrodiffusion or our numerical algorithms and meshes require more intensive considerations for these computations. In Chapters 5 and 6, we considered both deterministic and stochastic simulations of calcium influx into spines of different geometries and ultrastructures [3, 4]. Using this systematic approach, we highlighted how even at these fast timescales, spine ultrastructure and size can influence calcium readouts. Additionally, we utilized historical synaptic weight calculations to correlate calcium dynamics to synaptic weight updates and found size and shape dependent trends. In Chapters 7 and 8, we more closely considered the relationships between CaMKII and AMPAR, and biochemistry and trafficking, using both compartmental and spatial models [5]. We found that model architecture filtered upstream signaling dynamics and trafficking effects, and spine morphology showed volume dependent sensitivity to bound AMPAR steady state behavior in both idealized and realistic geometries. We concluded that neuronal morphology is a feature that can be tuned to control synaptic response, and various geometric aspects act as additional degrees of freedom to modify synaptic strength.

9.1.2 Future directions

Although these various modeling efforts have shed light on various aspects of structural plasticity, there are many open questions remaining. Additionally, our models contain many assumptions and potential limitations. It is be beneficial to consider the implications of those limitations and what remains to be explored.

Below we summarize some considerations that we think are important in models of synaptic and structural plasticity moving forward.

- Many of the signaling networks we investigated focused on key signaling species. However, biochemical signaling networks are notoriously complex and convoluted [103]; we must continue to discern between what signaling interactions can be abstracted to more simple interactions or grouped by timescale, versus what signaling interactions are key for model complexity. The line between justified simplification and loss of information is thin and requires some combination of understanding of the system, extensive data, and clever guesswork.

- Structural plasticity acts as a structure-function feedback loop. Here, we have only touched the surface on how dendritic spine morphology influence biochemical signaling. Future models need to complete the feedback loop and consider how biochemical signaling triggers morphological changes in dendritic spines. These morphological changes involve complex interplay between actin dynamics and membrane tension [23]. While we have investigated how actin and membrane dynamics could lead to characteristic dendritic spine shapes [27], we have not yet linked those dynamics to signaling triggers.

- Alongside spatial complexity, spatial localization is an important factor to consider for signaling dynamics. We touched on localization of membrane fluxes [3],

but many additional species localize their behavior to membrane regions or cytosolic nanodomains, and can experience activity dependent translocation between domains. For instance, it is hypothesized that calcineurin and CaMKII are preferentially localized at different distances to calcium microdomains to induce either LTP or LTD [187]. Thus, localization is another key feature that can tune the dynamics of synaptic plasticity.

- As a specific example of spatial localization, AMPAR is known to form clusters at the PSD which have acute spatial alignment with exocytosis regions in the active zone on the presynaptic terminal [215]. This alignment acts as another regulatory factor that affects synaptic transmission efficiency. However, we do not fully understand how these clusters are formed through membrane or protein interactions, or the biochemical consequences of these clusters on calcium and other species dynamics at the synapse.

- At a larger lengthscale, dendritic spines are seen to form clusters with resource specific characteristics during synaptic and structural plasticity [87]. Therefore, these spine clusters form another plasticity unit that integrates effects of synaptic plasticity on individual spines into a larger synaptic transmission readout.

We highlight the last two particularly interesting next steps below.

Formation and consequences of AMPAR clusters during synaptic plasticity

Ionotropic glutamateric receptors, such as NMDAR and AMPAR, are critical for proper synaptic transmission and function in neurons. They are known to form clusters with different distribution profiles at the postsynaptic membrane of dendritic spines. It has been shown that NMDAR and AMPAR localization relative to presynaptic release sites

can modulate synaptic transmission efficiency and subsequent postsynaptic potentials and signaling dynamics [215].

While both NMDAR and AMPAR conductances and localization are important for dendritic spine activation, AMPAR dynamics are of particular interest due to their role in synaptic plasticity. AMPAR density and cluster numbers play a vital part in plasticity by dynamically increasing or decreasing in response to various biochemical and electrical factors, thus modulating the sensitivity of the synapse to presynaptic stimuli. It is known that AMPAR trafficking involves a plethora of biochemical interactions and a combination of endocytosis and exocytosis, and lateral membrane diffusion. The relative contributions of each of these trafficking mechanisms remains debated, but there is wide consensus that AMPAR within the clusters at the postsynaptic density undergo constant exchange and interact with a host of membrane, membrane-bound, and cytosolic species.

The PSD is a protein rich region in the cytoplasm adjourning the postsynaptic membrane.Dendritic spines typically house one to two synapses and have characteristic shapes associated with spine stability, disease states, and aging. While it is known that spine size and shape somehow correlate to spine function and AMPAR density also correlates to spine function, it is not well known how dendritic spine morphology influences AMPAR dynamics at the PSD. In particular, the mechanism of AMPAR clustering and the potential influence of spine morphology are not well understood. Current literature suggests AMPAR cluster through a variety of mechanisms including protein crowding [213], and direct molecular interactions between AMPAR and some binding partner [197]. To investigate these potential mechanisms and the role of spine geometry on AMPAR cluster formation and maintenance, future models should consider membrane-protein dynamics that incorporate protein-protein aggregation, crowding, receptor exchange, and interaction energies with binding partners. This type of model could be used to address the follow-

ing questions: i) Which clustering mechanisms can produce stable AMPAR clusters? ii) What role does spine morphology play in cluster dynamics? iii) How do the energetics of membrane-protein and protein-protein interactions regarding AMPAR govern synaptic strength?

Biochemical integration of synaptic plasticity across clusters of dendritic spines

While we discussed dendritic spines as isolated subcompartments, it is true that they do interact with each other and their collective dynamics determine integrated calcium behavior at the dendrite. Synaptic clusters have been shown to be computational units of learning and memory, and are associated with clustered plasticity – the idea that localized biochemical activity supports memory formation [216]. Recently, [87] presented the idea of resource-rich and resource-poor spine clusters, which are regions of dendritic spines confined by asynaptic regions. These regions showed characteristic behavior depending on resource allocation. Specifically, regions with smooth ER (SER) and larger, more mature spines had higher spine density and preserved smaller spines during LTP, as compared to resource-poor spine clusters. Therefore, spine clustering serves as a means to distribute resources and balance synaptic enlargement, and the localized spine environment influences the collective dendrite dynamics. Therefore, there appear to be regions along the dendrite of known length that have specific spine behavior. Within these spine clusters, there must be collective biochemical decision-making and information integration. Recently, a study showed that individual dendrites can perform logic gating behavior [217], and previous studies have shown that dendritic integration of calcium and other biochemistry can be quite complex [218]. Potentially by combining these various factors, we can create a model of dendritic information processing and decision-making by considering the integrated effects of calcium dynamics within dendritic clusters. Through this model, we could begin

to elucidate the biophysical factors that determine the collective decision-making behavior.

9.1.3 Final thoughts

The brain is a fascinating organ. From a biological perspective, it is a energy hungry lump of fat and proteins. From a processing perspective, it is a sophisticated, hierarchical network that can integrate and process information across multiple lengthscales and timescales. Attempts to mimic the brain's amazing processing ability have lead to great advances in neural networks, machine learning, and artificial intelligence; but these fields often abstract out much of the biological complexity of the brain. We still have much to learn about how the brain holds information and what factors matter for its processing ability. As someone with a physics and engineering background, I have greatly enjoyed the process of investigating the brain, and specifically dendritic spines, with a biologically naive viewpoint. I do not know what biological aspects of dendritic spines matter, which makes anything a possibility. Therefore, it is beneficial to have multidisciplinary collaborations to investigate these intricate biological processes. Biology is complex and we need to know what biological components do, but we also need to consider everything from a function and circuit perspective. Essentially we need to consider the small and large pictures at the same time. Through collaborations and multidisciplinary efforts, we can start to filter through the different roles of various biochemical and structural features of dendritic spines and neurons. Modeling helps see across those scales, and I hope this collection of work has made inroads into parsing out the structure-function relationship in neurons and some small impact in the large, ambitious goal of understanding how the brain works.

Appendix A

Supplemental material of Stochastic simulations reveal that dendritic spine morphology regulates synaptic plasticity in a deterministic manner

A.1 Appendix for Stochastic simulations reveal that dendritic spine morphology regulates synaptic plasticity in a deterministic manner

We developed a stochastic reaction diffusion model in MCell [80]. The reactions are obtained from Bartol et al. [71] and Bell et al. [3] and are discussed in detail below.

A.1.1 Simulation Information and Parameters

Simulations were run for a total simulation time of 35 ms with a 500 ns time step. Each geometry is simulated in MCell over 50 distinct seeds to generate an appropriate sample size of results, and we use a write-out frequency of once per iteration to allow for reproducibility of results. At the beginning of each simulation, membrane proteins are distributed randomly over specified regions of the spine geometry surface area according to an assigned count or concentration. The reaction rates for all components in the model system were adjusted in [71] to reflect a system temperature between 34 °C and 37 °C.

A.1.2 A Note About the Treatment of Extracellular Calcium

Extracellular calcium was not explicitly modeled for ease of computational tractability. We assumed a constant extracellular calcium concentration that is negligibly impacted by the calcium influx to and efflux from the spine cytoplasm. The dynamics of Ca^{2+} are explicitly modeled once they enter the cell through channels located on the PM, and cease to be explicitly represented once they are pumped out of the cell.

A.1.3 Dynamics of calcium ions in the spine volume

We summarize the main reactions for Ca^{2+} in the volume. The values for the reaction rates and other important model parameters are located in Table A.1. In the spine volume, calcium decay took the form given below where k_d sets a decay time scale,

$$Ca^{2+} \xrightarrow{k_d} \varnothing \,. \tag{A.1}$$

The value of k_d is taken as $50\,s^{-1}$ based on [3]. We note that this is significantly smaller than the decay rate constant determined in the results. This is expected as this cytosolic

calcium decay is just one means of calcium clearing from the cytoplasm, along with the various pumps, and mobile and fixed buffers.

In the volume, calcium binds with fixed and mobile buffers in the cytoplasm, modeled here generically with $\mathrm{B}m$ to represent mobile calcium buffers, and $\mathrm{B}f$ to represent fixed buffers. Calcium-buffer binding is modeled in MCell with the reactions

$$\mathrm{Ca}^{2+} + \mathrm{B}f \underset{\mathrm{kBf,off}}{\overset{\mathrm{kBf,on}}{\rightleftharpoons}} \mathrm{Ca}\cdot\mathrm{B}f, \tag{A.2}$$

and

$$\mathrm{Ca}^{2+} + \mathrm{B}m \underset{\mathrm{kBm,off}}{\overset{\mathrm{kBm,on}}{\rightleftharpoons}} \mathrm{Ca}\cdot\mathrm{B}m. \tag{A.3}$$

Reaction rates for the mobile and fixed buffers are found in Table A.1.

Table A.1: **Parameters used in the model for volume.**

Variable	Value	Units	Reference
Init. $[\mathrm{Ca}^{2+}]_{\mathrm{cyto}}$	1e-7	M	[71, 157]
Init. $[\mathrm{Ca}^{2+}]_{\mathrm{ER}}$	6e-5	M	[71]
Init. $[\mathrm{Ca}^{2+}]_{\mathrm{ECS}}$	2	mM	[219]
k_d	50	s^{-1}	[3]
$D_{\mathrm{Ca}^{2+}}$	2.2e-6	$\mathrm{cm}^2\,\mathrm{s}^{-1}$	[44, 220]
$k_{\mathrm{B}f,on}$	1e6	$\mathrm{M}^{-1}\,\mathrm{s}^{-1}$	[71]
$k_{\mathrm{B}f,off}$	2	s^{-1}	[71]
$k_{\mathrm{B}m,on}$	1e6	$\mathrm{M}^{-1}\,\mathrm{s}^{-1}$	[221]
$k_{\mathrm{B}m,off}$	1	s^{-1}	[221]
$D_{\mathrm{B}m}$	2e-7	$\mathrm{cm}^2\,\mathrm{s}^{-1}$	[44]
$D_{\mathrm{Ca}\cdot\,\mathrm{B}m}$	2e-7	$\mathrm{cm}^2\,\mathrm{s}^{-1}$	[44]
Init. $[\mathrm{B}f]$	2e-5	M	[221]
Init. $[\mathrm{B}m]$	4791	molecule $\mu\mathrm{m}^{-2}$	[71]

A.1.4 Plasma Membrane

The primary influx of calcium through the plasma membrane occurs through NMDARs and VSCCs, and calcium is pumped out of the cell via two kinds of pumps: PMCA, and NCX. In this model, NMDARs are both voltage and glutamate dependent and are localized to the PSD region. VSCCs are voltage dependent and located throughout the plasma membrane surface. PMCA and NCX are calcium-dependent pumps and are also located throughout the plasma membrane surface.

NMDA receptors

NMDAR are localized to the PSD area with areal density $150\,\text{molecule}\,\mu\text{m}^{-2}$ [71]. The activation of NMDAR is modeled with an asymmetric trapping block kinetic scheme as proposed by Ref. [222]. The activation of NMDAR is dependent on the diffusion of glutamate through the synaptic cleft, and its binding to inactive receptors. In this study, a surface identical to the top of the spine head is displaced $2\,\mu\text{m}$ above the head, approximating the synaptic cleft. At time t = 0 in each simulation, 500 molecules of glutamate are released at the center of this synaptic cleft at the beginning of simulation, and subsequently diffuse through the space at a rate of $2.2\times10^{-6}\,\text{cm}^2\,\text{s}^{-1}$, where they bind to membrane-bound proteins. On the postsynaptic membrane, NMDARs compete with the glutamate receptor AMPAR for glutamate; thus, AMPARs are also included in the simulation to model this competition but they do not play a role in calcium influx. AMPAR is also localized to the PSD area. The binding of glutamate to AMPAR is modeled according to the kinetic scheme proposed by Ref. [223].

Calcium flux through open NMDARs is modeled in MCell with a simple monomolecular reaction.

$$\mathrm{NMDAR} \xrightarrow{\mathrm{kCa}} \mathrm{NMDAR} + \mathrm{Ca}^{2+}_{\mathrm{cyto}} \tag{A.4}$$

where the rate of calcium influx is given by

$$\mathrm{kCa}(V) = \gamma_{NMDAR} \cdot \frac{V - V_r}{2 \cdot 1.6 \times 10^{-19}}. \tag{A.5}$$

V is the membrane potential, and $\mathrm{V_r}$ is the reversal potential for NMDAR. The parameters for the NMDAR reactions are the same as given in [222] and the parameters for the AMPAR reactions are the same as given in Ref. [223].

Calcium influx through voltage-sensitive calcium channels

The influx of Ca^{2+} through an open VSCC is given by the reaction:

$$\mathrm{VSCC} \xrightarrow{\mathrm{kVSCC}} \mathrm{VSCC} + \mathrm{Ca}^{2+}_{\mathrm{cyto}} \tag{A.6}$$

where the rate of calcium influx is given by

$$\mathrm{kVSCC} = \frac{\gamma V(t) N_A [0.393 - \exp(\frac{-V(t)}{80.36})]}{2F[1 - \exp(\frac{V(t)}{80.36})]}. \tag{A.7}$$

The influx of Ca^{2+} through VSCCs is also dependent on the activation kinetics of VSCCs. The initial conditions for all the VSCCs is the closed state, and the activation of the channels is modeled here with a five state kinetic scheme as used in Ref. [71]. The parameters for Ca^{2+} influx through VSCCs are the same as in Ref. [71]. VSCCs were located on the PM with a density of $2\,\mathrm{molecule}\,\mu\mathrm{m}^{-2}$.

Voltage calculations in the model

Since the transmembrane potential is time-varying and the rate constants for NMDAR and VSCC are voltage-dependent, the values of these rate constants at each simulation step were pre-computed and passed into MCell. The voltage stimulus representing a single EPSP starting at time t = 0, followed by a single BPAP occurring at an offset of 10 ms was obtained from Ref. [71]. Note that this time offset is within the typical window for Spike-Timing Dependent Plasticity (STDP) to inducing LTP [44, 71].

PMCA and NCX

PMCA and NCX are located on the plasma membrane with areal density $998\,\text{molecule}\,\mu\text{m}^{-2}$ and $142\,\text{molecule}\,\mu\text{m}^{-2}$ respectively [71], forcing an efflux of calcium out of the cell. These pumps are modeled using the set of elementary reactions and reaction rates from Ref. [71].

Spine Apparatus

Calcium enters the spine apparatus via SERCA pumps, and exits by leakage. SERCA pumps are calcium dependent and located throughout the spine apparatus membrane at $1000\,\text{molecule}\,\mu\text{m}^{-2}$. SERCA influx is modeled as a series of elementary reactions with rates from Ref. [71]. Calcium leakage from the spine apparatus into the cytosol is modeled by the reaction

$$\text{Ca}^{2+}_{\text{ER}} \xrightarrow{\text{kleak}} \text{Ca}^{2+}_{\text{cyto}}, \tag{A.8}$$

where k_{leak} is $0.1608\,\text{s}^{-1}$ from Ref. [3].

A.1.5 Synaptic weight change

We considered the effects of a single instance of spine activation on cytosolic calcium dynamics and subsequent synaptic weight change. Therefore, we can interpret this synaptic weight change as an early indicator of longer synaptic weight changes. We modeled changes in synaptic weight, w, due to cytosolic calcium as a phenomenological relationship, inspired by [13, 100]. Synaptic weight change is given by

$$\frac{dw}{dt} = \frac{\Omega_w - w}{\tau_w}, \tag{A.9}$$

where τ_w is a learning rate given as

$$\tau_w = k_1 + \frac{k_2}{k_3 + 2\mathrm{Ca}^{2+}_{\mathrm{cyto}}(t)/(\theta_D + \theta_P)}, \tag{A.10}$$

and Ω_w describes calcium dependence in the regimes of LTP and LTD as

$$\Omega_w = \frac{1}{1 + exp(-\beta_P(\mathrm{Ca}^{2+}_{\mathrm{cyto}}(t) - \theta_P))} - \frac{0.5}{1 + exp(-\beta_D(\mathrm{Ca}^{2+}_{\mathrm{cyto}}(t) - \theta_D))}. \tag{A.11}$$

Cytosolic calcium, $\mathrm{Ca}^{2+}_{\mathrm{cyto}}(t)$, is input as total ions in the spine in the above equation. The differential equation for synaptic weight, w, is solved in MATLAB 2018b using ode23s, with an initial synaptic weight value of 0 so synaptic weight change and synaptic weight are the same value for this single stimulation event. Synaptic weight parameters are given in Table A.2.

Because we are working with a stochastic model and are considering Ca^{2+} in terms of ions, we converted the parameters in the synaptic weight equations from units involving concentration to units of molecules, based on average spine volumes and realistic numbers of calcium ions in dendritic spines. It is important to note that using total Ca^{2+} ions

is a global view of the dendritic spine while concentration can be considered as more of a local measurement. As mentioned, this synaptic weight change is a phenomenological relationship between Ca^{2+} and synaptic weight which captures the concept of synaptic strength change, and it remains unclear if using ions versus concentration is a better approach for predicting this change. We converted our results into average concentrations by dividing the calcium transients by the respective spine volume, converting our synaptic weight parameters into units of concentration, and rerunning our synaptic weight calculations, Figure A.8. Further investigation is required to understand the considerations behind these different approaches.

A.1.6 MATLAB Analysis of Ca^{2+} transients

We used MATLAB version 2018b to analyze the max Ca^{2+} peak and decay time constants for the stochastic Ca^{2+} results. For each realization of the Ca^{2+} transient, we used the `max()` function to find the peak Ca^{2+} value and corresponding time. We fit the transient after the peak using the `fit()` function set to 'exp1'. The parameters from each fit, corresponding to a realization from a random seed, and statistics such as the mean and standard deviations are computed. The standard error of the mean was found by dividing the standard deviation by the square root of the number of individual trials, in this case 50 trials.

A.1.7 Statistical Analysis

Statistical significance was determined using a two-tailed two-sample t-test assuming equal means and variance (`ttest2()` function) in MATLAB version 2018b with a significance cutoff at $p = 0.05$. Statistical comparisons were made between the distributions of observables yielded by the 50 simulations of the compared experimental conditions.

Table A.2: Parameters for Synaptic Weight.

Variable	Value	Units	Reference
Init. w	0	-	[100]
k_1	1	s	[100]
k_2	10	s	[100]
k_3	1e-3	-	[100]
θ_D	100	molecule	* [13, 100]
θ_P	400	molecule	* [13, 100]
β_D	0.2977	molecule^{-1}	* [13, 100]
β_P	0.2977	molecule^{-1}	* [13, 100]

* These parameters were converted from concentration units with adjustments for consistency.

Trends in the stochastic results data were fit using all 50 seeds for each of the simulations being considered in the fit. The reported trend lines are estimated using the data from all 50 seeds, as opposed to fitting to the means only. Linear fits and exponential fits were computed in MATLAB using the functions `fitlm()` and `fit()`, respectively. We highlight that we are using the classical approach of null-hypothesis significance testing, p-values, and statistically significant verbiage, which has been questioned as perilous and over-simplistic [101]. We have provided the p-values for each result comparison for closer consideration, Figure A.9. The linear and exponential trend lines shown have a range of r^2 values and are used to show general trends. We emphasize however that in some plots we are fitting to either very few data points or a small domain. Therefore, we reiterate that these factors limit the interpretation of the quantitative nature of the fits.

A.2 Geometries

Idealized, axisymmetric geometries are used to represent the structure of dendritic spines in this study. Three general spine shapes are represented – thin, mushroom, and

filopodia-shaped – and each shape is further varied in size and, for the thin and mushroom spines, neck radius.

A.2.1 Geometry generation

The geometries were generated from 2-dimensional ideal spine profiles obtained from Ref. [27] consisting of a series of points (r, z) which form the outline of the respective geometry's rotational cross-section. Using Netgen/NGSolve version 6.2 [224], we revolved these profiles about the z-axis to yield a rotationally-symmetric 3-dimensional spine geometry, Figure A.1. In all spine geometries, a circular PSD was centered at the top of the spine head. The PSD area was set as a function of spine volume according to the relationship observed in Ref. [225].

A.2.2 Size and neck variations

To further explore the effects of geometric variations on calcium transients and stochasticity, and to facilitate the comparison of spine geometries of similar volumes and different shapes, the base geometries of all three shapes are scaled to two additional volumes beyond the base shapes from [27]. The additional versions of the thin spine, initially smaller than the other spine shapes, are scaled such that their length measurements are 1.5 and 2 times their original values, resulting in volumes 3.375 and 8 times that of the initial thin spine, respectively. The base mushroom spine, intermediate in volume, is scaled to 0.66 and 1.33 times its original size, resulting in volumes 0.287 and 2.353 times their original value, respectively. And the base filopodia-shaped spine, initially the largest in volume, is scaled to 0.5 and 0.75 times its original size, resulting in volumes 0.125 and 0.422 times the original volume. This scheme ultimately results in three different sizes for each spine shape, spanning a similar range of volumes.

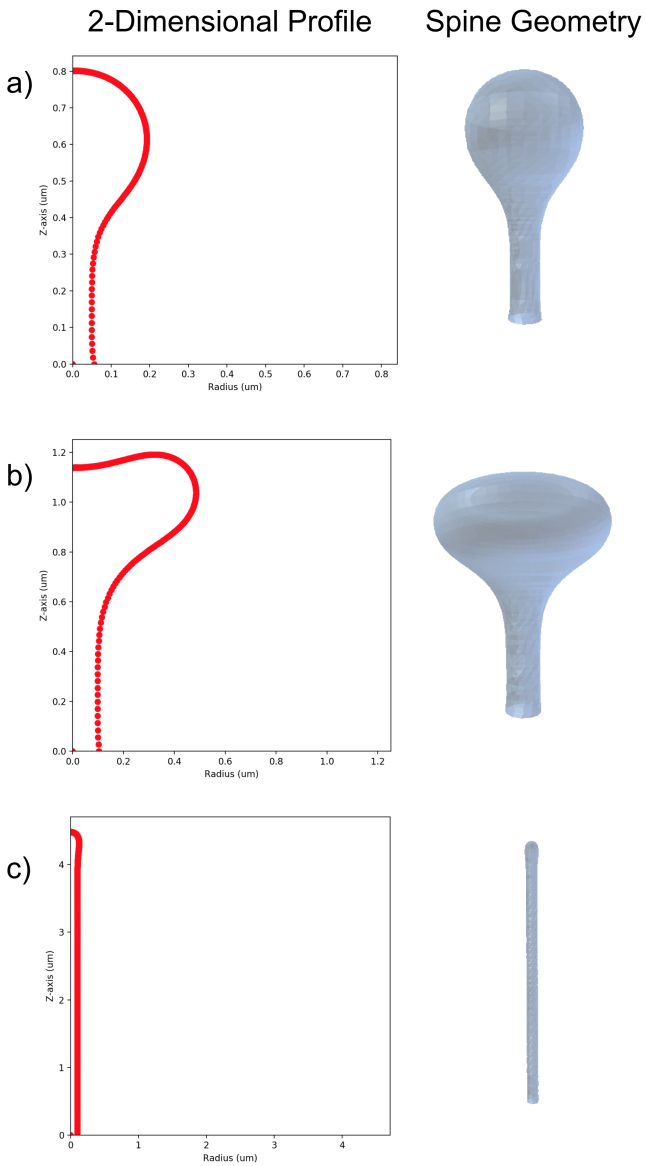

Figure A.1: The 2-dimensional spine profiles and the resultant rotationally-symmetric spine geometries for a) thin spines, b) mushroom spines, and c) filopodia.

The neck radius of the thin and mushroom spines is also varied, with neck length modified as well to preserve spine volume. To create the different spine sizes, the 2-dimensional spine profiles are dilated about the origin by a certain scale factor, and the resultant image is rotated about its vertical axis using Netgen/NGSolve to produce a scaled-up or scaled-down three-dimensional geometry. In the thin and mushroom 2-dimensional profiles, the x-values of points along the spine neck are scaled by a certain coefficient, and the length of the neck is then scaled by the squared inverse of the coefficient in order to maintain an approximately constant volume. A list of all spine geometries used, and their respective geometric measures, is found in Table A.3.

A.2.3 Spine Apparatus

Some dendritic spines are observed to have a spine apparatus denoted as SpApp, an extension of the smooth endoplasmic reticulum, extending from the dendrite into the neck and head of the spine [88]. In this study, the effects of the presence of the SpApp on calcium transients and stochasticity are investigated; to achieve this, the thin and mushroom spine geometries are further modified with the addition of a spine apparatus of varying sizes. For both spine shapes, the control-sized SpApp geometry is constructed by scaling down the original spine geometry and extending the spine apparatus neck, such that the SpApp occupies approximately 10 % of the spine volume and extends to the base of the spine. SpApp size is then varied by scaling the SpApp geometry up and down, changing the neck length such that the SpApp base coincides with the spine base. SpApp is not added to the filopodia-shaped geometry, as the spine apparatus is not generally found to be present in such spine shapes [88]. The SpApp-containing geometries are also listed in Table A.4.

Table A.3: A list of all geometric variations.

Geometry	Scale	Volume (µm³)	Surface Area (µm²)	Neck Radius (µm)	PSD Area (µm²)
Thin					
small	x1	0.035	0.611	0.06	0.045
thin neck	x1	0.034	0.653	0.04	0.045
thick neck	x1	0.035	0.590	0.07	0.045
medium	x1.5	0.119	1.378	0.08	0.112
large	x2	0.283	2.453	0.11	0.241
Mushroom					
small	x0.67	0.080	1.140	0.07	0.081
medium	x1	0.271	2.567	0.10	0.232
thin neck	x1	0.270	2.689	0.08	0.232
thick neck	x1	0.272	2.507	0.13	0.232
large	x1.33	0.643	4.568	0.13	0.526
filopodia-shaped					
small	x0.5	0.017	0.717	0.05	0.031
medium	x0.75	0.058	1.609	0.08	0.064
large	x1	0.138	2.860	0.10	0.127

Table A.4: A list of spine apparatus variations.

Geometry	SA size	SA Volume (µm³)	Cytoplasm Volume (µm³)
Thin	Small	0.00211	0.033
	Medium	0.00465	0.030
	Large	0.00867	0.026
Mushroom	Small	0.0160	0.255
	Medium	0.0358	0.235
	Large	0.0676	0.203

A.2.4 Realistic Geometries

Realistic geometries were chosen from among those on the full dendrite geometry generated in Ref. [91]. Briefly, the geometric meshes were generated from electron micrographs in Wu et al. [29] using GAMer 2 [226]. Individual spines with labeled PSD and volumes similar to the idealized geometries were selected from the realistic dendritic branch.

Table A.5: Table of values for realistic geometries.

Spine Number	Shape	Volume (μm^3)	Surface Area (μm^2)	PSD Area (μm^2)
13	Mushroom	0.157	2.457	0.26
17	Filopodia	0.091	1.916	0.06
18	Mushroom	0.243	3.383	0.14
37	Filopodia	0.075	1.756	0.03
39	Thin	0.045	1.078	0.04
41	Thin	0.091	1.710	0.07

A.3 Additional simulation results

A.3.1 Simulation results versus other geometric parameters show various trends

We plot max Ca^{2+} peak, decay time constant, and synaptic weight against volume for all size variations of filopodia-shaped spines, thin spines, mushroom spines, and mushroom spines with spine apparatus Figure A.2. We see similar trends across volume as we observe across volume-to-surface area ratio. We plot all results together on the same plot for max Ca^{2+} peak, decay time constant, and synaptic weight against volume-to-PSD area and volume, Figure A.3. We see almost no dependence on volume-to-PSD area for

any of the readouts. We see similar trend versus volume as we see in volume-to-surface area ratio.

A.3.2 Spine neck size shows differences in the large mushroom spines but not the smaller thin spines

The spine neck has long been discussed as a key parameter governing calcium signaling within dendritic spines [72]. We also explored the effects of varying spine length and radius, while preserving spine volume. We first varied the spine neck on thin spines of the control volume, Figure A.4a. We saw that while the calcium transients have considerable overlap, the thin-necked spine shows significant variance at later time points compared to the other spines, Figure A.4b-c. We see no statistically significant differences between peak calcium values and only decay differences between the thinnest and thickest necks, Figure A.4d-e. Synaptic weight changes for the thin spines with different neck geometries showed no significant differences but were trended towards negative weight changes for thicker necks, Figure A.4f. We next explored mushroom spines with thinner or thicker neck geometries but with the same volume as the mushroom control spine, Figure A.5a. While the mean of the calcium transients appeared quite close, there was significant difference in variance for the mushroom spine with the thick neck, Figure A.5b-c. We saw differences in peak calcium only between the thinnest and thickest of the mushroom neck cases, and no significant difference in decay time constant, Figure A.5d-e. Synaptic weight calculations show that presence of the thinnest versus thickest neck on a mushroom spine does lead to statistically significant differences in synaptic weight updates, Fig. A.5f. This indicates that spine neck morphology might have more implications for these larger mushroom spines, compared to the smaller thin spines.

A.3.3 The presence of spine apparatus in thin spines cause no clear trend in synaptic weight update

We vary the size of spine apparatus in thin control spines with the spine apparatus acting as a calcium sink with SERCA pumps, Figure A.6a. We see that the presence of spine apparatus makes the calcium transient response more complex with a double peak visible in the variance for thin spines, Figure A.6b-c. While we can fit the peak calcium values and decay time constant trends against both volume (Figure A.6d,e) and volume-to-surface area ratio (Figure A.6g,h), spine apparatus presence shows no clear trend in synaptic weight change for thin spines and the differences were not statistically significant, Figure A.6f.

A.3.4 Our previous deterministic results match the qualitative trends seen in these results

We previously published a deterministic reaction diffusion model of calcium dynamics in dendritic spines of different morphologies [3]. We found trends in the peak calcium concentration over spine volumes in that work and wanted to directly compare those results to our findings in this work. Using the results from [3], we integrate calcium concentration over the spine volume at each time point and find the peak calcium in ions and fit the decay dynamics of the calcium transient with an exponential decay function, $c \cdot \exp(-kt)$. We compare the peaks and decay time constants over both volume and volume-to-surface area ratio, and find the same qualitative trends as our findings in this currents work, Figure A.7.

A.3.5 Synaptic weight changes depends on calculations with ions versus concentration

Synaptic weight update equations are typically phenomenological relationships based on Ca^{2+}. Historically, many mathematical models considering synaptic weight changes have considered synaptic weight changes in terms of concentration [13, 57, 100]. In this model, we consider Ca^{2+} in terms of Ca^{2+} ions. We want to consider if the use of ions versus concentration influences the synaptic weight update results. We converted the synaptic weight equations by converting the parameters from units involving molecules to concentration by dividing by the average spine volume (0.09 μm^3) and converting to µM. We convert all the Ca^{2+} transients to µM by dividing by each respective spine geometry volume and modifying units. We plot the synaptic weight change at 35 ms for all simulations when considering ions versus concentration Figure A.8. We see that synaptic weight change does change between using ions versus concentration because the concentration also considers the volume of the spines. Using concentration leads to a decreasing trend in synaptic weight with increasing volume which is the opposite of the trend seen using ions. We do however still see protrusion-type specific trends within the overall dynamics. There are several considerations to make during this comparison. First, as mentioned, the synaptic weight equations used are phenomenological relationships between Ca^{2+} and the concept of synaptic weight which captures the idea of synaptic strengthening which would actually occur through the insertion of receptors, such as AMPAR, and potentially spine volume increase. It remains unclear if total ion count, which is a global consideration of the whole spine, or Ca^{2+} concentration, which considers the local environment, is the correct value to consider for synaptic weight calculations. Furthermore, we used average concentration in Figure A.8c-d) but dendritic spines are known to have signaling nanodomains, so it could be possible that it would be more accurate to consider peak concentration

instead of average concentration for this calculation. Additionally, it is possible that the thresholds for LTP versus LTD need to be modified for considering a global reading, such as total ions in the spine, versus a local measurement, such as local concentration. Should synaptic weight change depend on the total amount of Ca^{2+} influx or the local environment within the spine? This is an ongoing consideration that needs further analysis and discussion.

A.3.6 Two-tailed t-test results for all stochastic simulations

We conduct two-tailed t-test calculations between all stochastic simulations for both idealized and real geometries for max Ca^{2+} peak, decay time constant, and synaptic weight change. We display both the h and p-value for each comparison, Figure A.9. We use a p threshold of 0.05 to determine the binary h value. A p-value smaller than 0.05 indicates that the two results are statistically different and produce a h-value of 1. Reversely, a p-value larger than 0.05 indicates that the two results are not statistically different and produce a h-value of 0. p-values have been truncated at two decimal points.

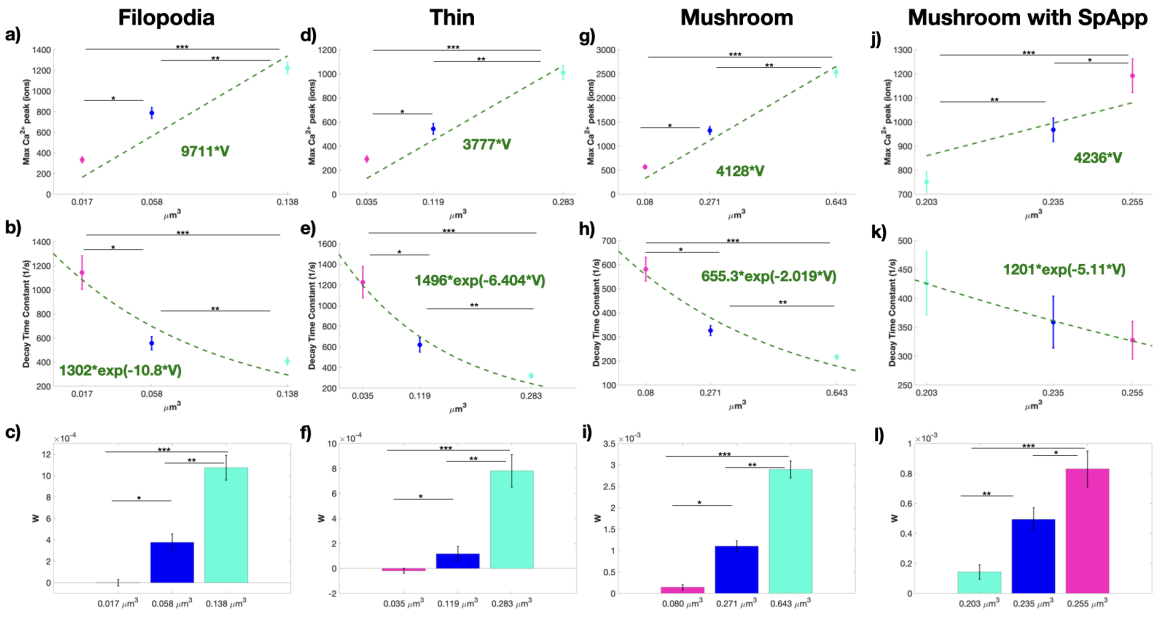

Figure A.2: **Trends across volume are similar to trends across volume-to-surface area ratio.** Peak calcium levels, decay time constant, and synaptic weight updates for size variations given as volumes for filopodia-shaped spines (a-c), thin spines (d-f), mushroom spines (g-i), and mushroom spines with spine apparatus (j-l). Peak calcium is fit with a line with a fixed zero intercept.

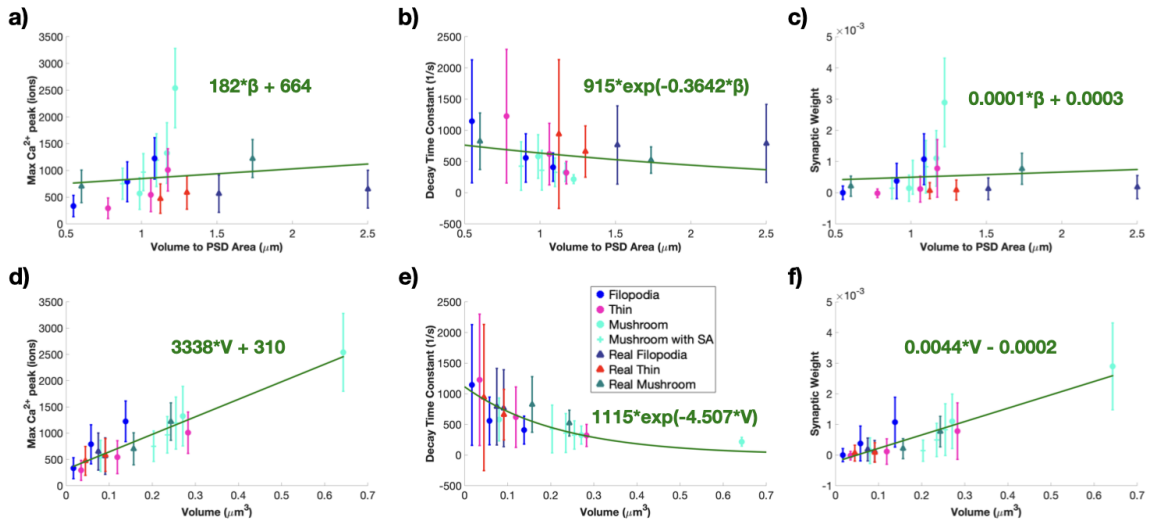

Figure A.3: **Trends across volume-to-PSD area ratio and across volume show different levels of significance.** a) All calcium peaks as mean and standard error (n=50) across volume-to-PSD area ratio show no dependence. We fit the trend in peak values with a linear function against the volume-to-PSD area ratio; $r^2 = 0.0152$ for the linear fit. b) We fit the decay dynamics of each calcium transient with $c \cdot \exp(-kt)$ and report the decay time constant, k, as a mean and standard error (n = 50) against volume-to-PSD area ratio. We fit the trend in decay time constants as a function of volume-to-PSD area ratio with an exponential $a \cdot \exp(-b\beta)$, where β is the volume-to-PSD area ratio; $r^2 = 0.0091$ for the fit. c) Calculated synaptic weight change mean and standard error (n = 50) at the last time point for all idealized and realistic spines shows no dependence on volume-to-PSD area ratio. We fit the trend in synaptic weight change with a linear function against the volume-to-PSD area ratio; $r^2 = 0.0060$ for the linear fit. d) All calcium peaks as mean and standard error (n=50) across volume show a clear increasing trend. We fit the trend in peak values with a linear function against volume; $r^2 = 0.5666$ for the linear fit. e) We fit the decay dynamics of each calcium transient with $c \cdot \exp(-kt)$ and report the decay time constant, k, as a mean and standard error (n = 50) against volume. We fit the trend in decay time constants as a function of volume with an exponential $a \cdot \exp(-bV)$, where V is the volume; $r^2 = 0.1478$ for the fit. f) Calculated synaptic weight change mean and standard error (n = 50) at the last time point for all idealized and realistic spines shows an increasing trend. We fit the trend in synaptic weight change with a linear function against volume; $r^2 = 0.4635$ for the linear fit.

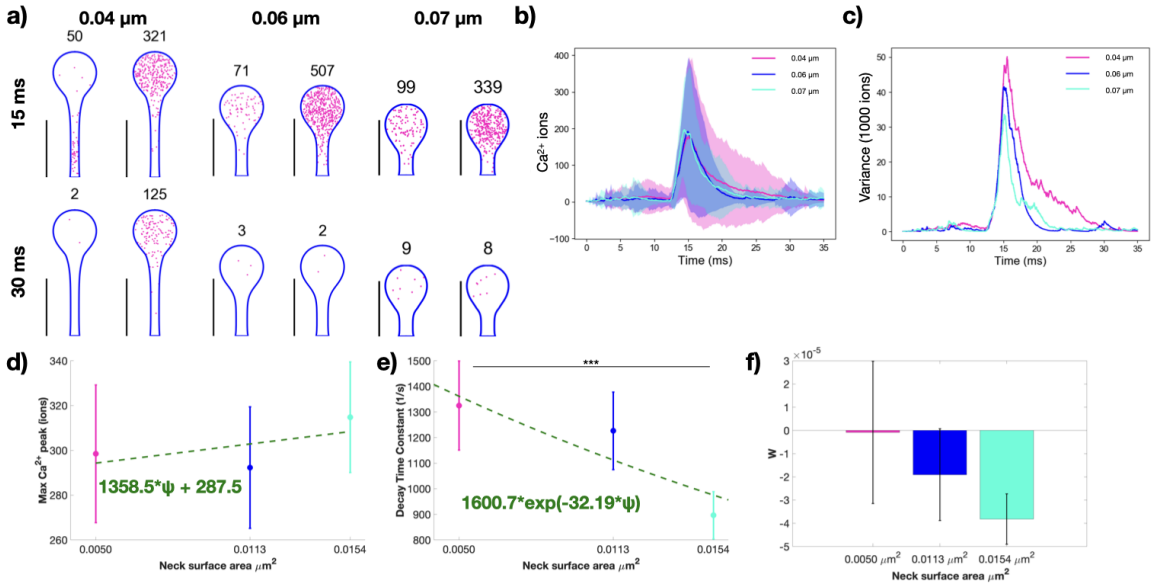

Figure A.4: **Effect of spine neck variation on synaptic plasticity in thin spines.** a) Spatial plots at 15 and 30 ms for thin spines of the same volume with different neck geometries (neck radius of 0.04, 0.06, 0.07 μm). The number above each spine corresponds to the number of calcium ions present at that time point. Scale bar: 2 µm. Calcium ions over time (b) and variance (c) for all three thin spines with different neck cases. Shaded regions in (b) denote standard deviation. d) Peak calcium ion number for each thin spine with the mean and standard error (n=50) show no statistically significant differences using a two-tailed t-test. We fit the trend in peak calcium as a linear function of spine neck base surface area; $r^2 = 0.0009$ for the linear fit. e) We fit the decay portion of each calcium transient with the exponential decay function $c \cdot \exp(-kt)$. The decay time constant mean and standard error (n=50), k, only shows statistically significant differences between the thin and thick necks; p*** $= 0.0322$ from a two-tailed t-test. We fit the trend in decay time constants as a function of spine neck base surface area with an exponential $a \cdot \exp(-b\psi)$, where ψ is the spine neck base surface area; $r^2 = 0.0256$ for the exponential fit. f) Calculated synaptic weight change at the last time point for all three thin spines shows no statistically significant difference due to neck size.

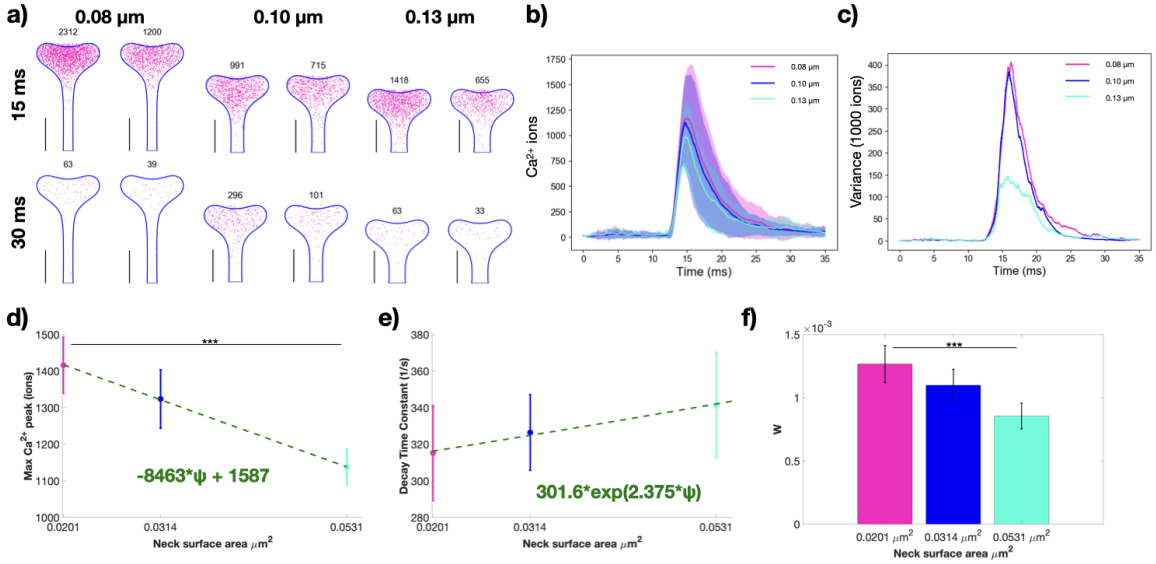

Figure A.5: **Effect of spine neck variation on synaptic plasticity in mushroom spines.** a) Spatial plots at 15 and 30 ms for mushroom spines of the same volume with different neck geometries (neck radius of 0.08, 0.10, 0.13 μm). The number above each spine corresponds to the number of calcium ions present at that time point. Scale bar: 2 µm. Calcium ions over time (b) and variance (c) for all three mushroom spines with different neck cases. Shaded regions in (b) denote standard deviation. d) Peak calcium ion number for each mushroom spine with the mean and standard error (n=50) show statistically significant differences between the thin and thick spines; p*** = 0.0029 using a two-tailed t-test. We fit the trend in peak calcium as a linear function of spine neck base surface area; $r^2 = 0.0528$ for the linear fit. e) We fit the decay portion of each calcium transient with the exponential decay function $c \cdot \exp(-kt)$. The decay time constant mean and standard error (n=50), k, shows no statistically significant differences from a two-tailed t-test. We fit the trend in decay time constants as a function of spine neck base surface area with an exponential $a \cdot \exp(-b\psi)$, where ψ is the spine neck base surface area; $r^2 = 0.0036$ for the exponential fit. f) Calculated synaptic weight change at the last time point for all three mushroom spines only shows a statistically significant difference between the thin and thick spines, p*** = 0.0244 from two-tailed t-test.

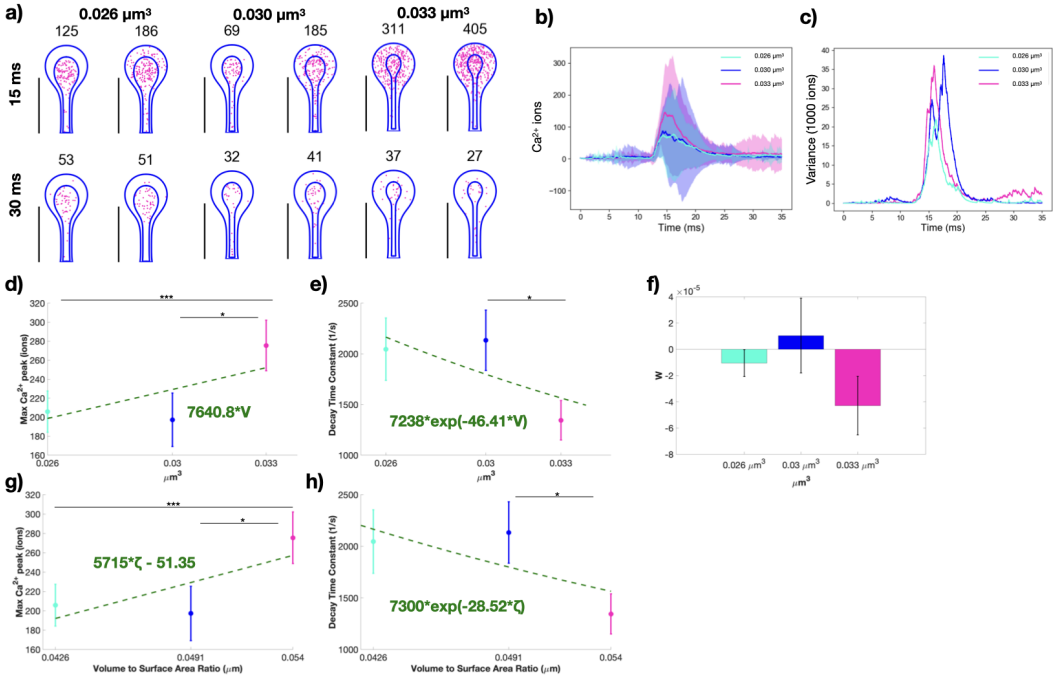

Figure A.6: **Spine apparatus size modulates synaptic weight change in thin spines.** a) Spatial plots at 15 and 30 ms for thin spines with spine apparatus of different volumes (spine cytosolic volumes of 0.026, 0.030, 0.0.033 μm^3). The numbers on top of the shape indicate the total number of calcium ions at that instant in both the spine apparatus and cytoplasm. Calcium ions over time as mean and standard deviation (b) and variance (c) for all three thin spines with different spine apparatus sizes. Shaded regions in (b) denote standard deviation. d) Peak calcium ion number for each thin spine with a spine apparatus, with the mean and standard error (n=50), show statistically significant differences between two of the three paired cases; p* = 0.0461; p*** = 0.0453 from two-tailed t-test. We fit the trend in peak values with a linear function against the cytoplasm volume; $r^2 = 0.0145$ for the linear fit. e) We fit the decay dynamics of each calcium transient with $c \cdot \exp(-kt)$ and report the decay time constant, k, as a mean and standard error (n = 50). We find only find statistically significant differences between the second and third spines; p* = 0.0289 from a two-tailed t-test. We fit the trend in decay time constants as a function of cytosolic volume with an exponential $a \cdot \exp(-bV)$, where V is the cytosolic volume; $r^2 = 0.0177$ for the fit. f) Calculated synaptic weight change at the last time point for all three thin spines shows no statistically significant difference due to spine apparatus size. We also plot peak calcium ion number and decay time constant against the cytosolic volume to surface area ratio, g and h, respectively. g) We fit the trend in peak values with a linear function against the volume-to-surface area ratio; $r^2 = 0.0214$ for the linear fit. h)We fit the trend in decay time constants as a function of volume-to-surface area ratio with an exponential $a \cdot \exp(-b\zeta)$, where ζ is the volume-to-surface area ratio; $r^2 = 0.0178$ for the fit.

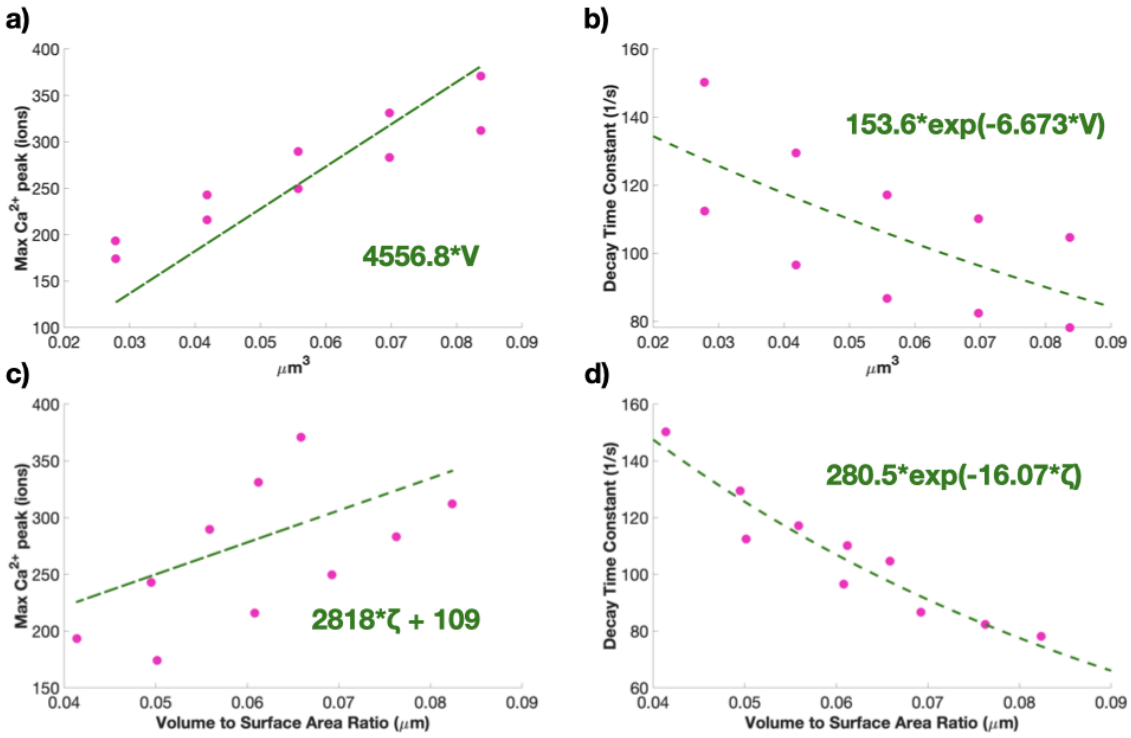

Figure A.7: **Previous calcium simulation results match the qualitative trends in these results.** a) We fit the trend in peak values with a linear function against the cytoplasm volume; $r^2 = 0.8242$ for the linear fit. We fix the y intercept at zero. b) We fit the decay dynamics of each calcium transient with $c \cdot \exp(-kt)$ and report the decay time constant, k. We fit the trend in decay time constants as a function of cytosolic volume with an exponential $a \cdot \exp(-bV)$, where V is the cytosolic volume; $r^2 = 0.4283$ for the fit. c) We fit the trend in peak values with a linear function against the volume-to-surface area ratio; $r^2 = 0.8776$ for the linear fit. h) We fit the trend in decay time constants as a function of volume-to-surface area ratio with an exponential $a \cdot \exp(-b\zeta)$, where ζ is the volume-to-surface area ratio; $r^2 = 0.9054$ for the fit.

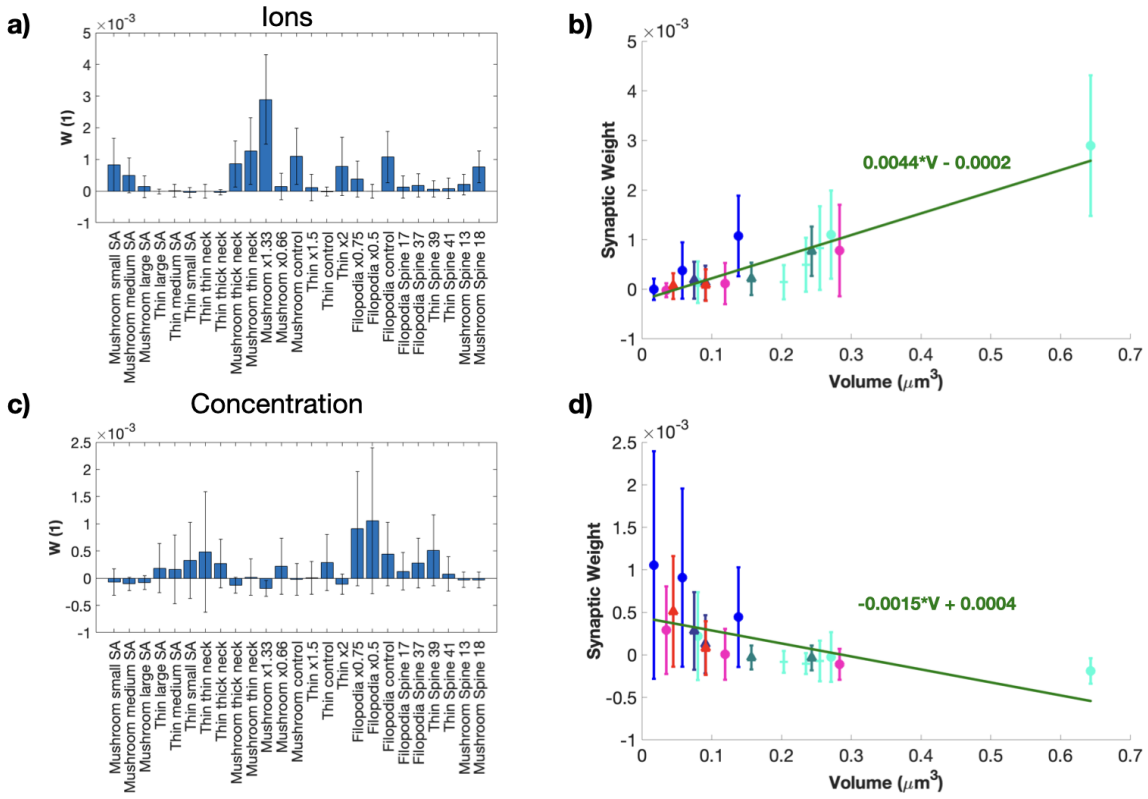

Figure A.8: **Synaptic weight updates when considering Ca^{2+} in terms of ions or concentration.** Synaptic weight updates for each stochastic idealized and real geometry simulation when synaptic weight calculations are in terms of ions (a-b) and concentration (c-d). We plot the synaptic weight changes against the spine volume for calculations using ions (b) and concentration (d). We fit the trends using a linear function of volume. We get $r^2 = 0.4635$ for the ion fit and $r^2 = 0.1229$ for the concentration fit.

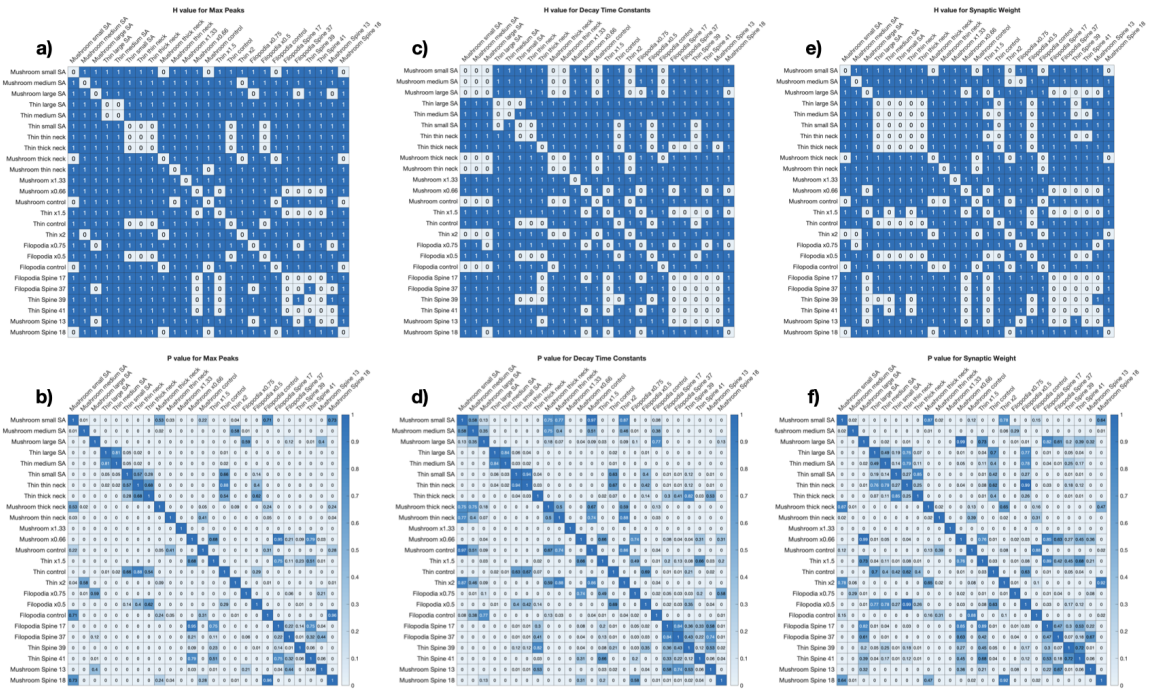

Figure A.9: **Two-tailed t-test comparison between all simulations.** We conduct two-tailed t-test between all simulations and display the h value and p-value for max Ca^{2+} peaks (a-b), decay rate constant (c-d), and synaptic weight change (e-f). Displayed p-values are truncated at two decimal points.

Appendix B

Supplemental material of Crosstalk between biochemical signaling & trafficking governs AMPAR dynamics in synaptic plasticity

B.1 Appendix for Crosstalk between biochemical signaling & trafficking governs AMPAR dynamics in synaptic plasticity

Equations for Compartmental Model

We constructed a compartmental ordinary differential equation model of signaling networks describing AMPAR dynamics in response to a single calcium influx event in

a dendritic spine of a hippocampal pyramidal neuron. The model is comprised of two compartments - the cytoplasm and the plasma membrane. The dendritic spine plasma membrane surface area was taken to be 0.8 μm^2 which corresponds to an average volume dendritic spine of approximately 0.06 μm^3. The lengthscale conversion between membrane and volume reactions was taken as 0.1011 μm, which was the averaged volume to surface area ratio of a realistic dendritic segment of a hippocampal neuron [148]. All reaction equations, parameters, and initial conditions are presented in the tables in the main text (Tables 7.1,7.2,7.3,7.4,7.5,7.6). Initial conditions for the cytosolic species were taken from [115,124], and initial conditions for the membrane species were approximated from [16,24, 161,227]. Various reaction parameters were taken from [110,115,116,124,137].

Calcium influx module

Calcium influx is driven by a voltage depolarization due to a excitatory postsynaptic potential (EPSP) and back propagating potential (BPAP) separated by 2 ms. Calcium comes into the spine through NMDAR and VSCC, and is pumped out of the spine through PMCA and NCX pumps. Additionally there is a correcting leak term. Calcium binds to CaM to form Ca^{2+}CaM (Ca/CaM complex). The various calcium flux terms are modified to have volumetric reaction units and are taken directly from [115]. See [115] for a sensitivity analysis of the different parameters in the calcium influx module.

Calmodulin, Kinases, and Phosphatases Modules

Calcium influx leads to activation of downstream signals such as CaM, CaN, CaMKII, and PP1. CaM is activated by binding to multiple Ca^{2+} ions and can be described as a multistage process where both CaM bound to either 2 or 4 Ca^{2+} ions can lead to downstream signaling activation [109,123]. However, for simplicity, we approximate the

reaction as a single binding event of CaM binding to 3 Ca^{2+} ions [124]. CaM also binds to neurogranin which acts as a CaM sink [228]. CaMKII and the phosphatase cascade have different equations for the bistable [124, 126] versus monostable models [137].

For the bistable model:

The bistable model is termed bistable because the system can produce multiple steady states for either CaMKII and PP1. CaMKII is activated by the Ca^{2+}CaM complex and then can autophosphorylate itself. Active CaMKII is deactivated by active PP1 [118, 124, 126]. CaN is activated by Ca^{2+}CaM complex and is deactivated by active CaMKII. Active CaN then activates I1 which is also deactivated by active CaMKII. This I1 species can be thought of as a representation of I1 downstream effects rather than the exact dynamics of I1. I1 inhibits PP1 activity [229], so this species can be thought of as the result of CaN deactivating I1 which then would trigger an increase in PP1 activity [127]. Therefore, this I1 representative species activates PP1. PP1 will then autoactivate itself and be deactivated by active CaMKII [124, 126].

For the monostable model:

The monostable model has Ca^{2+}CaM complex activate both CaMKII and PP1 directly. Both species then decay exponentially with linear dependence on their own concentrations [122, 129, 153].

AMPAR and scaffold module

AMPAR exists in both compartments - Aint in the volume, and Amem and Abound on the membrane. Aint represents AMPAR in endosomes in the cytoplasm. Amem represents free AMPAR on the plasma membrane. AMPAR interacts with many different

proteins in the PSD region, but here we specifically model PSD95 on the PSD membrane where it binds membrane AMPAR and localizes it to the PSD region. PSD95 has been found to be vital for AMPAR localization to the PSD [14, 161]. Abound represents membrane AMPAR bound to PSD95.

On the membrane, Amem undergoes endocytosis and exocytosis and has an active CaMKII-dependent boundary flux at the base of the spine neck. The equation for Amem is given by

$$\frac{d[Amem]}{dt} = ([CaMKIIp]c_1 + c_3)[Aint]n - (c_2[PP1] + c_4)[Amem] \\ -(k_{bind}[PSD95][Amem]) - k_{release}[ABound]) + P_{base}/\tau_{base} exp(-t/\tau_{decay})[CaMKIIp], \tag{B.1}$$

where $P_{base} = 0.9069\ \mu m$, $\tau_{base} = 800$ s, $\tau_{decay} = 60$ s, and n $= 0.1011\ \mu m$ is the spine neck base perimeter, timescale of influx, timescale of CaMKII activity, and the lengthscale conversion factor, respectively. This CaMKII-mediated influx is inspired by [141]. Endocytosis and exocytosis rates were taken from [110]. Endocytosis and exocytosis affects both Aint and Amem. The reactions for Aint have units of $\frac{\mu M}{s}$, while the reactions for Amem has units of $\frac{moles}{\mu m^2 \cdot s}$. Therefore, we use the lengthscale factor n to convert between units for these reactions.

Trafficking conditions and model variations

We investigate two forms of AMPAR trafficking during LTP - endo/exocytosis and influx from extrasynaptic pools of membrane AMPAR outside of the spine. We considered the control case when both trafficking modalities were present, the no endo/exocytosis case when there was only a CaMKII-mediated influx, and the no influx case when there was

only endo/exocytosis. We also varied the initial condition of inactive CaMKII and inactive PP1 from 0-20 µM and 0-0.5 µM, respectively. We varied contributions to endocytosis and exocytosis from 0-500 when scaling c_1 and c_2, and from 0-1 when scaling the whole endocytosis and exocytosis terms. We also varied the frequency of input to the model by applying spikes of Ca^{2+}CaM at different frequencies to the model. Therefore, the stimulus of the simulations in Figure 7.7 and Figure B.9 is Ca^{2+}CaM, instead of the previous Ca^{2+} influx.

Numerical details

We ran all model results in MATLAB 2018b or 2020b, and conducted the sensitivity analysis in COPASI. For time to peak and max values of different species, we used the function max() in MATLAB. For Figure 7.2 and Figure 7.3, steady state was designated as when the rate of change was below 1×10^{-3} for all cytosolic species except Aint and the membrane species. We designate steady state for Aint, Amem, PSD95, and Abound as when the rate is below 1×10^{-4}, 1×10^{-3}, 5×10^{-3}, and 5×10^{-3}, respectively. If time to steady state and steady state value is not achieved, then we take the value at the end of the simulation peak (500 s). For Figure 7.4 and Figure 7.5, steady state is taken as the value at 500 s.

Sensitivity Analysis

We conducted a sensitivity analysis for both the bistable and monostable models with respect to the final readout, bound AMPAR. The analysis was run in COPASI with respect to all model parameters and initial conditions (Figure 7.3f-k). Both models showed similar sensitivities to parameters and initial conditions. The most sensitivity was shown toward the PSD95 and AMPAR species initial conditions and parameters, and the AMPAR

influx terms. By far the most sensitivity was towards the initial condition for bound AMPAR which is expected. Both models were also sensitive to the reaction rates for membrane AMPAR binding to PSD95 and AMPAR influx. Lastly, the models showed sensitivity to the initial condition of inactive CaMKII, which matches our findings.

Supplemental Figures

Variations in CaMKII/PP1 initial conditions alter CaMKII/PP1 and AMPAR dynamics in a model dependent manner

We vary the initial conditions of CaMKII and PP1 for both models to observe the effects on CaMKII, PP1, and bound AMPAR dynamics, Figure B.1 and Figure B.3. In the bistable model, CaMKII and PP1 can achieve different steady states depending on IC (ex. steady states of 12 vs 20 µM and of 12 vs 0 µM for CaMKII, steady states of 0 versus 0.5 µM for PP1; Figure B.2b, left and middle column). Furthermore, for the same CaMKII IC but different PP1 IC, bound AMPAR increases with the same dynamics initially before diverging to a lower steady state for the higher PP1 condition. We quantify the peak values and time to peak values for a range of CaMKII and PP1 initial conditions (0-20 µM and 0-0.5 µM, respectively) for both the bistable and monostable models in Figure B.2. For the bistable model, active CaMKII peak value shows no dependence on PP1 IC, while time to peak value shows dependence for low PP1 IC and low CaMKII IC; this is because for the zero CaMKII IC, the peak value is taken as time zero. CaMKII peaks rapidly for all IC for the bistable model (before 500 ms). CaMKII steady state for the bistable model shows dependence on both CaMKII and PP1 IC and ranges from 0 - 20 µM (Figure 7.4). In the bistable model, PP1 dynamics and steady states are also different based on both the CaMKII and PP1 IC (Figure 7.4). The PP1 peak value time does show some variations

in the CaMKII/PP1 dependence trend with a few regions of slower peak value times for lower PP1 ICs at both low and high CaMKII IC (ex. CaMKII IC 4 µM and PP1 IC 0.05 µM; Figure B.2a, middle row and right column). PP1 steady states also range across the whole accessible concentration regime from 0 - 0.5 µM (Figure 7.4). These different CaMKII and PP1 dynamics translate to different bound AMPAR dynamics in the bistable model for the different IC combinations; in particular, higher CaMKII IC lead to higher bound AMPAR peak values that took longer to reach steady state, due to the increased CaMKII-mediated AMPAR influx. The time to peak value was particularly striking, with a clear distinction between CaMKII dominance and PP1 dominance (diagonal stepping line, Figure B.2).

For the monostable model, there was much less coupling between the IC variations (Figure B.1). CaMKII dynamics for peak value and time to peak value only showed dependence on CaMKII IC, and PP1 dynamics were likewise dependent on PP1 IC. Both CaMKII and PP1 peaked very quickly in the monostable model with all peaks by about 300 ms (Figure B.2c). As seen in Figure B.1c-d, the monostable model produces a single steady state for both CaMKII and PP1 of zero; this is in sharp contrast to the range of steady states seen in the bistable model. While bound AMPAR peak value and steady state appears entirely dependent on CaMKII IC, the time to peak value again showed coupled CaMKII/PP1 IC dependence (Figure B.2c), however with the opposite trend as the bistable model. For the monostable model, higher PP1 IC lead to a slower time to peak, while for the bistable model, higher PP1 lead to faster peak time. We note that the small differences within the longer peak value times of the bound AMPAR in the monostable model are small numerical differences.

We also considered these IC variations for knockout trafficking conditions, Figure B.3. The no endo/exocytosis case showed similar bound AMPAR dynamics to the

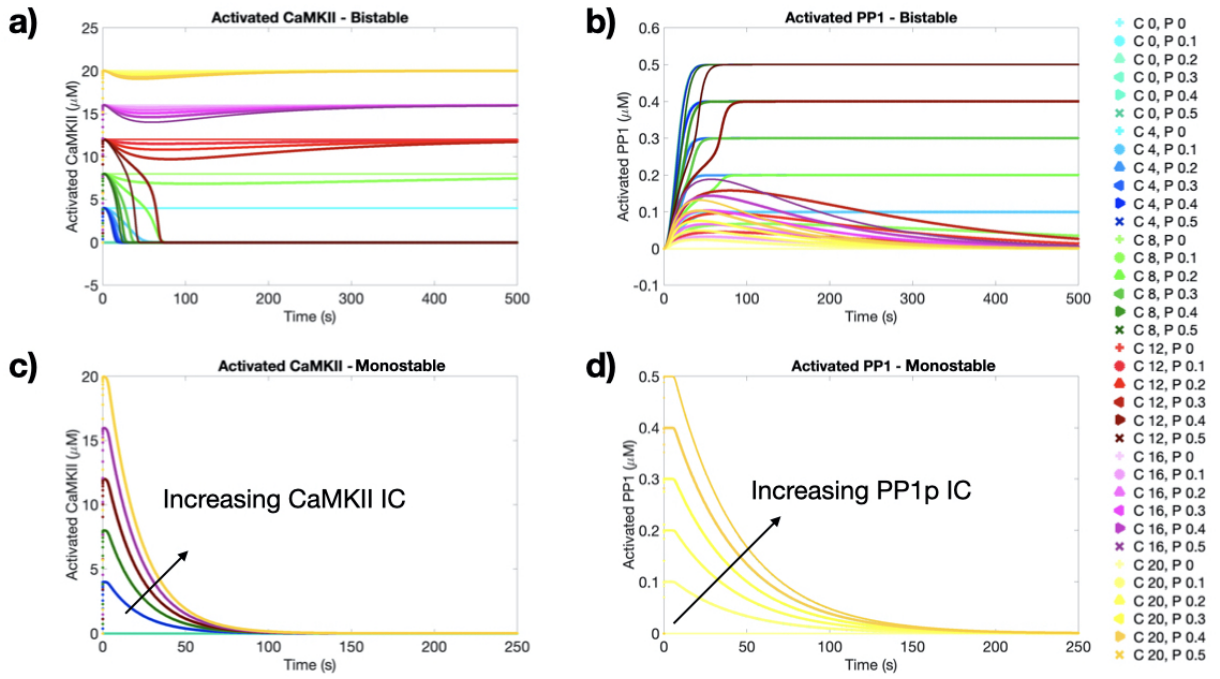

Figure B.1: Temporal dynamics for CaMKII and PP1 for both the bistable and monostable models for all CaMKII and PP1 IC combinations. Active CaMKII (a) and active PP1 (b) dynamics for the bistable model show that the coupling between CaMKII and PP1 allows for a variety of different steady states dependent on IC. Active CaMKII (c) and active PP1 (d) dynamics for the monostable model show that CaMKII and PP1 dynamics depend only on their own respective concentration and all species decay back to zero. The C and P in legend stand for CaMKII and PP1, respectively.

control case, while the no influx case showed bistable bound AMPAR behavior for the bistable model and a monostable bound AMPAR for the monostable model, fittingly.

Variations in endo/exocytosis rates

We considered four different cases for both the bistable and monostable models. We considered the model without and with the influx term (with and without mass balance for membrane AMPAR), and with two different initial conditions for CaMKII, 10 and 20 µM, but only one IC for PP1 (0.25 µM). We also considered two methods to vary endocytosis and exocytosis; 1. vary the c_1 and c_2 activity dependent terms; and 2. vary the whole

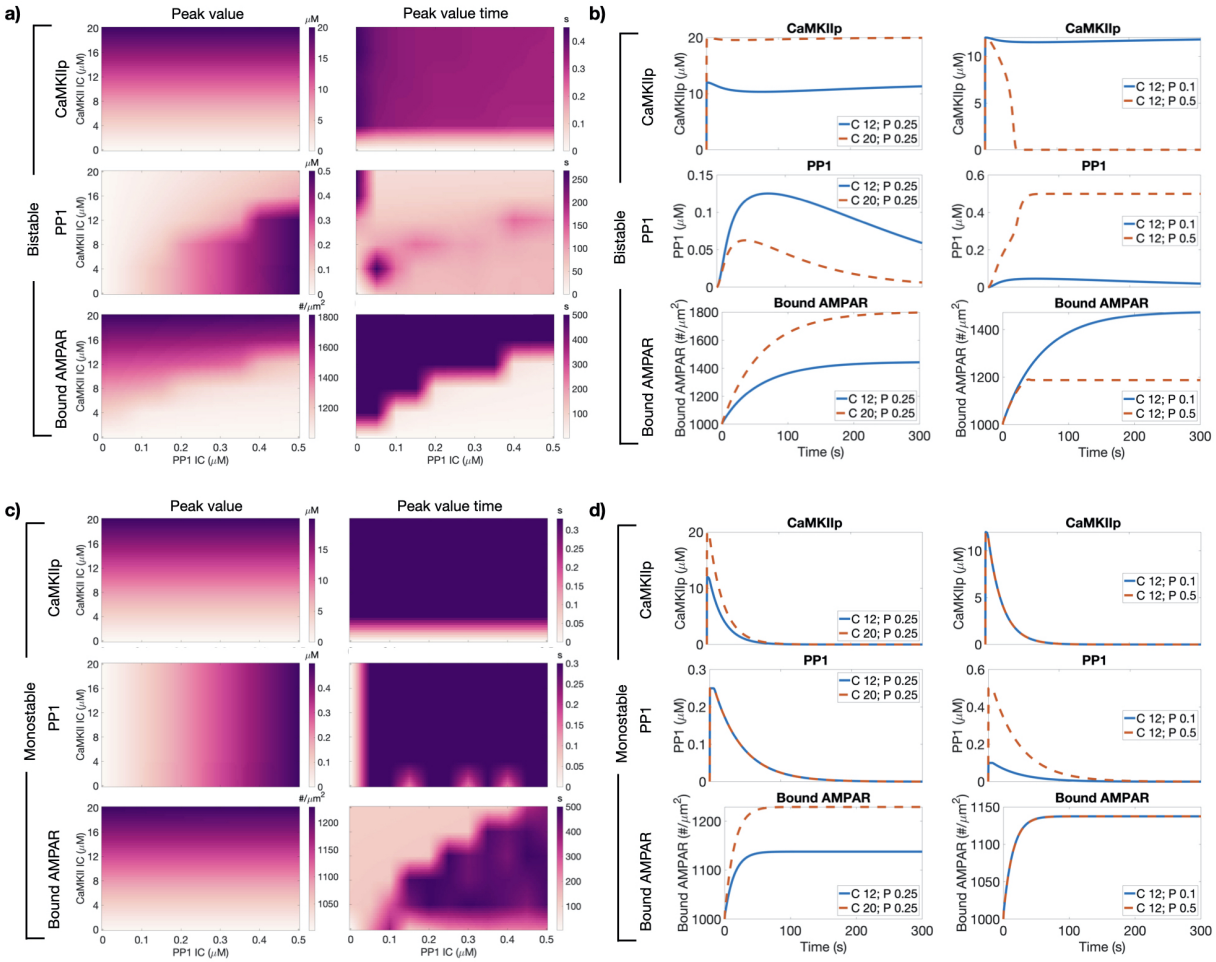

Figure B.2: Variations in initial conditions for inactive CaMKII and PP1 influences active CaMKII, active PP1, and bound AMPAR dynamics. a) Peak value and time of peak value (left and right columns respectively) for active CaMKII, active PP1, and bound AMPAR (top to bottom row, respectively) for the bistable model. b) Temporal dynamics for active CaMKII, active PP1, and bound AMPAR (left to right columns, respectively) for a set PP1 IC and varied CaMKII IC (top row) and for a set CaMKII IC and varied PP1 IC (bottom row) for the bistable model. c) Peak value and time of peak value (left and right columns respectively) for active CaMKII, active PP1, and bound AMPAR (top to bottom row, respectively) for the monostable model. d) Temporal dynamics for active CaMKII, active PP1, and bound AMPAR (left to right columns, respectively) for a set PP1 IC and varied CaMKII IC (top row) and for a set CaMKII IC and varied PP1 IC (bottom row) for the monostable model.

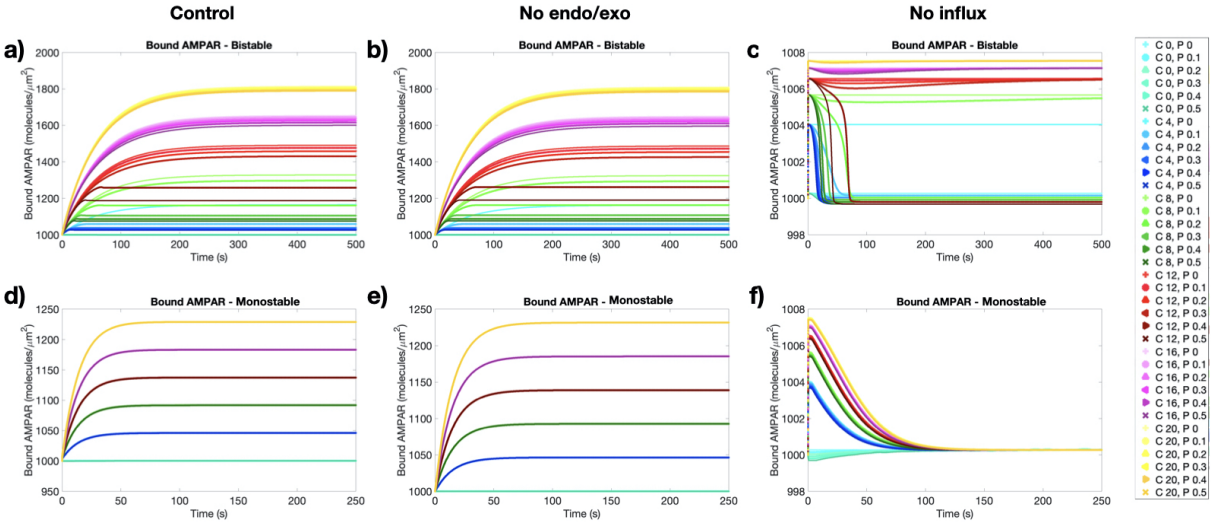

Figure B.3: Temporal dynamics for bound AMPAR for both the bistable and monostable models for all CaMKII and PP1 IC combinations for the various trafficking cases. The control case (a), no endo/exocytosis case (b), and no influx case (c) for the bistable model show coupled dependence on the CaMKII/PP1 IC. The control case (d), no endo/exocytosis case (e), and no influx case (f) for the monostable model only show dependence on the CaMKII IC. The C and P in legend stand for CaMKII and PP1, respectively.

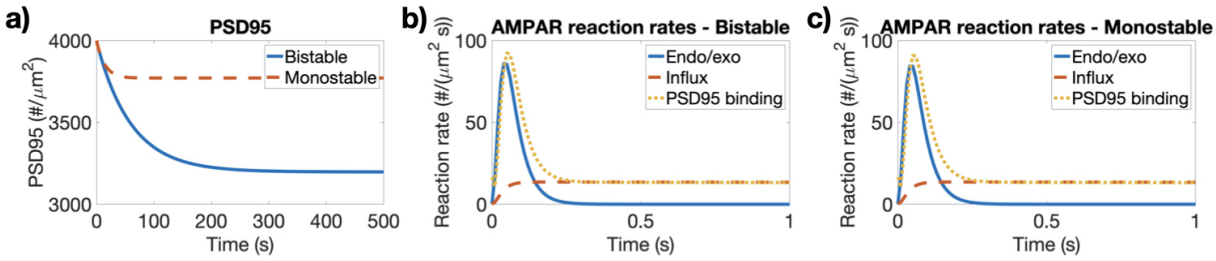

Figure B.4: a) Temporal dynamics for PSD95 in the control trafficking case with control IC of 20 µM for CaMKII and 0.25 µM for PP1. Reaction rates for the different trafficking contributions that influence AMPAR dynamics for the bistable (b) and monostable (c) models show similar trends with large rapid PSD95 binding, a smaller endo/exocytosis activity over similar timescales, and then a sustained smaller contribution due to CaMKII-mediated influx.

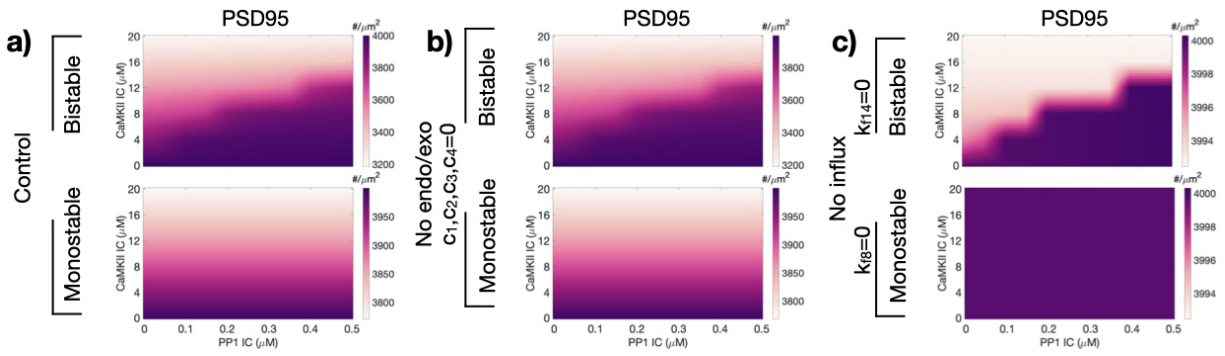

Figure B.5: Heatmaps of PSD95 at 500s for a variety of CaMKII and PP1 initial conditions. a) Steady state values for the control trafficking case with all trafficking contributions show dependence on both CaMKII and PP1 IC for the bistable model (top row), but on only CaMKII IC for the monostable model (bottom row). b) Steady state values for the no endo/exocytosis show similar trends as the control case for both the bistable model (top row) and monostable model (bottom row), showing how the CaMKII/PP1 coupling can influence bound AMPAR dynamics despite not directly impacting Amem through endocytosis and exocytosis. c) Steady state values for the no influx case show clear dependence on both CaMKII and PP1 IC for the bistable model (top row), but homogeneous results for the monostable model (bottom row). Without an influx that leads to an increase in membrane AMPAR, the monostable case has a transient decrease in PSD95 but then returns to its initial condition.

endocytosis and exocytosis terms. We considered bound AMPAR for each of these various conditions, see Figure B.6,Figure B.7, and Figure B.8.

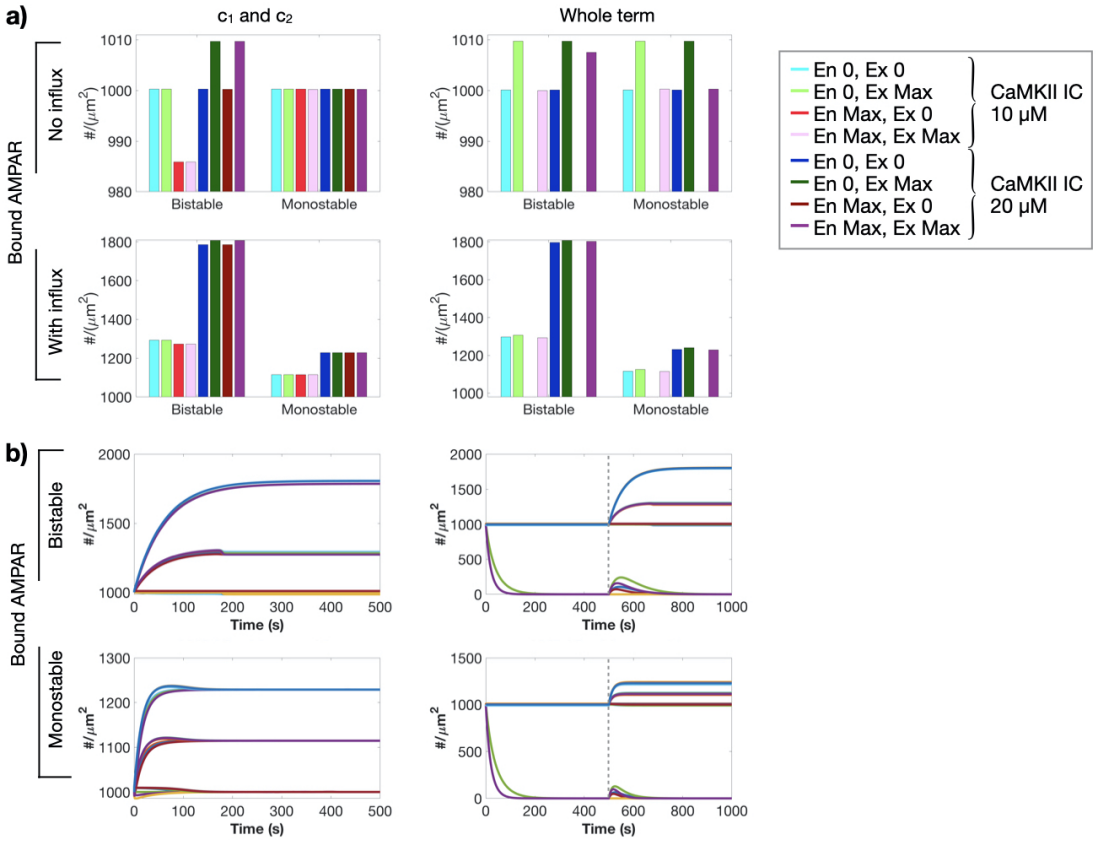

Figure B.6: Effect of endocytosis and exocytosis, CaMKII initial condition, and AMPAR influx on bound AMPAR for two different scaling methods. Endocytosis and exocytosis were varied in two different ways: Left column (c_1 and c_2): the species dependent rates of c_1 and c_2 were scaled; and Right column (Whole term): the whole exocytosis and endocytosis term was scaled. a) Bound AMPAR values at 500 s for the no influx (top row) and with influx (bottom row) cases for different scaling terms of the exocytosis and endocytosis rates (c_1 and c_2, respectively) for the two CaMKII ICs for both the bistable and monostable model. We consider two different types of exocytosis and endocytosis scaling, scaling just the c_1 and c_2 terms versus scaling the whole endocytosis and exocytosis terms. For the bars that appear vacant, those values are equal to zero (light and dark red bars in the whole term graphs). Gray inset: Legend for panel a where general color corresponds to a set endocytosis (En)/exocytosis (Ex) scaling in this order (En 0, Ex 0; En 0, Ex Max; En Max, Ex 0; En Max, Ex Max), light and dark colors indicate the 10 μM and 20 μM CaMKII IC, respectively. b) Temporal dynamics of bound AMPAR for the bistable (top row) and monostable (bottom row) models for two different CaMKII initial conditions (10 μM and 20 μM), different contributions of endocytosis and exocytosis, and with and without influx.

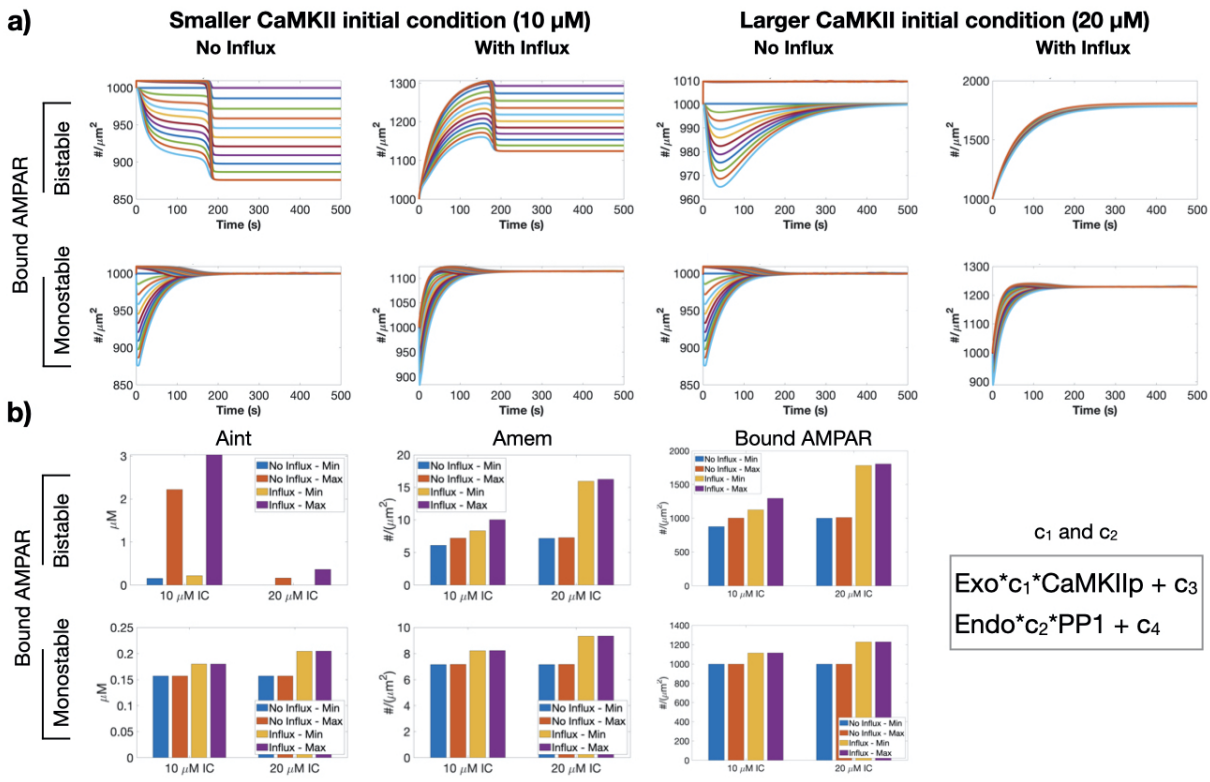

Figure B.7: Effect of endocytosis and exocytosis, CaMKII initial condition, and AMPAR influx on bound AMPAR when scaling c_1 and c_2. a) Temporal dynamics of bound AMPAR for the bistable (top row) and monostable model (bottom row) for two different CaMKII initial conditions (10 μM, left two columns; 20 μM, right two columns) with and without the membrane AMPAR influx. b) Minimum and maximum bound AMPAR steady states for each CaMKII IC, with and without the influx term for both the bistable and monostable models (top and bottom row, respectively). Gray inset: mathematical representation of how the exocytosis and endocytosis terms are scaled by Exo and Endo.

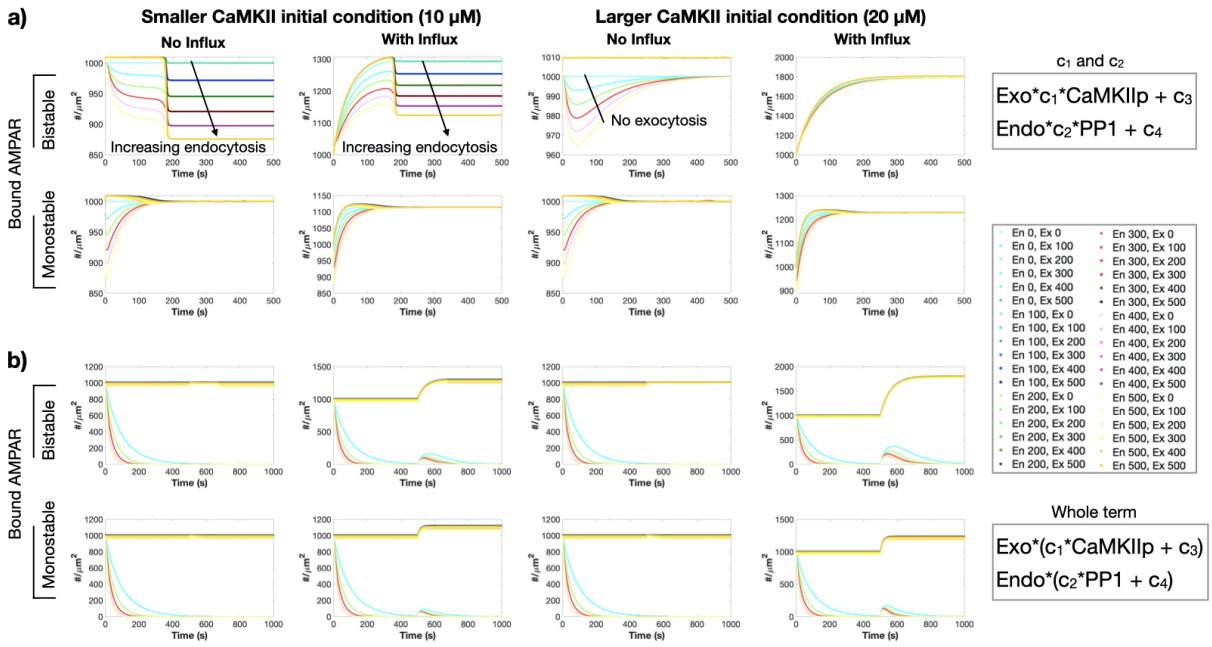

Figure B.8: Effect of endocytosis and exocytosis, CaMKII initial condition, and AMPAR influx on bound AMPAR temporal dynamics for two different scaling methods. Endocytosis and exocytosis were varied in two different ways: a) (c_1 and c_2): the species dependent rates of c_1 and c_2 were scaled (gray inset: mathematical representation); and b) (Whole term): the whole exocytosis and endocytosis terms ere scaled (gray inset: mathematical representation). a) Temporal dynamics of bound AMPAR for the bistable (top row) and monostable model (bottom row) for two different CaMKII initial conditions (10 µM, left two columns; 20 µM, right two columns) with and without the membrane AMPAR influx when varying c_1 and c_2. b) Temporal dynamics of bound AMPAR for the bistable (top row) and monostable model (bottom row) for two different CaMKII initial conditions (10 µM, left two columns; 20 µM, right two columns) with and without the membrane AMPAR influx when varying the whole endocytosis and exocytosis terms. Middle gray inset: Legend for panel a. Panel b has the same scaling pattern but the scaling is from 0 to 1 in steps of 0.1. A general color represents a endocytosis scaling, while gradients within that color correspond to exocytosis scalings.

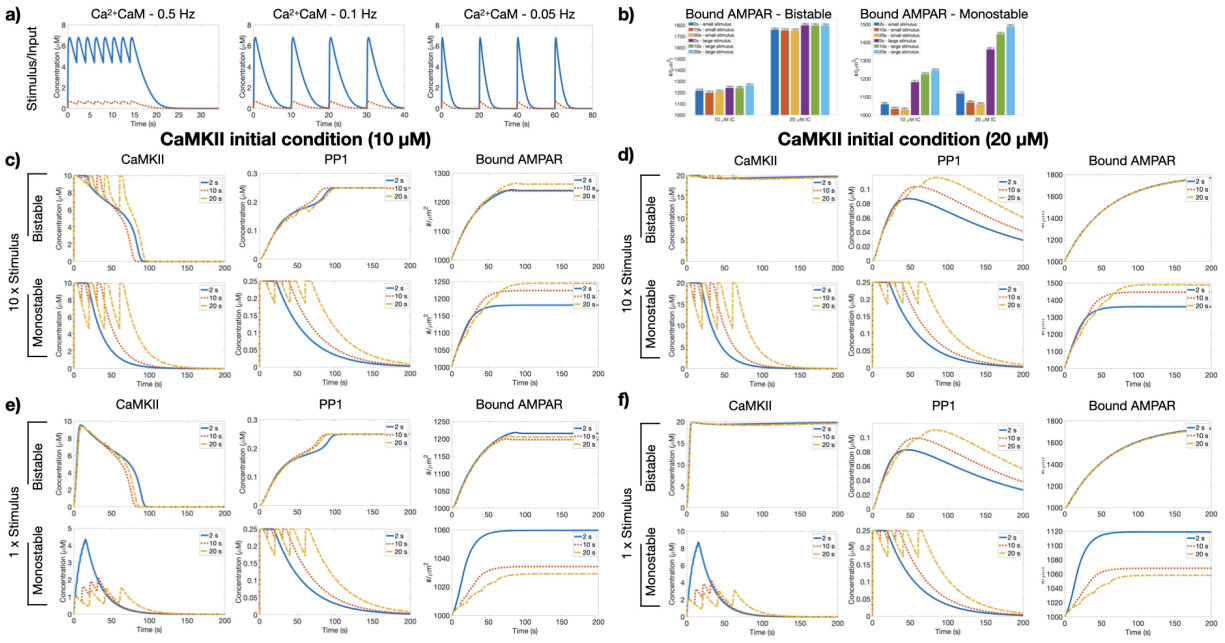

Figure B.9: Effect of multiple active Calmodulin spikes on CaMKII, PP1, and bound AMPAR dynamics for different stimulus strengths and CaMKII IC. a) Multiple spikes of active CaM were input into the different model systems at different frequencies (0.5 Hz, 0.1 Hz, 0.05 Hz; left, middle, and right, respectively) at two different amplitudes (large - blue, small - red). b) Steady state values of bound AMPAR for all conditions shown here for both the bistable and monostable models. c) Active CaMKII, active PP1, and bound AMPAR dynamics for both the bistable and monostable model for the large Ca^{2+}CaM stimulus and CaMKII IC of 10 μM. d) Active CaMKII, active PP1, and bound AMPAR dynamics for both the bistable and monostable model for the large Ca^{2+}CaM stimulus and CaMKII IC of 20 μM. e) Active CaMKII, active PP1, and bound AMPAR dynamics for both the bistable and monostable model for the small Ca^{2+}CaM stimulus and CaMKII IC of 10 μM. f) Active CaMKII, active PP1, and bound AMPAR dynamics for both the bistable and monostable model for the small Ca^{2+}CaM stimulus and CaMKII IC of 20 μM.

Appendix C

Supplemental material of Mechanochemical modeling of AMPAR trafficking

C.1 Appendix for Mechanochemical modeling of AMPAR trafficking

C.1.1 Spatial model - Reaction Diffusion equations

We construct a spatial model of signaling molecule dynamics both on membrane and in the volume, where the spatiotemporal dynamics of a species C are given by the reaction-diffusion equation,

$$\frac{\partial C}{dt} = D_C \nabla^2 C - f(C, ...), \tag{C.1}$$

and boundary conditions are given by membrane flux in the form of

$$- D_C(\mathbf{n} \cdot \nabla C)|_{\partial\Omega} = J_C, \tag{C.2}$$

where J_C captures any membrane flux reaction terms for the species C through specified boundary $\partial\Omega$.

C.1.2 Model Development for simplified AMPAR signaling network

The network of interest spans from calcium influx due to membrane voltage depolarization, kinase and phosphatase activation, and finally AMPAR trafficking, see Tables C.1 and C.2 for the initial conditions and diffusion rates of the various species. We break the signaling network into three modules.

Calcium influx Module

We take calcium dynamics from [115] with the exception of the cytosolic and membrane bound buffers and SERCA pumps. Calcium influx is due to activation of NMDAR localized to the PSD region and voltage sensitive calcium channels (VSCC) distributed across the whole plasma membrane. Calcium efflux is due to PMCA and NCX pumps across the plasma membrane.

Kinase and Phosphatase Module

Calcium influx activates calmodulin which then activates neurogranin, CaMKII, and a phosphatase cascade. We include two different models of CaMKII and phosphatase cascade - termed bistable and monostable to differentiate. In the bistable model, CaMKII is activated by calmodulin, autophosphorylates, and is dephosphorylated by active PP1.

The phosphatase cascade in the bistable model starts with calmodulin activating calcineurin which activates phosphatases I1 and PP1 in a cascade. All phosphatases are deactivated by active CaMKII, and PP1 also autoactivates itself. This model structure allows CaMKII to be perpetually active depending on the magnitude of calcium influx and initial conditions for CaMKII and PP1 [124, 126]. All reactions and reaction rates are found in Table C.4.

In the monostable model, CaMKII and PP1 are both directly activated by calmodulin and their rate of decay depends linearly on their own active concentration. This model structure leads to exponential decay dynamics for both CaMKII and PP1. All reactions and reaction rates are found in Table C.5.

AMPAR Module

The level of activated CaMKII and PP1 determines the rate of endo/exocytosis of cytosolic AMPAR (Aint) and membrane bound free AMPAR (Amem), which is modelled as a boundary condition. Free AMPAR exists on the whole plasma membrane while PSD95 and bound AMPAR (ABound) only exist within the PSD region. Free AMPAR within the PSD reversibly binds to PSD95 to form bound AMPAR which has a reduced diffusion coefficient. Free AMPAR enters onto the membrane through a boundary condition at the base of the spine neck representing a pool of extrasynaptic AMPAR on the dendrite. The rate of free AMPAR influx is dependent on the concentration of activated CaMKII that diffuses to the base of the spine neck. All reactions and reaction rates are found in Tables C.6, C.7, and C.8.

C.1.3 Trafficking conditions

AMPAR trafficking during LTP is thought to include endo/exocytosis, lateral membrane diffusion, and extrasynaptic pools of AMPAR. We include all three of these sources with our computational model and systematically turn off these various features to get five trafficking cases. The first case is the control case that includes all trafficking modalities; the second case has no extrasynaptic pool; the third case has no influx and no endo/exocytosis; the fourth case has no endo/exocytosis, and finally the fifth case has no membrane diffusion of free AMPAR. The model changes for these cases are show in Table C.9.

C.2 Spine geometries

Idealized spines are picked to be representative of thin and mushroom spines and the outlines are taken from [27] and used as 2D axisymmetric geometries. We varied the idealized spines to 50% and 150% of the respective control volume, see Table C.10.

Real spines were selected from a curated meshed geometry based on EM image stacks from [29]. The segmented EM stacks were curated with GAMer in Blender to produce an exportable mesh to import into COMSOL [148]. It should be noted that a mesh of appropriate quality is necessary for successful import and for the numerical solver to run on the geometry. Realistic spine dimensions are shown in Table C.11.

C.3 Simplified biochemical network for realistic spine simulations

For the realistic spines, we ran a simplified bistable signaling network. Specifically, due to the homogeneous dynamics of CaMKII and the phosphatases, the temporal dynamics of active CaMKII and PP1 from the thin control spine are taken at the top of the PSD and used as direct input into the realistic spines. Therefore, the model system only involves the AMPAR species and PSD95, with active CaMKII and PP1 temporal dynamics as the model stimulus. Additionally, to reduce model complexity, endocytosis and exocytosis were only modeled at the PSD region for the realistic spines. Because we are focusing on steady state dynamics, we do not believe that this simplification has major consequences on the readout.

C.3.1 Experimental Data Fitting

For the monostable CaMKII model, we fit CaMKII and PP1 decay dynamics to available experimental and computational dynamics, see [201].

C.3.2 Supplemental Figures

Table C.1: **Species in the cytoplasm**

Species	**Initial condition** $[\mu M]$	**Diffusion rate** $[\frac{\mu m^2}{s}]$	**Ref**
Ca_{cyto}	0.1	220	[115]
CaM	10	10	[124]
CaCaM	0	10	[124]
Ng	20	10	[124]
CaMNg	0	10	[124]
CaMKIIp	0	0.1	[124]
CaMKII	20	0.1	[124]
CaN	0	10	[124]
CaNp	1	10	[124]
I1	0	10	[124]
I1p	1.8	10	[124]
PP1	0	10	[124]
PP1p	0.27	10	[124]
Aint*	0.2628	0.45	[103]

* Simulations were started with these initial conditions and run to steady state. See additional table for individual simulation steady states.

Table C.2: **Species on the membrane**

Species	**Initial condition** $[\frac{molecules}{\mu m^2}]$	**Diffusion rate** $[\frac{\mu m^2}{s}]$	**Ref**
Amem*	12	0.45	[16, 24]
PSD95*	4000	0.015	[161, 227]
ABound*	1000	0.0045	[16]

* Simulations were started with these initial conditions and run to steady state. See additional table for individual simulation steady states.

Table C.3: **Idealized Spine initial conditions for different spine volumes**

Spine type	Aint [µM]	Amem [#/µm^2]	PSD95 [#/µm^2]	Bound AMPAR [#/µm^2]
Thin 0.5	0.1725	7.875	3922.55	1077.45
Thin 0.75	0.1735	7.92	3918	1082.025
Thin 1	0.174	7.95	3914.5	1085
Thin 1.25	0.17485	7.98	3911.5	1088.5
Thin 1.5	0.1755	8.01	3908.1	1091.9
Mushroom 0.5	0.17045	7.78	3933	1067
Mushroom 0.75	0.1715	7.83	3927.8	1072.2
Mushroom 1	0.17233	7.865	3923.8	1076.2
Mushroom 1.25	0.173	7.9	3920.4	1079.6
Mushroom 1.5	0.1736	7.925	3917.5	1082.45

Table C.4: **Cytosolic Reactions for bistable system**

Reaction	Reaction flux	Kinetic Parameters	Reaction type	Ref
Ca_{cyto} + CaM $\rightleftharpoons$ CaCaM	$k_f * Ca^3_{cyto} CaM - k_r * CaCaM$	$k_f = 7.75[\frac{1}{\mu M^3 \cdot s}]$, $k_r = 1[\frac{1}{s}]$	MA	[124]
Ng + CaM $\rightleftharpoons$ CaMNg	$k_f * CaM * Ng - k_r * CaMNg$	$k_f = 5[\frac{1}{\mu M \cdot s}]$, $k_r = 1[\frac{1}{s}]$	MA	[124]
CaMKII $\xrightarrow{CaCaM}$ CaMKIIp	$\frac{k_{cat}*(CaCaM^4)*CaMKII}{(K_m^4+CaCaM^4)}$	$k_{cat} = 120[\frac{1}{s}]$, $K_m = 4[\mu M]$	MM	[124]
CaMKII $\xrightarrow{CaMKIIp}$ CaMKIIp	$\frac{k_{cat}*(CaMKIIp)*CaMKII}{(K_m+CaMKII)}$	$k_{cat} = 1[\frac{1}{s}]$, $K_m = 10[\mu M]$	MM	[124]
CaMKIIp $\xrightarrow{PP1}$ CaMKII	$\frac{k_{cat}*(PP1)*CaMKIIp}{(K_m+CaMKIIp)}$	$k_{cat} = 15[\frac{1}{s}]$, $K_m = 3[\mu M]$	MM	[124]
CaNp $\xrightarrow{CaCaM}$ CaN	$\frac{k_{cat}*(CaNp)*CaCaM^4}{(K_m^4+CaCaM^4)}$	$k_{cat} = 127[\frac{1}{s}]$, K_m= 0.34[µM]	MM	[124]
CaN $\xrightarrow{CaMKIIp}$ CaNp	$\frac{k_{cat}*(CaMKIIp)*CaN}{(K_m+CaN)}$	$k_{cat} = 0.34[\frac{1}{s}]$, K_m= 127[µM]	MM	[124]
I1p $\xrightarrow{CaN}$ I1	$\frac{k_{cat}*(CaN)*I1p}{(K_m+I1p)}$	$k_{cat} = 0.034[\frac{1}{s}]$, $K_m = 4.97[\mu M]$	MM	[124]
I1 $\xrightarrow{CaMKIIp}$ I1p	$\frac{k_{cat}*(CaMKIIp)*I1}{(K_m+I1)}$	$k_{cat} = 0.0688[\frac{1}{s}]$, $K_m = 127[\mu M]$	MM	[124]
PP1p $\xrightarrow{I1}$ PP1	$\frac{k_{cat}*(I1)*PP1p}{(K_m+PP1p)}$	$k_{cat} = 50[\frac{1}{s}]$, $K_m = 80[\mu M]$	MM	[124]
PP1 $\xrightarrow{CaMKIIp}$ PP1p	$\frac{k_{cat}*(CaMKIIp)*PP1}{(K_m+PP1)}$	$k_{cat} = 0.07166[\frac{1}{s}]$, $K_m = 4.97[\mu M]$	MM	[124]
PP1p $\xrightarrow{PP1}$ PP1	$\frac{k_{cat}*(PP1)*PP1p}{(K_m+PP1p)}$	$k_{cat} = 2[\frac{1}{s}]$, $K_m = 80[\mu M]$	MM	[124]

Table notes: Reaction type refers to either mass action (MA) or Michaelis Menten (MM) kinetics.

Table C.5: **Cytosolic Reactions for monostable system**

Reaction	Reaction flux	Kinetic Parameters	Reaction type	Ref
Ca_{cyto} + CaM ⇌ CaCaM	$k_f * Ca_{cyto}^3 CaM - k_r * CaCaM$	$k_f = 7.75[\frac{1}{\mu M^3 \cdot s}]$, $k_r = 1[\frac{1}{s}]$	MA	[124]
Ng + CaM ⇌ CaMNg	$k_f * CaM * Ng - k_r * CaMNg$	$k_f = 5[\frac{1}{\mu M \cdot s}]$, $k_r = 1[\frac{1}{s}]$	MA	[124]
CaMKII $\xrightarrow{CaCaM}$ CaMKIIp	$\frac{k_{cat} * (CaCaM^4) * CaMKII}{(K_m^4 + CaCaM^4)}$	$k_{cat} = 120[\frac{1}{s}]$, $K_m = 4[\mu M]$	MM	[124]
CaMKIIp → CaMKII	$k_r * CaMKIIp$	$k_r = 0.05[\frac{1}{s}]$	MA	fitted [137]
PP1p $\xrightarrow{CaCaM}$ PP1	$\frac{k_{cat} * (PP1p) * CaCaM^4}{(K_m^4 + CaCaM^4)}$	$k_{cat} = 127[\frac{1}{s}]$, K_m= 0.34[μM]	MM	modified from [124]
PP1 → PP1p	$k_r * PP1$	$k_r = 0.025[\frac{1}{s}]$	MA	fitted [116]

Table notes: Reaction type refers to either mass action (MA) or Michaelis Menten (MM) kinetics.

Table C.6: **Membrane Flux Reactions**

Reaction	Reaction flux	Kinetic Parameters	Reaction type	Ref
Ca_{ECS} → Ca_{cyto}	JNMDAR+JVSCC+JLeak	see [115]	-	[115]
Ca_{cyto} → Ca_{ECS}	JPMCA+JNCX	see [115]	-	[115]
Aint ⇌ Amem	$(c_1 * CaMKIIp + c_3)Aint * n - (c_2 * PP1 + c_4)Amem$	$c_1 = 1[\frac{1}{\mu M \cdot s}]$, $c_2 = 1[\frac{1}{\mu M \cdot s}]$,$c_3 = 6[\frac{1}{s}]$,$c_4 = 8[\frac{1}{s}]$	MA	[110]

Table notes: Reaction type refers to either mass action (MA) or Michaelis Menten (MM) kinetics.

Table C.7: **Membrane surface reactions**

Reaction	Reaction flux	Kinetic Parameters	Reaction type	Ref
Aint ⇌ Amem	$(c_1 * CaMKIIp + c_3)Aint * n - (c_2 * PP1 + c_4)Amem$	$c_1 = 1[\frac{1}{\mu M \cdot s}]$, $c_2 = 1[\frac{1}{\mu M \cdot s}]$,$c_3 = 6[\frac{1}{s}]$,$c_4 = 8[\frac{1}{s}]$	MA	[124]
PSD95 + Amem ⇌ ABound	$k_f * PSD95 * Amem - k_r * ABound$	$k_f = 0.0349[\frac{\mu m^2}{molecules \cdot s}]$, $k_r = 1[\frac{1}{s}]$	MA	this work

Table notes: Reaction type refers to either mass action (MA) or Michaelis Menten (MM) kinetics.

Table C.8: **Membrane Surface Boundary Flux**

Reaction	Reaction flux	Kinetic Parameters	Ref
Apool → Amem	$A_{base}/\tau_{base} exp(-t/\tau_{decay})$*[CaMKIIp]	A_{base} = 0.06546 [μm^2], τ_{base}=800 [s], τ_{decay} = 60 [s]	this work, inspired by [141]

Table C.9: **Trafficking variations in terms of mathematical terms**

Case	Description
No endo/exo	rmem = 0
No pool	Apool = 0
No membrane diffusion	DAm=0

Table C.10: **Idealized Spine geometries**

Spine type	**Volume** [μm^3]	**PM Area** [μm^2]	**PSD Area** [μm^2]	**Base Area** [μm^2]
Thin 0.5	0.020575	0.43873	0.025332	0.041
Thin 0.75	0.030863	0.57489	0.033195	0.054
Thin 1	0.040655	0.69644	0.040212	0.065
Thin 1.25	0.051438	0.80814	0.046662	0.076
Thin 1.5	0.061726	0.91259	0.051647	0.086
Mushroom 0.5	0.13869	1.6364	0.19236	0.073
Mushroom 0.75	0.20803	2.1443	0.25206	0.096
Mushroom 1	0.27738	2.5976	0.30535	0.116
Mushroom 1.25	0.34672	3.0142	0.35432	0.135
Mushroom 1.5	0.41607	3.4038	0.40012	0.153

Table C.11: **Real Spine Geometries**

Spine type	**Volume** [μm^3]	**PM Area** [μm^2]	**PSD Area** [μm^2]	**Base Area** [μm^2]
1	0.091617	1.6743	0.071662	0.0386
2	0.11693	2.0386	0.033992	0.0295
3	0.041183	0.94775	0.041607	0.0365
4	0.075234	1.7054	0.02253	0.0354
5	0.025315	0.57447	0.040337	0.0142
6	0.46798	5.4388	0.41509	0.0451
7	0.23961	3.2347	0.13887	0.015

Table C.12: **Realistic Spine initial conditions**

Spine type	**Aint [µM]**	**Amem [#/µm^2]**	**PSD95 [#/µm^2]**	**Bound AMPAR [#/µm^2]**
1	0.1812	8.5	3856.8	1143.2
2	0.21	9.58	3747.3	1252.7
3	0.183	8.355	3871.8	1128.2
4	0.213	9.72	3734.25	1265.75
5	0.1758	8.02	3907	1093
6	0.1791	8.175	3891.8	1109.2
7	0.1891	8.63	3843.4	1156.6

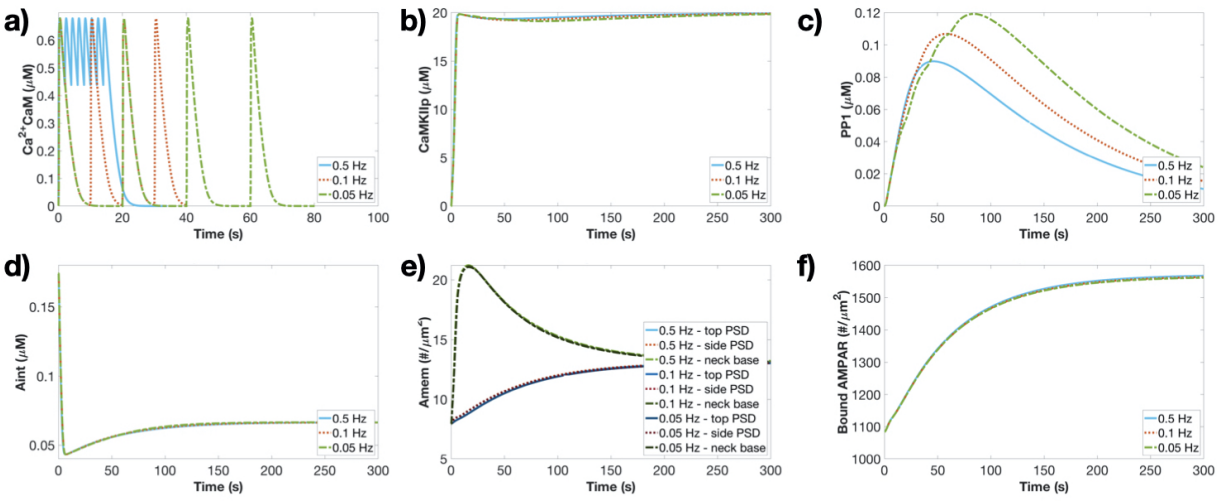

Figure C.1: **Temporal dynamics of bistable model for Ca^{2+}CaM pulses of different frequencies.** a) Ca^{2+}CaM temporal dynamics at three different frequencies (0.5, 0.1, and 0.05 Hz) at the top of the PSD region for the monostable model. Temporal dynamics of active CaMKII (b), active PP1 (c), cytosolic AMPAR (d), membrane AMPAR (e), and bound AMPAR (f) for three different frequencies for the bistable model.

Bibliography

[1] M. K. Bell and P. Rangamani, "Design decisions for incorporating spatial and mechanical aspects in models of signaling networks," *Current Opinion in Systems Biology*, 2021.

[2] K. M. Pearce, M. Bell, W. H. Linthicum, Q. Wen, J. Srinivasan, P. Rangamani, and S. Scarlata, "Gαq-mediated calcium dynamics and membrane tension modulate neurite plasticity," *Molecular biology of the cell*, vol. 31, no. 7, pp. 683–694, 2020.

[3] M. Bell, T. Bartol, T. Sejnowski, and P. Rangamani, "Dendritic spine geometry and spine apparatus organization govern the spatiotemporal dynamics of calcium," *Journal of General Physiology*, vol. 151, no. 8, pp. 1017–1034, 2019.

[4] M. V. Holst, M. K. Bell, C. T. Lee, and P. Rangamani, "Stochastic simulations reveal that dendritic spine morphology regulates synaptic plasticity in a deterministic manner," *bioRxiv*, 2021.

[5] M. K. Bell and P. Rangamani, "Crosstalk between biochemical signaling and trafficking determines ampar dynamics in synaptic plasticity," *bioRxiv*, 2021.

[6] H. Murakoshi and R. Yasuda, "Postsynaptic signaling during plasticity of dendritic spines," *Trends in neurosciences*, vol. 35, no. 2, pp. 135–143, 2012.

[7] K. F. Lee, C. Soares, and J.-C. Béïque, "Examining form and function of dendritic spines," *Neural plasticity*, vol. 2012, 2012.

[8] L. A. Colgan and R. Yasuda, "Plasticity of dendritic spines: subcompartmentalization of signaling," *Annual review of physiology*, vol. 76, pp. 365–385, 2014.

[9] M. J. Higley and B. L. Sabatini, "Calcium signaling in dendritic spines," *Cold Spring Harbor perspectives in biology*, vol. 4, no. 4, p. a005686, 2012.

[10] V. A. Derkach, M. C. Oh, E. S. Guire, and T. R. Soderling, "Regulatory mechanisms of ampa receptors in synaptic plasticity," *Nature Reviews Neuroscience*, vol. 8, no. 2, pp. 101–113, 2007.

[11] K. Basnayake, D. Mazaud, A. Bemelmans, N. Rouach, E. Korkotian, and D. Holcman, "Fast calcium transients in dendritic spines driven by extreme statistics," *PLoS biology*, vol. 17, no. 6, p. e2006202, 2019.

[12] L. C. Yeung, H. Z. Shouval, B. S. Blais, and L. N. Cooper, "Synaptic homeostasis and input selectivity follow from a calcium-dependent plasticity model," *Proceedings of the National Academy of Sciences*, vol. 101, no. 41, pp. 14943–14948, 2004.

[13] H. Z. Shouval, M. F. Bear, and L. N. Cooper, "A unified model of nmda receptor-dependent bidirectional synaptic plasticity," *Proceedings of the National Academy of Sciences*, vol. 99, no. 16, pp. 10831–10836, 2002.

[14] J. Lisman, R. Yasuda, and S. Raghavachari, "Mechanisms of camkii action in long-term potentiation," *Nature reviews neuroscience*, vol. 13, no. 3, pp. 169–182, 2012.

[15] J.-D. Ding, M. B. Kennedy, and R. J. Weinberg, "Subcellular organization of camkii in rat hippocampal pyramidal neurons," *Journal of Comparative Neurology*, vol. 521, no. 15, pp. 3570–3583, 2013.

[16] C. Bats, L. Groc, and D. Choquet, "The interaction between stargazin and psd-95 regulates ampa receptor surface trafficking," *Neuron*, vol. 53, no. 5, pp. 719–734, 2007.

[17] A. Triller and D. Choquet, "Synaptic structure and diffusion dynamics of synaptic receptors," *Biology of the Cell*, vol. 95, no. 7, pp. 465–476, 2003.

[18] E. Pchitskaya and I. Bezprozvanny, "Dendritic spines shape analysis—classification or clusterization? perspective," *Frontiers in Synaptic Neuroscience*, vol. 12, p. 31, 2020.

[19] H. Hering and M. Sheng, "Dentritic spines: structure, dynamics and regulation," *Nature Reviews Neuroscience*, vol. 2, no. 12, p. 880, 2001.

[20] K. P. Berry and E. Nedivi, "Spine dynamics: are they all the same?," *Neuron*, vol. 96, no. 1, pp. 43–55, 2017.

[21] M. Matsuzaki, G. C. Ellis-Davies, T. Nemoto, Y. Miyashita, M. Iino, and H. Kasai, "Dendritic spine geometry is critical for ampa receptor expression in hippocampal ca1 pyramidal neurons," *Nature neuroscience*, vol. 4, no. 11, pp. 1086–1092, 2001.

[22] P. Hotulainen and C. C. Hoogenraad, "Actin in dendritic spines: connecting dynamics to function," *The Journal of cell biology*, vol. 189, no. 4, pp. 619–629, 2010.

[23] M. Bonilla-Quintana, F. Wörgötter, C. Tetzlaff, and M. Fauth, "Modeling the shape of synaptic spines by their actin dynamics," *Frontiers in synaptic neuroscience*, vol. 12, p. 9, 2020.

[24] S. H. Lee, C. Jin, E. Cai, P. Ge, Y. Ishitsuka, K. W. Teng, A. A. De Thomaz, D. Nall, M. Baday, O. Jeyifous, *et al.*, "Super-resolution imaging of synaptic and extra-synaptic ampa receptors with different-sized fluorescent probes," *Elife*, vol. 6, p. e27744, 2017.

[25] A. Penn, C. Zhang, F. Georges, L. Royer, C. Breillat, E. Hosy, J. Petersen, Y. Humeau, and D. Choquet, "Hippocampal ltp and contextual learning require surface diffusion of ampa receptors," *Nature*, vol. 549, no. 7672, pp. 384–388, 2017.

[26] A. Triller and D. Choquet, "Surface trafficking of receptors between synaptic and extrasynaptic membranes: and yet they do move!," *Trends in neurosciences*, vol. 28, no. 3, pp. 133–139, 2005.

[27] H. Alimohamadi, M. Bell, S. Halpain, and P. Rangamani, "Mechanical principles governing the shapes of dendritic spines," *bioRxiv*, 2020.

[28] P. Rangamani, G. Y. Xiong, and R. Iyengar, "Multiscale modeling of cell shape from the actin cytoskeleton," *Progress in molecular biology and translational science*, vol. 123, pp. 143–167, 2014.

[29] Y. Wu, C. Whiteus, C. S. Xu, K. J. Hayworth, R. J. Weinberg, H. F. Hess, and P. De Camilli, "Contacts between the endoplasmic reticulum and other membranes in neurons," *Proceedings of the National Academy of Sciences*, vol. 114, no. 24, pp. E4859–E4867, 2017.

[30] O. Alvarez and R. Latorre, "The enduring legacy of the "constant-field equation" in membrane ion transport," *Journal of General Physiology*, vol. 149, no. 10, pp. 911–920, 2017.

[31] A. L. Hodgkin and A. F. Huxley, "A quantitative description of membrane current and its application to conduction and excitation in nerve," *The Journal of physiology*, vol. 117, no. 4, p. 500, 1952.

[32] J. Magee, D. Hoffman, C. Colbert, and D. Johnston, "Electrical and calcium signaling in dendrites of hippocampal pyramidal neurons," *Annual review of physiology*, vol. 60, no. 1, pp. 327–346, 1998.

[33] P. Vetter, A. Roth, and M. Häusser, "Propagation of action potentials in dendrites depends on dendritic morphology," *Journal of neurophysiology*, vol. 85, no. 2, pp. 926–937, 2001.

[34] R. Yuste, *Dendritic spines*. MIT press, 2010.

[35] B. L. Bloodgood, A. J. Giessel, and B. L. Sabatini, "Biphasic synaptic ca influx arising from compartmentalized electrical signals in dendritic spines," *PLoS biology*, vol. 7, no. 9, p. e1000190, 2009.

[36] N. Iannella, T. Launey, D. Abbott, and S. Tanaka, "A nonlinear cable framework for bidirectional synaptic plasticity," *Plos one*, vol. 9, no. 8, p. e102601, 2014.

[37] J. Cartailler, T. Kwon, R. Yuste, and D. Holcman, "Deconvolution of voltage sensor time series and electro-diffusion modeling reveal the role of spine geometry in controlling synaptic strength," *Neuron*, vol. 97, no. 5, pp. 1126–1136, 2018.

[38] D. Tsay and R. Yuste, "Role of dendritic spines in action potential backpropagation: a numerical simulation study," *Journal of neurophysiology*, vol. 88, no. 5, pp. 2834–2845, 2002.

[39] S. R. Williams and G. J. Stuart, "Action potential backpropagation and somatodendritic distribution of ion channels in thalamocortical neurons," *Journal of Neuroscience*, vol. 20, no. 4, pp. 1307–1317, 2000.

[40] F. Bezanilla, "How membrane proteins sense voltage," *Nature reviews Molecular cell biology*, vol. 9, no. 4, pp. 323–332, 2008.

[41] K. Tsumoto, H. Kitajima, T. Yoshinaga, K. Aihara, and H. Kawakami, "Bifurcations in morris–lecar neuron model," *Neurocomputing*, vol. 69, no. 4-6, pp. 293–316, 2006.

[42] B. Chiovini, G. F. Turi, G. Katona, A. Kaszás, D. Pálfi, P. Maák, G. Szalay, M. F. Szabó, G. Szabó, Z. Szadai, *et al.*, "Dendritic spikes induce ripples in parvalbumin interneurons during hippocampal sharp waves," *Neuron*, vol. 82, no. 4, pp. 908–924, 2014.

[43] N. Hübel, E. Schöll, and M. A. Dahlem, "Bistable dynamics underlying excitability of ion homeostasis in neuron models," *PLoS computational biology*, vol. 10, no. 5, p. e1003551, 2014.

[44] T. Griffith, K. Tsaneva-Atanasova, and J. R. Mellor, "Control of ca2+ influx and calmodulin activation by sk-channels in dendritic spines," *PLoS computational biology*, vol. 12, no. 5, p. e1004949, 2016.

[45] M. S. Rad, L. B. Cohen, O. Braubach, and B. J. Baker, "Monitoring voltage fluctuations of intracellular membranes," *Scientific reports*, vol. 8, no. 1, p. 6911, 2018.

[46] B. S. Donahue and R. Abercrombie, "Free diffusion coefficient of ionic calcium in cytoplasm," *Cell calcium*, vol. 8, no. 6, pp. 437–448, 1987.

[47] T. D. Sangrey, W. O. Friesen, and W. B. Levy, "Analysis of the optimal channel density of the squid giant axon using a reparameterized hodgkin–huxley model," *Journal of neurophysiology*, vol. 91, no. 6, pp. 2541–2550, 2004.

[48] H. Kim, K. E. Jones, and C. Heckman, "Asymmetry in signal propagation between the soma and dendrites plays a key role in determining dendritic excitability in motoneurons," *PLoS One*, vol. 9, no. 8, p. e95454, 2014.

[49] Z. Wu, M. Su, C. Tong, M. Wu, and J. Liu, "Membrane shape-mediated wave propagation of cortical protein dynamics," *Nature communications*, vol. 9, no. 1, pp. 1–12, 2018.

[50] O. Puls and Q. Yang, "The rise of ultrafast waves," *Developmental cell*, vol. 47, no. 5, pp. 532–534, 2018.

[51] T. Lagache, K. Jayant, and R. Yuste, "Electrodiffusion models of synaptic potentials in dendritic spines," *Journal of computational neuroscience*, vol. 47, no. 1, pp. 77–89, 2019.

[52] L. P. Savtchenko, M. M. Poo, and D. A. Rusakov, "Electrodiffusion phenomena in neuroscience: a neglected companion," *Nature reviews Neuroscience*, vol. 18, no. 10, pp. 598–612, 2017.

[53] J. Nishiyama and R. Yasuda, "Biochemical computation for spine structural plasticity," *Neuron*, vol. 87, no. 1, pp. 63–75, 2015.

[54] R. Yuste and W. Denk, "Dendritic spines as basic functional units of neuronal integration," *Nature*, vol. 375, no. 6533, p. 682, 1995.

[55] R. Yuste, A. Majewska, and K. Holthoff, "From form to function: calcium compartmentalization in dendritic spines," *Nature neuroscience*, vol. 3, no. 7, p. 653, 2000.

[56] G. J. Augustine, F. Santamaria, and K. Tanaka, "Local calcium signaling in neurons," *Neuron*, vol. 40, no. 2, pp. 331–346, 2003.

[57] C. E. Jahr and C. F. Stevens, "Calcium permeability of the n-methyl-d-aspartate receptor channel in hippocampal neurons in culture," *Proceedings of the National Academy of Sciences*, vol. 90, no. 24, pp. 11573–11577, 1993.

[58] M. Graupner and N. Brunel, "Calcium-based plasticity model explains sensitivity of synaptic changes to spike pattern, rate, and dendritic location," *Proceedings of the National Academy of Sciences*, vol. 109, no. 10, pp. 3991–3996, 2012.

[59] C. O'Donnell, M. F. Nolan, and M. C. van Rossum, "Dendritic spine dynamics regulate the long-term stability of synaptic plasticity," *Journal of Neuroscience*, vol. 31, no. 45, pp. 16142–16156, 2011.

[60] R. C. Malenka, J. A. Kauer, R. S. Zucker, and R. A. Nicoll, "Postsynaptic calcium is sufficient for potentiation of hippocampal synaptic transmission," *Science*, vol. 242, no. 4875, pp. 81–84, 1988.

[61] J. A. Cummings, R. M. Mulkey, R. A. Nicoll, and R. C. Malenka, "Ca2+ signaling requirements for long-term depression in the hippocampus," *Neuron*, vol. 16, no. 4, pp. 825–833, 1996.

[62] J. Lisman, "Glutamatergic synapses are structurally and biochemically complex because of multiple plasticity processes: long-term potentiation, long-term depression, short-term potentiation and scaling," *Philosophical Transactions of the Royal Society B: Biological Sciences*, vol. 372, no. 1715, p. 20160260, 2017.

[63] B. A. Earnshaw and P. C. Bressloff, "Biophysical model of ampa receptor trafficking and its regulation during long-term potentiation/long-term depression," *Journal of Neuroscience*, vol. 26, no. 47, pp. 12362–12373, 2006.

[64] J. Jedrzejewska-Szmek, S. Damodaran, D. B. Dorman, and K. T. Blackwell, "Calcium dynamics predict direction of synaptic plasticity in striatal spiny projection neurons," *European Journal of Neuroscience*, vol. 45, no. 8, pp. 1044–1056, 2017.

[65] J. N. Bourne and K. M. Harris, "Balancing structure and function at hippocampal dendritic spines," *Annu. Rev. Neurosci.*, vol. 31, pp. 47–67, 2008.

[66] R. Calizo, M. Bell, A. Ron, M. Hu, S. Bhattacharya, N. Wong, W. Janssen, G. Perumal, P. Pederson, S. Scarlata, *et al.*, "Cell shape regulates subcellular organelle location to control early ca 2+ signal dynamics in vascular smooth muscle cells," *Scientific reports*, vol. 10, no. 1, pp. 1–17, 2020.

[67] S. R. Neves, P. Tsokas, A. Sarkar, E. A. Grace, P. Rangamani, S. M. Taubenfeld, C. M. Alberini, J. C. Schaff, R. D. Blitzer, I. I. Moraru, *et al.*, "Cell shape and negative links in regulatory motifs together control spatial information flow in signaling networks," *Cell*, vol. 133, no. 4, pp. 666–680, 2008.

[68] P. Rangamani, A. Lipshtat, E. U. Azeloglu, R. C. Calizo, M. Hu, S. Ghassemi, J. Hone, S. Scarlata, S. R. Neves, and R. Iyengar, "Decoding information in cell shape," *Cell*, vol. 154, no. 6, pp. 1356–1369, 2013.

[69] L. Héja, Z. Szabó, M. Péter, and J. Kardos, "Spontaneous ca2+ fluctuations arise in thin astrocytic processes with real 3d geometry," *Frontiers in Cellular Neuroscience*, vol. 15, p. 14, 2021.

[70] A. Cugno, T. M. Bartol, T. J. Sejnowski, R. Iyengar, and P. Rangamani, "Geometric principles of second messenger dynamics in dendritic spines," *Scientific reports*, vol. 9, no. 1, pp. 1–18, 2019.

[71] T. M. Bartol, D. X. Keller, J. P. Kinney, C. L. Bajaj, K. M. Harris, T. J. Sejnowski, and M. B. Kennedy, "Computational reconstitution of spine calcium transients from individual proteins," *Frontiers in synaptic neuroscience*, vol. 7, p. 17, 2015.

[72] N. Volfovsky, H. Parnas, M. Segal, and E. Korkotian, "Geometry of dendritic spines affects calcium dynamics in hippocampal neurons: theory and experiments," *Journal of neurophysiology*, vol. 82, no. 1, pp. 450–462, 1999.

[73] D. Holcman, Z. Schuss, and E. Korkotian, "Calcium dynamics in dendritic spines and spine motility," *Biophysical journal*, vol. 87, no. 1, pp. 81–91, 2004.

[74] M. J. Higley and B. L. Sabatini, "Calcium signaling in dendrites and spines: practical and functional considerations," *Neuron*, vol. 59, no. 6, pp. 902–913, 2008.

[75] H. Anwar, I. Hepburn, H. Nedelescu, W. Chen, and E. De Schutter, "Stochastic calcium mechanisms cause dendritic calcium spike variability," *Journal of Neuroscience*, vol. 33, no. 40, pp. 15848–15867, 2013.

[76] J. T. Dudman and M. F. Nolan, "Stochastically gating ion channels enable patterned spike firing through activity-dependent modulation of spike probability," *PLoS Comput Biol*, vol. 5, no. 2, p. e1000290, 2009.

[77] A. A. Faisal, J. A. White, and S. B. Laughlin, "Ion-channel noise places limits on the miniaturization of the brain's wiring," *Current Biology*, vol. 15, no. 12, pp. 1143–1149, 2005.

[78] R. C. Cannon, C. O'Donnell, and M. F. Nolan, "Stochastic ion channel gating in dendritic neurons: morphology dependence and probabilistic synaptic activation of dendritic spikes," *PLoS Comput Biol*, vol. 6, no. 8, p. e1000886, 2010.

[79] C. O'Donnell and M. F. Nolan, "Stochastic ion channel gating and probabilistic computation in dendritic neurons," in *The Computing Dendrite*, pp. 397–414, Springer, 2014.

[80] J. R. Stiles, T. M. Bartol, *et al.*, "Monte carlo methods for simulating realistic synaptic microphysiology using mcell," *Computational neuroscience: realistic modeling for experimentalists*, pp. 87–127, 2001.

[81] J. R. Stiles, D. Van Helden, T. M. Bartol, E. E. Salpeter, and M. M. Salpeter, "Miniature endplate current rise times¡ 100 μ s from improved dual recordings can be modeled with passive acetylcholine diffusion from a synaptic vesicle," *Proceedings of the National Academy of Sciences of the United States of America*, pp. 5747–5752, 1996.

[82] R. A. Kerr, T. M. Bartol, B. Kaminsky, M. Dittrich, J.-C. J. Chang, S. B. Baden, T. J. Sejnowski, and J. R. Stiles, "Fast monte carlo simulation methods for biological reaction-diffusion systems in solution and on surfaces," *SIAM journal on scientific computing*, vol. 30, no. 6, pp. 3126–3149, 2008.

[83] A. S. Ozcan, "Filopodia: a rapid structural plasticity substrate for fast learning," *Frontiers in synaptic neuroscience*, vol. 9, p. 12, 2017.

[84] P. García-López, V. García-Marín, and M. Freire, "Dendritic spines and development: towards a unifying model of spinogenesis—a present day review of cajal's histological slides and drawings," *Neural plasticity*, vol. 2010, 2010.

[85] N. Ofer, D. R. Berger, N. Kasthuri, J. W. Lichtman, and R. Yuste, "Ultrastructural analysis of dendritic spine necks reveals a continuum of spine morphologies," *bioRxiv*, 2021.

[86] M. Jasinska, E. Jasek-Gajda, O. Woznicka, G. J. Lis, E. Pyza, and J. A. Litwin, "Circadian clock regulates the shape and content of dendritic spines in mouse barrel cortex," *PloS one*, vol. 14, no. 11, p. e0225394, 2019.

[87] M. A. Chirillo, M. S. Waters, L. F. Lindsey, J. N. Bourne, and K. M. Harris, "Local resources of polyribosomes and ser promote synapse enlargement and spine clustering after long-term potentiation in adult rat hippocampus," *Scientific reports*, vol. 9, no. 1, pp. 1–14, 2019.

[88] J. Spacek and K. M. Harris, "Three-dimensional organization of smooth endoplasmic reticulum in hippocampal ca1 dendrites and dendritic spines of the immature and mature rat," *Journal of Neuroscience*, vol. 17, no. 1, pp. 190–203, 1997.

[89] A. Perez-Alvarez, S. Yin, C. Schulze, J. A. Hammer, W. Wagner, and T. G. Oertner, "Endoplasmic reticulum visits highly active spines and prevents runaway potentiation of synapses," *Nature communications*, vol. 11, no. 1, pp. 1–10, 2020.

[90] B. L. Sabatini, T. G. Oertner, and K. Svoboda, "The life cycle of ca2+ ions in dendritic spines," *Neuron*, vol. 33, no. 3, pp. 439–452, 2002.

[91] C. T. Lee, J. G. Laughlin, N. A. de La Beaumelle, R. E. Amaro, J. A. McCammon, R. Ramamoorthi, M. Holst, and P. Rangamani, "3d mesh processing using gamer 2 to enable reaction-diffusion simulations in realistic cellular geometries," *PLOS Comp Bio*, 2020.

[92] J. H. Kotaleski and K. T. Blackwell, "Modelling the molecular mechanisms of synaptic plasticity using systems biology approaches," *Nature Reviews Neuroscience*, vol. 11, no. 4, p. nrn2807, 2010.

[93] R. Yasuda, "Biophysics of biochemical signaling in dendritic spines: Implications in synaptic plasticity," *Biophysical Journal*, 2017.

[94] V. N. Friedhoff, G. Antunes, M. Falcke, and F. M. S. de Souza, "Stochastic reaction-diffusion modeling of calcium dynamics in 3d-dendritic spines of purkinje cells," *Biophysical Journal*, 2021.

[95] R. Yuste and T. Bonhoeffer, "Genesis of dendritic spines: insights from ultrastructural and imaging studies," *Nature Reviews Neuroscience*, vol. 5, no. 1, pp. 24–34, 2004.

[96] I. S. Stein and K. Zito, "Dendritic spine elimination: molecular mechanisms and implications," *The Neuroscientist*, vol. 25, no. 1, pp. 27–47, 2019.

[97] D. A. Ruhl, E. Bomba-Warczak, E. T. Watson, M. M. Bradberry, T. A. Peterson, T. Basu, A. Frelka, C. S. Evans, J. S. Briguglio, T. Basta, *et al.*, "Synaptotagmin 17 controls neurite outgrowth and synaptic physiology via distinct cellular pathways," *Nature communications*, vol. 10, no. 1, pp. 1–14, 2019.

[98] C. Lohmann and T. Bonhoeffer, "A role for local calcium signaling in rapid synaptic partner selection by dendritic filopodia," *Neuron*, vol. 59, no. 2, pp. 253–260, 2008.

[99] K. E. Sorra and K. M. Harris, "Overview on the structure, composition, function, development, and plasticity of hippocampal dendritic spines," *Hippocampus*, vol. 10, no. 5, pp. 501–511, 2000.

[100] G. Mahajan and S. Nadkarni, "Intracellular calcium stores mediate metaplasticity at hippocampal dendritic spines," *The Journal of physiology*, vol. 597, no. 13, pp. 3473–3502, 2019.

[101] R. L. Wasserstein, A. L. Schirm, and N. A. Lazar, "Moving to a world beyond "p¡ 0.05"," 2019.

[102] D. Ohadi and P. Rangamani, "Geometric control of frequency modulation of camp oscillations due to calcium in dendritic spines," *Biophysical journal*, vol. 117, no. 10, pp. 1981–1994, 2019.

[103] T. Mäki-Marttunen, N. Iannella, A. G. Edwards, G. Einevoll, and K. T. Blackwell, "A unified computational model for cortical post-synaptic plasticity," *bioRxiv*, 2020.

[104] U. S. Bhalla, "Signaling in small subcellular volumes. i. stochastic and diffusion effects on individual pathways," *Biophysical Journal*, vol. 87, no. 2, pp. 733–744, 2004.

[105] D. Ohadi, D. L. Schmitt, B. Calabrese, S. Halpain, J. Zhang, and P. Rangamani, "Computational modeling reveals frequency modulation of calcium-camp/pka pathway in dendritic spines," *Biophysical journal*, vol. 117, no. 10, pp. 1963–1980, 2019.

[106] C. Miermans, R. Kusters, C. Hoogenraad, and C. Storm, "Biophysical model of the role of actin remodeling on dendritic spine morphology," *PloS one*, vol. 12, no. 2, p. e0170113, 2017.

[107] C. T. Lee, M. Akamatsu, and P. Rangamani, "Value of models for membrane budding," *Current Opinion in Cell Biology*, vol. 71, pp. 38–45, 2021.

[108] A. Hayer and U. S. Bhalla, "Molecular switches at the synapse emerge from receptor and kinase traffic," *PLoS Comput Biol*, vol. 1, no. 2, p. e20, 2005.

[109] M. Ordyan, T. Bartol, M. Kennedy, P. Rangamani, and T. Sejnowski, "Interactions between calmodulin and neurogranin govern the dynamics of camkii as a leaky integrator," *PLoS computational biology*, vol. 16, no. 7, p. e1008015, 2020.

[110] H. J. Pi and J. E. Lisman, "Coupled phosphatase and kinase switches produce the tristability required for long-term potentiation and long-term depression," *Journal of Neuroscience*, vol. 28, no. 49, pp. 13132–13138, 2008.

[111] B. E. Herring and R. A. Nicoll, "Long-term potentiation: from camkii to ampa receptor trafficking," *Annual review of physiology*, vol. 78, pp. 351–365, 2016.

[112] M. A. Patterson, E. M. Szatmari, and R. Yasuda, "Ampa receptors are exocytosed in stimulated spines and adjacent dendrites in a ras-erk–dependent manner during long-term potentiation," *Proceedings of the National Academy of Sciences*, vol. 107, no. 36, pp. 15951–15956, 2010.

[113] A. R. Gallimore, A. R. Aricescu, M. Yuzaki, and R. Calinescu, "A computational model for the ampa receptor phosphorylation master switch regulating cerebellar long-term depression," *PLoS computational biology*, vol. 12, no. 1, p. e1004664, 2016.

[114] M. C. Ashby, S. R. Maier, A. Nishimune, and J. M. Henley, "Lateral diffusion drives constitutive exchange of ampa receptors at dendritic spines and is regulated by spine morphology," *Journal of Neuroscience*, vol. 26, no. 26, pp. 7046–7055, 2006.

[115] M. Bell, T. Bartol, T. Sejnowski, and P. Rangamani, "Dendritic spine geometry and spine apparatus organization govern the spatiotemporal dynamics of calcium," *The Journal of General Physiology*, 2019.

[116] L. Li, M. I. Stefan, and N. Le Novère, "Calcium input frequency, duration and amplitude differentially modulate the relative activation of calcineurin and camkii," *PloS one*, vol. 7, no. 9, p. e43810, 2012.

[117] D. X. Keller, K. M. Franks, T. M. Bartol Jr, and T. J. Sejnowski, "Calmodulin activation by calcium transients in the postsynaptic density of dendritic spines," *PLoS One*, vol. 3, no. 4, p. e2045, 2008.

[118] R. J. Colbran, "Protein phosphatases and calcium/calmodulin-dependent protein kinase ii-dependent synaptic plasticity," *Journal of Neuroscience*, vol. 24, no. 39, pp. 8404–8409, 2004.

[119] H. Schmidt, "Three functional facets of calbindin d-28k," *Frontiers in molecular neuroscience*, vol. 5, p. 25, 2012.

[120] M. Sanhueza and J. Lisman, "The camkii/nmdar complex as a molecular memory," *Molecular brain*, vol. 6, no. 1, pp. 1–8, 2013.

[121] J. Lisman, H. Schulman, and H. Cline, "The molecular basis of camkii function in synaptic and behavioural memory," *Nature Reviews Neuroscience*, vol. 3, no. 3, pp. 175–190, 2002.

[122] S.-J. R. Lee, Y. Escobedo-Lozoya, E. M. Szatmari, and R. Yasuda, "Activation of camkii in single dendritic spines during long-term potentiation," *Nature*, vol. 458, no. 7236, p. 299, 2009.

[123] G. Dupont, G. Houart, and P. De Koninck, "Sensitivity of cam kinase ii to the frequency of ca2+ oscillations: a simple model," *Cell calcium*, vol. 34, no. 6, pp. 485–497, 2003.

[124] P. Rangamani, M. G. Levy, S. Khan, and G. Oster, "Paradoxical signaling regulates structural plasticity in dendritic spines," *Proceedings of the National Academy of Sciences*, vol. 113, no. 36, pp. E5298–E5307, 2016.

[125] D. Genoux, U. Haditsch, M. Knobloch, A. Michalon, D. Storm, and I. M. Mansuy, "Protein phosphatase 1 is a molecular constraint on learning and memory," *Nature*, vol. 418, no. 6901, pp. 970–975, 2002.

[126] J. E. Lisman and A. M. Zhabotinsky, "A model of synaptic memory: a camkii/pp1 switch that potentiates transmission by organizing an ampa receptor anchoring assembly," *Neuron*, vol. 31, no. 2, pp. 191–201, 2001.

[127] P. Miller, A. M. Zhabotinsky, J. E. Lisman, and X.-J. Wang, "The stability of a stochastic camkii switch: dependence on the number of enzyme molecules and protein turnover," *PLoS Biol*, vol. 3, no. 4, p. e107, 2005.

[128] A. M. Zhabotinsky, "Bistability in the ca2+/calmodulin-dependent protein kinase-phosphatase system," *Biophysical journal*, vol. 79, no. 5, pp. 2211–2221, 2000.

[129] I. Lengyel, K. Voss, M. Cammarota, K. Bradshaw, V. Brent, K. Murphy, K. Giese, J. Rostas, and T. Bliss, "Autonomous activity of camkii is only transiently increased following the induction of long-term potentiation in the rat hippocampus," *European Journal of Neuroscience*, vol. 20, no. 11, pp. 3063–3072, 2004.

[130] J. M. Bradshaw, Y. Kubota, T. Meyer, and H. Schulman, "An ultrasensitive ca2+/calmodulin-dependent protein kinase ii-protein phosphatase 1 switch facilitates specificity in postsynaptic calcium signaling," *Proceedings of the National Academy of Sciences*, vol. 100, no. 18, pp. 10512–10517, 2003.

[131] P. J. Michalski, "First demonstration of bistability in camkii, a memory-related kinase," *Biophysical Journal*, vol. 106, no. 6, pp. 1233–1235, 2014.

[132] H. Urakubo, M. Sato, S. Ishii, and S. Kuroda, "In vitro reconstitution of a camkii memory switch by an nmda receptor-derived peptide," *Biophysical journal*, vol. 106, no. 6, pp. 1414–1420, 2014.

[133] D. Singh and U. S. Bhalla, "Subunit exchange enhances information retention by camkii in dendritic spines," *Elife*, vol. 7, p. e41412, 2018.

[134] P. Michalski, "The delicate bistability of camkii," *Biophysical journal*, vol. 105, no. 3, pp. 794–806, 2013.

[135] K. P. Giese, N. B. Fedorov, R. K. Filipkowski, and A. J. Silva, "Autophosphorylation at thr286 of the α calcium-calmodulin kinase ii in ltp and learning," *Science*, vol. 279, no. 5352, pp. 870–873, 1998.

[136] N. Otmakhov, S. Regmi, and J. E. Lisman, "Fast decay of camkii fret sensor signal in spines after ltp induction is not due to its dephosphorylation," *PLoS One*, vol. 10, no. 6, p. e0130457, 2015.

[137] J.-Y. Chang, P. Parra-Bueno, T. Laviv, E. M. Szatmari, S.-J. R. Lee, and R. Yasuda, "Camkii autophosphorylation is necessary for optimal integration of ca2+ signals during ltp induction, but not maintenance," *Neuron*, vol. 94, no. 4, pp. 800–808, 2017.

[138] P. B. Allen, C. C. Ouimet, and P. Greengard, "Spinophilin, a novel protein phosphatase 1 binding protein localized to dendritic spines," *Proceedings of the National Academy of Sciences*, vol. 94, no. 18, pp. 9956–9961, 1997.

[139] W. Morishita, J. H. Connor, H. Xia, E. M. Quinlan, S. Shenolikar, and R. C. Malenka, "Regulation of synaptic strength by protein phosphatase 1," *Neuron*, vol. 32, no. 6, pp. 1133–1148, 2001.

[140] M. Sheng and M. J. Kim, "Postsynaptic signaling and plasticity mechanisms," *Science*, vol. 298, no. 5594, pp. 776–780, 2002.

[141] S.-H. Shi, Y. Hayashi, R. S. Petralia, S. H. Zaman, R. J. Wenthold, K. Svoboda, and R. Malinow, "Rapid spine delivery and redistribution of ampa receptors after synaptic nmda receptor activation," *Science*, vol. 284, no. 5421, pp. 1811–1816, 1999.

[142] A. R. Gallimore, T. Kim, K. Tanaka-Yamamoto, and E. De Schutter, "Switching on depression and potentiation in the cerebellum," *Cell reports*, vol. 22, no. 3, pp. 722–733, 2018.

[143] E. Thiels, E. Norman, G. Barrionuevo, and E. Klann, "Transient and persistent increases in protein phosphatase activity during long-term depression in the adult hippocampus in vivo," *Neuroscience*, vol. 86, no. 4, pp. 1023–1029, 1998.

[144] S. S. Correia, S. Bassani, T. C. Brown, M.-F. Lisé, D. S. Backos, A. El-Husseini, M. Passafaro, and J. A. Esteban, "Motor protein–dependent transport of ampa receptors into spines during long-term potentiation," *Nature neuroscience*, vol. 11, no. 4, pp. 457–466, 2008.

[145] M. J. Kim, K. Futai, J. Jo, Y. Hayashi, K. Cho, and M. Sheng, "Synaptic accumulation of psd-95 and synaptic function regulated by phosphorylation of serine-295 of psd-95," *Neuron*, vol. 56, no. 3, pp. 488–502, 2007.

[146] R. Kusters, L. C. Kapitein, C. C. Hoogenraad, and C. Storm, "Shape-induced asymmetric diffusion in dendritic spines allows efficient synaptic ampa receptor trapping," *Biophysical journal*, vol. 105, no. 12, pp. 2743–2750, 2013.

[147] J. I. Arellano, R. Benavides-Piccione, J. DeFelipe, and R. Yuste, "Ultrastructure of dendritic spines: correlation between synaptic and spine morphologies," *Frontiers in neuroscience*, vol. 1, p. 10, 2007.

[148] C. T. Lee, J. G. Laughlin, N. A. de La Beaumelle, R. E. Amaro, J. A. McCammon, R. Ramamoorthi, M. Holst, and P. Rangamani, "3d mesh processing using gamer 2 to enable reaction-diffusion simulations in realistic cellular geometries," *PLoS computational biology*, vol. 16, no. 4, p. e1007756, 2020.

[149] P. Opazo, S. Labrecque, C. M. Tigaret, A. Frouin, P. W. Wiseman, P. De Koninck, and D. Choquet, "Camkii triggers the diffusional trapping of surface ampars through phosphorylation of stargazin," *Neuron*, vol. 67, no. 2, pp. 239–252, 2010.

[150] S. G. Miller and M. B. Kennedy, "Regulation of brain type ii ca2+ calmodulin-dependent protein kinase by autophosphorylation: A ca2+-triggered molecular switch," *Cell*, vol. 44, no. 6, pp. 861–870, 1986.

[151] R. M. Mulkey, S. Endo, S. Shenolikar, and R. C. Malenka, "Involvement of a calcineurin/inhibitor-1 phosphatase cascade in hippocampal long-term depression," *Nature*, vol. 369, no. 6480, pp. 486–488, 1994.

[152] N. Shioda and K. Fukunaga, "Physiological and pathological roles of camkii-pp1 signaling in the brain," *International Journal of Molecular Sciences*, vol. 19, no. 1, p. 20, 2018.

[153] S. Yagishita, A. Hayashi-Takagi, G. C. Ellis-Davies, H. Urakubo, S. Ishii, and H. Kasai, "A critical time window for dopamine actions on the structural plasticity of dendritic spines," *Science*, vol. 345, no. 6204, pp. 1616–1620, 2014.

[154] M. Park, J. M. Salgado, L. Ostroff, T. D. Helton, C. G. Robinson, K. M. Harris, and M. D. Ehlers, "Plasticity-induced growth of dendritic spines by exocytic trafficking from recycling endosomes," *Neuron*, vol. 52, no. 5, pp. 817–830, 2006.

[155] M. Park, E. C. Penick, J. G. Edwards, J. A. Kauer, and M. D. Ehlers, "Recycling endosomes supply ampa receptors for ltp," *Science*, vol. 305, no. 5692, pp. 1972–1975, 2004.

[156] J. D. Shepherd and R. L. Huganir, "The cell biology of synaptic plasticity: Ampa receptor trafficking," *Annu. Rev. Cell Dev. Biol.*, vol. 23, pp. 613–643, 2007.

[157] L. N. Cornelisse, R. A. van Elburg, R. M. Meredith, R. Yuste, and H. D. Mansvelder, "High speed two-photon imaging of calcium dynamics in dendritic spines: consequences for spine calcium kinetics and buffer capacity," *PloS one*, vol. 2, no. 10, p. e1073, 2007.

[158] K. Holthoff and D. Tsay, "Calcium dynamics in spines: link to synaptic plasticity," *Experimental physiology*, vol. 87, no. 6, pp. 725–731, 2002.

[159] A. Petersen and N. Z. Gerges, "Neurogranin regulates cam dynamics at dendritic spines," *Scientific reports*, vol. 5, no. 1, pp. 1–10, 2015.

[160] M. B. Kennedy, H. C. Beale, H. J. Carlisle, and L. R. Washburn, "Integration of biochemical signalling in spines," *Nature Reviews Neuroscience*, vol. 6, no. 6, pp. 423–434, 2005.

[161] M. J. Broadhead, M. H. Horrocks, F. Zhu, L. Muresan, R. Benavides-Piccione, J. DeFelipe, D. Fricker, M. V. Kopanitsa, R. R. Duncan, D. Klenerman, *et al.*, "Psd95 nanoclusters are postsynaptic building blocks in hippocampus circuits," *Scientific reports*, vol. 6, no. 1, pp. 1–14, 2016.

[162] R. P. Bhattacharyya, A. Reményi, B. J. Yeh, and W. A. Lim, "Domains, motifs, and scaffolds: the role of modular interactions in the evolution and wiring of cell signaling circuits," *Annu. Rev. Biochem.*, vol. 75, pp. 655–680, 2006.

[163] L. P. Savtchenko and D. A. Rusakov, "Moderate ampa receptor clustering on the nanoscale can efficiently potentiate synaptic current," *Philosophical Transactions of the Royal Society B: Biological Sciences*, vol. 369, no. 1633, p. 20130167, 2014.

[164] J.-i. Tanaka, M. Matsuzaki, E. Tarusawa, A. Momiyama, E. Molnar, H. Kasai, and R. Shigemoto, "Number and density of ampa receptors in single synapses in immature cerebellum," *Journal of Neuroscience*, vol. 25, no. 4, pp. 799–807, 2005.

[165] D. Freche, U. Pannasch, N. Rouach, and D. Holcman, "Synapse geometry and receptor dynamics modulate synaptic strength," *PloS one*, vol. 6, no. 10, p. e25122, 2011.

[166] J. Montes, J. M. Peña, J. DeFelipe, O. Herreras, and A. Merchan-Perez, "The influence of synaptic size on ampa receptor activation: a monte carlo model," *PloS one*, vol. 10, no. 6, p. e0130924, 2015.

[167] Y. Fukazawa and R. Shigemoto, "Intra-synapse-type and inter-synapse-type relationships between synaptic size and ampar expression," *Current opinion in neurobiology*, vol. 22, no. 3, pp. 446–452, 2012.

[168] E. Tarusawa, K. Matsui, T. Budisantoso, E. Molnár, M. Watanabe, M. Matsui, Y. Fukazawa, and R. Shigemoto, "Input-specific intrasynaptic arrangements of ionotropic glutamate receptors and their impact on postsynaptic responses," *Journal of Neuroscience*, vol. 29, no. 41, pp. 12896–12908, 2009.

[169] S. Hoops, S. Sahle, R. Gauges, C. Lee, J. Pahle, N. Simus, M. Singhal, L. Xu, P. Mendes, and U. Kummer, "Copasi—a complex pathway simulator," *Bioinformatics*, vol. 22, no. 24, pp. 3067–3074, 2006.

[170] R. C. Carroll, E. C. Beattie, M. Von Zastrow, and R. C. Malenka, "Role of ampa receptor endocytosis in synaptic plasticity," *Nature Reviews Neuroscience*, vol. 2, no. 5, pp. 315–324, 2001.

[171] J.-Y. Chang, Y. Nakahata, Y. Hayano, and R. Yasuda, "Mechanisms of ca 2+/calmodulin-dependent kinase ii activation in single dendritic spines," *Nature communications*, vol. 10, no. 1, pp. 1–12, 2019.

[172] M. Park, "Ampa receptor trafficking for postsynaptic potentiation," *Frontiers in cellular neuroscience*, vol. 12, p. 361, 2018.

[173] D. Choquet, "Linking nanoscale dynamics of ampa receptor organization to plasticity of excitatory synapses and learning," *Journal of Neuroscience*, vol. 38, no. 44, pp. 9318–9329, 2018.

[174] R. C. Malenka and M. F. Bear, "Ltp and ltd: an embarrassment of riches," *Neuron*, vol. 44, no. 1, pp. 5–21, 2004.

[175] H. Zhang and C. R. Bramham, "Bidirectional dysregulation of ampa receptor-mediated synaptic transmission and plasticity in brain disorders," *Frontiers in Synaptic Neuroscience*, vol. 12, p. 26, 2020.

[176] J. E. Hassinger, G. Oster, D. G. Drubin, and P. Rangamani, "Design principles for robust vesiculation in clathrin-mediated endocytosis," *Proceedings of the national academy of sciences*, vol. 114, no. 7, pp. E1118–E1127, 2017.

[177] S. Watanabe, B. R. Rost, M. Camacho-Pérez, M. W. Davis, B. Söhl-Kielczynski, C. Rosenmund, and E. M. Jorgensen, "Ultrafast endocytosis at mouse hippocampal synapses," *Nature*, vol. 504, no. 7479, pp. 242–247, 2013.

[178] C. G. Dotti, J. A. Esteban, and M. D. Ledesma, "Lipid dynamics at dendritic spines," *Frontiers in neuroanatomy*, vol. 8, p. 76, 2014.

[179] S. Okabe, "Regulation of actin dynamics in dendritic spines: Nanostructure, molecular mobility, and signaling mechanisms," *Molecular and Cellular Neuroscience*, p. 103564, 2020.

[180] S. J. Coultrap, R. K. Freund, H. O'Leary, J. L. Sanderson, K. W. Roche, M. L. Dell'Acqua, and K. U. Bayer, "Autonomous camkii mediates both ltp and ltd using a mechanism for differential substrate site selection," *Cell reports*, vol. 6, no. 3, pp. 431–437, 2014.

[181] Y. E. Rodrigues, C. M. Tigaret, H. Marie, C. O'Donnell, and R. Veltz, "A stochastic model of hippocampal synaptic plasticity with geometrical readout of enzyme dynamics," *bioRxiv*, 2021.

[182] M. Matolcsi and N. Giordano, "A novel explanation for observed camkii dynamics in dendritic spines with added egta or bapta," *Biophysical journal*, vol. 108, no. 4, pp. 975–985, 2015.

[183] C. M. Robinson, M. R. Patel, and D. J. Webb, "Super resolution microscopy is poised to reveal new insights into the formation and maturation of dendritic spines," *F1000Research*, vol. 5, 2016.

[184] R. Yasuda, "Studying signal transduction in single dendritic spines," *Cold Spring Harbor perspectives in biology*, vol. 4, no. 10, p. a005611, 2012.

[185] M. Zeng, Y. Shang, Y. Araki, T. Guo, R. L. Huganir, and M. Zhang, "Phase transition in postsynaptic densities underlies formation of synaptic complexes and synaptic plasticity," *Cell*, vol. 166, no. 5, pp. 1163–1175, 2016.

[186] L. Zhong and N. Z. Gerges, "Neurogranin regulates metaplasticity," *Frontiers in molecular neuroscience*, vol. 12, p. 322, 2020.

[187] C. J. Penny and M. G. Gold, "Mechanisms for localising calcineurin and camkii in dendritic spines," *Cellular signalling*, vol. 49, pp. 46–58, 2018.

[188] M. F. Becker and C. Tetzlaff, "The biophysical basis underlying the maintenance of early phase long-term potentiation," *PLoS computational biology*, vol. 17, no. 3, p. e1008813, 2021.

[189] N. Scheefhals and H. D. MacGillavry, "Functional organization of postsynaptic glutamate receptors," *Molecular and Cellular Neuroscience*, vol. 91, pp. 82–94, 2018.

[190] J. Z. Zhang, T.-W. Lu, L. M. Stolerman, B. Tenner, J. R. Yang, J.-F. Zhang, M. Falcke, P. Rangamani, S. S. Taylor, S. Mehta, *et al.*, "Phase separation of a pka regulatory subunit controls camp compartmentation and oncogenic signaling," *Cell*, vol. 182, no. 6, pp. 1531–1544, 2020.

[191] C. Tetzlaff, C. Kolodziejski, I. Markelic, and F. Wörgötter, "Time scales of memory, learning, and plasticity," *Biological cybernetics*, vol. 106, no. 11-12, pp. 715–726, 2012.

[192] A. Pinggera, J. F. Watson, and I. H. Greger, *AMPA Receptors*, pp. 635–644. American Cancer Society, 2020.

[193] K. Czöndör, M. Mondin, M. Garcia, M. Heine, R. Frischknecht, D. Choquet, J.-B. Sibarita, and O. R. Thoumine, "Unified quantitative model of ampa receptor trafficking at synapses," *Proceedings of the National Academy of Sciences*, vol. 109, no. 9, pp. 3522–3527, 2012.

[194] D. Choquet and A. Triller, "The role of receptor diffusion in the organization of the postsynaptic membrane," *Nature Reviews Neuroscience*, vol. 4, no. 4, pp. 251–265, 2003.

[195] J. G. Hanley, "Ampa receptor trafficking pathways and links to dendritic spine morphogenesis," *Cell adhesion & migration*, vol. 2, no. 4, pp. 276–282, 2008.

[196] D. Nair, E. Hosy, J. D. Petersen, A. Constals, G. Giannone, D. Choquet, and J.-B. Sibarita, "Super-resolution imaging reveals that ampa receptors inside synapses are dynamically organized in nanodomains regulated by psd95," *Journal of Neuroscience*, vol. 33, no. 32, pp. 13204–13224, 2013.

[197] N. Hoze, D. Nair, E. Hosy, C. Sieben, S. Manley, A. Herrmann, J.-B. Sibarita, D. Choquet, and D. Holcman, "Heterogeneity of ampa receptor trafficking and molecular interactions revealed by superresolution analysis of live cell imaging," *Proceedings of the National Academy of Sciences*, vol. 109, no. 42, pp. 17052–17057, 2012.

[198] A. Dani, B. Huang, J. Bergan, C. Dulac, and X. Zhuang, "Superresolution imaging of chemical synapses in the brain," *Neuron*, vol. 68, no. 5, pp. 843–856, 2010.

[199] H. Makino and R. Malinow, "Ampa receptor incorporation into synapses during ltp: the role of lateral movement and exocytosis," *Neuron*, vol. 64, no. 3, pp. 381–390, 2009.

[200] Y. Hayashi, S.-H. Shi, J. A. Esteban, A. Piccini, J.-C. Poncer, and R. Malinow, "Driving ampa receptors into synapses by ltp and camkii: requirement for glur1 and pdz domain interaction," *Science*, vol. 287, no. 5461, pp. 2262–2267, 2000.

[201] M. K. Bell and P. Rangamani, "Crosstalk between biochemical signaling and trafficking determines ampar dynamics in synaptic plasticity," *bioRxiv*, 2021.

[202] Y. Hayashi and A. K. Majewska, "Dendritic spine geometry: functional implication and regulation," *Neuron*, vol. 46, no. 4, pp. 529–532, 2005.

[203] K. M. Harris and J. K. Stevens, "Dendritic spines of ca 1 pyramidal cells in the rat hippocampus: serial electron microscopy with reference to their biophysical characteristics," *Journal of Neuroscience*, vol. 9, no. 8, pp. 2982–2997, 1989.

[204] Y. Shinohara and H. Hirase, "Size and receptor density of glutamatergic synapses: a viewpoint from left-right asymmetry of ca3-ca1 connections," *Frontiers in neuroanatomy*, vol. 3, p. 10, 2009.

[205] M. Borczyk, M. A. Śliwińska, A. Caly, T. Bernas, and K. Radwanska, "Neuronal plasticity affects correlation between the size of dendritic spine and its postsynaptic density," *Scientific reports*, vol. 9, no. 1, pp. 1–12, 2019.

[206] J. M. Henley, E. A. Barker, and O. O. Glebov, "Routes, destinations and delays: recent advances in ampa receptor trafficking," *Trends in neurosciences*, vol. 34, no. 5, pp. 258–268, 2011.

[207] T. A. Blanpied, D. B. Scott, and M. D. Ehlers, "Dynamics and regulation of clathrin coats at specialized endocytic zones of dendrites and spines," *Neuron*, vol. 36, no. 3, pp. 435–449, 2002.

[208] V. Anggono and R. L. Huganir, "Regulation of ampa receptor trafficking and synaptic plasticity," *Current opinion in neurobiology*, vol. 22, no. 3, pp. 461–469, 2012.

[209] A. Triller and D. Choquet, "New concepts in synaptic biology derived from single-molecule imaging," *Neuron*, vol. 59, no. 3, pp. 359–374, 2008.

[210] Y. Chen and B. L. Sabatini, "Signaling in dendritic spines and spine microdomains," *Current opinion in neurobiology*, vol. 22, no. 3, pp. 389–396, 2012.

[211] M. V. Holst, M. K. Bell, C. T. Lee, and P. Rangamani, "Stochastic simulations reveal that dendritic spine morphology regulates synaptic plasticity in a deterministic manner," *bioRxiv*, 2021.

[212] D. Wu, T. Bacaj, W. Morishita, D. Goswami, K. L. Arendt, W. Xu, L. Chen, R. C. Malenka, and T. C. Südhof, "Postsynaptic synaptotagmins mediate ampa receptor exocytosis during ltp," *Nature*, vol. 544, no. 7650, pp. 316–321, 2017.

[213] F. Santamaria, J. Gonzalez, G. J. Augustine, and S. Raghavachari, "Quantifying the effects of elastic collisions and non-covalent binding on glutamate receptor trafficking in the post-synaptic density," *PLoS Comput Biol*, vol. 6, no. 5, p. e1000780, 2010.

[214] A. Denizot, H. Berry, and S. Venugopal, "Intracellular calcium signals in astrocytes, computational modeling of," 2020.

[215] K. T. Haas, B. Compans, M. Letellier, T. M. Bartol, D. Grillo-Bosch, T. J. Sejnowski, M. Sainlos, D. Choquet, O. Thoumine, and E. Hosy, "Pre-post synaptic alignment through neuroligin-1 tunes synaptic transmission efficiency," *Elife*, vol. 7, p. e31755, 2018.

[216] A. Govindarajan, R. J. Kelleher, and S. Tonegawa, "A clustered plasticity model of long-term memory engrams," *Nature Reviews Neuroscience*, vol. 7, no. 7, pp. 575–583, 2006.

[217] A. Gidon, T. A. Zolnik, P. Fidzinski, F. Bolduan, A. Papoutsi, P. Poirazi, M. Holtkamp, I. Vida, and M. E. Larkum, "Dendritic action potentials and computation in human layer 2/3 cortical neurons," *Science*, vol. 367, no. 6473, pp. 83–87, 2020.

[218] R. Francavilla, V. Villette, O. Martel, and L. Topolnik, "Calcium dynamics in dendrites of hippocampal ca1 interneurons in awake mice," *Frontiers in Cellular Neuroscience*, vol. 13, p. 98, 2019.

[219] R. Robinson and R. Stokes, "Electrolyte solutions, butterworths scientific publications," 1959.

[220] M. Naraghi and E. Neher, "Linearized buffered ca2+ diffusion in microdomains and its implications for calculation of [ca2+] at the mouth of a calcium channel," *Journal of Neuroscience*, vol. 17, no. 18, pp. 6961–6973, 1997.

[221] B. Schwaller, "Cytosolic ca2+ buffers," *Cold Spring Harbor perspectives in biology*, p. a004051, 2010.

[222] M. Vargas-Caballero and H. P. Robinson, "Fast and slow voltage-dependend dynamics of magnesium block in the nmda receptor: The asymmetric trapping block model," *Journal of Neuroscience*, vol. 24, no. 27, pp. 6171–6180, 2004.

[223] P. Jonas, G. Major, and B. Sakmann, "Quantal components of unitary epscs at the mossy fibre synapse on ca3 pyramidal cells of rat hippocampus.," *Journal of Physiology*, vol. 472, pp. 615–663, 1993.

[224] J. Schoberl, "Netgen an advancing front 2d/3d-mesh generator based on abstract rules," *Comput Visual Sci*, vol. 1, pp. 41–52, 1997.

[225] M. Borczyk, M. A. Sliwinska, A. Caly, T. Bernas, and K. Radwanska, "Neuronal plasticity affects correlation between the size of dendritic spine and its postsynaptic density," *Scientific Reports*, vol. 9, no. 1963, 2019.

[226] C. T. Lee, J. G. Laughlin, J. B. Moody, R. E. Amaro, J. A. McCammon, M. Holst, and P. Rangamani, "An Open-Source Mesh Generation Platform for Biophysical Modeling Using Realistic Cellular Geometries," *Biophysical Journal*, vol. 118, no. 5, pp. 1003–1008, 2020.

[227] X. Chen, J. M. Levy, A. Hou, C. Winters, R. Azzam, A. A. Sousa, R. D. Leapman, R. A. Nicoll, and T. S. Reese, "Psd-95 family maguks are essential for anchoring ampa and nmda receptor complexes at the postsynaptic density," *Proceedings of the National Academy of Sciences*, vol. 112, no. 50, pp. E6983–E6992, 2015.

[228] L. Li, M. Lai, S. Cole, N. Le Novère, and S. J. Edelstein, "Neurogranin stimulates ca2+/calmodulin-dependent kinase ii by suppressing calcineurin activity at specific calcium spike frequencies," *PLoS computational biology*, vol. 16, no. 2, p. e1006991, 2020.

[229] R. P. Munton, S. Vizi, and I. M. Mansuy, "The role of protein phosphatase-1 in the modulation of synaptic and structural plasticity," *FEBS letters*, vol. 567, no. 1, pp. 121–128, 2004.